SELF-EXCITED OSCILLATIONS OF THE IMPINGING MULTI-SLOT PLANAR JET

SELF-EXCITED OSCILLATIONS OF THE IMPINGING MULTI-SLOT PLANAR JET

By

DÓNAL FINNERTY, B.A., B.A.I., M.A.Sc.

A Thesis

Submitted to the School of Graduate Studies in

Partial Fulfillment of the Requirements for the Degree

Doctor of Philosophy

McMaster University

Doctor of Philosophy (2019)	McMaster University
(Mechanical Engineering)	Hamilton, Ontario, Canada

TITLE:	Self-excited oscillations of the impinging multi-slot planar jet
AUTHOR:	Dónal Finnerty B.A., (Applied Mathematics) B.A.I., (Mechanical and Manufacturing Engineering) Trinity College, Dublin University M.A.Sc. (Mechanical Engineering) McMaster University
SUPERVISORS:	Dr. Joseph R. McDermid Dr. Samir Ziada
NUMBER OF PAGES:	xxi, 116

Nil boni hodie. Diem perdidi.

I did nothing good today. I have lost a day.

-A sundial quote found on the
Mission Cemetery Sundial - Santa Barbara, CA

Melius cras fore.

Tomorrow will be better

-A note scribbled in the acoustics lab in encouragement
after a fruitless night of Particle Image Velocimetry

ABSTRACT

Impinging high-speed planar jets are susceptible to self-excited aeroacoustic feedback mechanisms due to the coupling of the highly unstable shear layer and upstream travelling pressure waves created by the jet impingement. This aeroacoustic feedback mechanism results in intense narrowband acoustic tones and large amplitude oscillations of the jet column which are undesirable for its use as an actuator for coating weight control in the continuous gas-jet wiping line. This thesis experimentally investigates the use of auxiliary high-speed planar jets for the purpose of interrupting and reducing the amplitude of the negative effects of the aeroacoustic feedback mechanism.

Testing was performed using a planar multi-slot nozzle jet over a range of impingement distances, velocities and nozzle widths. The amplitudes of the acoustic tones were found to be a function of the ratio of velocities between the main and auxiliary jets with the tones found to be eliminated at sufficiently high-velocity ratios. Larger auxiliary jet widths were found to further reduce the amplitude of the tones in conjunction with the velocity ratio. The reduction of the amplitude of the tones was accompanied by a reduction in the maximum fluctuating pressure at the plate by 75% and an increase in the maximum static pressure by 30% indicating a reduction in the oscillations of the jet column.

A proper orthogonal decomposition of particle image velocimetry vector fields revealed that an increase in the auxiliary jet velocity increased the percentage of the kinetic energy of the mean flow field of the jet but decreased the percentage of the kinetic energy of the modes associated with the aeroacoustic feedback mechanism. The vorticity of the

modes associated with the aeroacoustic feedback mechanism shows that the coherent structures inherent to the feedback mechanism reduce in size and strength with increasing auxiliary jet velocity. Time-averaged particle image velocimetry vector fields revealed that at jet conditions where the acoustic tones were reduced, the interaction of the auxiliary jets reduced the maximum vorticity of the shear layer by 35% at the jet exit. Smaller amplitude and thicker shear layers are known to result in smaller maximum growth rates of disturbances in shear layers. The reduced growth rate resulted in smaller coherent structures in the jet shear layer which resulted in the smaller jet column oscillations and the elimination of the acoustic tones.

ACKNOWLEDGEMENTS

This thesis would not have been possible if it was not for the patience and guidance of my supervisors. Not only were both men exceedingly generous with their time and advice but, on multiple occasions, they both made me re-evaluate the amount of patience and compassion possible from a boss.

This document definitely took a setback with the unfortunate passing of Dr. Samir Ziada. His death has saddened all of us students who worked so closely with him but the example he set in living life now, rather than later, will stay with us for the years to come.

There are legitimately too many people who need to be acknowledged for helping me complete this work and keep my sanity but a condensed list: My family, my lab mates, my friends, the technicians, mech eng staff and the softball team.

TABLE OF CONTENTS

NOMENCLATURE

a	Auxiliary jet slot width
c	Speed of sound in air
d	Main jet slot width
f	Frequency
h	Impingement distance
κ	Convection coefficient
s	Setback distance of the auxiliary jet nozzle
St	Strouhal Number
St_{eff}	Effective Strouhal Number
V_A	Auxiliary jet slot velocity
V_C	Convection velocity of coherent structures
V_{Calib}	Velocity of a calibrated P.I.V. vector
V_{eff}	Effective velocity of the coherent structures
V_M	Main jet slot velocity
V_{PIV}	Velocity of a P.I.V. vector
x	Axial distance from the jet nozzle lip
y	Radial distance from the jet nozzle lip

LIST OF TABLES

LIST OF FIGURES

Chapter 1
Introduction

Steel is a major component in the automotive and construction industries and in the manufacture of consumer goods due to its high strength and low cost. However, due to its susceptibility to corrosion, steel must be protected in order to maintain its expected performance and meet durability expectations. Continuous hot-dip galvanising is an extremely cost-effective method used to protect sheet steel against atmospheric corrosion for use in these industries [1], [2]. Galvanized coatings from the continuous galvanising line provide the desired corrosion protection in the form of a well-bonded, tough barrier coating as well as a sacrificial anode to protect the steel if the barrier protection is breached.

In the continuous hot-dip galvanising process, coils of sheet steel are unrolled and fed as a continuous sheet through various cleaning and heat treatments in preparation for galvanising. The steel sheet is then continuously fed into a bath of molten Zn-Al alloys, where the metallic coating system reactively wets the substrate and is then extracted vertically to control the coating weight thickness and to allow the coating to solidify. Coating thickness or coating weight control is accomplished using two large, high-velocity planar jets, referred to as air-knives, impinging upon the sheet with the objective of removing the excess liquid coating material from the substrate, allowing it to fall back into the molten bath. When the coating material has solidified, the steel sheet goes through postprocesses such as temper rolling, tension levelling and the addition of lubricant before being inspected, re-coiled and sent to the client.

The pressure gradients and shear stress at the substrate created by the planar jets, in conjunction with gravity, "squeegee" excess coating material back into the bath [3]. The design and operating parameters of the air-knives result in different pressure gradients and shear stress profiles at the substrate. The planar jet design and control of the operating parameters control the final Zn-alloy coating weight on the substrate.

The impingement of jet flows on rigid surfaces is known to generate high amplitude acoustic tones due to the interaction of the instabilities in the jet flow with the perturbations in the pressure field created by the jet impingement. Instabilities at the nozzle exit generate vortices in the jet shear layer, which grow as they are convected by the jet flow to impinge upon the relatively rigid substrate surface. The impingement of the vortices on the substrate generates a pressure wave that travels upstream to cause an instability at the nozzle. The vortex creation at the nozzle and the generation of the pressure wave eventually "lock-in" and become periodic, resulting in a robust feedback mechanism. The vortices growing in the shear layer as they are convected by the jet cause the jet column to oscillate. The periodic pressure waves are the source of the high amplitude acoustic tones. The acoustic tones can interact with the volume of air between the nozzle and the rigid surface, exciting a trapped standing wave. The resonance of the volume causes the vortices to be further amplified resulting in larger oscillations of the jet column and higher amplitude acoustic tones. This interaction between the jet instabilities and the feedback acoustic pressure waves is an example of an aeroacoustic feedback mechanism.

Aeroacoustic feedback mechanisms present two specific problems for continuous hot-dip galvanising. The first problem is the amplitude of the noise being produced by the air-knives impinging upon the substrate. The second problem is the large oscillations of the jet column.

Acoustic tones generated by jet impingement can be in excess of 120 dB, which creates a workplace hygiene issue due to occupational exposure limits for employees. OSHA defines acceptable exposure for the 8 hour workday week as 87 dB. This regulation means a worker exposed to 120 dB for 6 minutes would have to spend the rest of their day in a quiet environment [4]. This requires that employers limit employee’s time in the vicinity of the air-knives and commit time and money on mitigation strategies, training and equipment.

The final coating weight from the continuous galvanising line is not of uniform thickness and there has been much speculation that coating weight variations on the sheet steel are the result of jet instabilities and motion of the jet column [5], [6]. The lifetime of galvanised steel is proportional to the thickness of the coating material on the substrate and, thus, variations in the coating weight require that manufacturers “overcoat” the sheet steel to comply with client’s minimum coating weight requirements. This overcoating results in a financial loss to the manufacturer due to the relatively high cost of the metallic components of the coating materials.

While patents have been granted for multiple slot planar jet designs for use in continuous hot-dip galvanizing [7], the technology has not yet been implemented on industrial continuous galvanising lines, remaining a niche design of air-knife used mainly on experimental galvanizing facilities. There have been several proposed benefits for the use of multiple slot air-knives:

- a delay in the onset of splashing: the complete stripping of the coating from the substrate that results in an inferior coating of the steel [8];
- a method of eliminating spanwise vortices which have been attributed to be the cause of “check-mark” stain, an undesirable coating defect [9];
- an improved method for the control of coating weight over traditional air-knife designs [10], [11].

However, despite existing research on shear layers that indicates that multiple jets could influence the growth rate of convected vortices, there has been no significant research into the influence of multiple slot jets on the aeroacoustic feedback mechanism.

Fundamental work on shear layer instabilities has shown that the growth rate of perturbations in shear layers is proportional to the velocity gradient across it [12], [13]. An auxiliary jet could have the capability to reduce the velocity gradient of the shear layer of an air-knife. The growth rate of shear layer vortices of a multiple jet air-knife design could be controlled depending on the velocity gradient created by the interaction between adjacent jets. Decreasing the growth rate of the vortices such that their size at impingement does not result in a pressure wave of sufficient strength to trigger instabilities at the jet nozzle would break down the feedback mechanism. Without the aeroacoustic feedback mechanism, the oscillations of the jet column and the intense tones of the jet should be eliminated and the coating weight consistency and acoustic environment of the continuous galvanising line improved.

1.1 Scope of work

Experiments were performed on a to-scale model of a multi-slot jet containing a main planar jet with two auxiliary planar jets either side. The purpose of this investigation is to ascertain the influence of the auxiliary jets on the acoustic tones and oscillations of the main jet due to the aeroacoustic feedback mechanism. The acoustic noise produced by the multi-slot jet, the jet-flow and the pressure on the impingement plate were measured experimentally to characterise the aeroacoustic feedback mechanism of the main jet and the effect of the auxiliary jets on that feedback mechanism.

A parametric study of the influence of different main jet and auxiliary jet operating parameters on the large amplitude, narrow-band acoustic tones produced by the jet impingement was conducted. The change in the amplitude and frequency of the tones generated by the main jet was characterised for different parameters and speeds of the auxiliary jets. The ability of the auxiliary jets to diminish the acoustic tones provided an initial insight into the manner in which the auxiliary jets interacted with the aeroacoustic feedback mechanism.

The pressure profile at the plate was measured to provide clearer insight as to how the auxiliary jets would affect the wiping process at the substrate. Profiles of the static and fluctuating pressures at the plate were measured to determine if the change in amplitude and frequency of the acoustic tones was accompanied by a similar change in the jet oscillations.

The effect of the auxiliary jets on the oscillations of the air-knife flow field was further determined through direct observation using particle image velocimetry (PIV). The PIV allowed for a comparison between the shear layer, spread rate and potential core length of the air-knife with different auxiliary jet velocities and operating parameters. This comparison allowed for an inference to a relationship between the auxiliary jet operating parameters and the change in amplitude and frequency of the tones and oscillations produced by the aeroacoustic feedback mechanism. A proper orthogonal decomposition was performed on the PIV data to determine the change in the "modes" of the velocity field that were associated with the jet oscillation and the energy of those modes.

The data gathered from the different experiments was used to determine the mechanism by which the auxiliary jet operating parameters influenced the noise and oscillation of the aeroacoustic feedback mechanism of the impinging planar jet.

1.2 Thesis outline

This thesis is comprised of five following chapters organised as follows. Chapter 2 is a comprehensive literature review covering shear layer instabilities, the aeroacoustic feedback mechanism, the current state of knowledge on multiple planar jets and the use of P.O.D. for structure identification in fluid mechanics. Chapter 3 describes the experimental apparatuses used in this investigation, the various main and auxiliary jet operating parameters explored experimentally along with specifics on the procedures used for data analysis. Chapter 4 contains the results of the different stages of the research. Chapter 5 discusses how the findings in the previous chapter relate to the understanding of the physics of the multi-slot jet. Chapter 6 is the final chapter in the thesis containing a brief summary of the results in the previous section and summarizes the original contributions the data and analysis represents.

Chapter 2

Literature Review

2.1 Free shear layer instabilities

A shear layer, or mixing layer, is the merging of two flows of different velocities that are travelling in the same direction. In the case of jet flows the shear layer is formed between the flow of the jet and the ambient fluid into which the jet discharges. Shear layers have long been known to be inherently unstable. Rayleigh [14] made the first attempt to model the stability of jet velocity profiles by applying an inviscid linear stability analysis. Rayleigh's work was the first to establish that velocity profiles with inflection points become unstable when certain disturbances are applied. Significant work was done over the following years on modelling the hydrodynamic instability of shear layers. Modelling of the effect of disturbances on a shear layer had been modelled as temporally growing disturbances until Michalke [15] modelled the growth of the disturbances in a hyperbolic-tangent velocity profile as growing spatially. Modelling the spatial growth of the disturbances allowed for the prediction of the essential features of the disturbed shear layer that temporal considerations could not accurately predict. The work by Michalke [15] was later confirmed by Freymuth [16]; the comparison of their data sets is presented in Figure 2.1. Freymuth [16] performed an experimental investigation into the transition to turbulence in a laminar free jet that was acoustically excited. The author found the disturbances in the shear layer grew exponentially before saturating at the transition to

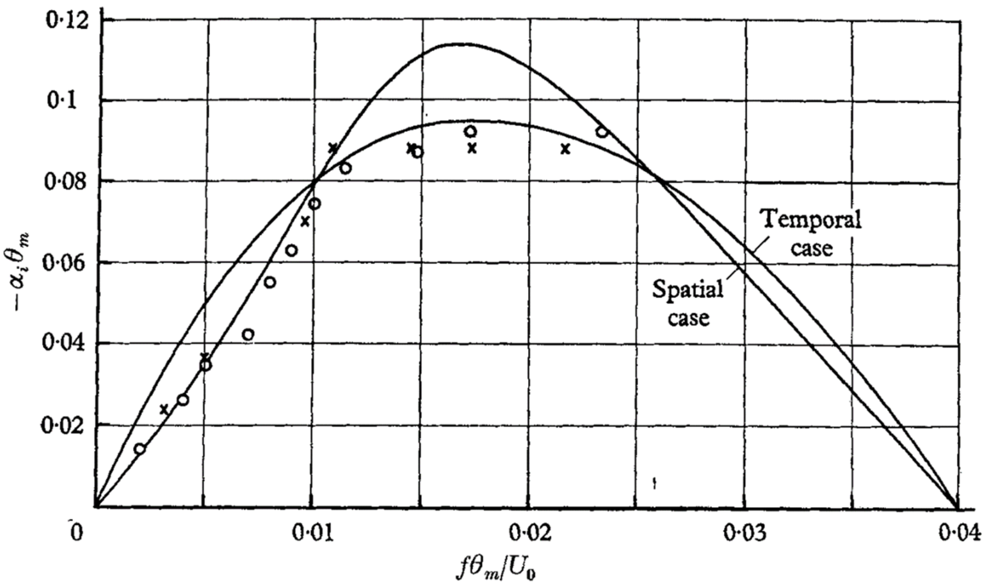

Figure 2.1 Growth rate as a function of the Strouhal number. Experimental data by Freymuth [16]: "X"s, planar jet; Circles, axisymmetric jet. Numerical modelling by Michalke [15]: Solid lines with modelling method for the growth of the instabilities indicated.

turbulence, Figure 2.2, and that the growth rates of the disturbances were proportional to the Strouhal number of the excitation of the jet.

Monkewitz and Heurre [12] performed a spatial instability analysis of shear layers for different non-dimensional velocity ratios. They found through their analysis that the spatial growth rate of the disturbances in the mixing layer is a function of the velocity ratio with the maximum amplification rate being a linear function of the non-dimensional velocity ratio for a Blasius velocity profile and approximately linear for a tangent velocity profile. Their calculated disturbance growth rates as a function of Strouhal number are presented in Figure 2.3.

In an effort to determine the stability of more realistic velocity profiles, Michalke and

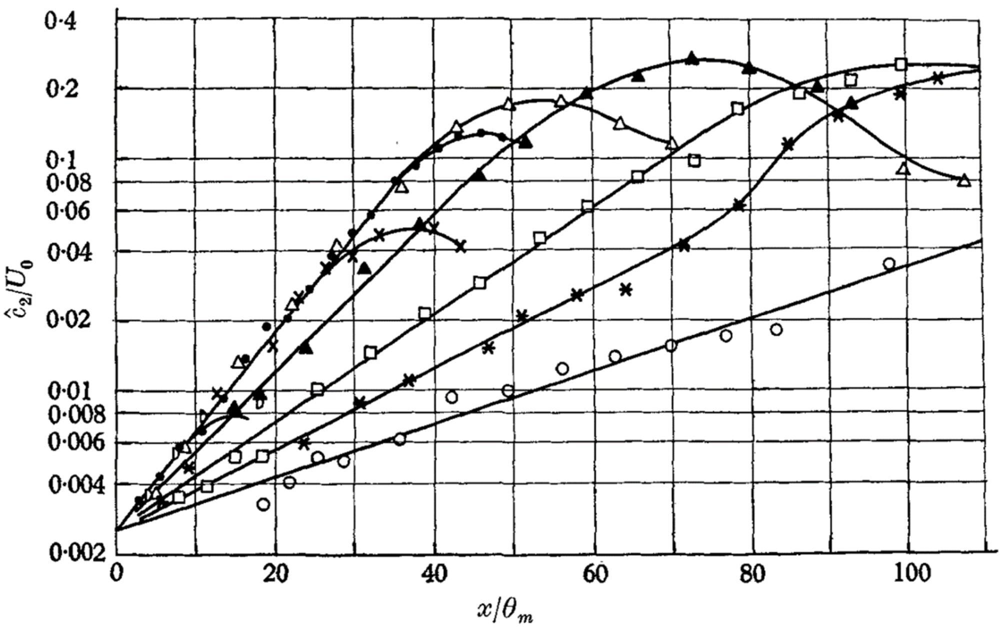

Figure 2.2 Amplitude of cross-stream flow instabilities normalised by jet velocity as a function of downstream position for an acoustically excited planar jet with varying forcing frequencies: Hollow circles, St = 0.0034; Stars, St = 0.005; Hollow squares, St = 0.007; Filled triangles, St = 0.0084; Hollow triangles, St = 0.0109; Filled circles, St = 0.0146, "X"s, St = 0.0178; Semi-circles, St = 0.0218 U_M = 8 m/s, d = 40 mm. Freymuth [16].

Hermann [13] applied their method of predicting the spatial growth rate of disturbances to an axisymmetric jet with external flow. The analysis was limited to the excitation of the axisymmetric and first azimuthal components of turbulence which had been previously established as the most dominant components. Their analysis was done with different jet velocity profiles at different distances from the jet exit that they defined using the non-dimensional momentum boundary layer thickness of the jet shear layer, "R/θ". They found that the velocity profiles with thicker boundary layers showed lower maximum growth rates of both turbulence components but the frequency of unstable disturbances increased as seen in Figure 2.4. Michalke and Hermann [13] concluded, for these realistic velocity

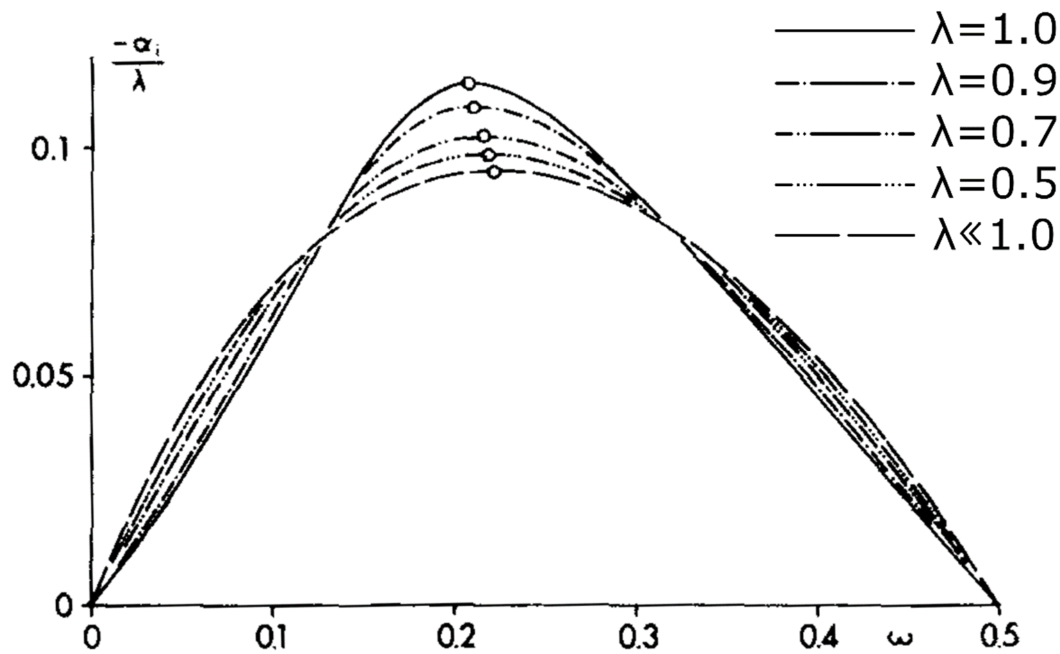

Figure 2.3 Spatial amplification rate, "-a$_i$" normalised by non-dimensional velocity ratio "λ" as a function of disturbance frequency "ω" of a hyperbolic-tangent velocity profile. Modified figure from Monkewitz and Heurre [12].

profiles of a circular jet, that the spatial growth rate of the disturbances was reduced for the external flow velocity with the range of unstable frequencies increasing.

Work done by Miksad [17] on the effect of acoustic excitation on the transition to turbulence of a laminar shear layer found that, in the initial region of the jet, the exponential growth of the instabilities agreed well with the linear theory used to model the instability growth. Subsequent regions of the jet are non-linear and involve the development of harmonics and subharmonics of the most-amplified frequency. Subsequent work by Miksad on laminar shear layers [18] investigated the effect of acoustically exciting the shear layer by two frequencies simultaneously and found that the harmonics and subharmonics of the frequencies suppressed the growth at the excited disturbance

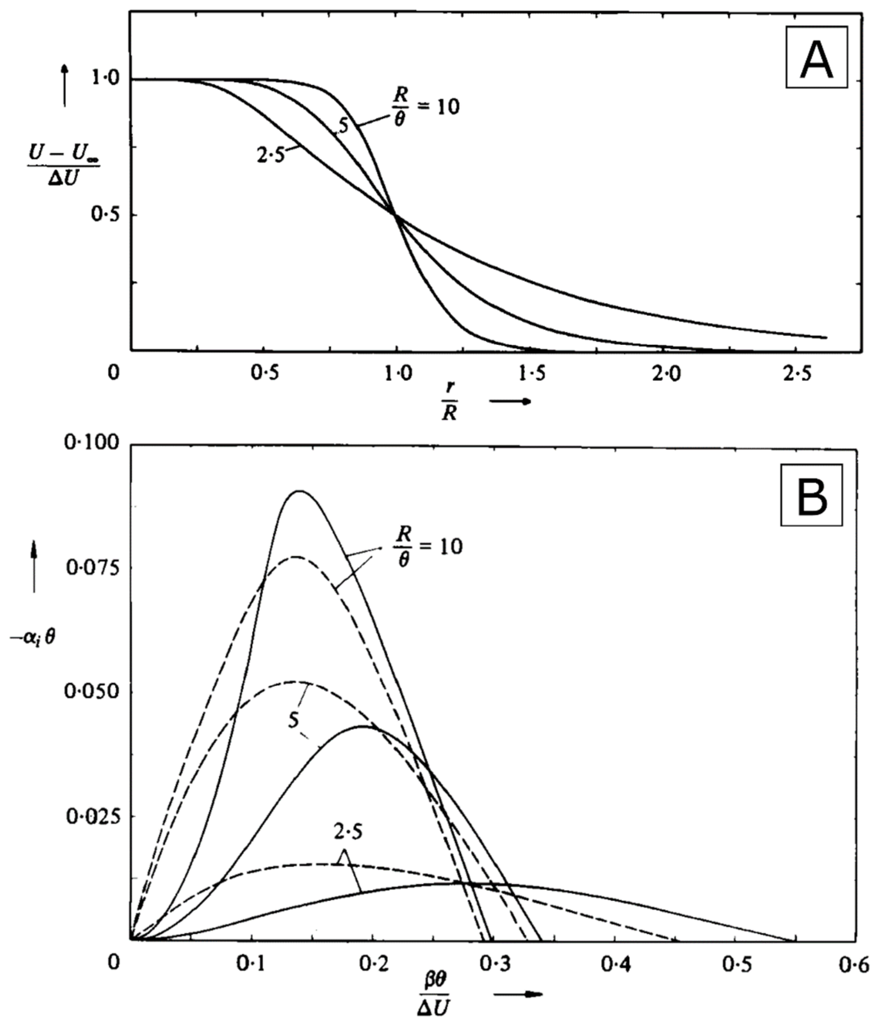

Figure 2.4 A: Normalised velocity profiles investigated ("U_∞" ambient velocity, "ΔU" velocity difference between ambient flow and jet exit velocity). B: Growth rates of disturbances as a function of Strouhal number ("$-\alpha_i\theta$" vs "$\beta\theta/\Delta U$") for the axisymmetric component (solid) and first azimuthal component (dashed) of turbulence for the velocity profiles in panel A. Michalke and Hermann [13].

frequencies.

Ho and Huang [19] found that the growth rate of vortices generated in the shear layer through a disturbance wave experienced a sudden jump when subjected to a specific forcing frequency. This rapid growth was due to the merging of sequential vortices through excitation of the shear layer at subharmonic frequencies of the most-amplified frequency of the shear layer. This method, dubbed “collective interaction” by the authors, could be used to accelerate the growth of the vortical structures as lower subharmonic frequencies could be used to merge three or four vortices together in a single merging event, bypassing the sequential merging of pairs of vortices. Ho and Huang [19] found that their measured amplification rates agreed well with the models of Monkewitz and Heurre [12] and their data agreed that the maximum amplification rate of the instabilities for their experiments was a linear function of the velocity ratio. Figure 2.5 shows a schematic of the mechanism of collective interaction, where the hollow circles represent the individual vortices produced by the shear layer that then “roll up” into a larger coherent structure.

Shear layer instabilities evolve into vortices, which through collective interaction, merge into a coherent structure. In this context, a coherent structure is, as defined by Hussain [20], a “large-scale turbulent fluid mass with spatially phase-correlated vorticity.” A more general definition of a coherent structure would be an identifiable vortical motion which retains its form and shape as it is convected over a significant distance inside the shear layer.

Further work on the mechanism of vortex merging was done by Hsiao and Huang [21] who performed velocity and pressure measurements on the acoustically excited shear layer of a planar jet. Their research found that, once the fundamental instability of the shear layer had grown to saturation, i.e. its largest size, the subharmonic became the most unstable frequency and absorbed energy from the mean flow and the fundamental instabilities

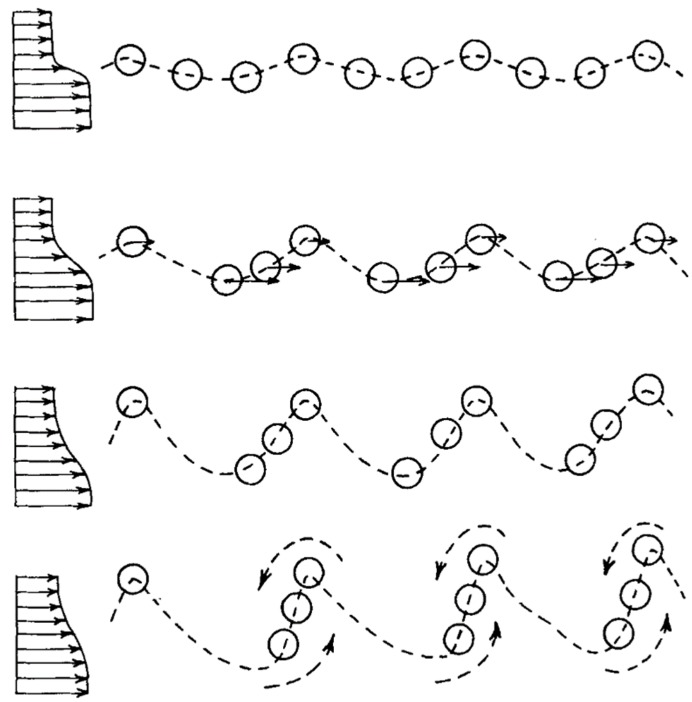

Figure 2.5 Schematic of collective interaction: multiple vortices merging simultaneously into a larger coherent structure. Ho and Huang [19].

to grow in size. The subharmonic eventually saturated and the next subharmonic became the most unstable frequency and absorbed energy from the mean flow and other instabilities. This cycle of saturation and evolution of the next subharmonic instability happened on each subsequent harmonic until the flow devolved into turbulent flow without the coherent structures.

2.2 Self-excited jets

The growth of instabilities in shear layers can be affected by external sources such as acoustic or hydrodynamic excitation. There are situations in which shear layers can be self-excited where the inherent instabilities of the shear layer generate a feedback mechanism that excites the shear layer. This phenomenon occurs with multiple geometries that are

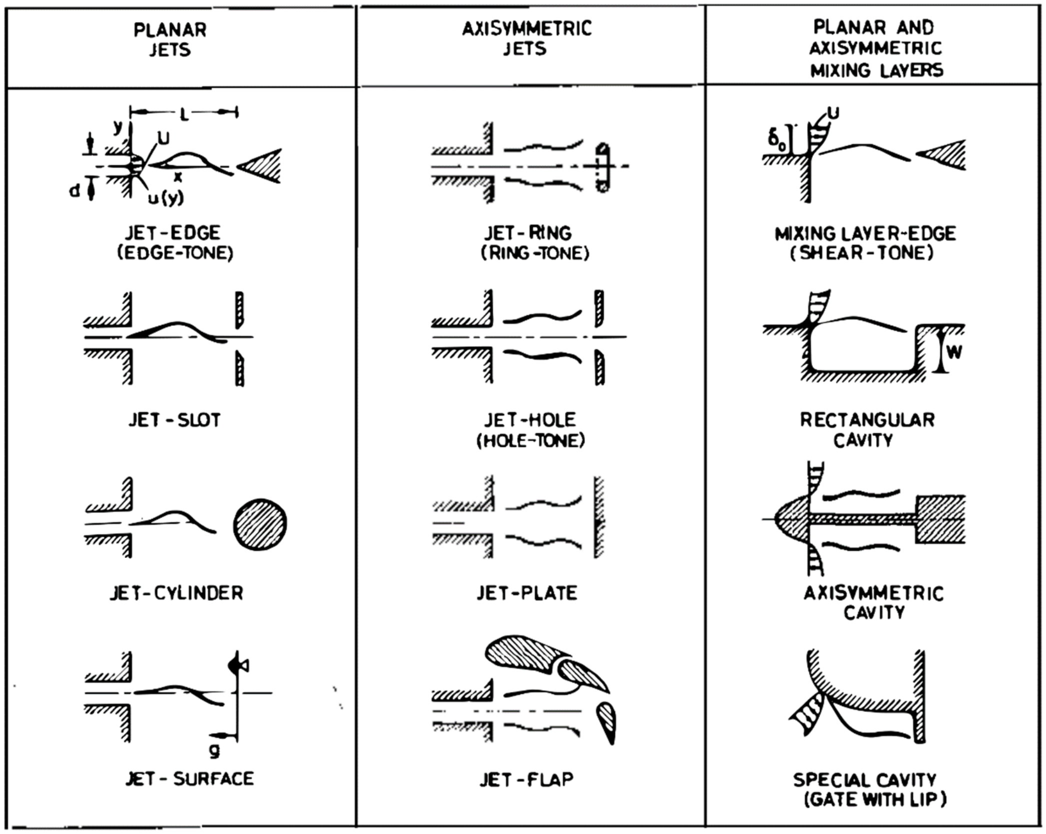

Figure 2.6 Basic configurations of shear layer and impingement-edge geometries that produce self-sustained oscillations. Rockwell & Naudascher [22].

summarised in Figure 2.6. For these configurations, the impingement of the shear layer generates a hydrodynamic or acoustic feedback to the initial region of the shear layer that accelerates the growth of the instabilities, as seen in §2.1. These larger instabilities increase the amplitude of the feedback mechanism.

Marsh [23] was the first to measure the noise generated by an axisymmetric jet at Mach 0.66 impinging upon a flat rigid plate for different impingement distances. Marsh found that both the frequency and amplitude of the noise generated by the impinging jet was affected by the plate. It was determined that the amplitude of the noise with the plate was louder by as much as 18dB over the jet without a plate. The frequency of the noise was found to exhibit a peak that decreased in frequency and became broader as the impingement distance was increased.

Similar characteristics of an impinging jet were noted by Wagner [24], whose investigation showed that, while the pressure fluctuations generated by a free jet generally have a broad energy spectrum, the pressure fluctuations of the impinging jet showed a concentration of energy at a single frequency. Figure 2.7 shows the imaging, microphone and hot wire results of Wagner's [24] study for both the free jet and impinging jet. Panels D and F show the microphone, M, and hot wire, HR, results of the free and impinging jets, respectively. The Figure clearly shows that the pressure and noise of the free jet were random but were a single frequency for the impinging jet. The flash shadow images show that a comparison between the free jet (panel A) and the impinging jet (panel B and C) indicate that the impinging jet had coherent structures whereas the free jet did not.

Wagner [24] investigated a number of jet operating parameters and found, in agreement with Marsh [23], that the frequency of the pressure fluctuations was proportional to the impingement distance between the plate and jet, decreasing as the impingement distance was increased. Wagner [24] also found that the frequency of the pressure fluctuations spontaneously jumped when the impingement distance was changed. This phenomenon, referred to as jet staging, is a characteristic of the feedback mechanism of self-excited shear layer impingement edge phenomenon. Wagner [24] proposed that this jump in frequency was related to a "positive feedback mechanism between the flow and the pressure field created by it upon impact on the wall". This feedback mechanism requires an integer

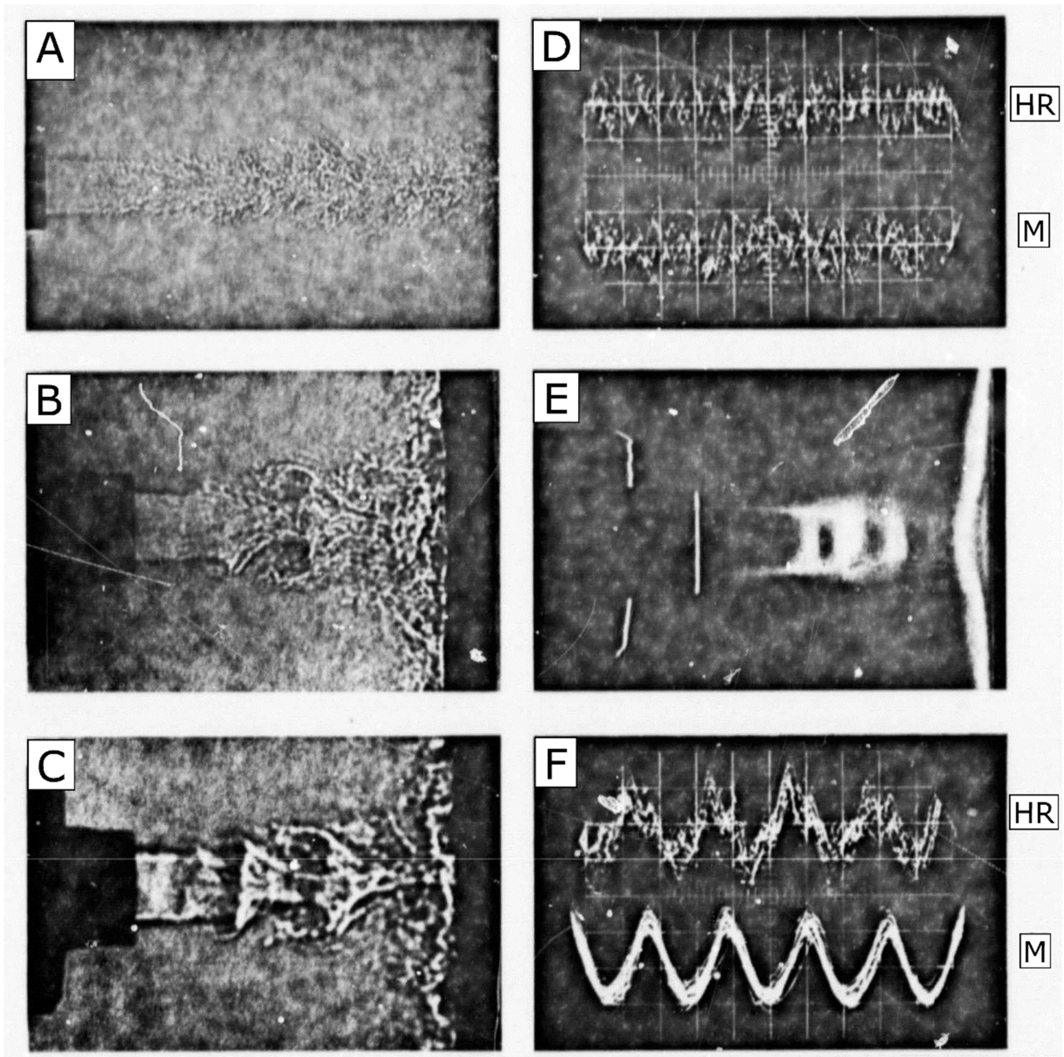

Figure 2.7 A: Flash shadow image of the free jet. B and C: Flash shadow images of the impinging jet. V_M = 0.85 Ma, d = 13.6 mm, h/d = 4.25. D: Hot-wire (HR) and microphone (M) signals corresponding to the free jet. E: Schlieren image of the impinging jet. F: Hot-wire (HR) and microphone (M) signals corresponding to the impinging jet. Modified from Wagner [24].

multiple of wavelengths between the jet edge and impingement plate to preserve the resonance of the system. As the impingement distance was changed, the wavelength of the feedback mechanism changed to preserve the integer multiple of wavelengths between the jet edge and impingement plate, resulting in a change in frequency. Further changes in the

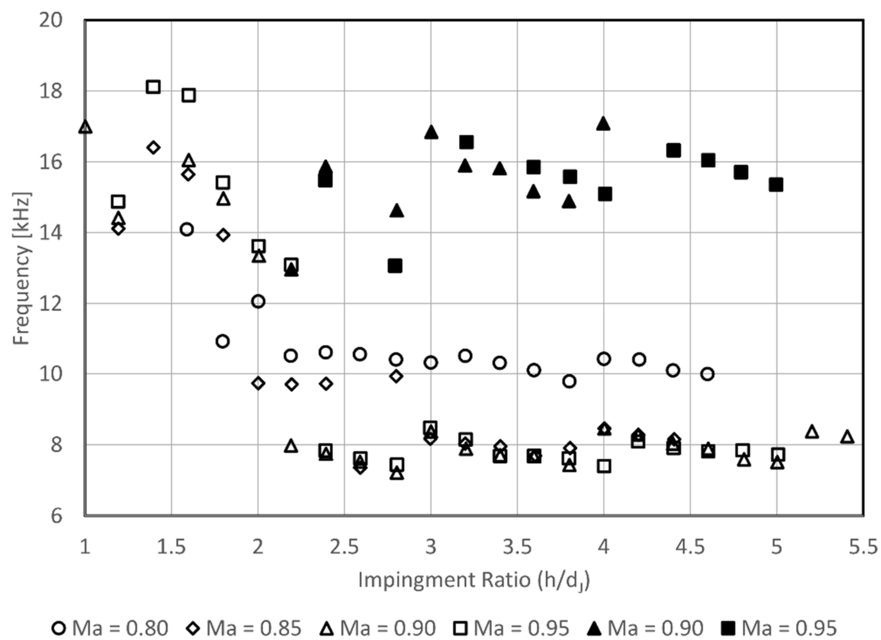

Figure 2.8 A replot of the data of Wagner [24]. Frequency of the impinging jet, "f", as a function of the impingement ratio, "h/d$_J$", and jet exit Mach number.

impingement distance caused the wavelength to deviate too far from that of the fundamental instability wave of the shear layer. In such instances, to maintain resonance, the integer number of wavelengths between the nozzle and plate changed, resulting in a sudden jump in the frequency and a wavelength closer to the fundamental instability wave. Figure 2.8 shows the results of Wagner's [24] experiments on the noise generated by the impinging planar jet. The data clearly shows how the frequency decreased with increasing impingement distance and the jumps in frequency at different impingement distances.

Further hypotheses of the feedback mechanism that governs self-excited impinging jets were made in the years following the work by Wagner [24] (Ho and Nosseir [25], Nosseir and Ho [26] Tam and Ahuja [27]). The work of Ho and Nosseir [25], [26] was an extensive

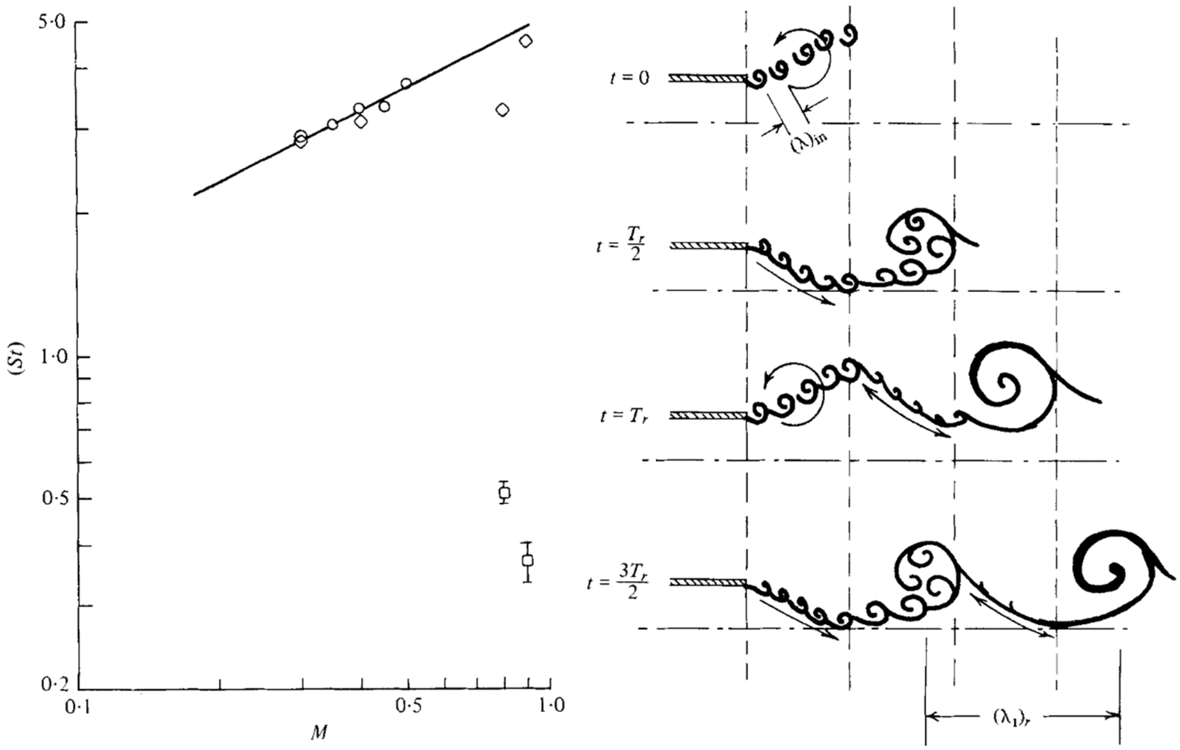

Figure 2.9 Left: Instability and resonant Strouhal numbers for free and impinging jets as a function of Mach number (circles: instabilities of the free jet; diamonds: instabilities of the impinging jet; squares: resonance of the impinging jet). Right: Schematic of the collective interaction at different phases in the resonant cycle. Ho and Nosseir [25].

experimental investigation into the dynamics of an impinging jet to determine the mechanism for the self-excited oscillations exhibited by impinging jets. Ho and Nosseir [25] argued that the final size of the coherent structures and the frequency of the self-excited impinging jet could not be accounted for by the sequential pairing of vortices over the impingement distance. The left-hand side of Figure 2.9 shows the approximate order of magnitude difference between the Strouhal number of the fundamental instabilities of the impinging and free jets and the resonance of the impinging jet. The order of magnitude difference between the frequency of the instabilities and resonance of the self-excited jet

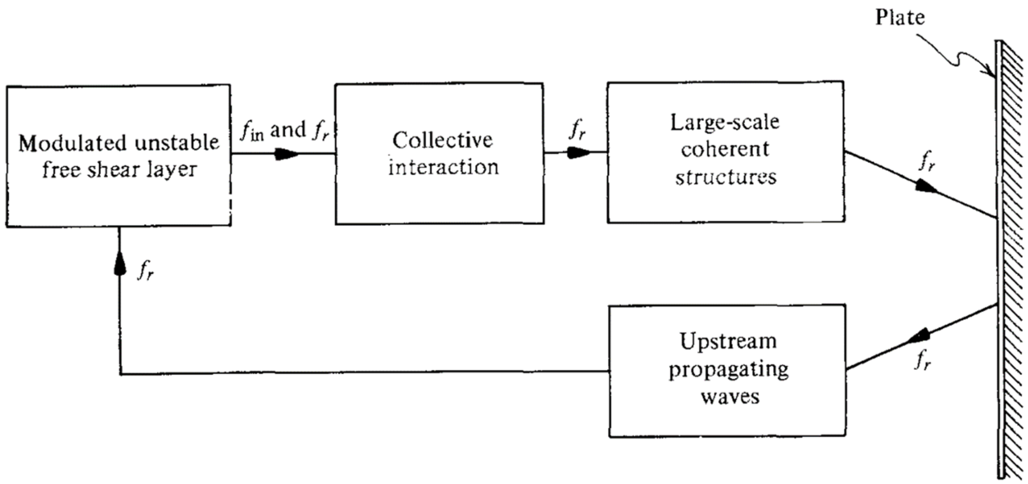

Figure 2.10 Feedback model proposed by Ho and Nosseir [25] for a self-excited impinging jet. The indicated frequencies are for the fundamental instability, f_i, and the resonance, f_r.

indicated the merging of a large number of vortices which could only be possible through collective interaction. Given the rate at which two vortices can merge and the relatively small impingement distances the vortices could not reach the observed size through sequential merging and, as such, the collective interaction proposed by Ho and Huang [19] must be a part of the feedback mechanism. The right-hand side of Figure 2.9 has a schematic of the collective interaction with the indicated sizes of the fundamental instability, λ_{in}, and resonance, λ_r.

Ho and Nosseir [26] experimentally confirmed the lock-in of the frequency of the upstream propagating waves generated from the impingement of the coherent structures and the generation of coherent structures from inherent instabilities of the shear layer through collective interaction. It is this lock-in that is responsible for the concentration of the energy at a single frequency, as found by Wagner [24] and seen in Figure 2.7. The regular impingement of coherent structures on the plate generated large-amplitude, intense acoustic tones which were of a much larger sound pressure level than that of the free jet.

The proposed mechanism for the self-excited impinging jets was expanded further by Tam and Ahuja [27] who proposed that the acoustic waves generated by the impingement of the vortical structures excited intrinsic neutral waves of the jet mean flow. This mechanism was used for both subsonic and supersonic jet impingement to predict the helical instabilities found in impinging axisymmetric jets. This method also accurately predicted the Strouhal number of the feedback mechanism as the Strouhal number of the least dispersive neutral wave. Panickar and Raman [28], [29] further expanded the modelling of Tam and Ahuja to higher supersonic jet velocities in an effort to explain the helical modes they found experimentally that the original modelling of Tam and Ahuja stated were not possible. Their inclusion of momentum thickness in the analysis allowed them to predict the existence of helical modes based on the impingement distance and their models predicted well the helical modes they found experimentally.

A significant body of work on the self-excited subsonic impinging planar jet was performed by Arthurs and Ziada [30]–[32]. Arthurs and Ziada [32] performed experiments using a scaled version of the planar jets used in the continuous galvanising line – commonly referred to as air-knives – to investigate the relationship between the aeroacoustic noise generated by the planar impinging jet and the pressure fluctuations on the impingement plate. The pressures generated by the impingement of the planar jet on the plate, both the mean static and fluctuating, are presented in Figure 2.11. The frequency of the fluctuating pressure at the plate was measured to be the same frequency as the acoustic tone produced

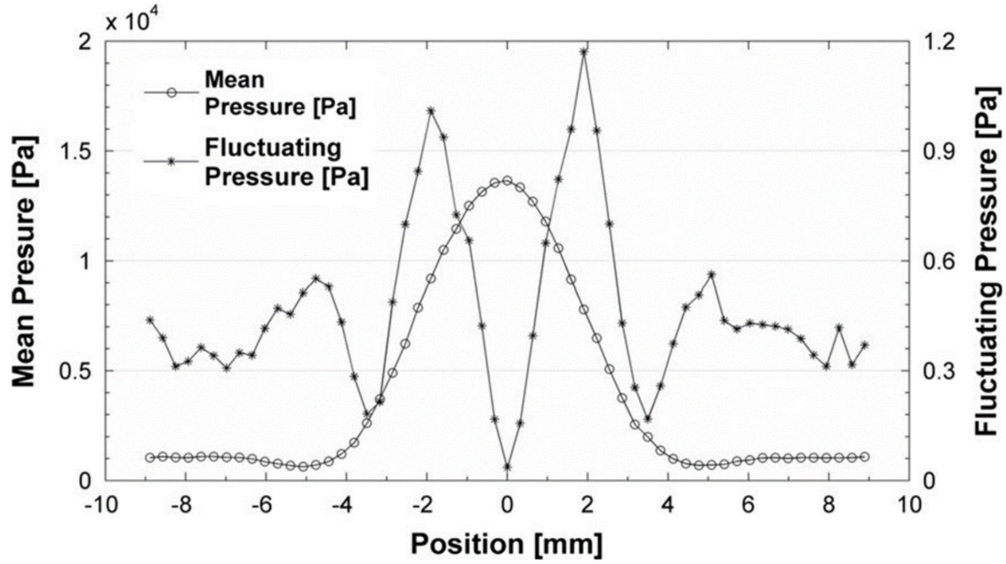

Figure 2.11 Mean static pressure and RMS fluctuating pressure on the impingement plate as a function of distance from jet centerline for V_M=174 m/s and h/d = 12. Arthurs and Ziada [30].

by the jet. The relative phase between the acoustic tone and the fluctuating pressure at the plate shows a 180° phase shift across the stagnation point indicating that the fluctuating pressures were produced by the impingement of axisymmetric coherent structures.

Arthurs and Ziada [30] found that the impinging planar jet produced acoustic tones for relatively low jet velocities that were distinguishable between a linear hydrodynamic regime and a fluid resonant regime. The dynamics of both the linear and resonant regimes were as described by Ho and Nosseir [25] but the acoustic tones generated in the fluid resonant regime acoustically excited the volume between the jet and plate. The excitation of the trapped acoustic modes of the volume led to the increased acoustic amplitude of the generated tones.

Particle image velocimetry (PIV) allowed Arthurs and Ziada [30] to observe the dynamics of the jet and the generated coherent structures. Phase-locked PIV allowed the convection of the coherent structures of the jet to be tracked for different impingement distances. This tracking technique allowed Arthurs and Ziada [30] to define two distinct equations for the convection velocity of the coherent structures: one for impingement distances in the range of the potential core and another for larger impingement distances where the convection of the coherent structures slowed. This convection velocity allowed for Arthurs and Ziada [30] to modify a semi-empirical formula developed by Rossiter [33] to predict the frequency of the resonant instabilities in cavity flows. Rossiter's [33] model was based on the hypothesis that the velocity scale associated with the hydrodynamic instabilities is the freestream velocity. Arthurs and Ziada [32] proposed a formula for predicting the frequency of the jet-plate oscillator based on the combined velocity scale of the experimentally measured convection velocity of the coherent structures and the velocity scale of the acoustic pressure waves of the feedback path. A Strouhal number calculated with the convection velocity, rather than the jet velocity, resulted in Arthur and Ziada's [31] data to collapse into well-defined jet stages. PIV imaging revealed that the jet-plate oscillator contained the same quantity of coherent structures in between the jet and plate as the integer number of the excited jet stage. These stages were further subdivided by the specific resonant acoustic mode occurring in the air volume between the jet and plate. The jet-stage map of the planar jet-plate oscillator is included in Figure 2.12, where the area for each jet stage is indicated in by the Arabic numerals and the sub-stage by the roman numerals. Phase-locked PIV images of velocity fields for different jet stages are inset around the map overlaid with the outlines of the coherent structures as defined by the discriminant of the velocity field. Arthurs and Ziada [30] found that the velocity field of the jet stage contained the same number of coherent structures in the jet shear layers between the jet and plate as the jet stage number.

Arthurs and Ziada found in a subsequent publication (Arthurs and Ziada [32]) that the amplitude and frequency of the dominant acoustic tones were not a function of the jet nozzle width. At larger impingement distances, for larger nozzle widths, it was found that the tones were not produced by the impinging planar jet, where the authors speculated that tones were not produced at these larger impingement distances because the smaller aspect ratio of the larger jet nozzle widths (100 for d = 1 mm, 25 for d = 4 mm) resulted in 3D effects of the flow degrading the 2D tone generation mechanism. They also found that the jet nozzle thickness did not affect the amplitude or frequency of the tones produced by the impinging planar jet.

Modelling by Pfeiler et al. [5] on the impinging planar jets used in the continuous galvanising line has shown that there is a link between the instabilities of the impinging jets and the variations in the coating weight produced by the gas jet wiping process. Pheiler et al. [5] used a two-phase large eddy simulation to model the planar jets, moving substrate and liquid zinc coating material involved in the gas jet wiping process and found that the models accurately reflected the high-resolution images of the liquid zinc film taken during industrial processing and were in good agreement with the XRF-thickness measurements of the solid coating. The authors found that the frequency of the pressure fluctuations

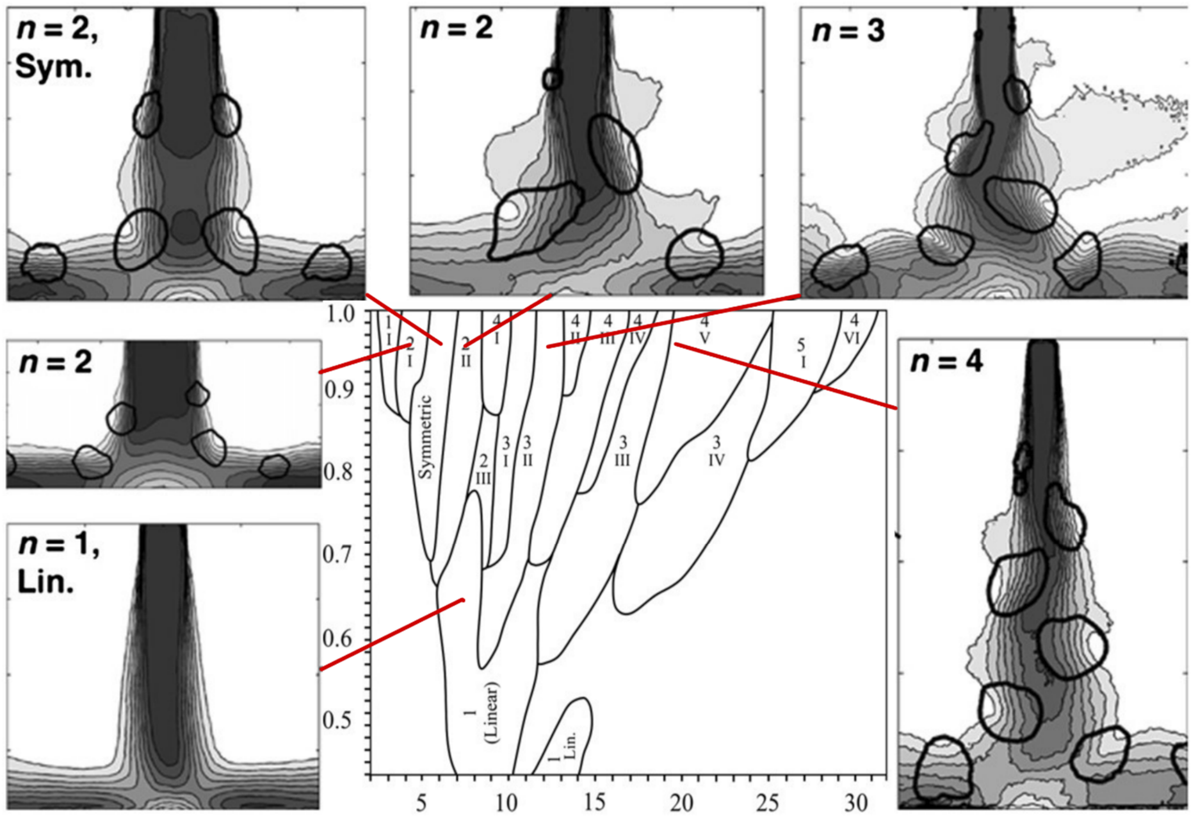

Figure 2.12 Center: Map of the different jet stages and sub-stages of the self-excited jet-plate impingement as a function of impingement ratio, h/d, (x-axis) and jet Mach number (y-axis). Surrounding panels contain phase-locked velocity fields of the indicated jet-stages with black outlines indicating the coherent structures. Modified from Arthurs and Ziada [31].

of the impinging jet was not directly related to the waves on the zinc film surface due to the inertia difference between the liquid zinc and jet flow but the lower frequency components of the pressure correlated well with the waves on the zinc surface. A proper orthogonal decomposition (POD) analysis of the same modelling technique performed in a later paper from the same group, Eßl et al. [34], showed that low frequency fluctuations of the first POD mode associated with the large scale coherent structures of the turbulent wiping gas flow aligned with the frequency of the film height. The left-hand panel of

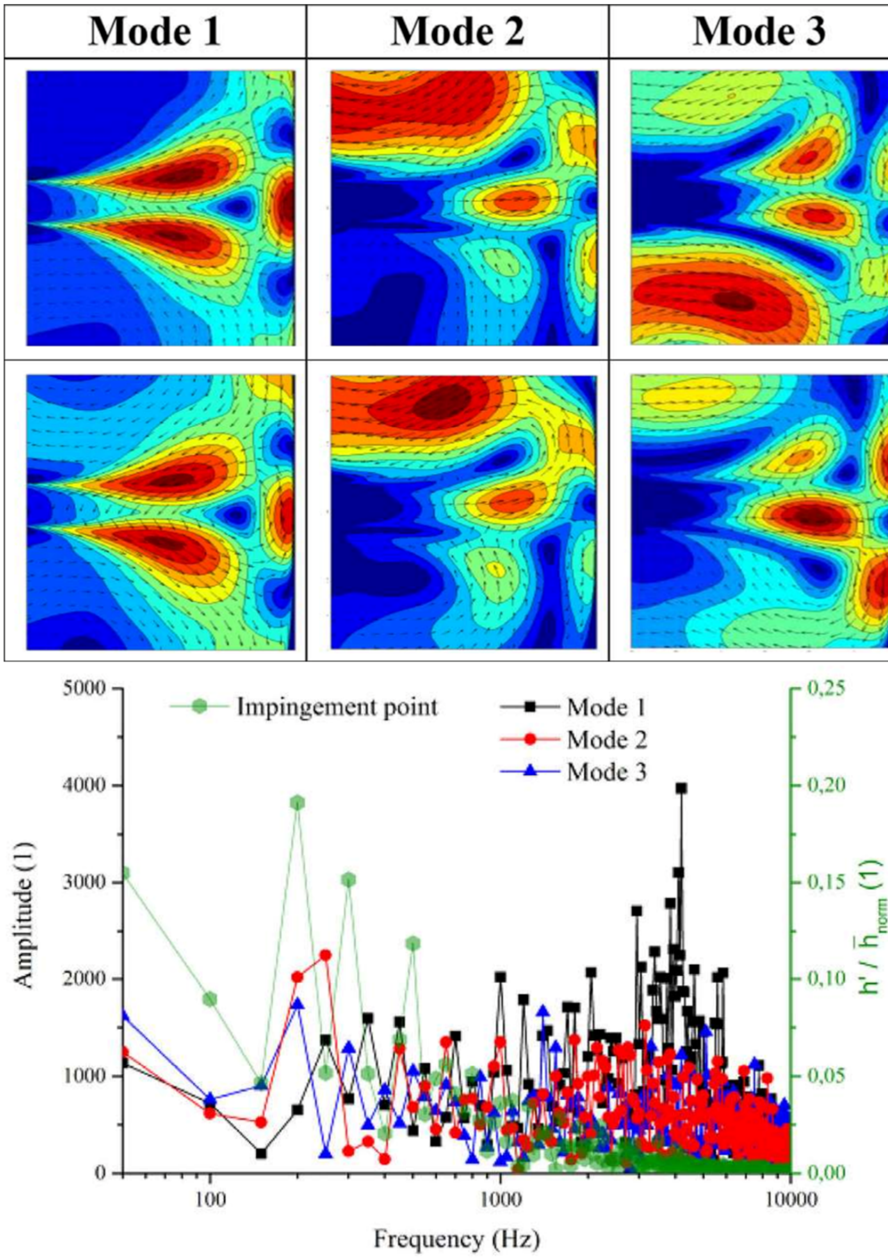

Figure 2.13 Left: Modes 0, 1 and 2 of the impinging planar jet with and without the simulated zinc coating. Right: Frequency of the height of the zinc coating material normalised by the mean height plotted alongside frequency amplitude of the first three modes of the POD analysis with the simulated zinc coating. Eßl et al. [34].

Figure 2.13 contains the first three modes of the POD of Eßl et al's [34] results with and without the zinc film included in the model. Mode 1 was associated with the flapping of the jet due to the large coherent structures. Modes 2 and 3 were associated with the axial fluctuations of the jet column. The right panel of the same figure shows the frequency amplitude of the three modes of the analysis that included the zinc film alongside the frequency of the normalised height of the zinc film. The largest frequency amplitudes of the zinc film heights occurred between 100 Hz and 400 Hz which coincided with the significant frequency amplitudes of the first three POD modes which indicated that the large coherent structures and axial fluctuations of the impinging planar jet were linked to the waves seen on the zinc film.

Further work into modelling the interaction of the unsteady behaviour of the jet and the variations of the free surface of the coating produced by the gas-wiping process was performed by Johnstone et al. [6]. Johnstone modelled the zinc film on a moving steel substrate subject to pressure and shear stress profiles with the magnitude and position of the jet impingement varying sinusoidally with time. Johnstone et al. [6] found that the magnitude of the coating thickness fluctuations was a function of the dimensionless frequency of the pressure and shear stress. Significant coating fluctuations were found for dimensionless frequencies less than unity and for values above unity, the amplitude of the fluctuations of the coating weight was not significant. The variations in the coating weight height were found to have the largest amplitude due to the pressure and shear stress fluctuations at the dimensionless frequency of 0.22 and that, for practical gas jet wiping purposes, the dimensionless frequency of the jet oscillations should be above unity to reduce coating weight fluctuations.

2.3 Multiple jets

2.3.1 Multiple jets for the control of self-excited jets

Research into the use of auxiliary jets to control the aeroacoustic feedback mechanism of impinging jets was performed by Sheplak [35] and Sheplak and Spina [36], [37], who were investigating subsonic and supersonic axisymmetric jets used in VSTOL (vertical and/or short take-off and landing) aircraft. This research used a co-axial jet design in which the main axisymmetric jet was surrounded by a larger diameter "co-axial" axisymmetric jet the velocity of which could be controlled independently of the main. The phase-locked Schlieren images captured by Sheplak and Spina [36], reproduced in Figure 2.14, compare the impinging supersonic axisymmetric jet to the same impinging jet with a co-axial jet. Panel A shows how the expected shock cell structure of the supersonic axisymmetric jet was disrupted due to the instability of the jet column and developed into a helical

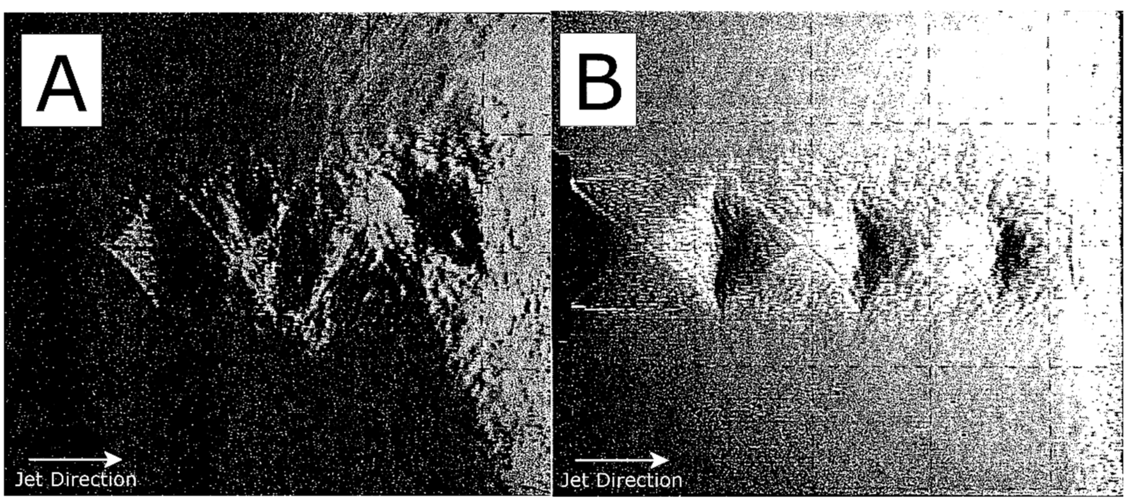

Figure 2.14 Phase-locked Schlieren images of an A: Impinging axisymmetric jet $d_ø$ = 25.4 mm, V_M = 1.37Ma, h/d =4.5. B: Impinging co-axial jet V_M = 1.37Ma, $d_ø$ = 25.4 mm, $a_ø$ = 37.3 mm, V_A = 0.58Ma, h/d =4.5. Sheplak [36].

instability with large coherent structures due to the aeroacoustic feedback mechanism. Panel B shows the same impinging axisymmetric jet with a co-axial jet at a velocity such that the disruption of the shock cell structures did not occur and the helical coherent structures did not develop. The authors also found that the auxiliary jets effectively reduced the noise produced by the impinging axisymmetric jet i.e. – both the amplitude of the overall sound pressure level and the tones produced by the aeroacoustic feedback mechanism. The acoustic results of the experiments by Sheplak [35] are reproduced in

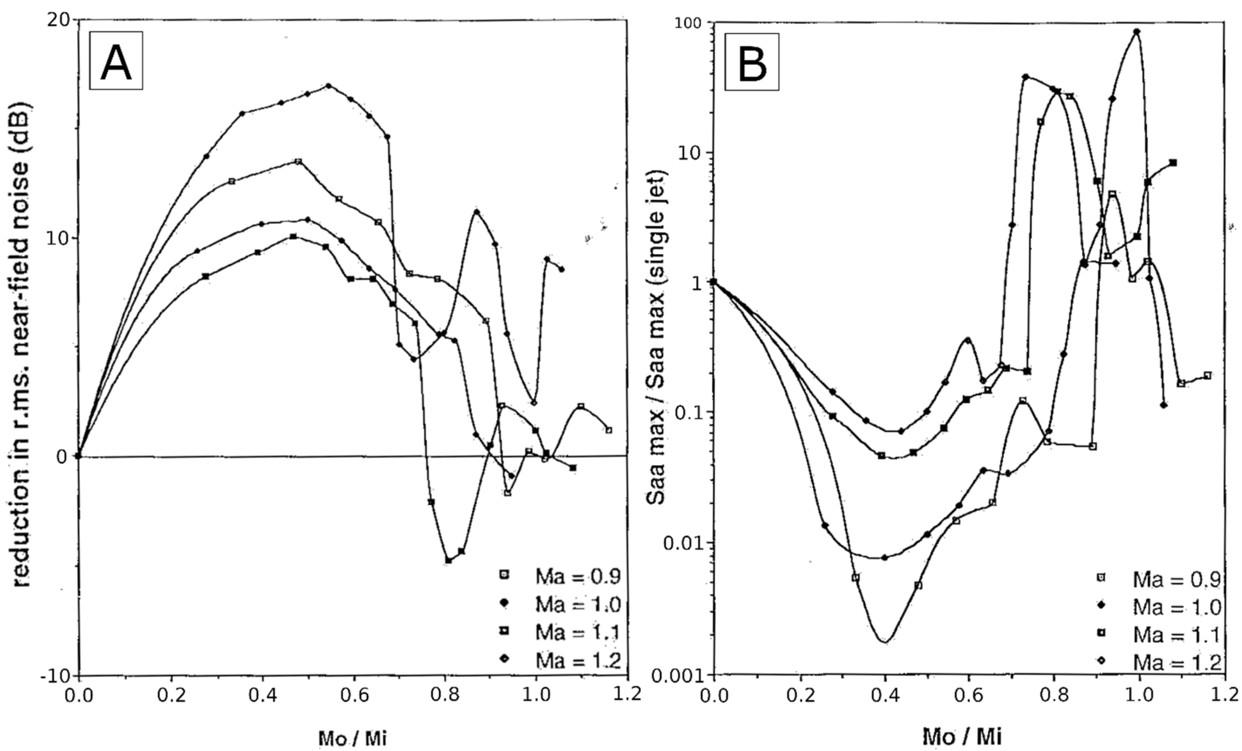

Figure 2.15 A: Reduction in the RMS noise generated by the co-axial jet as a function of velocity ratio Mo/Mi (outer jet Mach number divided by inner jet Mach number). B: Ratio of the dominant peak amplitude of the co-axial jet (Saa max) to the dominant peak amplitude of the single jet (Saa max (single jet)) as a function of velocity ratio Mo/Mi. The Mach number of the main jet velocity, V_M, is indicated in the figure legend, $d_ø$ = 25.4 mm, $a_ø$ = 37.3 mm, h/d = 3. Sheplak [35].

Figure 2.15 and show the reduction in the noise of the jet. Panel A shows that the overall sound pressure level produced by the jets were reduced but returned to the original levels when the auxiliary jet and main jet were at the same velocity. The amplitude of the tones, Panel B, showed a similar decrease with auxiliary jet velocity, but at higher velocity ratios the amplitude of the tones was found to be amplified above those of the main jet alone. Sheplak and Spina [37] proposed that the mechanism that reduced the amplitude of the noise was due to the outer co-axial jet flow "acoustically shielding" the initial region of the main jet. Acoustic shielding was measured using the same facility by Dosanjh and Ahuja [38], who found that the perceived amplitude of the noise produced by a free jet could be reduced by the co-axial jet which "acoustically shielded" the receiver. The hypothesis by Sheplak [35] and Sheplak and Spina [37] was that the co-axial jet reduced the amplitude of the feedback pressure reaching the jet nozzle such that the collective interaction of the vortices was reduced. The reduction of the collective interaction of the instabilities was such that they did not develop into coherent structures by the time the jet impinged. Sheplak and Spina [37] did also allow for the thickening of the shear layer resulting in a lower growth rate of the coherent structures as a possible mechanism for the elimination of the acoustic tones and observed hydrodynamic modes.

2.3.2 Micro-jets for the control of self-excited jets.

Research into co-axial jets as a means of controlling the resonance of the impinging jets used in VSTOL aircraft did not go beyond the work by Sheplak [35] and Sheplak and Spina [36], [37] as the outer jet required roughly 20% of the mass flow rate of the main jet to be effective. Research using an array of micro-jets at the nozzle lip of the jet to disrupt the shear layer provided two benefits over a co-axial jet: simplicity in its manufacture and a much lower mass flow rate roughly 0.5% of the mass-flux of the main jet.

Initial research by Alvi et al. [39] consisted of 16 400 μm supersonic micro-jets equally spaced around an axisymmetric supersonic jet. Each micro-jet exit was on the same plane as the main jet exit, placed 2 mm from the main jet nozzle edge and angled at 20° to the main jet axis. The initial investigation was performed with steady flow from the microjets into an ideally expanded supersonic jet impinging at different impingement distances. The results showed the microjets had a significant effect on the aeroacoustic feedback mechanism, reducing the fluctuating pressures on the impingement plate and jet lift plate by 10-11 dB. The authors also reported that the "discrete, high-amplitude impinging tones were either eliminated or significantly attenuated." The "lift loss" associated with these SVTOL jets, thought to be associated with the enhanced entrainment caused by the large scale structures in the shear layer, was reduced by as much as 40% with the micro-jets. While the micro-jets resulted in a reduction in the pressures and lift-loss at all impingement ratios, the reduction was not uniform nor monotonic, varying significantly with the investigated impingement ratios.

The physical mechanism that leads to the reduction in the aeroacoustic feedback mechanism was not found in Alvi et al's [39] initial work. Research by Lou et al. [40] sought to determine the mechanism that reduced the fluctuating pressures of the impinging jet. PIV imaging showed that the micro-jets each generated two counter-rotating vortices in the cross-plane of the jet flow. An order of magnitude analysis performed by the authors indicated that the micro-jets could only be responsible for 10% of the vorticity in those counter-rotating vortices, suggesting a significant portion of the vorticity was derived from the primary shear layer. This indicated that the micro-jets were breaking down the large scale axisymmetric structures involved in the aeroacoustic feedback mechanism and introducing more three-dimensionality to the flow. Lou et al. [41] actively controlled the flow of the micro-jets to achieve more consistent performance from the micro-jets at different impingement distances. The authors specifically targeted the azimuthal pressure distributions close to the nozzle edge identified by POD for the different impingement distances and found that active control could further reduce fluctuating pressure by 8-10 dB, but failed to make the performance more uniform over the range of investigated impingement distances.

PIV imaging performed by Alvi et al. [42] and Kumar et al. [43] provided further insight into the mechanism of the micro-jet suppression of the aeroacoustic feedback mechanism. Three-component PIV, performed by the former authors, indicated that the reduction in the azimuthal vorticity, associated with the coherent structures of the aeroacoustic feedback mechanism, was due to it being redirected by tilting and stretching to the strong and well organised streamwise vorticity of the micro-jet vortices. The thickening of the initial shear layer by the micro-jet flow, coupled with the decrease in the peak azimuthal vorticity, suppressed the growth of the shear layer instability responsible for the aeroacoustic feedback mechanism. Phase-locked imaging by Kumar et al. [43] allowed for the direct comparison of the swirl of the azimuthal vortices of the impinging supersonic jet with and without micro-jets, which are presented in Figure 2.16. The figure

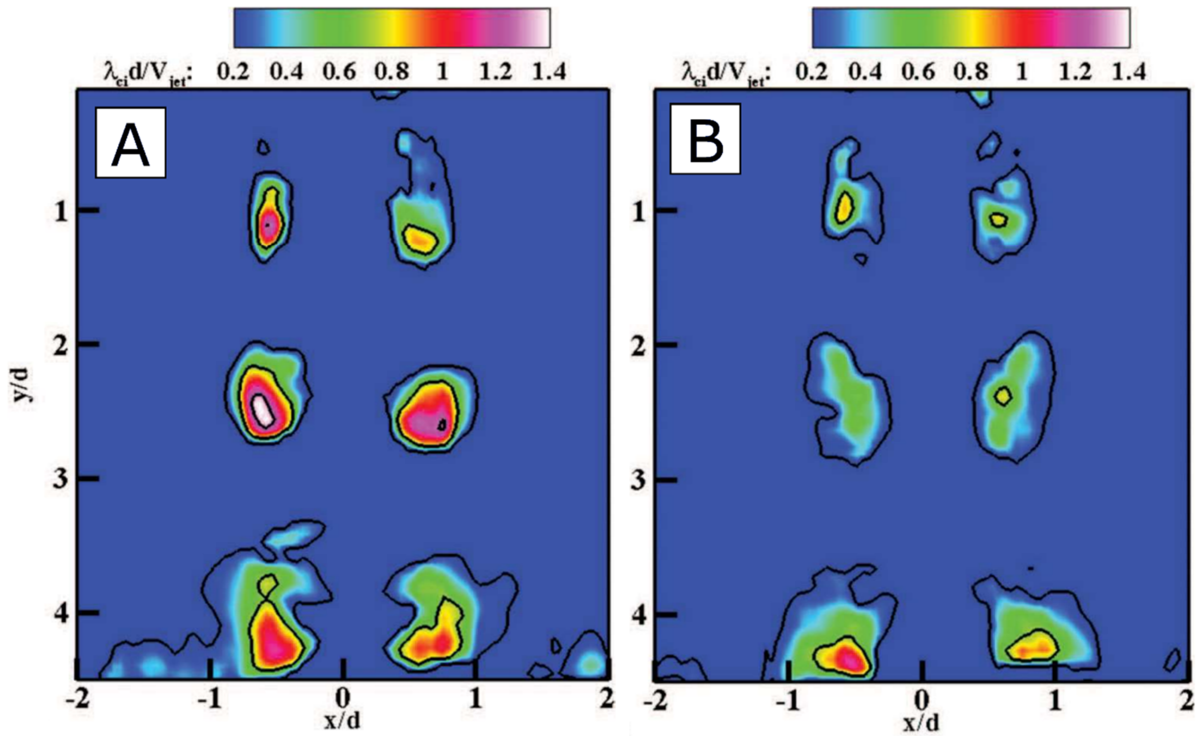

Figure 2.16 Swirl strength distribution of the central plane of an impinging supersonic axisymmetric jet with and without micro-jet control; panel A and B respectively. Kumar et al. [43].

clearly shows that the case with micro-jets has vortices of significantly reduced strength which agreed with their acoustic measurements, the noise levels of which were reduced in magnitude but where an aeroacoustic tone was still present. The authors speculated that a sufficiently high supply pressure for the micro-jets would result in them further penetrating the shear layer and breaking the coherence of the structures as seen in the work by Lou et al. [41], where the reduction in pressure magnitude was a function of the micro-jet supply pressure.

2.3.3 Multiple jets used in the gas jet wiping process

Research of the aeroacoustic feedback mechanism of transonic and supersonic impinging jets used in aerospace and aircraft has been well documented. The control of this phenomena in axisymmetric jets through co-axial jets and microjets has been explored. There has been little research in the area of auxiliary planar jets used for the control of a self-excited planar jet. Research in the area of multiple jets for the use in gas jet wiping has been sporadic and generally focussed on reducing or improving control of the final coating weight on the substrate.

In the gas jet wiping process as applied to the continuous galvanizing process, a check-mark stain is a coating defect that presents as an oblique pattern in the zinc coating of the substrate. To investigate the cause of “check-mark” stain, Yoon et al. [9] modelled an air-knife and moving substrate as a 3D compressible flow using a LES turbulence model. The author’s CFD analysis indicated that the source of the “check-mark” stain was alternating stream-wise vortices impinging on the steel strip that moved quasi-periodically along the stagnation line of the air-knife due to instabilities in the jet. In an effort to eliminate the check-mark stain Yoon and Chung [44] proposed a multi-slot jet design with two slots: a main jet and a “guide jet”, which was a full-length planar jet that immediately preceded the main jet in the gas jet wiping process. Figure 2.17 shows a comparison between the instantaneous velocity fields of the two nozzle designs and the spanwise pressure distribution on the impingement plate. The guide jet was found to make the flow field of the main jet more stable and it was reported by the authors to improve the ability of the air-knives to remove zinc from the substrate. The increased stability of the jet can be seen in

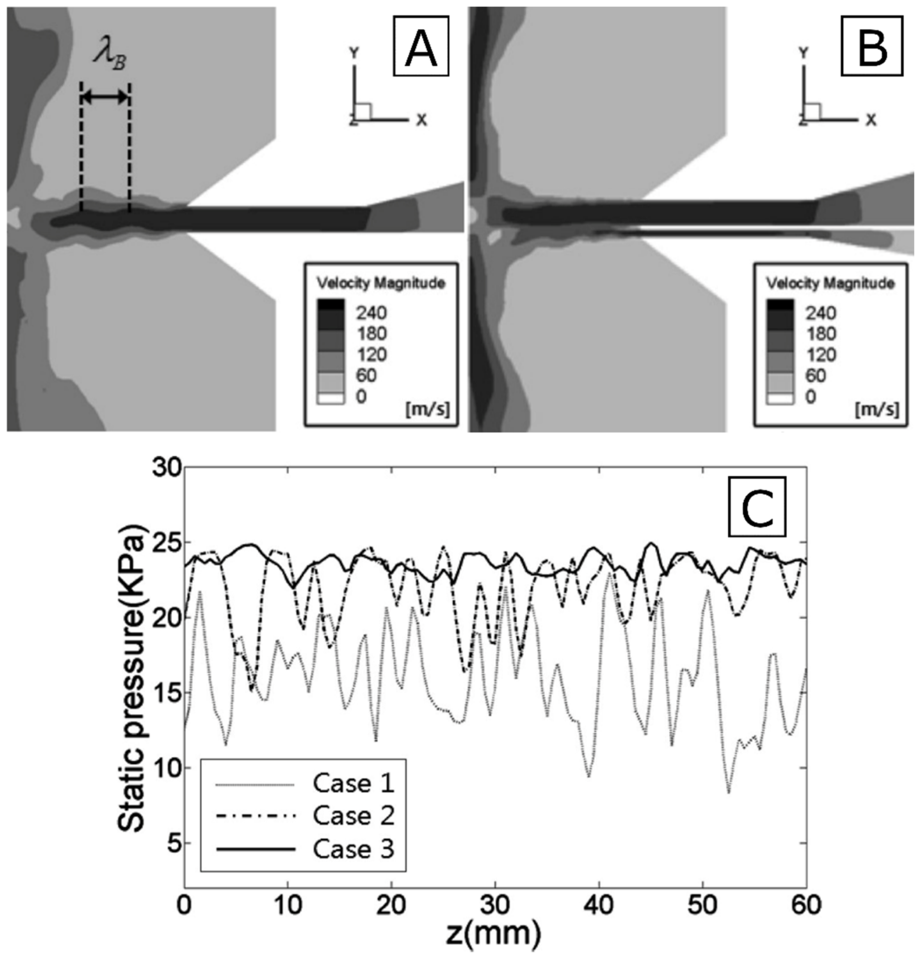

Figure 2.17 Contour plots of velocity magnitude for the single slot nozzle jet (A) and the multi-slot nozzle jet (B). The plot of static pressure generated on the impingement surface along the impingement plane created by the impingement of the single slot air-knife, Case 1, and the multi-slot nozzle jet, Case 3 (C). Yoon and Chung [44].

the comparison of panel A, the single slot nozzle jet, and panel B, the multi-slot nozzle jet in Figure 2.17. Yoon and Chung [44] attributed the increased stability of the jet column to the guide jet suppressing the buckling of the main jet, as seen in panel A. Case 1 and 2, referenced in panel C, are single slot nozzles 1.5 mm and 2.0 mm wide, respectively, while Case 3 is the multiple slot nozzle with a main jet width of 1.5 mm and guide jet width of

0.5 mm. A comparison of Cases 1 and 3 in panel C shows that the guide jets were found to result in a more uniform spanwise pressure distribution at the impingement plane which would make for a more consistent coating weight. The pressure inside the jet plenums was maintained at 25 kPa for all three cases and the plotted pressures show that the nozzle with the guide jet, Case 3, shows significantly less pressure loss over the impingement distance than the single slot nozzle, Case 1.

Further CFD modelling of multiple slot and single slot jet nozzle designs were performed by Tamadonfar [10]. The authors used a 2D flow field with a standard k-ε turbulence model to simulate the impingement of the jets upon a moving substrate. The pressure and shear stress profiles returned by the simulations were used by the authors, along with the Elsaadawy et al. [45] model for predicting coating weights, and compared the coating weight predicted for multiple slot and single slot jets. The maximum dimensionless pressure and coating weight predictions of the different nozzles are presented in Figure 2.18 as a function of the impingement ratio, Reynold's number and substrate speed. Although the maximum dimensionless pressure of the multiple slot jet is larger than the single slot jet at every impingement distance the coating weights that result from the wiping of the multi-slot jet are all thicker than the single jet at all conditions of the tested parameters of impingement ratio, Reynolds number and substrate speed. An experimental investigation into the pressure profiles generated on the impingement plate by both a single slot planar jet and the multiple slot planar jet was conducted by Alibeigi [11]. The influence of the auxiliary jets on the pressure profiles at the plate as a function of main and auxiliary jet Reynolds number can be seen in panels A and B in Figure 2.19.

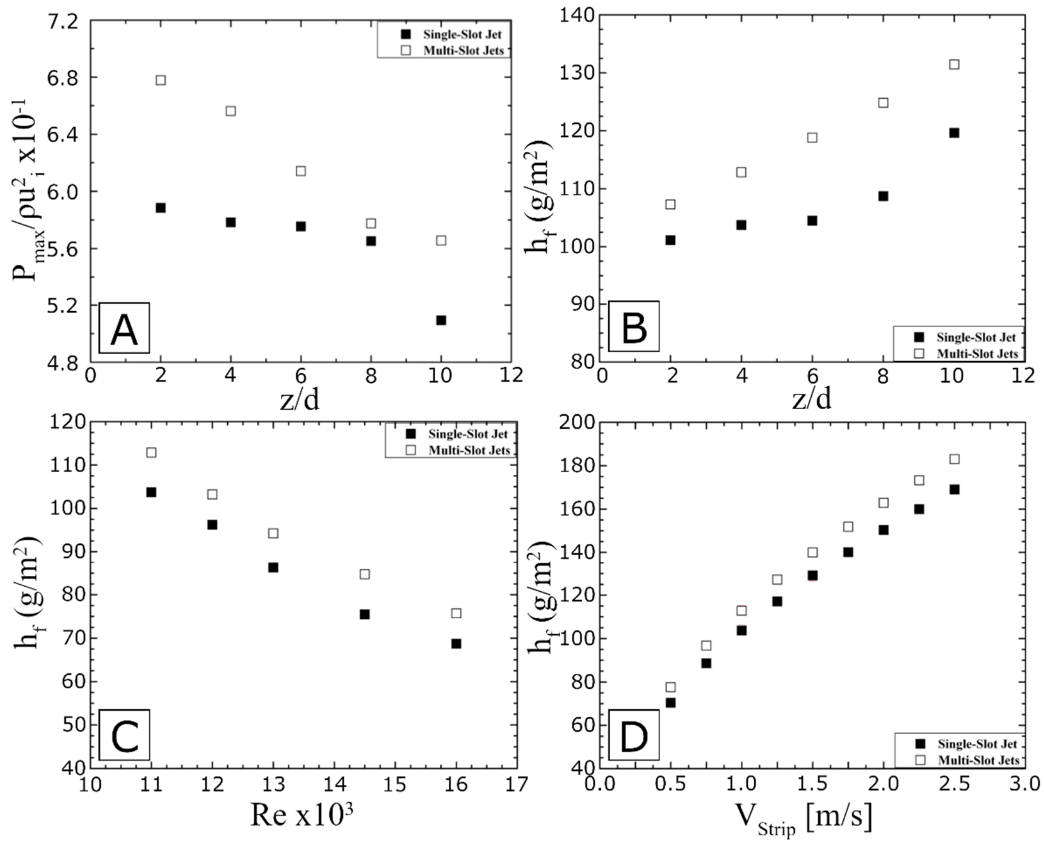

Figure 2.18 Comparison of the data from a multi-slot and single-slot planar jet from Tamadonfar [10]. The Reynolds number for the main and both auxiliary jets was equal for all data above. Main jet thickness 1.52 mm and auxiliary jet thickness 3.04 mm. Unless stated z/d = 4, V_{strip} = 1 m/s and Re = 11,000. Panel A: Dimensionless pressure ($P/\rho u^2$) measured at the impingement plate for different impingement ratios (z/d). Panel B: Coating weight (h_f) as a function of impingement ratio. Panel C: Coating weight as a function of Reynold's number. Panel D: Coating weight as a function of substrate velocity.

The maximum pressure and maximum pressure gradient generated by the multi-slot and single slot jet are presented in panels C and D of Figure 2.19 respectively. Similar to the work of Tamadonfar [10], the pressure of the multi-slot jet is greater than the single slot jet but the maximum pressure gradient, which is a significant parameter used in coating weight models, is lower. However, the maximum pressure gradient of the multi-slot jet exceeds the single slot jet at the higher Reynolds number of 13,000.

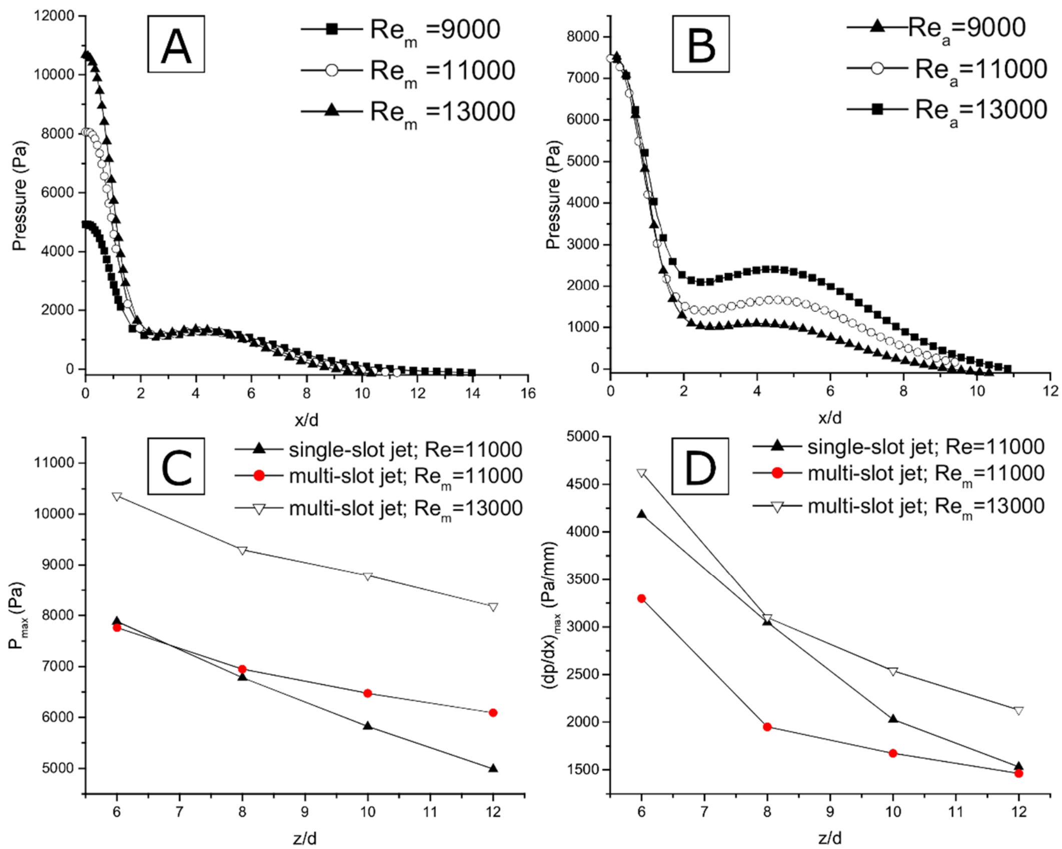

Figure 2.19 Pressure profiles at the impingement plate, the maximum pressure and maximum pressure gradients of the single-slot and multi-slot jets measured by Alibeigi [11]. For all experiments the main jet thickness d = 1.5 mm and the auxiliary jet thickness a = 3 mm. Panel A: pressure profiles at z/d = 4 and Re_a = 11,000. Panel B: pressure profiles at z/d = 4 and Re_m = 11,000. Maximum pressure (panel C) and maximum pressure gradients (panel D) at the plate as a function of impingement ratio with Re_a = 11,000.

Experimental work was performed on a multi-slot jet by Takeda et al. [46] to compare with computational models of the same jet geometry. The multi-slot jet had been simulated using a 2D steady-state analysis with the turbulence modelled using a realizable k-ω model. The experimental work consisted of static pressure profiles measured on the impingement plate. Figure 2.20 shows the modelled pressure results, panel 1, and the measured pressure profiles, panel 2, for three jet operating parameters: the main jet alone, the main jet with

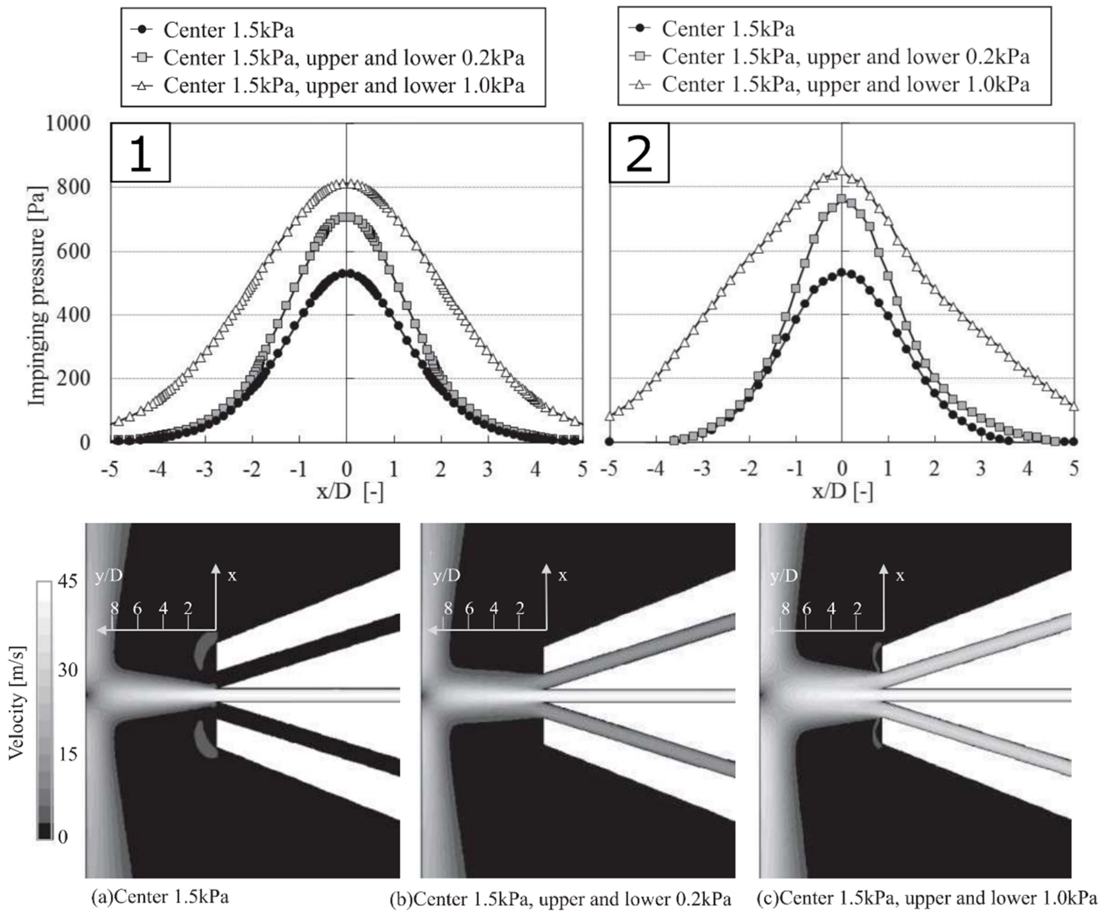

Figure 2.20 1: Static pressure profiles at the impingement plate extracted from the multiple jet CFD model. 2: Static pressure profiles experimentally measured at the impingement plate. Contour plots of velocity for a) the main jet alone b) the main jet with low-speed auxiliary jets c) the main jet with the high-speed auxiliary jets. Takeda et al. [46].

low-speed auxiliary jets and the main jet with the high-speed auxiliary jets. Contour plots of the three jet multiple slot jet operating parameters are presented in Figure 2.20. A comparison between the experimental and modelling results showed that the model had the ability to accurately predict the magnitude and the profile shape of the static pressure generated by the impingement of the multi-slot jet. The ability of the air-knife to wipe the excess coating material from the substrate is related to the static pressure gradient on the substrate. The results by Takeda et al. [46] showed that the auxiliary jets had the ability to increase the static pressure gradient, as seen with the low-speed auxiliary jets, but for the higher auxiliary jet velocity, the static pressure gradient was reduced. This showed that there existed a range of auxiliary jet velocities where they auxiliary jets improved the ability of the jets to wipe but, at some higher limit, the auxiliary jets caused the multi-slot jet to have a similar static pressure gradient as the main jet alone.

A more extensive numerical parametric study of the multi-slot jet was performed by Yahyaee-Soufiani et al. [47], who used the shear stress and pressure profiles predicted by a k-ε simulation of the jet flow to determine the substrate coating weights achievable with the multi-slot nozzle using the analytical model of Elsaadawy et al. [45]. The authors found that the ideal configuration of the multi-slot jet which resulted in thinner coatings had the centerlines of the auxiliary and main jet centerlines coinciding at the substrate surface.

Neither the experimental work of Takeda [46] or Alibeigi [11] reported on acoustic tones produced by the jet impingement. The lack of the authors reporting acoustic tones could be due to the velocities of the jets used in their experiments being too low to result in tones for the jet design (45 m/s in Takeda's [46] experiments and 90-130 m/s in Alibeigi's [11] experiments). Arthurs and Ziada [31] observed acoustic tones of significant amplitudes at main jet velocities of 0.4 Ma, roughly 137 m/s. Alibeigi [11] referred to the oscillation of the jet in proposing a possible reason for the difference in the measured experimental data compared to the numerical results of Tamadonfar [10] as Tamadonfar's steady-state simulations did not capture the jet oscillations.

2.4 Coherent structure identification using P.O.D.

Proper Orthogonal Decomposition (POD) extracts the most energetic modes from a set of snapshots of a system. These modes can be used as basis functions for a Galerkin projection of the underlying system that has a reduced order of dimensions. Models of systems of varying complexity can be created through weighted linear combinations of different basis functions. POD has been used as an analysis tool in multiple disciplines including turbulence in fluid mechanics, data compression, image processing, stochastic processes, signal analysis, process identification and control. Similar variants of POD such as Principal Component Analysis and Karhunen–Loève Transform can be found in many areas of science and mathematics.

In fluid mechanics, the POD technique is widely used to identify and analyse the coherent structures found in many fluid mechanics systems and as a tool to reduce fluid mechanic phenomena to reduced-order models that describe the dominant features of the flow. Since the first application of the POD technique to fluid mechanics problems by Lumley [48], its use has been found in the analysis of multiple different fluid mechanics problems. Bakewell and Lumley [49] used the technique in their analysis of the boundary layer in a fully developed pipe to identify randomly distributed counter-rotating eddy pairs as a dominant feature of the wall region. Rempfer [50] used the POD technique to develop a system of equations that describe the coherent structures found in the transition region of the boundary layer of a flat plate. Arndt et al. [51] analysed the pressure fluctuations in the mixing layer of a turbulent jet and were able to monitor the growth and saturation of instability waves as well as find evidence of the merging of vortices. Delville et al. [52]

examined the dominant modes of the mixing layer and found evidence of the coherent structures associated with the unstable shear layer. The data from a large array of 138 hot-wire anemometers were analysed by Citriniti and George [53], who used the POD technique to extract the shape and characteristics of azimuthal modes exhibited by the axisymmetric jet from their data. The PIV velocity fields of an impinging axisymmetric jet were analysed by Hammad and Milanovic [54] to identify flow structures of the jet that could be significant in jet impingement heat transfer. In the area of combustion Gadiraju et al. [55] used the POD technique to isolate the dominant flame shapes of an emission nozzle and found that the frequency of the low order reconstruction could accurately capture the pressure fluctuations measured.

In this work, POD will be utilised to extract modes from vector fields of the jet flow to identify significant features. These modes and their energies will be used in conjunction with acoustic and pressure data to correlate these features to both the aeroacoustic feedback mechanism and give a measure of the influence of the auxiliary jets on these features and the jet flow as a whole.

2.5 Summary

The generation and growth of instabilities in a shear layer have been extensively investigated both mathematically and experimentally from the spatial solution of the linearized inviscid theory of Michalke [15] and the corroborating experiments of Freymuth [16] to the collective action first documented by Ho and Huang [19]. These fundamentals allowed for the understanding of the role of the instabilities and coherent structures in the aeroacoustic feedback mechanism of the self-excited impinging jets as exemplified in the work of Nosseir and Ho [25], [26].

There has been significantly less work into the interaction of multiple jets and the effect on the aeroacoustic feedback mechanism. Michalke and Hermann [13] did a small amount of work looking at jets with external flow but specifically focusing on the instabilities of a free jet. There has been a lot of work in the area of SVTOL aircraft specifically into the influence of micro-jets on the forces and noise generated by the aeroacoustic feedback in impinging high-speed jets. Sheplak and Spina [36], [37] investigated the influence of an auxiliary co-axial axisymmetric jet on the aeroacoustic feedback mechanism of the inner axisymmetric jet impinging upon a rigid plate. While Sheplak and Spina's work [36], [37] was for high speed (Ma = 0.9-1.1) axisymmetric jets, their work was similar to the present investigation in that the interaction between the main and auxiliary jets was continuous along the shear layer. Their work found a reduction in the noise and forces generated by the jet. This thesis is an investigation into planar jets and if auxiliary planar jets can be used to influence the aeroacoustic feedback mechanism resulting in a similar reduction in the noise and forces generated by the jet through the aeroacoustic feedback mechanism.

Chapter 3
Experimental Apparatus

The investigation into the current multi-slot jet design began with the work of Tamadonfar [10] who numerically simulated the flow characteristics and resulting in impingement pressure and shear stress profiles of different multi-slot designs. The most effective design, based on the patent application of Kim et al. [7], was then fabricated by Alibeigi who experimentally investigated the resulting pressure profiles [56] in order to validate the numerical models of Tamadonnfar [10]. Modifications were further made to the nozzle plates of the main jet for this investigation. The rigidity of the nozzle plates was increased by shortening them in the axial direction and creating a method by which they could be clamped nearer to the nozzle edge to maintain their shape under the high pressures necessary for the experiments.

3.1 Multi-slot jet apparatus

The multi-slot jet apparatus consisted of three independent planar jets: the main jet and two auxiliary jets located on either side of the main jet. Each jet is comprised of a flow distribution tube, a settling plenum, a mesh screen acting as a flow conditioner, a nozzle chamber and a jet nozzle. Figure 3.1 is an annotated schematic of these features. The distribution tube ensured a uniform spanwise distribution of the jet flow. The mesh screen provided a significant pressure drop which allowed the air to settle in the plenum chamber and resulted in a more uniform flow as it broke down large scale coherent turbulent structures. Such mesh generates small scale random turbulence which can be ignored in the analysis of the large scale flow features investigated in this thesis. The nozzle chamber created the contraction to the jet nozzle and was comprised of plates that could be moved to investigate the effect of altering the jet nozzle geometry.

The air supply for the main jet was provided by the facility's compressed airline. The compressed airline was maintained at 590 kPa (85 psi) with the flow to the main jet controlled via an ARO 860 kPa (125 psi) regulator. The air supply for the auxiliary jets was supplied by a Sonic 70 centrifugal blower. The flow to each auxiliary jet could be controlled independently via a manifold of gate valves containing a bypass valve for excess air. The flow for all three jets entered the apparatus through individual distribution tubes. The distribution tubes were made from 25 mm inner diameter aluminium tubes with rows of holes of decreasing diameter drilled along the length of the tube and capped at one end. The distribution tubes were designed to ensure a uniform velocity along the span of the jet (Arthurs & Ziada [30]). The flow then passed through mesh flow conditioning screens to break down any existing turbulent structures. The flow conditioning screens consisted of two layers of stainless steel cloth (70 wires per inch) with an open area ratio of β=0.58 (Mehta & Bradshaw [57]). The flow for each jet settled in a plenum located after the flow screen immediately before exiting via the nozzle. The magnified inset in Figure 3.1 specifies the nozzle geometry parameters: the main jet width, "*d*", the auxiliary jet widths, "*a*", the axial distance between the main and auxiliary jet nozzles, "*s*", as well as the impingement distance between the multi-slot jet and impingement plate "*h*".

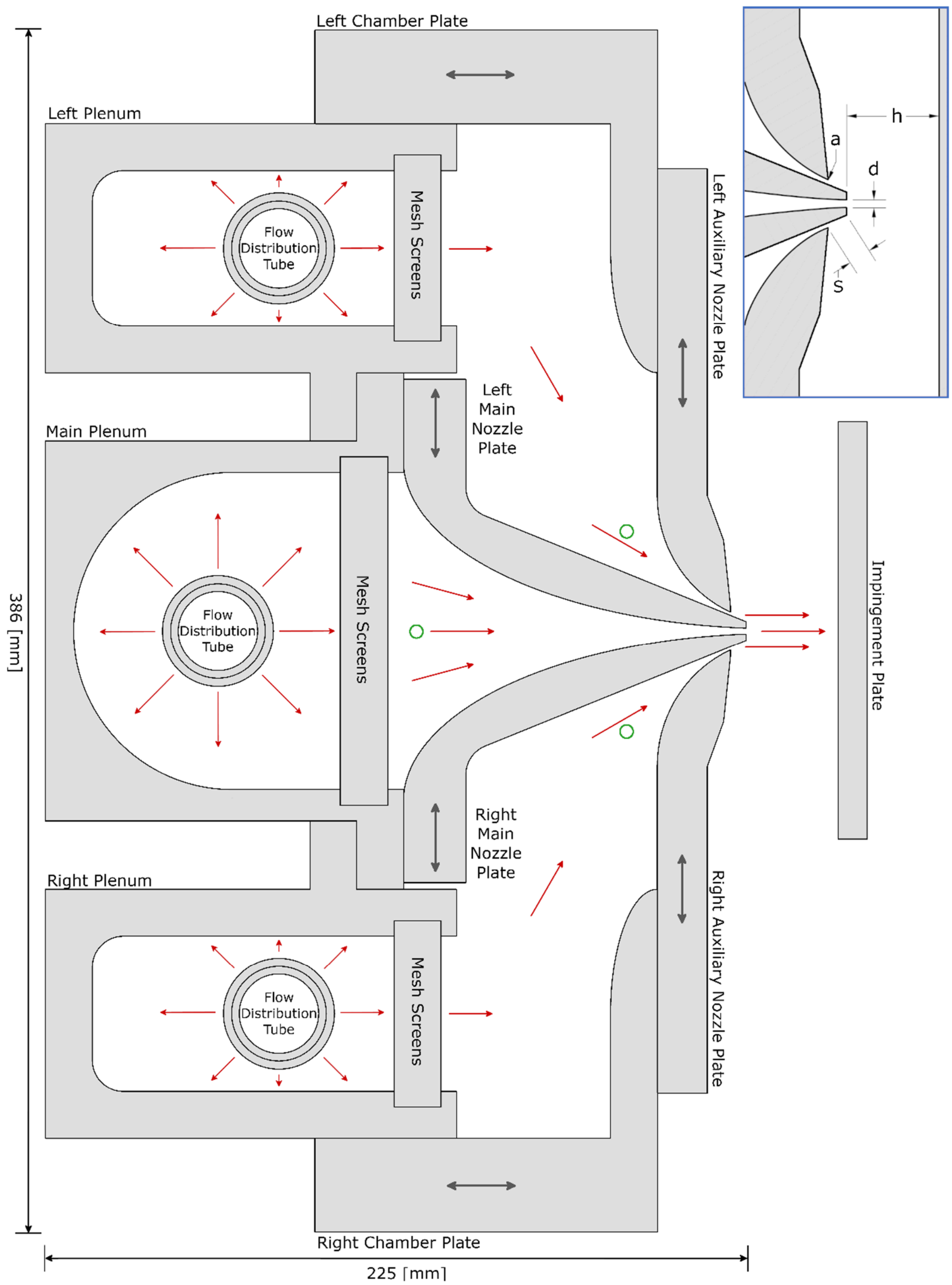

Figure 3.1 Schematic of the multi-slot jet apparatus. Red arrows indicate the airflow through the jet. Gray arrows indicate the direction of movement of different plates to change the geometry of the apparatus. The green circles indicate the position of the pressure taps used to measure the plenum pressures. The insert in the top right of the image shows a close up of the jet exit and indicates the geometric parameters of the multi-slot jet.

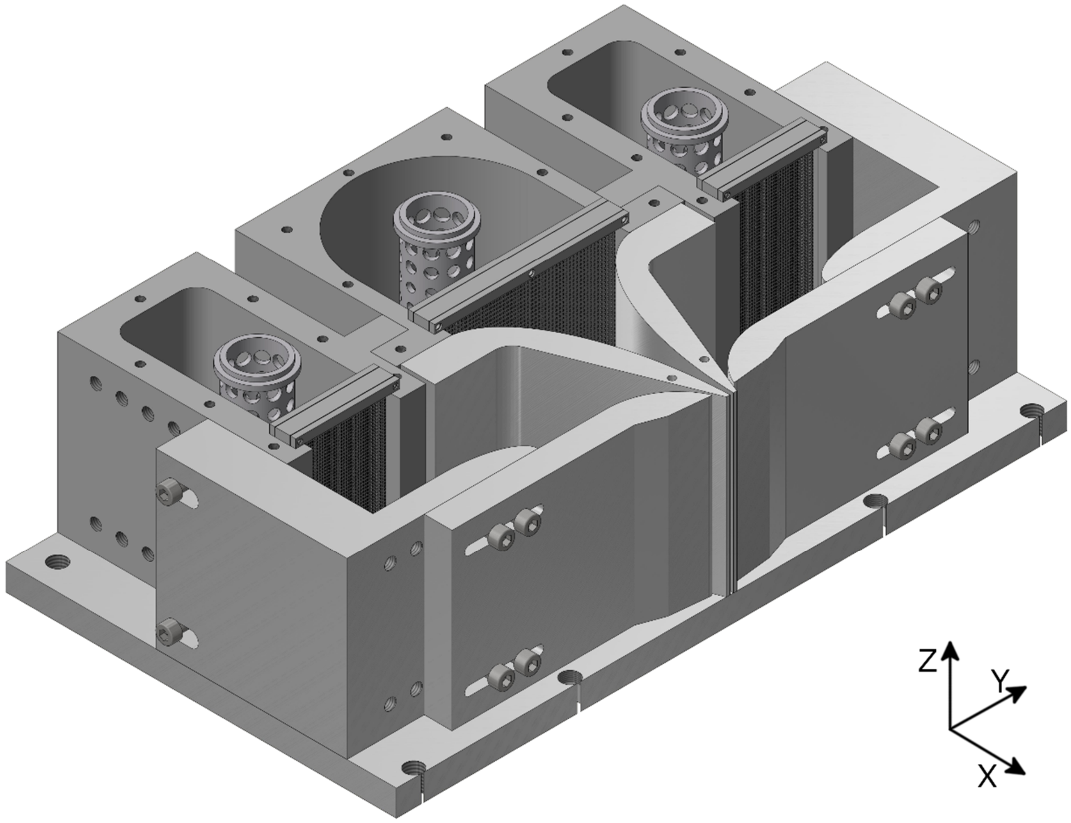

Figure 3.2 3D rendering of the Multiple Slot Jet

The nozzle of the main jet was formed from two movable aluminium plates. These nozzle plates were machined with an elliptical profile with major and minor axes of 110 mm and 54 mm respectively. The dimensions of the main nozzle plates resulted in a nozzle contraction ratio of 55 for a main jet nozzle width of 2 mm. The main jet nozzle width, “d”, could be set to 1-5 mm with a fixed spanwise length of 100 mm. The inner surfaces of each auxiliary jet nozzle were formed from the flat outer surface of a main jet nozzle plate and a separate aluminum auxiliary nozzle plate with an elliptical profile. The elliptical profile of the auxiliary nozzle plates had major and minor axes of 74 mm and 46 mm, respectively. The auxiliary jet nozzle thickness, “a”, could be varied between 0-50 mm. The plane of each auxiliary jets was inclined by 22° relative to the main jet centreline. The distance between the exit of the main jet and the exit of each auxiliary jet in the axial direction of the auxiliary jet, “s”, could be set between 0-45 mm through moving the chamber plates (labelled in Figure 3.1). Figure 3.2 shows a 3D rendering of the multi-slot jet with the top plate removed to show the shape of the nozzle plate and the internal components.

The shear layers of a jet are defined by the profiles of the nozzles of the jet. Elliptical nozzle profiles allow for significant contraction of the jet nozzle while maintaining a positive pressure gradient, resulting in a “top-hat” profile Figure 3.3. The design of the multi-slot jet ensured a consistent elliptical profile for the main jet at all nozzle widths. The outer nozzle profile of the auxiliary jets was elliptical however, due to design constraints the inner nozzle profile was a flat plate. The contraction of the auxiliary jets was consistent and resulted in a positive pressure gradient. The condition of the auxiliary jet shear layers at the point they merge with the main jet shear layers was heavily influenced by the auxiliary jet setback distance “s” (Figure 3.1). With a non-zero setback distance, the auxiliary jets would develop as wall jets before merging with the main jet. The larger the setback distance the larger distance over which the wall jet profile would develop before interacting with the main jet shear layers. The displacement, disturbance and momentum thicknesses of the jet shear layers of the multi-slot jet were measured and reported by Alibeigi [58].

The multiple slot jet apparatus was mounted on a Velmex motorised uni-slide traverse with a lead screw error of 0.18 mm per 254 mm. The impingement plate for this investigation was a machined flat aluminium plate which was secured at the end of the traverse. The plate was mounted on a Newport rotary stage allowing for control of the angle of the plate to the multi-slot jet with an accuracy of ±0.5°. For all the experiments in this study, the angle between the plate and multi-slot jet was controlled such that the plate was perpendicular to the jet centerline. The rotary stage was affixed to a second Velmex manual uni-slide traverse which allowed for the plate to be moved perpendicular to the axial direction of the jet. The distance between the multi-slot jet and the plate was controlled by a Slo-Syn stepper motor with the minimum division of 5μm. For the experiments reported in this study the impingement ratio (h/d) – i.e. the ratio of the main jet nozzle width to the impingement distance – was varied between 6 and 16.

3.2 Pressure

The jet plenum pressure was measured through pressure taps located after the flow conditioning screens. The pressure was measured using a Validyne DP 15 pressure transducer coupled with a Validyne CD23 carrier demodulator. The pressure transducer and demodulator were calibrated using a Crystal IS33 pressure calibrator. The data acquisition card used to acquire the data was a National Instruments PCI card 4452 with a sampling rate of 204.8 kHz. The pressure measured in the plenum was used to calculate the velocity of the jets at the nozzle exit using the gas dynamics formula (equation 3.1), where "c" is the speed of sound (≈343 m/s for this investigation), "η" is the isentropic efficiency of the jet, "γ" is the ratio of specific heats of air and "P_S" and "P_∞" are the plenum and ambient pressures respectively.

$$V = c \cdot \eta \cdot \sqrt{\frac{2}{\gamma - 1}\left[\left(\frac{P_S + P_\infty}{P_\infty}\right)^{\left({\gamma-1}/{\gamma}\right)} - 1\right]} \tag{3.1}$$

The velocity of the main jet was tested between 200 m/s and 300 m/s, corresponding to plenum pressures of 181 kPa and 451 kPa respectively. The velocities of the auxiliary jets were maintained under 120 m/s or a plenum pressure of 62 kPa. The velocity profile at the exit of the jet was characterised using a simple Pitot tube with a diameter of 0.1 mm and the pressure transducers discussed above. The main jet pressure profile at the jet exit exhibited a top-hat profile, as seen in Figure 3.3.

Profiles of both static and fluctuating pressure were measured at the impingement plate. The static pressure was measured using a 0.0635 mm hole drilled into the impingement

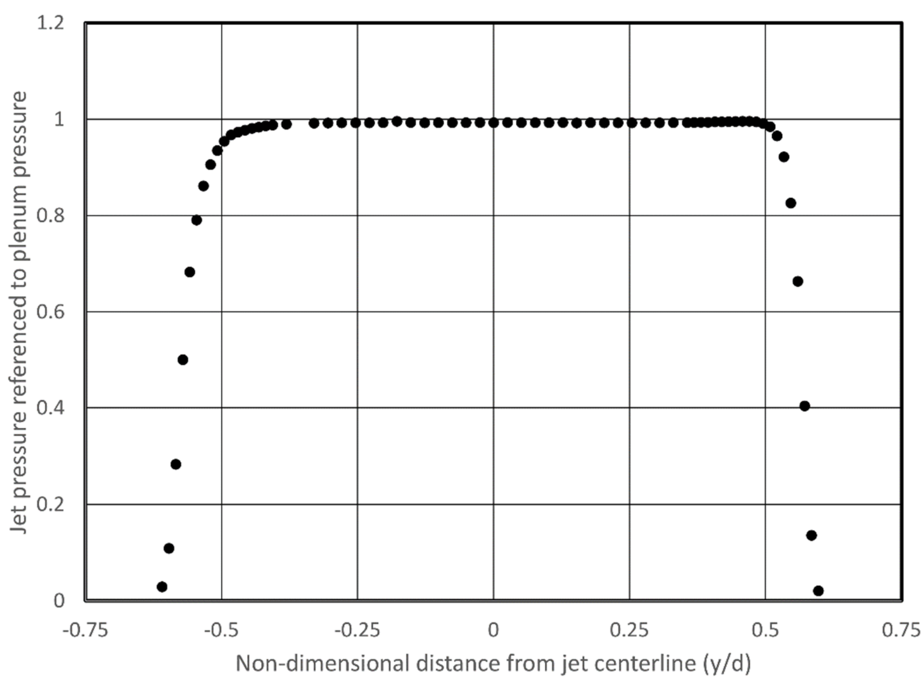

Figure 3.3 Pressure profile of the main jet nozzle exit for the main jet velocity of 250 m/s and a nozzle thickness of 2 mm referenced to the measured plenum pressure.

plate connected to the DP15/CD23 pressure measurement system described above. The fluctuating pressure at the impingement plate was determined using a PCB Piezotronics pressure transducer flush mounted to the impingement plate coupled with a Kistler 4 Channel Piezoelectric Sensor Power Supply and Signal Conditioner. As discussed previously, the plate was mounted on a uni-slide traverse allowing the plate and sensors to be moved perpendicular to the jet axis to capture both the static and fluctuating pressure profiles at the plate; see Figure 3.5.

3.3 Acoustics

Acoustics measurements were made with a GRAS 40BP microphone coupled with a GRAS 26AB pre-amplifier and GRAS 12AA power supply. The microphone position was maintained for all experiments performed. This position, which is indicated in Figure 3.5, was 193 mm to the left of the centerline of the main jet, 70 mm above the spanwise centerline of the multi-slot jet and 6 mm from the impingement plate to which it was mounted. This position was found to capture the clearest acoustic signal from the impinging jet and was maintained for all experiments to ensure a comparison of the results of different experiments was possible.

The microphone has a stated flat frequency response from 10 Hz-25 kHz of ±1 dB. The data acquisition of the acoustic signals was done using the same National Instruments PCI 4452 card as used for the pressure data. The microphones were calibrated using a GRAS 42AB pistonphone. The microphone and transducers communicated to the data acquisition card via a NI BNC 2140 signal conditioner. The acoustic data presented in this thesis are reported as RMS spectra: an average of fifty individual frequency spectra of the root mean square, RMS, of the microphone signal.

3.4 Particle Image Velocimetry

Particle image velocimetry is a measurement technique which can capture a high-resolution vector field of a fluid's velocity. A laser sheet illuminates seeding particles dispersed in the flow twice in rapid succession separated in time by a well-defined delay. The illumination of the particles is captured in two separate images. These images are segmented into a regular grid of "interrogation regions" and software (Insight 4G) is used to determine where the pattern of illuminated particles of an interrogation region in the first image can be found in the second image. The software returns the pixel difference between the locations of each interrogation region pattern on the different images. A calibration image of a known length measures the distance travelled per pixel which in conjunction with the time delay between the two image captures allows the software to calculate the velocity vector of each interrogation region. This technique results in the instantaneous velocity field of the captured region expressed as a matrix of vectors which can then be used to analyse various aspects of the flow such as turbulence intensity, Reynold's stresses, vorticity and has been expanded to pressure for low velocity flows.

Particle Image Velocimetry (PIV) was performed to capture the velocity field of the jet for a configuration where the jet was generating an acoustic tone that could be suppressed using the auxiliary jets: V_M = 250 m/s, d = 2 mm, a = 1 mm, s = 5 mm, h/d = 12 with V_A = 0 m/s and 100 m/s respectively. The flow was seeded with tracer particles of Bis(2-ethylhexyl) sebacate. The seeding particles were injected separately to the three jet air

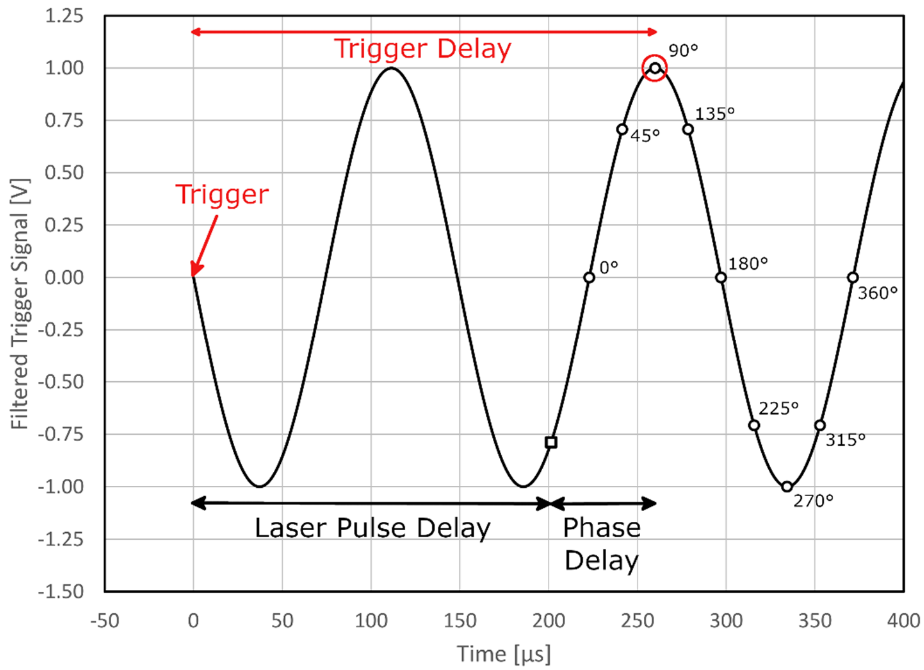

Figure 3.4 Filtered acoustic signal with indicated delays for phase-locked PIV.

supply lines after the regulator and manifolds controlling the jet velocity, one meter upstream from the multi-slot jet apparatus. The flow of the seeding material was controlled independently for each jet using a manifold of valves. The seeding material was atomised using a six-nozzle Laskin aerosol generator. The average resulting particle diameter was 1µm, which results in a Stokes number < 0.1. As reported by Melling [59], a Stokes number in the range of 0.05 – 0.1 results in a particle tracking error of less than 2%. The PIV images were captured using a PowerView 4MP camera. The camera was mounted to look down on a plan view of the flow field, as indicated in Figure 3.5. The PowerView 4MP is a 12-bit camera and takes 2048 x 2048 pixel images. The seeding particles were illuminated via a 532nm New Wave Solo 120 XT pulsed Nd: YAG laser. Laser optics were used to convert the laser beam into a laser sheet to illuminate the flow area. The camera and laser timing were controlled using a TSI LaserPulse 610035 synchroniser. A custom-designed trigger coupled with an Alligator signal filter was used to capture images at a specific point in the signal oscillation for the purpose of phase-locked PIV. Figure 3.4 shows a typical example of the filtered acoustic signal and the delays associated with triggering the camera. The custom-designed trigger pulses at detected falling zero-cross of the acoustic signal. The synchroniser has two delays after the pulse input. The laser pulse delay is the time required for the laser to achieve the required energy. The phase delay is a controllable delay that can be varied to capture an image of the flow at specific points in the acoustic cycle.

The vector fields of each PIV field were obtained using a deformation-based scheme. Interrogation regions were 24×24 pixels and had 75% overlap in both the x and y-directions. All PIV images below a validation rate of 99% were rejected. Vector replacement and interpolation schemes were performed on each image to eliminate erroneous vectors. A minimum of 100 vector fields was averaged to create the time-averaged PIV images presented in this thesis. The same replacement and interpolation schemes were used to generate the vector fields used in the POD analysis. A minimum of 400 vector fields was used for the POD analysis of each auxiliary jet velocity analysed.

The PIV was calibrated using the velocity of the potential core as measured by a Pitot tube immersed in the flow. The calibration curve used for the PIV velocity is presented in Figure 3.6. The data points on the graph are the velocity of the main jet of the multi-slot jet measured using the two different methods for the same jet conditions. The solid line in the graph is where the data points should fall if the velocity measurements from the PIV completely agreed with the measurements calculated from the Pitot tube. The PIV

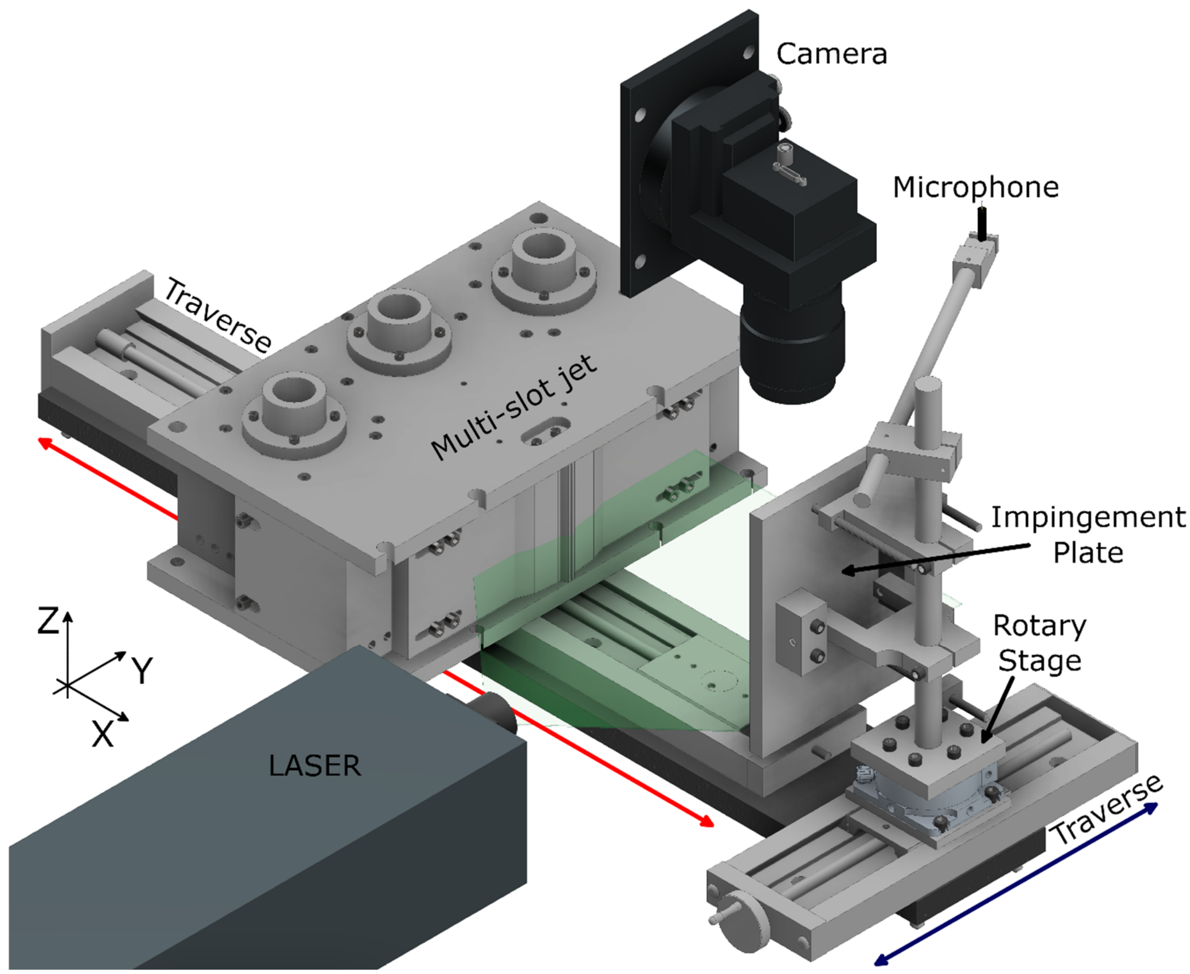

Figure 3.5 3D sketch of the PIV apparatus setup. The red arrow shows the travel of the multi-slot jet and the blue arrow shows the travel of the rotary stage and impingement plate.

measurements were an average of 100 averages of PIV vector fields of the potential core of the jet while the Pitot tube measurements were an average of 1 minute of collected pressure data. The data points indicate that the velocity reported by the PIV is lower than those measured directly by the Pitot tube. A full discussion of the calibration methodology and the error associated with the PIV is presented in Appendix A.

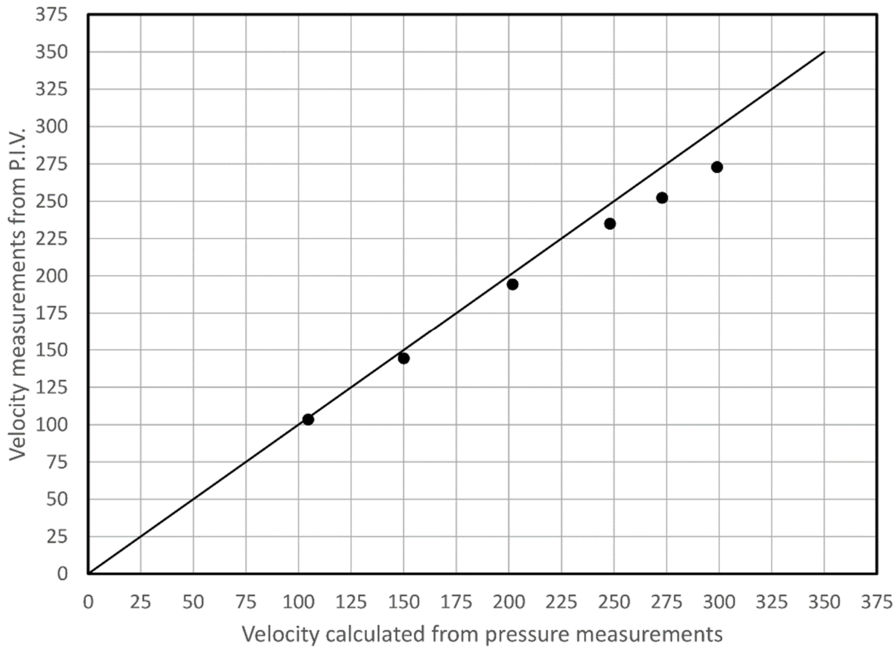

Figure 3.6 Calibration curve of the PIV calibrated against Pitot tube measurements. Both measurements are performed in the potential core of the jet.

The calibration of the PIV showed that the measurements from the PIV under-reported the flow velocities when jet velocities exceeded 100 m/s. To account for the difference in the velocities predicted by the PIV, the individual vectors of the PIV data were corrected with a second-order polynomial derived from the calibration curve of the data in Figure 3.6. The calibration equation is given below and has an R-squared value of 0.9994.

$$Vel_{Calib} = 9.36 \times 10^{-4} \times {Vel_{PIV}}^{2} + 9.70 \times 10^{-1} \times Vel_{PIV} + 2.47 \quad (3.2)$$

3.5 Proper Orthogonal Decomposition

Proper Orthogonal Decomposition is an analysis tool used to reduce a phenomenon to a set of fundamental basis. In the analysis, a set of independent measurements of a phenomenon are converted to a set of basis functions such that those basis functions are orthogonal and the original measurements could be represented as a weighted sum of these basis functions. For this work, the input measurements were PIV vector fields of the data that were taken at random for a given operating condition of the jet. The POD analysis calculates the eigenfunctions and eigenvalues from the covariance matrix of those input measurements. The eigenfunctions, commonly referred to as “modes” in the literature, are the basis function and in this analysis, they were velocity vector fields. The eigenvalues are the weights attributed to each eigenfunction for the reconstruction of the original input measurements via a weighted sum. As the covariance matrix in this analysis was the product of the velocity fields with their transpose, the eigenvalues were essentially a kinetic energy term and in literature are commonly referred to as the “energy” associated with each mode [60]. The modes with the larger weights, and thus larger energy, are more significant to defining the flow field of the phenomenon. If a phenomenon exhibits any regular motion it should be expressed by the POD analysis as a high energy mode, or group of modes, in the analysis. As the oscillation of self-excited impinging jets is known to be a significant flow feature it should be able to be isolated as a set of high-energy modes. Comparing the change of the shape of the modes and their energy with auxiliary jet velocity should show the effect of the auxiliary jet velocity on the oscillation of the jet.

POD allowed for the measurement of the oscillation of that jet column in the absence of an acoustic tone with which to phase-lock the camera. PIV images of the velocity field were taken at random for different auxiliary jet velocities with a jet configuration which generated an acoustic tone that was suppressed by the auxiliary jets: $V_M = 250$ m/s, d = 2 mm, a = 1 mm, s = 5 mm, h/d = 12. Four hundred vector fields of the multi-slot jets were taken at random and used for the POD analysis. The mode shapes and energies returned by the POD will be used to infer if the jet was oscillating and to determine the magnitude of any oscillations.

3.6 Experiment matrix

Table 3.1 and Table 3.2 outline the experimental conditions that were used to investigate the effect of different operating parameters, or combinations of operating parameters, of the multi-slot jet on the acoustic tones and jet oscillations produced by the jet impingement. The leftmost column in both tables outlines, in brief, the parameters being investigated by the stated conditions. The range of main jet parameters investigated was chosen to reflect the parameters used in the industry. The auxiliary jet parameters were informed by the previous work of Tamadonfar and Alibeigi [10], [56].

The experiment parameters in Table 3.1 were the experiments that are presented and discussed in depth in later chapters as those combinations of parameters were found to produce distinct and observable trends. The experiments in Table 3.2 yielded no unique trends to discuss in further chapters but the results of these experiments were included in global data trends of Strouhal number, velocity ratio, etc..

Table 3.1 Experimental parameters for the investigation into the influence of different jet parameters on the tones generated by the multi-slot jet.

<table>
<tr><th rowspan="2"></th><th>V_M</th><th>d</th><th>a</th><th>a/d</th><th>s</th><th>h/d</th><th colspan="5">V_A</th></tr>
<tr><th>m/s</th><th>mm</th><th>mm</th><th>-</th><th>mm</th><th>-</th><th colspan="5">m/s</th></tr>
<tr><td rowspan="3">Effect of main jet velocity</td><td>200</td><td rowspan="3">2</td><td rowspan="3">1</td><td rowspan="3">0.5</td><td rowspan="3">5</td><td rowspan="3">6-16</td><td>0</td><td>30</td><td>50</td><td>65</td><td>80</td></tr>
<tr><td>250</td><td>0</td><td>40</td><td>60</td><td>80</td><td>100</td></tr>
<tr><td>300</td><td>0</td><td>50</td><td>70</td><td>95</td><td>120</td></tr>
<tr><td rowspan="4">Effect of “s”</td><td rowspan="4">250</td><td rowspan="4">2</td><td rowspan="4">1</td><td rowspan="4">0.5</td><td>0</td><td rowspan="4">6-16</td><td rowspan="4">0</td><td rowspan="4">40</td><td rowspan="4">60</td><td rowspan="3">80</td><td rowspan="3">100</td></tr>
<tr><td>5</td></tr>
<tr><td>11</td></tr>
<tr><td>22</td><td>-</td><td>-</td></tr>
<tr><td rowspan="3">Effect of “a”</td><td rowspan="3">250</td><td rowspan="3">3</td><td>1</td><td>0.33</td><td rowspan="3">5</td><td rowspan="3">6-16</td><td rowspan="3">0</td><td rowspan="3">40</td><td rowspan="3">60</td><td rowspan="3">80</td><td rowspan="3">100</td></tr>
<tr><td>1.5</td><td>0.5</td></tr>
<tr><td>3</td><td>1</td></tr>
</table>

Table 3.2 Experimental parameters for the investigation into the influence of different jet parameters on the tones generated by the multi-slot jet that yielded no unique trends.

<table>
<tr><th rowspan="2"></th><th>V_M</th><th>d</th><th>a</th><th>a/d</th><th>s</th><th>h/d</th><th colspan="5">V_A</th></tr>
<tr><th>m/s</th><th>mm</th><th>mm</th><th>-</th><th>mm</th><th>-</th><th colspan="5">m/s</th></tr>
<tr><td rowspan="3">Effect of “d” with a constant “a”</td><td rowspan="3">250</td><td>1</td><td rowspan="3">1</td><td>1</td><td rowspan="3">5</td><td rowspan="3">6-16</td><td rowspan="3">0</td><td rowspan="3">40</td><td rowspan="3">60</td><td rowspan="3">80</td><td rowspan="3">100</td></tr>
<tr><td>2</td><td>0.5</td></tr>
<tr><td>3</td><td>0.33</td></tr>
<tr><td rowspan="3">“a/d” = 0.5</td><td rowspan="3">250</td><td>1</td><td>0.5</td><td rowspan="3">0.5</td><td rowspan="3">5</td><td rowspan="3">6-16</td><td rowspan="3">0</td><td rowspan="3">40</td><td rowspan="3">60</td><td rowspan="3">80</td><td rowspan="3">100</td></tr>
<tr><td>2</td><td>1</td></tr>
<tr><td>3</td><td>1.5</td></tr>
<tr><td rowspan="3">“a” = “d”</td><td rowspan="3">250</td><td>1</td><td>1</td><td rowspan="3">1</td><td rowspan="3">5</td><td rowspan="3">6-16</td><td rowspan="3">0</td><td rowspan="3">40</td><td rowspan="3">60</td><td rowspan="3">80</td><td rowspan="3">100</td></tr>
<tr><td>2</td><td>2</td></tr>
<tr><td>3</td><td>3</td></tr>
</table>

A set of jet parameters was identified to generate a strong acoustic tone that was suppressed by increasing auxiliary jet velocity. This specific set of jet parameters was used in testing the influence of the auxiliary jets on the pressure at the plate, and the flow field using PIV. Table 3.3 contains the jet parameters used for the pressure and PIV measurements. As the PIV data was measured at those parameters, the POD analysis is also at those jet parameters.

Table 3.3 Jet parameters used for pressure, PIV and POD experiments.

	V_M	d	a	a/d	s	h/d
Parameters used for pressure, PIV and POD experiments	**m/s**	**mm**	**mm**	**-**	**mm**	**-**
	250	2	1	0.5	5	12

Chapter 4
Results

The data presented in this chapter are the results of different methods of investigation into the influence of auxiliary planar jets on the flow field of, and the intense narrow-band acoustic tones produced by, the impingement of a planar jet on a rigid plate.

Initial acoustic testing of the multi-slot planar jet confirmed that the main jet alone impinging upon a plate generated acoustic tones of similar frequency and amplitude to those found in previous investigations. This can be seen in Figure 4.1 where the acoustic

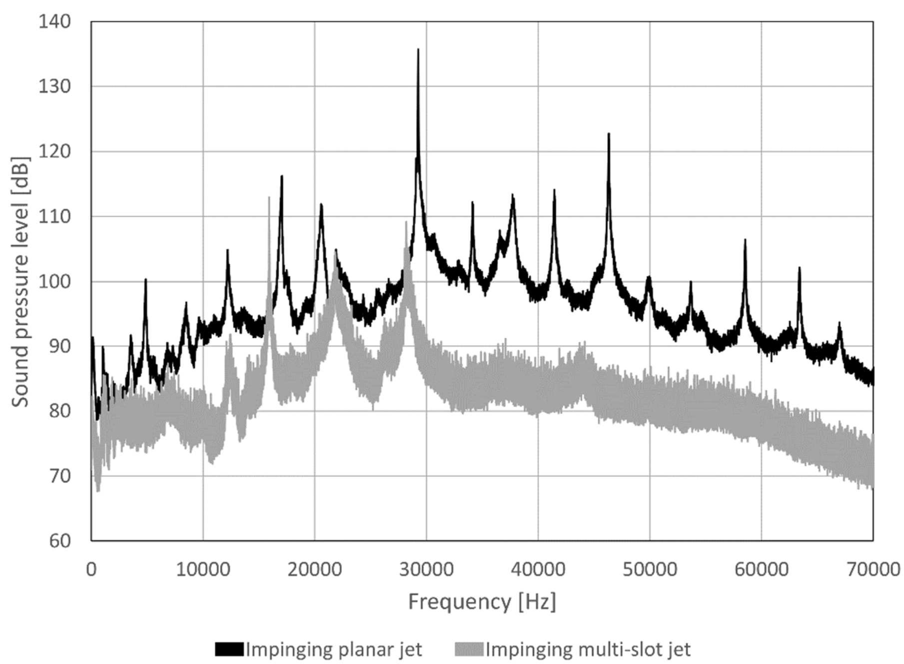

Figure 4.1 Sample spectrum of the impinging planar jet, data provided by Arthurs & Ziada (V_M=300 m/s, d=2 mm, h/d=8) compared to the impinging multiple slot jet (V_M=300 m/s, d=2 mm, h/d=8).

spectrum of the multi-slot jet is compared to data from the work of Arthurs and Ziada [30] provided via private communication.

There are some quantitative differences between the spectrum of Arthus' single slot jet and the multi-slot jet, as shown in Figure 4.1: Arthurs' spectrum had larger amplitude tones, the tones were more numerous and larger amplitude background noise. However, the purpose of Figure 4.1 is to show that the noise of both jets are qualitatively similar in that they both produce large amplitude intense acoustic tones. The difference in the amplitude and number of the tones can be attributed to the difference in the nozzle shapes between the two jets. Arthurs' jet had a much shorter, much more rigid nozzle (an ellipse of 45 mm x 30 mm) [31] in comparison to the main jet nozzle of the multi-slot jet (an ellipse of 74 mm x 46 mm). The different jet nozzle shapes result in different jet shear layers which are reflected in the disturbance, displacement and momentum thicknesses of the jet which were measured by Arthurs to be roughly two thirds the thicknesses of the main jet of the multi-slot jet [31], [58].

§4.1 will present the results of the noise produced by the multi-slot jet for a wide range of jet parameters that were outlined in Chapter 3. The acoustic results will then be presented to show the effect the auxiliary jet nozzle width, velocity and setback distance had on the tones produced by the aeroacoustic feedback mechanism of the planar impinging jet.

Static and fluctuating pressure data, measured at the impingement plate, will be presented in §4.2 to show how the jet oscillation due to the aeroacoustic feedback mechanism affected the pressures at the plate. The pressures were measured for conditions

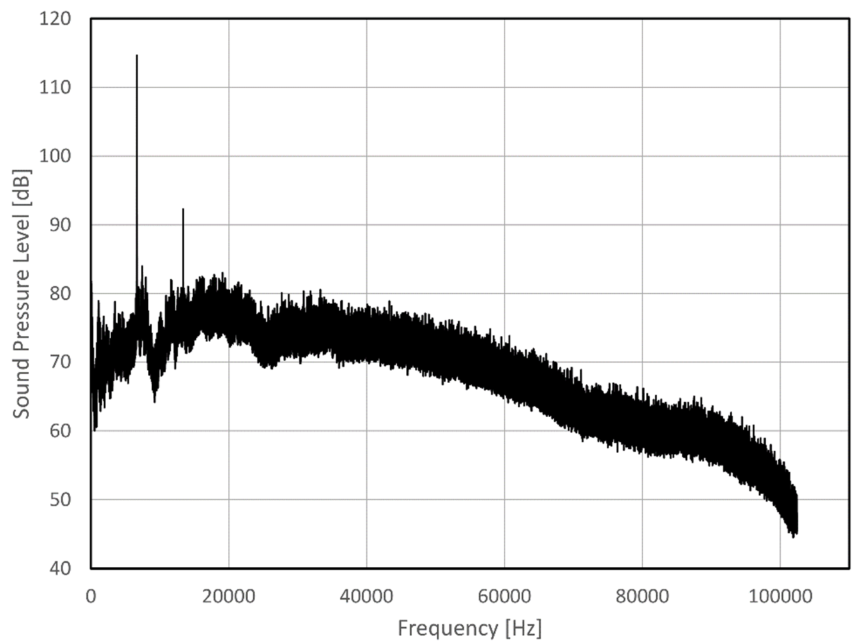

Figure 4.2 Acoustic spectra for the multi-slot jet impinging upon a rigid plate with no auxiliary jets. V_M = 250 m/s, d = 2 mm, h/d = 12.

at which the auxiliary jets had diminished and eliminated the acoustic tones to determine whether the noise reduction was accompanied by a change in the pressures at the plate.

The flow field of the multi-slot jet was investigated using Particle Image Velocimetry (PIV) and Proper Orthogonal Decomposition (POD). The results of this data and analysis will be presented in §4.3 and §4.4. The PIV results were used to show the influence of the auxiliary jets on the mean jet flow field. The POD analysis allowed for specific aspects of the flow-field to be measured more directly. In §4.4 on the POD analysis, the results pertaining specifically to the jet oscillation due to the aeroacoustic feedback mechanism will be presented.

4.1 Effect of jet parameters on jet noise

Impinging planar jets that experience an aeroacoustic feedback mechanism generate large-amplitude, narrowband acoustic tones. Acoustic tests of the impinging main jet alone showed that the multi-slot jet exhibited such tones, as shown in Figure 4.2. The impingement of the main jet alone produced a tone of 10.7 kPa (114.64 dB) at 6686 Hz. The amplitude and frequency of this tone were similar to those tones produced by impinging planar jets in the studies by Arthurs and Ziada [30]–[32]. The spectrum in Figure 4.2 was taken at a single impingement distance of h/d = 12. Combining the acoustic spectra produced by the multi-slot jet over a range of impingement distances produced a waterfall plot like Figure 4.3. The results in Figure 4.3 are presented as kilopascals to better emphasise the contrast between the background noise produced by the jet and the tones due to the aeroacoustic feedback mechanism. As the impingement ratio was increased, the frequency of the tones decreased and can be seen to jump suddenly to different jet stages. It's also possible to see the higher harmonics of the tones in these waterfall plots.

The data from the waterfall plot in Figure 4.3 is summarised in Figure 4.4. In this Figure, the dominant tone of the jet, the largest amplitude tone in a spectrum, at each impingement ratio is plotted alongside the amplitude of that peak. This Figure more clearly shows the decrease in the frequency of the dominant acoustic tone and the sudden transition between the different jet stages. It's also possible to see that the amplitude of the tones does not follow as predictable a pattern as their frequency. In between the impingement ratios of 7 and 10, the jet produced tones in the same

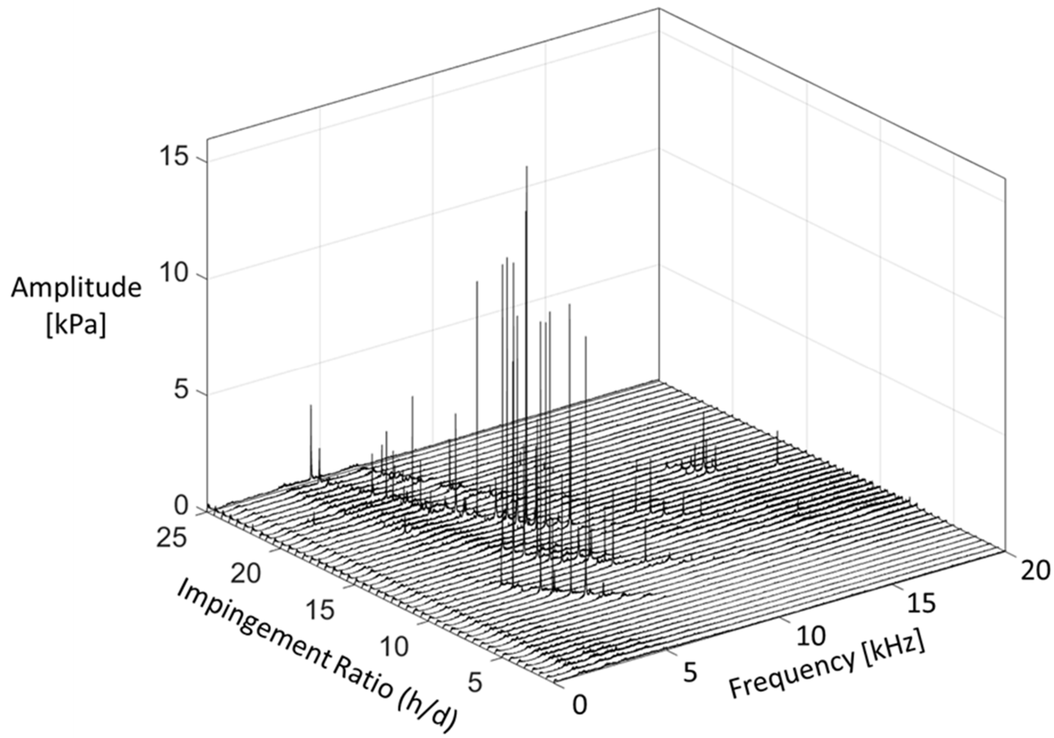

Figure 4.3 Waterfall plot of sound produced by multi-slot jet main jet impinging on a flat plate. VM = 250 m/s, d = 2 mm

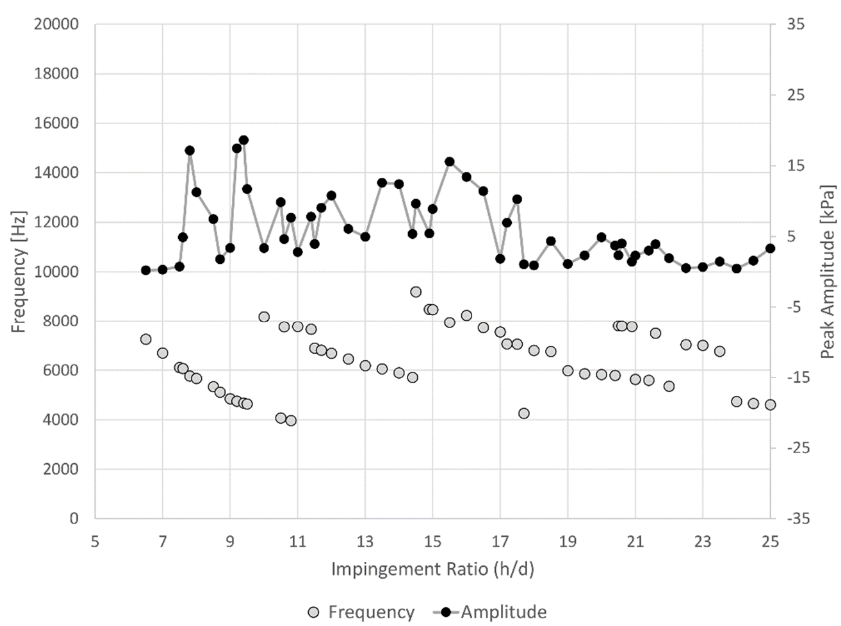

Figure 4.4 Frequency and amplitude of the dominant acoustic tones produced by the main jet alone of the impinging multi-slot jet. VM = 250 m/s, d = 2 mm.

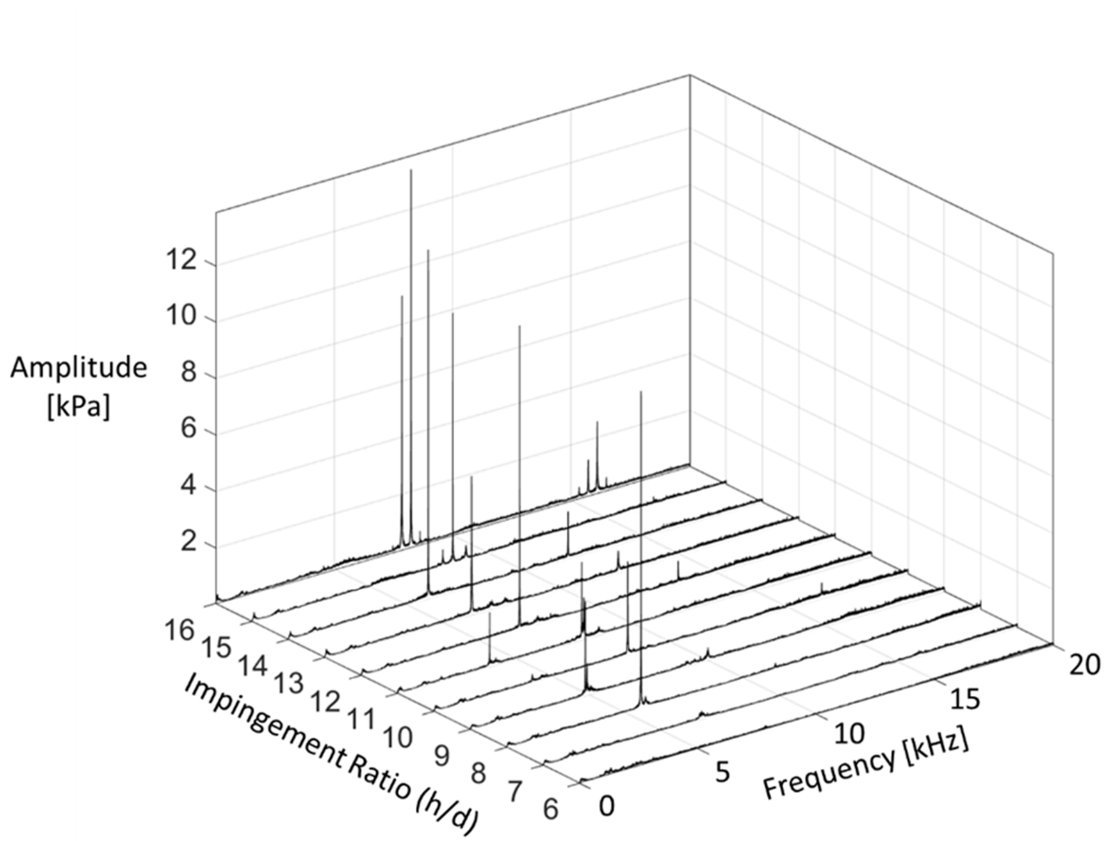

Figure 4.5 Waterfall plot of the sound produced by the impinging multi-slot jet in the impingement ratios of interest. VM = 250 m/s, d = 2 mm, h/d = 6-16.

jet stage but the amplitude of the jet tone increased from 0.0 kPa to 17.5 kPa. It then dropped to 1.8 kPa to then increase again to 18.6 kPa.

The potential core of the jet was found to be 4-6 jet widths from the nozzle. Continuous gas jet wiping is not commonly done so close to the jet exit due to the movement of the substrate and the possibility of splashing coating material solidifying on the nozzle. Impingement ratios greater than 16 are not commonly used industrially, particularly for the lighter coatings usually associated with the automotive industry. Due to those two factors, the investigation was limited to impingement ratios between 6 and 16. Figure 4.5 shows the waterfall plot of the jet with a 2 mm jet nozzle width at a velocity of 250 m/s within the impingement ratios of interest.

To investigate the effect of the auxiliary jets on the sound produced by the main jet, the same configuration of the main jet was tested with four different auxiliary jet velocities with 1 mm auxiliary jet nozzle widths. The results of those tests are presented in the waterfall plots in Figure 4.6 (larger versions of these Figures can be found in Appendix D). Comparing these results with those in Figure 4.5 shows that, at 40 m/s, the amplitude of the tones had significantly reduced, while at 60 m/s the amplitude of the majority of tones produced at this auxiliary jet velocity had reduced and the tones had decreased in number. In panel C in Figure 4.6, an auxiliary jet velocity of 80 m/s, all the tones produced by the impinging jet were eliminated aside from two very low amplitude tones. However, at 100 m/s, the amplitude of the tones at 80 m/s had increased to be as strong as those produced by the jet alone: 13.4 kPa vs 13.9 kPa.

The high amplitude tones found at 100 m/s could be similar to the phenomenon as seen by Sheplak & Spina [36], [37] in their work on high-speed co-axial axisymmetric jets. They saw at velocities of the co-axial similar to the main jet the acoustic tones were amplified above the jet tones produced by the main jet alone. Sheplak's data shows that the co-axial jet could reduce the amplitude of the dominant tone of the main jet by 90% but at higher velocity ratios the amplitude of the tones could reach 4.75 times that of the main jet alone.

To better examine the effect of the auxiliary jet velocity on a tone produced by the impinging planar jet, the acoustic spectra at a single impingement distance, h/d = 12,

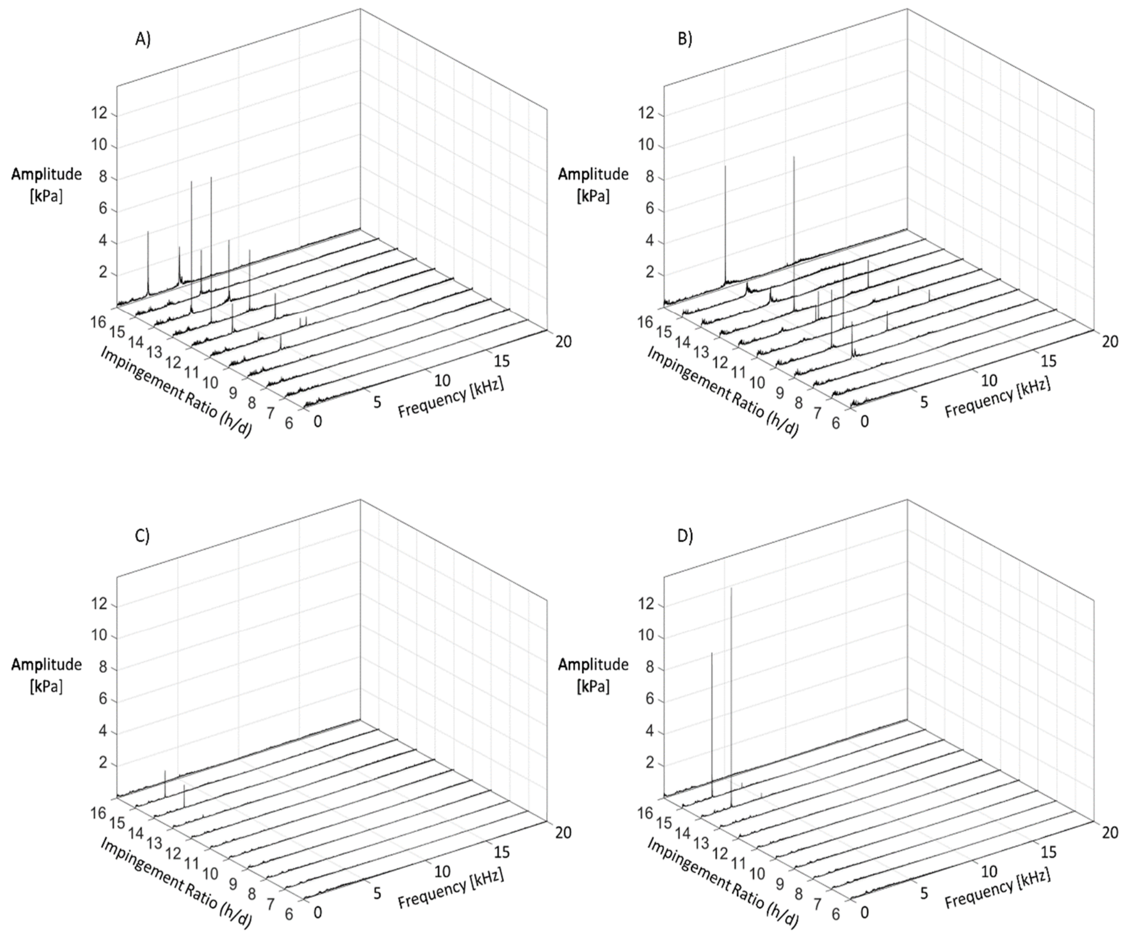

Figure 4.6 Waterfall plots of the sound produced by the impinging multi-slot jet with varying auxiliary jet velocity A) VA = 40 m/s, B) VA = 60 m/s, C) VA = 80 m/s and D) VA = 100 m/s. VM = 250 m/s, d = 2 mm, a = 1 mm, s = 5 mm, h/d = 6-16.

from the data shown in Figure 4.5 and Figure 4.6 are plotted in Figure 4.7 at the auxiliary jet velocities of 0, 40, 60, 80 and 100 m/s.

The tone produced by the multi-slot jet with no auxiliary jets, Figure 4.7(A), was a high-frequency tone, 6685 Hz, with a large amplitude, 10.8 kPa. The second harmonic of this tone was found at double the tone frequency, 13370 Hz, at the lower amplitude of 0.82 kPa. With an auxiliary jet velocity of 40 m/s, Figure 4.7(B), the multi-slot jet produced two tones of roughly equivalent amplitude; 1.989 kPa at 3342 Hz and 1.787 kPa at 6859 Hz.

The frequencies of the tones indicated that one is not a harmonic or subharmonic of the other and instead the jet is switching between two jet stages. As the lower frequency tone in this spectrum had the larger amplitude it was considered the dominant acoustic tone of the jet. Comparing the frequency of this tone (Figure 4.7(B)) to the dominant tone in Figure 4.7(A), the auxiliary jet velocity caused the stage of the jet to change.

At an auxiliary jet velocity of 60 m/s, Figure 4.7(C), the dominant tone, with an amplitude of 1.97 kPa and frequency of 6568 Hz, had switched back to the same stage of the multi-slot jet as the tone in Figure 4.7(A) – i.e. with the main jet alone. At this auxiliary jet velocity, two other tones were present, the second harmonic of the dominant tone at 13136 Hz and 0.71 kPa and a second unrelated tone of 1.20 kPa at 6336 Hz. With auxiliary jet velocities of 80 m/s and 100 m/s, the tones seen at lower velocities were eliminated with no remnants discernable in the acoustic spectra, although, as can be seen from Figure 4.6, this is not true for all impingement ratios for these jet parameters.

Extracting only the amplitude of the dominant acoustic tones from Figure 4.5 and Figure 4.6, the data can be plotted in a simpler fashion. These data are plotted in Figure 4.8 alongside two additional sets of experiments on the effect of auxiliary jet velocity as a function of the velocity ratio between the main and auxiliary jets (V_A/V_M).

In Figure 4.8, if a tone was not produced at an impingement ratio the maximum amplitude of the broadband noise taken from the spectrum was plotted at that impingement ratio. Figure 4.8(A) shows that the amplitude of the tones produced by the main jet alone at 200 m/s were not as significant when compared to those tones already presented in

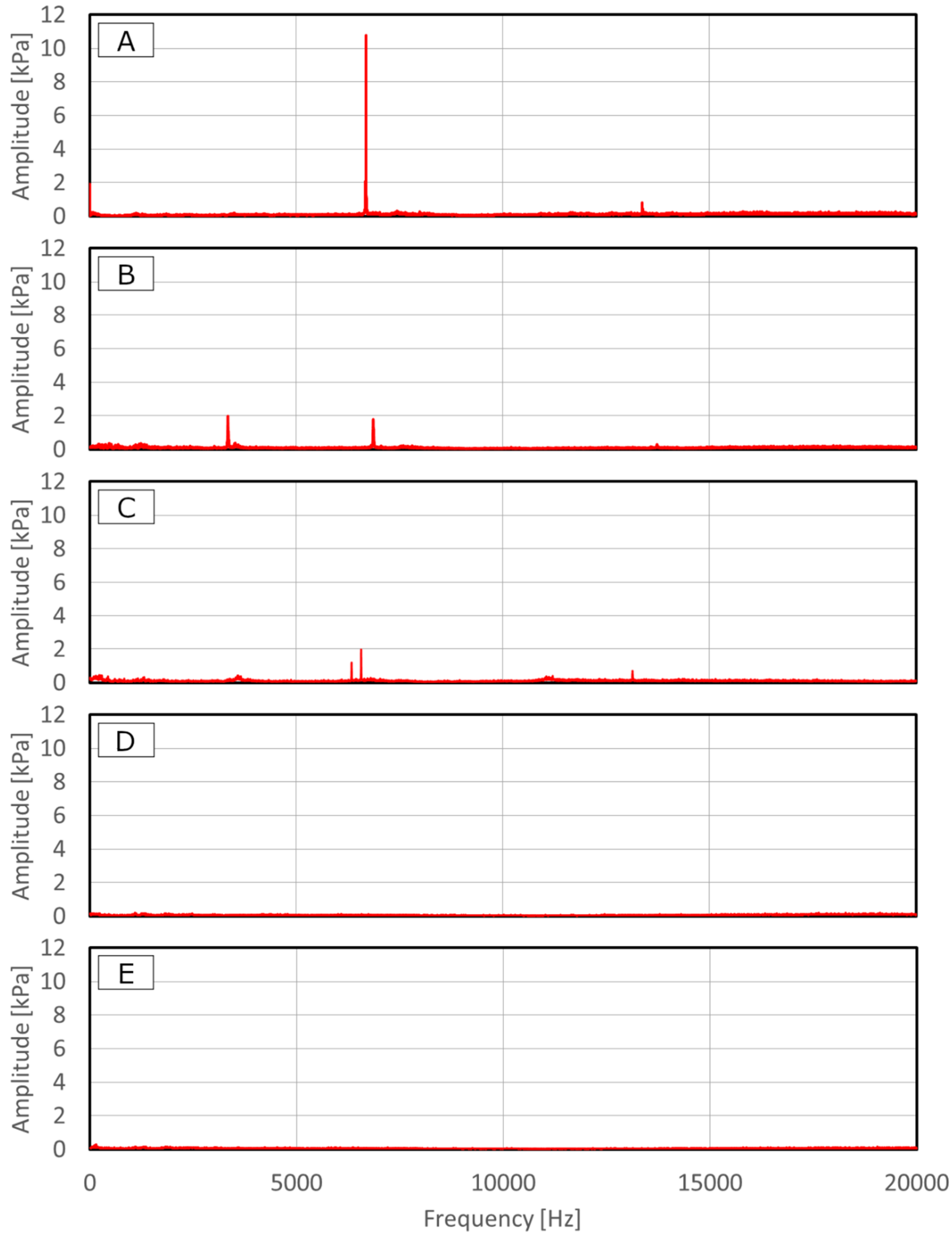

Figure 4.7 Acoustic spectra of the impinging multi-slot planar jet for varying auxiliary jet velocities. The main jet had a 2 mm nozzle width (d = 2 mm) and was maintained an impingement ratio h/d = 12 and a velocity of 250 m/s while the auxiliary jets, with fixed nozzle width (a=1 mm) and setback distance (s=5 mm), were varied between velocities of A: 0 m/s, B: 40 m/s, C: 60 m/s, D: 80 m/s and E: 100 m/s.

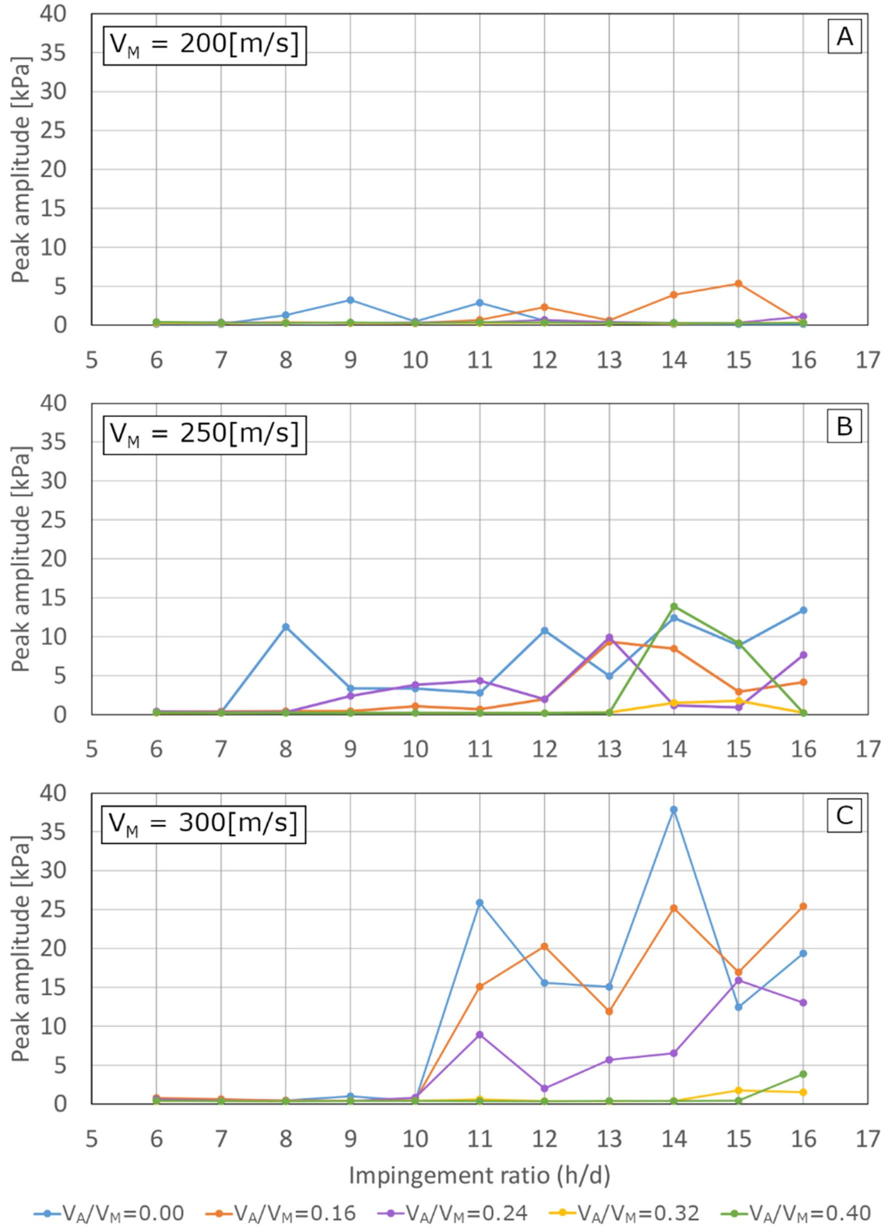

Figure 4.8 Effect of the velocity ratio, V_A/V_M, on the amplitude of the dominant acoustic tone for the multi-slot jet at main jet velocities of 200 m/s, 250 m/s and 300 m/s. d = 2 mm, a = 1 mm, s = 5 mm.

Figure 4.4-4.7 for the main jet velocity of 250 m/s. The maximum tone amplitude produced at 200 m/s for the main jet alone was 3.24 kPa. These tones were found to be suppressed at an auxiliary jet velocity ratio of 0.16 but new tones were produced at higher impingement ratios, some with amplitudes larger than those of the main jet alone base case; i.e. one tone reached 5.34 kPa. At jet velocity ratios larger than 0.16 no significant tones were present.

Figure 4.8(B) shows the dominant tones from Figure 4.5 and Figure 4.6 for the main jet velocity of 250 m/s. In this Figure, it is clearly seen that, in general, the auxiliary jets decreased the amplitude of the tones produced by the main jet. This is a general trend and not applicable at every instance, as can be seen for the impingement ratios of 14 and 15 (Figure 4.8(B)). At these impingement ratios the auxiliary jets successfully reduced the amplitude of the tones at the velocity ratios of 0.16, 0.24 and 0.32, but at the velocity ratio of 0.4 tones were produced by the multi-slot jet with amplitudes similar to those produced by the main jet alone.

Figure 4.8(C) shows the effect of auxiliary jets on the main jet tones with a velocity of 300 m/s. In this panel, the general trend of the amplitude of the main jet's tones decreasing with increasing auxiliary jet velocity is more obvious than in the other two panels.

The data in all panels of Figure 4.8 shows that, while the general trend of increasing the auxiliary jet velocity is a reduction in tone amplitude, increasing auxiliary jet velocities can amplify tones or generate tones that were not present at lower auxiliary jet velocities. Jet shear layers are defined by the jet flow and the flow conditions at the jet nozzle exit. For the multi-slot jet, the nozzle exit flow conditions are determined by the setback distance, auxiliary jet width and auxiliary jet velocity. The setback distance and auxiliary jet width affect the entrainment of the quiescent flow and the merging of the main and

Table 4.1 Percentage change of the amplitude of the dominant tones averaged over the impingement ratios of 6-16 for different main jet velocities with auxiliary jet velocity ratios. d = 2 mm, a = 1 mm, s = 5 mm.

	V_M		
V_A/V_M	**200**	**250**	**300**
0	100%	100%	100%
0.16	155%	42%	91%
0.24	50%	46%	42%
0.32	34%	7%	5%
0.40	37%	35%	6%

auxiliary jets. This amplification of existing, or generation of new, tones was due to the change in jet exit flow conditions which caused the main jet shear layer to become more unstable and amplifying the aeroacoustic feedback mechanism. This thesis attempts to use the auxiliary jets to manipulate this surrounding flow such that the tones are suppressed. However, the influence of the auxiliary jets and the interaction of the auxiliary and main jets seems to, for certain conditions, result in flow conditions that result in a more unstable jet shear layer causing acoustic tones to be amplified or generated.

To better identify the general trend of the reduction in dominant acoustic tone amplitude with increasing auxiliary jet velocity, table 4.1 shows the percentage change in the average amplitude of the dominant tones presented in Figure 4.8. The table shows the general trend of the decrease with auxiliary jet velocity. The sudden percentage increase at the velocity ratio of 0.16 for the 200 m/s main jet velocity is a small amplitude increase but a significant percentage increase. The increase at the auxiliary jet ratio at 0.40 for the 250 m/s is due to the large amplitude tones produced at the impingement ratios of 14 and 15.

Varying the setback distance of the auxiliary jets changed two aspects of the multi-slot jet geometry. The smaller the setback distance, the closer the auxiliary jet plates were to the impingement plate (Figure 3.2), which resulted in a more confined space between the jet and the plate. The confinement of the jet could affect the flow of the quiescent air close to the jet nozzle exit with the larger setback distances allowing for a larger area for circulation of the flow due to the entrainment of the quiescent air. The change in the proximity of the auxiliary jet plates to the area immediately surrounding the main jet nozzle changed the geometry in the vicinity of the main jet nozzle exit. This change in geometry affected how the main jet entrained the quiescent flow to generate the main jet shear layer. These changes in the geometry, and thus changes in the flow conditions at the jet exit, alter the main jet shear layer and result in a more unstable jet shear layer that generated and amplified acoustic tones where previously there were none. The larger the setback distance "s" also provided for a longer distance over which the auxiliary jets developed as wall jets before interacting with the main jet.

Figure 4.9 summarises the effect of the auxiliary jet setback distance on the dominant tones generated by the multi-slot jet. The curves of the peak amplitude at an auxiliary jet velocity of 0 m/s (Figure 4.9(A-D)) shows the effect of the setback distance on the tones produced by the main jet alone for V_M = 250 m/s. These curves show that the larger the setback distance, the fewer tones that were produced by the multi-slot jet and the smaller the amplitude of the tones produced. This could imply that the larger circulation zones allowed by the larger setback distances had a stabilising effect on the flow at the jet exit.

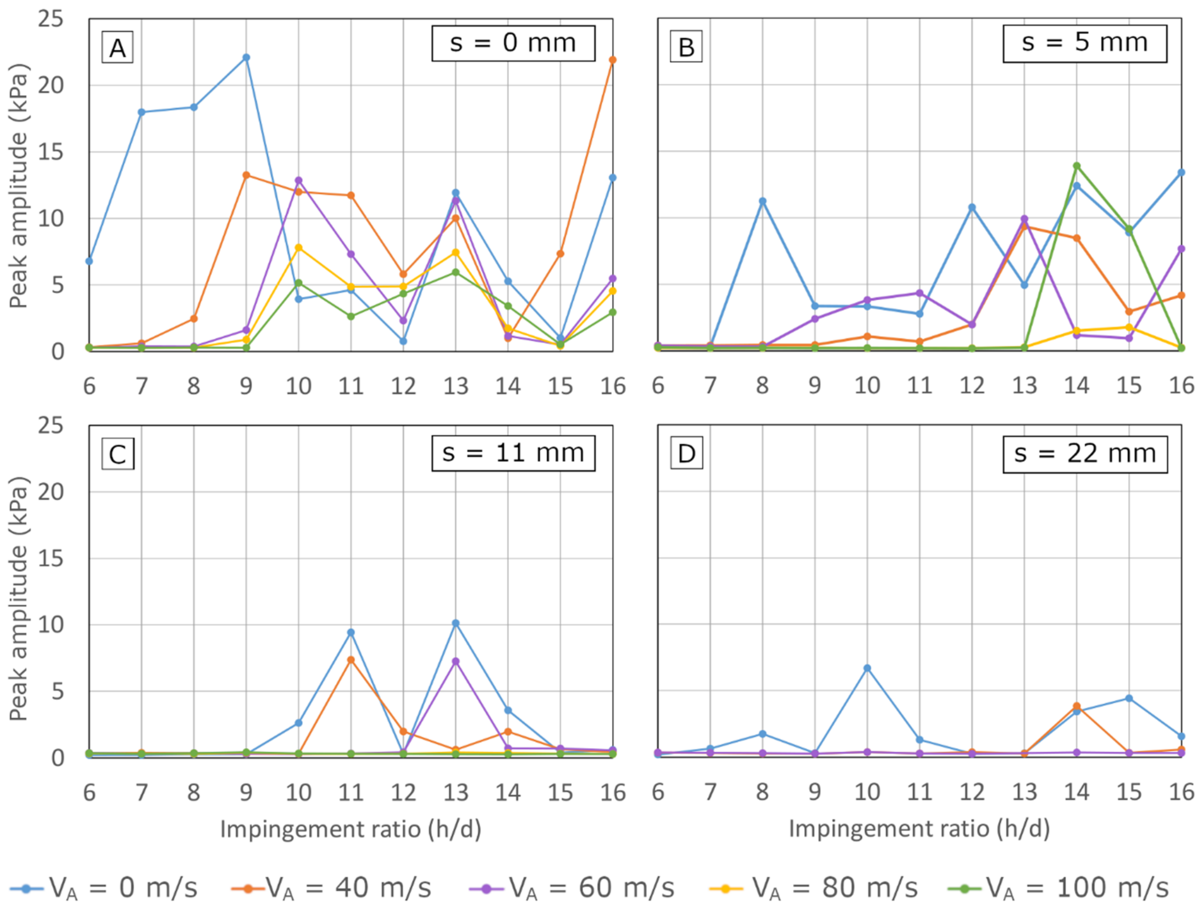

Figure 4.9 Effect of the setback distance, "s", on the amplitude of the dominant acoustic tones produced by the multi-slot jet over a range of auxiliary jet velocities. V_M = 250, d = 2 mm, a = 1 mm.

The effect of the auxiliary jet velocity at all different setback distances confirms what has been seen in the previous data: auxiliary jets have the ability to reduce the amplitude of dominant acoustic tones generated by the impingement of the main jet and, in general, the faster the auxiliary jets the larger that reduction. It is also clear from Figure 4.9 that the auxiliary jets can also amplify tones that were present at or generate tones that were not found at lower auxiliary jet velocities which, as noted earlier, is due to the auxiliary jets creating flow conditions immediately at the nozzle of the jet that resulted in more unstable jet shear layers.

The data in Figure 4.9 would seem to indicate that at larger setback distances, and thus longer developing lengths of the auxiliary jets, the more effective the auxiliary jets are at suppressing the acoustic tones at lower auxiliary jet velocities. Unfortunately, the design of the multi-slot jet does not allow for the two parameters, longer development length and increased confinement, to be separated and as such, it is not possible to confirm the influence of the development length of the auxiliary jets.

The effect of the auxiliary jet nozzle width on the tones produced by the impinging multi-slot jet was investigated for a main jet nozzle width of 3 mm. The results of those experiments are summarised in Figure 4.10 with auxiliary jet nozzle widths of a = 1 mm, 1.5 mm and 3 mm, a ratio of jet nozzle widths of $^1/_3$, $^1/_2$ and 1 respectively with auxiliary jet velocities ranging between 0-100 m/s maintaining a constant main jet velocity at V_M = 250 m/s.

The results in Figure 4.10 show that, for the same auxiliary jet velocity ratio, the larger auxiliary jet nozzle widths result in a larger reduction of the tones produced by the main jet alone. This trend would indicate that the larger auxiliary jet thickness results in a thicker shear layer and reduction in the velocity gradient that is a fundamental component of the aeroacoustic feedback mechanism.

In their investigation of a planar impinging jet, Arthurs and Ziada [31] suggested an effective Strouhal number for the tones generated through the aeroacoustic phenomena of near-sonic impinging jets. The effective Strouhal number, St_{eff}, (equation 4.1) contained a modified, or effective velocity, V_{eff}, (equation 4.2), as the velocity scale for the complete

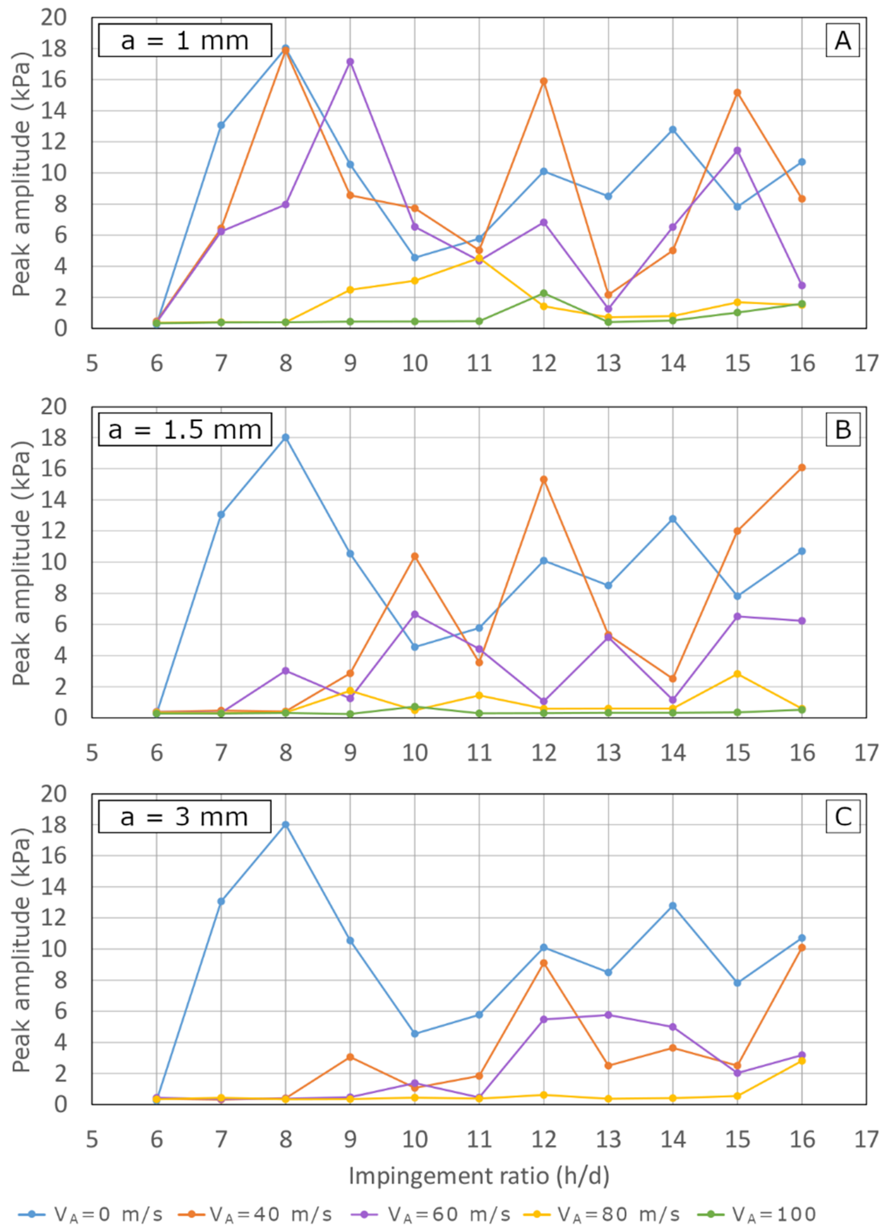

Figure 4.10 Effect of the auxiliary jet nozzle widths and velocity on the amplitude of the dominant acoustic tones produced by the multi-slot jet. V_M = 250 m/s, d =3 mm, s = 5 mm.

feedback process. The effective velocity was modified to account for the comparable speeds of the acoustic disturbances and coherent structures involved in the aeroacoustic feedback mechanism:

$$St_{eff} = \frac{f \cdot h}{V_{eff}} \tag{4.1}$$

$$V_{eff} = \frac{2 \cdot V_C \cdot c}{V_C + c} \tag{4.2}$$

where "f" is the tone frequency, "h", the impingement distance, "V_C", the convection velocity of the coherent structures and, "c", the speed of sound in air. The convection velocity of the coherent structures was measured in their study using PIV imaging and from that, the authors derived two equations for the convection velocity depending on the impingement ratio:

$$V_C = \kappa \cdot V_M \qquad {}^{h}/_{d} \leq 9.4 \tag{4.3}$$

$$V_C = 2.1 \cdot \kappa \cdot V_M \cdot \left({}^{h}/_{d}\right)^{1/3} \qquad {}^{h}/_{d} > 9.4 \tag{4.4}$$

where "V_M" is the main jet velocity and "h" is the impingement distance. "κ" is the convection coefficient, which is generally experimentally fitted to the data. In Ziada and Arthur's model, the convection coefficient was 0.58 [32].

Figure 4.11 shows the effective Strouhal numbers for all the significant acoustic tones found in the course of this investigation. Peaks were considered significant if they were 10 times the amplitude, i.e. 20 dB greater, than the average amplitude of the signal. The data clearly shows that the multi-slot jet exhibited the jet-staging phenomena seen in previous studies of impinging jets [24]. The effective Strouhal numbers predicted by the Arthurs and Ziada modified Rossiter model [31], [32] have been plotted alongside the data from the present study and it can be seen that they are of a similar magnitude. The discrepancy

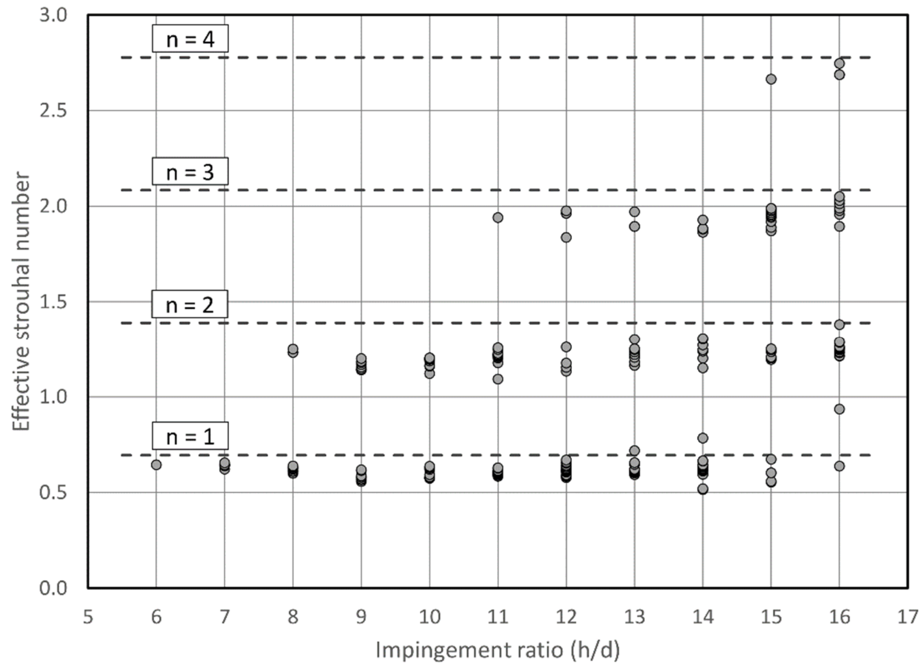

Figure 4.11 Effective Strouhal number for all dominant peaks found in the course of the investigation (circles) compared to the modified Rossiter model of Arthurs and Ziada [31], [32] for different jet stages: n=1,2,3,4 (dashed lines).

between the current study's data and the model was most likely due to the differences in the convection velocity of the coherent structures. Arthurs and Ziada empirically obtained the convection velocity and those values were used to calculate the effective Strouhal numbers in Figure 4.11. As the Strouhal numbers of the multi-slot jet are consistently below the lines of the Rossiter model it indicates that the convection velocity of the multi-slot jet was faster than the planar jet used in the study by Arthurs and Ziada.

4.2 Static and fluctuating pressures at the impingement plate

In the continuous galvanizing gas jet wiping process, the predictive models for the coating weight use the pressure gradient at the substrate as one of the significant input process variables [3], [45]. To investigate the effect of the auxiliary jets on the pressure profile at the impingement plate, a static and a dynamic pressure sensor were mounted on the impingement plate. The plate was then traversed across the jet flow to obtain static and fluctuating pressure profiles at the plate.

The pressure profiles were measured for the main jet width of 2 mm at 250 m/s with an impingement ratio of 12. The auxiliary jets had 1 mm nozzles and the auxiliary jet velocities were set at 0 m/s, 60 m/s and 100 m/s (velocity ratios, V_A/V_M, of 0.00, 0.24 and 0.32 respectively). The tonal noise produced by these jet conditions can be found in panels (A), (C) and (E) of Figure 4.7. These jet parameters were chosen to measure the pressure profiles for a jet generating a large-amplitude acoustic tone due to the aeroacoustic feedback mechanism, a reduced amplitude acoustic tone and no tone.

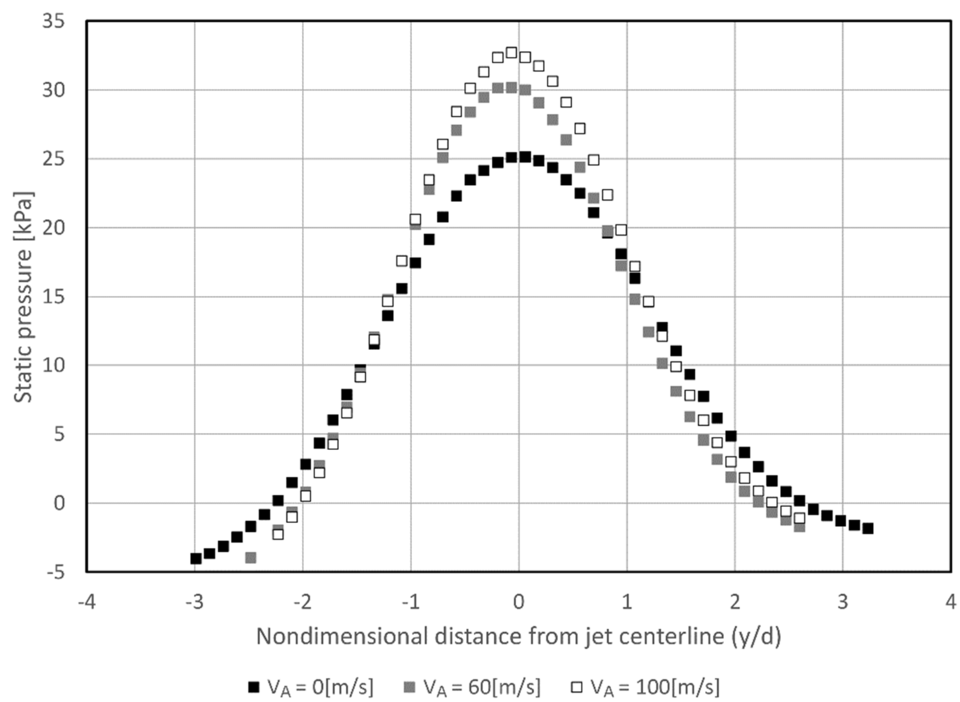

Figure 4.12 Static pressure at the plate as a result of the multi-slot jet for different auxiliary jet velocities. (V_M = 250 m/s, d = 2 mm, a = 1 mm, s = 5 mm, h/d = 12)

Figure 4.12 shows the effect of the auxiliary jets on the static pressure. The maximum static pressure at the plate increased by 20% (30.2 kPa) with an auxiliary jet velocity of 60 m/s and by 30% (32.7 kPa) with an auxiliary jet velocity of 100 m/s. The width of the pressure profile was also seen to be somewhat narrower with the auxiliary jets. These changes in the static pressure profile at the plate coincide with the reduction of the high amplitude acoustic tones produced by the jet. The tones produced by the aeroacoustic feedback mechanism are associated with oscillations of the jet column. A reduction of the amplitude of these would result in the jet impinging the plate over a smaller area, resulting in the narrower profile at the higher auxiliary jet velocities. The reduced amplitude of the jet oscillations would result in the jet entraining less quiescent air and thus maintaining the

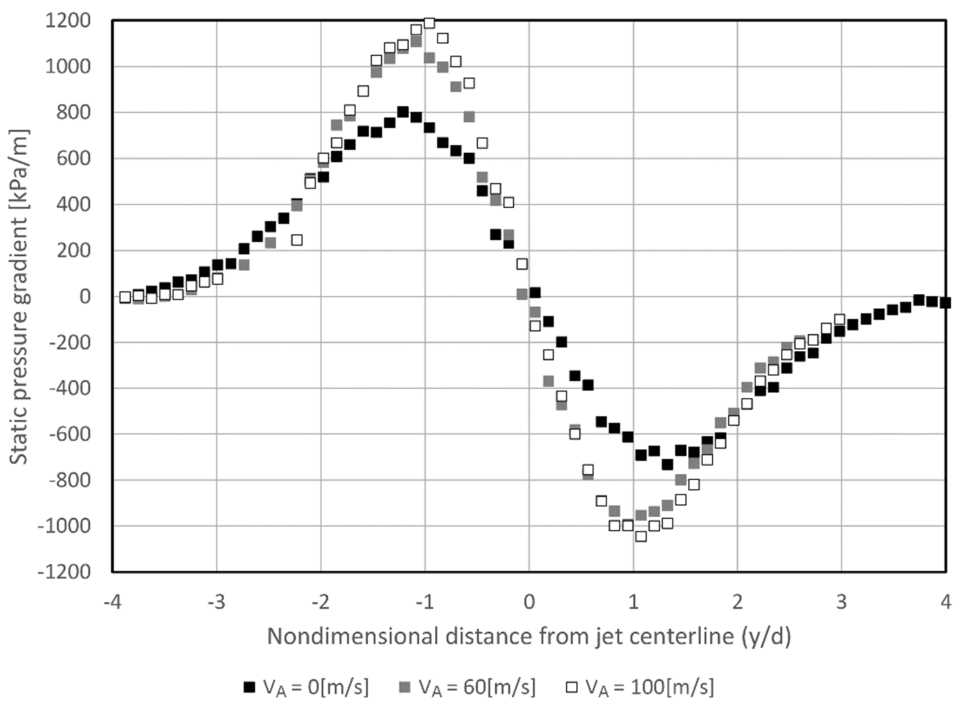

Figure 4.13 Static pressure gradient at the plate as a result of the multi-slot jet for different auxiliary jet velocities. (V_M = 250 m/s, d = 2 mm, a = 1 mm, s = 5 mm, h/d = 12)

momentum of the main jet over a longer distance from the jet exit. The higher momentum of the jet column would result in the higher static pressures at the plate.

The increase in the maximum static pressure and the narrowing of the static pressure profile both contribute to an increase in the static pressure gradient at the plate which is plotted in Figure 4.13. The narrowing of the static pressure profiles is clearer in Figure 4.13 with the maximum and minimum gradients closer to the jet centerline with increasing auxiliary jet velocity. For the auxiliary jets of 60 m/s and 100 m/s the maximum static pressure gradient increased from 801.5 kPa/m for the main jet alone to 1108 kPa/m and 1188 kPa/m respectively. This increase in the maximum static pressure gradient of 37% and 46% indicates an increase in the wiping power of the multi-slot jet over conventional planar jets.

A frequency spectrum of the fluctuating pressure at the impingement plate for the multi-slot jet operating at V_M = 250 m/s, V_A = 0 m/s and d = 2 mm for h/d = 12 is presented in Figure 4.14. This frequency spectrum of the fluctuating pressure was taken one main jet width from the jet centerline, i.e. at y/d = -1. The spectrum shows that the fluctuating pressure at the plate exhibited large amplitude oscillations at 6885 Hz, the same frequency of the acoustic tone produced for these jet operating conditions, as seen in Figure 4.7(A). As the frequency of the acoustic tone is the same as the frequency of the pressure fluctuations at the plate, it is clear that these fluctuating pressures and the tonal noise produced by the jet impingement are due to the same phenomenon. As was seen in Figure 4.7(C), there were two tones of roughly equivalent amplitude produced by the jet at an auxiliary jet velocity of V_A = 60 m/s. To compare the amplitude of the fluctuations of a

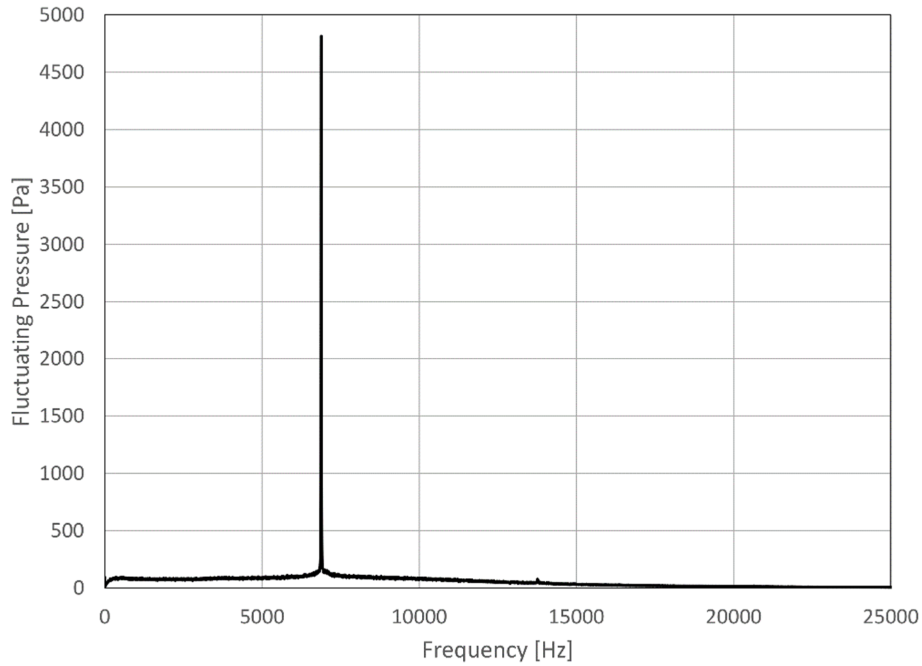

Figure 4.14 The frequency spectrum of the fluctuating pressure of the multi-slot jet measured at the impingement plate. V_M = 250 m/s, d = 2 mm, V_A = 0 m/s, a = 1 mm, s = 5 mm, h/d = 12, y/d = -1.

spectrum with two tones to the fluctuations of a single tone, the RMS of a range of frequencies large enough to capture both tones were calculated for every spectrum. This frequency band was 400 Hz wide to ensure that the amplitude of both peaks at 60 m/s was captured in the RMS value. For spectra with a single tone, the 400 Hz band was centred on the frequency of the dominant fluctuating peak. These RMS of the fluctuating peaks are plotted in Figure 4.15.

The fluctuating pressure profile of the multi-slot jet with an auxiliary jet velocity of 0 m/s showed two areas of large amplitude fluctuations near the jet centerline and two outer lobes of fluctuating pressure located further from the jet centerline (y/d ≈ 7.5). At the auxiliary jet velocities of V_A = 60 m/s and 100 m/s, the profiles of the fluctuating pressure

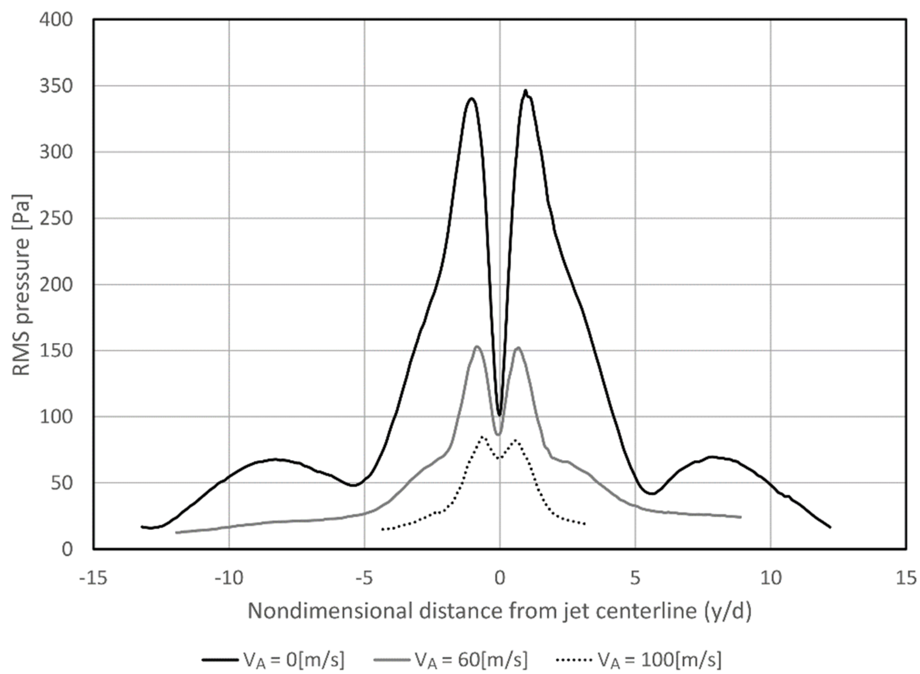

Figure 4.15 Profiles of the fluctuating pressure of the multi-slot jet for different auxiliary jet velocities. The RMS presented was calculated over a 400 Hz bandwidth around the dominant peak. (V_M = 250 m/s, d = 2 mm, a = 1 mm, s = 5 mm, h/d = 12)

also had areas of relatively large fluctuating pressure near the jet centerline but did not exhibit the outer lobes seen for V_A = 0 m/s. The frequencies of the pressure fluctuations at 0 m/s and 60 m/s were the same as the acoustic tones produced by the jet; ≈ 6600 Hz (Figure 4.7(A), (C)). The frequency of the fluctuations at 100 m/s was 7260 Hz; however, no significant acoustic tones were produced by the multi-slot jet at this auxiliary jet velocity for these jet parameters (Figure 4.7(E)). The two areas of large amplitude fluctuations near the jet centerline were most likely caused by a combination of the oscillation of the jet column and the impingement of the coherent structures. As the outer lobes in the fluctuating pressure profiles of the 0 m/s auxiliary jet velocity were the same frequency as the larger amplitude fluctuations closer to the jet centerline, these lobes were most likely caused by the coherent vortices as they were convected along the plate. The auxiliary jets reduced the maximum amplitude of the fluctuating pressure from 346.6 kPa, for the main jet alone, to 152.4 kPa for a velocity of 60 m/s and 84.7 kPa for a velocity of 100 m/s, a reduction of 56% and 75% respectively. From Figure 4.15, it can be seen that the position of the maximum fluctuating pressure on the plate was closer to the centerline of the jet for higher auxiliary jet velocities. For the main jet alone, the fluctuating pressure maximums were located at approximately $y/d = \pm 1$, while at the higher jet velocities of 60 m/s and 100 m/s the maximums were located at approximately $y/d = \pm 0.75$ and ± 0.6 respectively.

The decreasing distance of the maximum fluctuating pressure from the jet centerline with increasing auxiliary jet velocity indicates a similar decrease in the amplitude of the oscillations of the jet column, consistent with the narrowing of the static pressure profiles. The lack of outer lobes in the fluctuating pressure profiles at 60 m/s and 100 m/s indicates a significant reduction in the strength or size of the coherent structures due to the auxiliary jets.

The reduction of the fluctuating pressure at the plate indicates that the auxiliary jets, in reducing the amplitude of the acoustic tones, also reduced the oscillation of the jet associated with those tones. With decreased oscillations of the jet column, the momentum of the jet was not lost due to entrainment of the surrounding air and, as such, the static pressure at the plate increased.

4.3 Particle Image Velocimetry

Particle image velocimetry was employed to observe the flow field of the multi-slot jet generating acoustic tones due to the aeroacoustic feedback mechanism versus the flow field

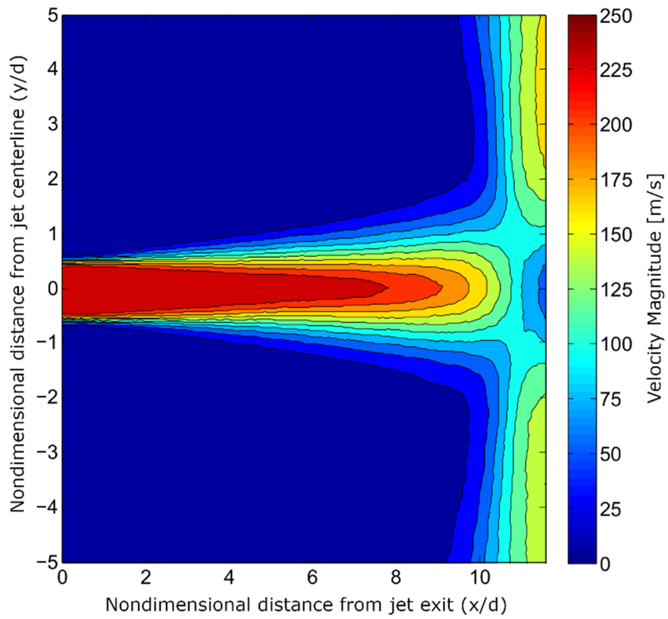

Figure 4.16 Time-averaged flow-field of an acoustic tone producing flow of the multi-slot jet impinging on a rigid plate. V_M = 250 m/s, V_A = 0 m/s, d = 2 mm, s = 5 mm, h/d = 12.

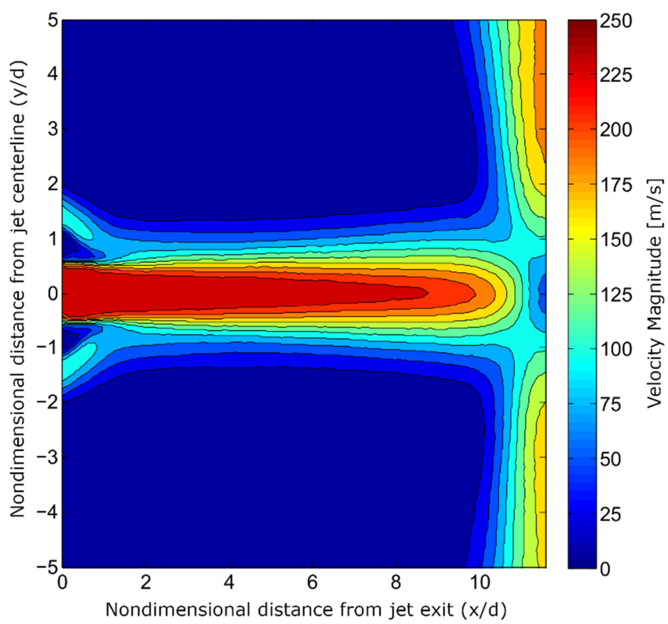

Figure 4.17 Time-averaged flow-field of a tone suppressed flow of the multi-slot jet impinging on a rigid plate. V_M = 250 m/s, d = 2 mm, V_A = 100 m/s, a = 1 mm, s = 5 mm, h/d = 12.

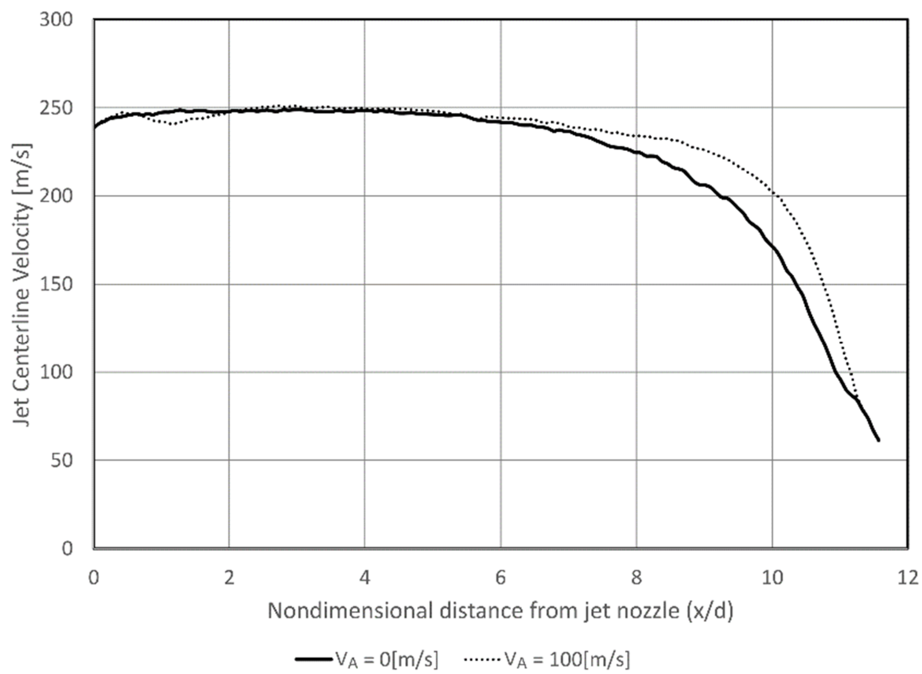

Figure 4.18 Centerline velocity of the impinging multi-slot jet with auxiliary jets velocities of V_A = 0 m/s and 100 m/s V_M = 250 m/s, d = 2 mm, a = 1 mm, s = 5 mm, h/d = 12.

with those tones suppressed by the auxiliary jets. The multi-slot jet parameters of Figure 4.7(A) and Figure 4.7(E) were used in the PIV experiments as the main jet generated a strong acoustic tone in the former and the dominant tone was suppressed by the auxiliary jets in the latter. The jet parameters in Figure 4.7(A) were: the main jet velocity was V_M = 250 m/s with a nozzle width of d = 2 mm at an impingement ratio of h/d = 12. At these jet parameters, the multi-slot jet produced a 10.8 kPa at 6685 Hz. In Figure 4.7(E) the tone was suppressed with auxiliary jets setback at 5 mm at an auxiliary jet velocity of V_A = 100 m/s with an auxiliary nozzle width of a = 1 mm.

The flow fields of the multi-slot jet generating and not generating an acoustic tone are presented as contour plots in Figure 4.16 and Figure 4.17, respectively. The contour plots show that the potential core of the main jet was slightly longer for the case with auxiliary jets. Centerline velocities of the main jets taken from the PIV data are presented in Figure 4.18 for both cases. It confirms that the potential core for an impinging jet with the auxiliary jets operating at V_A = 100 m/s was preserved longer than the case of the main jet alone. Using the data of Figure 4.18, if we define the length of the potential core as the distance the jet travels before the centerline velocity drops to 95% of the initial region, then the potential core for the main jet alone was 7.1 nozzle widths with the auxiliary jets extending that potential core to 8.1 nozzle widths. This increased length of the potential core is consistent with the observed increase in the static pressure at the plate (Figure 4.12).

Velocity profiles of the jet, extracted from the PIV data, were plotted to allow a more detailed examination of the interactions and development of the jet flows. Unavoidable laser reflections from the solid edges of the jet nozzle resulted in some erroneous vectors in the PIV analysis that can be seen in the velocity profiles immediately at the jet exit (x/d = 0).

Velocity profiles extracted from both tone producing and tone suppressed flow fields close to the jet exit, x/d ≤ 2, are presented in Figure 4.19 and Figure 4.20. The profiles of the tone producing flow field, Figure 4.19, show very little change of the jet velocity profiles in this initial region of the jet. There is a slight widening of the profile as the jet entrained the surrounding quiescent flow which can be seen in comparing the profile at x/d = 0.5 and 2.0. The transition between the quiescent flow and the jet column for the x/d = 0.5 profile is much sharper than the transition at x/d = 2.

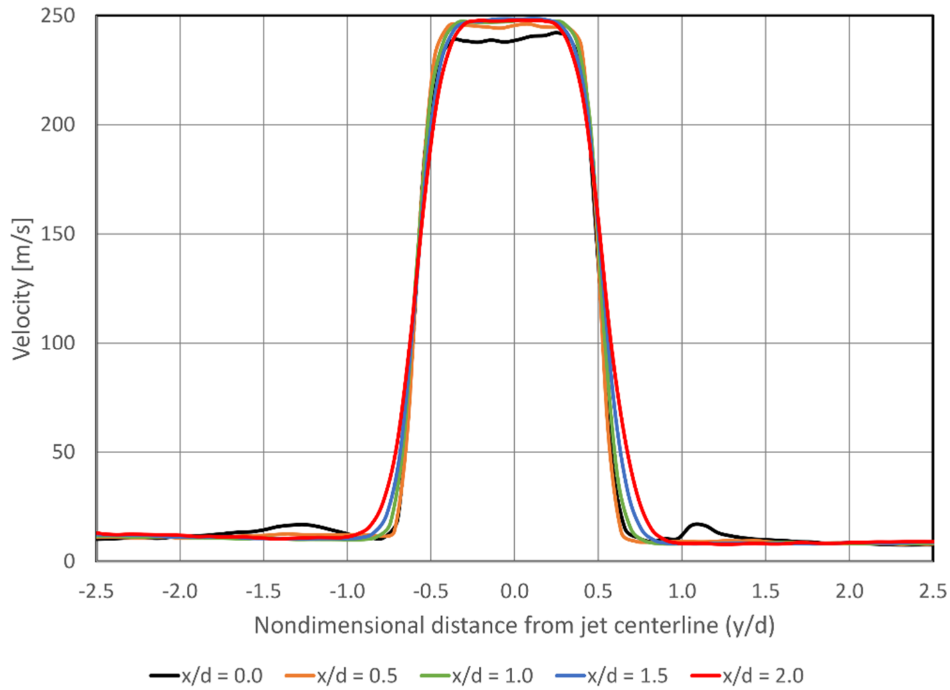

Figure 4.19 Velocity profiles of the impinging multi-slot jet close to the jet nozzle. V_M = 250 m/s, d = 2 mm, V_A = 0 m/s, a = 1 mm, s = 5 mm, h/d = 12.

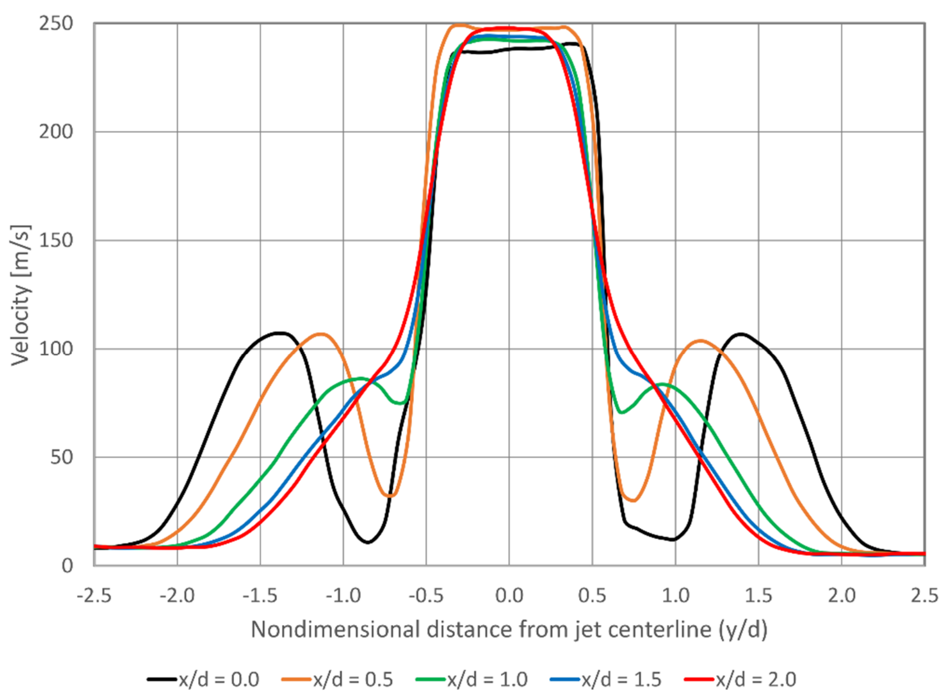

Figure 4.20 Velocity profiles of the impinging multi-slot jet close to the jet nozzle. V_M = 250 m/s, d = 2 mm, V_A = 100 m/s, a = 1 mm, s = 5 mm, h/d = 12.

Velocity profiles extracted from the flow field where the acoustic tone is suppressed, Figure 4.20, show that at the jet nozzle exit (x/d = 0), the three jets are distinct. However, due to the relatively sharp angle between the main and auxiliary jets, within one and a half nozzle widths (x/d = 1.5) the main and auxiliary jets had merged into a single, if slightly distorted, velocity profile.

The vorticity profiles corresponding to the velocity profiles shown in Figure 4.19 and Figure 4.20 are presented in Figure 4.21 and Figure 4.22, respectively, though the profiles immediately at the jet exit, x/d = 0, have been removed as the reflection errors mentioned above resulted in significantly distorted profiles. The profiles from the tone producing flow field, Figure 4.21, show the magnitude of the vorticity in both shear layers decreased as the jet progressed downstream from the nozzle. This was the expected behaviour of the jet shear layers as the jet entrained the quiescent air, as seen in the velocity profiles presented in Figure 4.19.

The vorticity profiles closest to the jet exit of the tone suppressed flow field, x/d = 0.5 in Figure 4.22, contained three distinct sets of shear layers for the three jets – i.e. main jet and two auxiliary jets. For the main jet shear layer, the peaks at y/d = ±0.6, were of a similar magnitude and shape to that in the tone producing case (Figure 4.21). The shear layers of the auxiliary jets were located at y/d = ±0.85 and at y/d = ±1.5. The shape of the auxiliary jet shear layer further from the jet centerline was due to the setback distance of 5 mm, which resulted in the auxiliary jets developing as wall jets over that distance. As is the case with a wall jet, the outer shear layer degraded as the auxiliary jet spread, while the inner shear layer was maintained by the proximity to the wall.

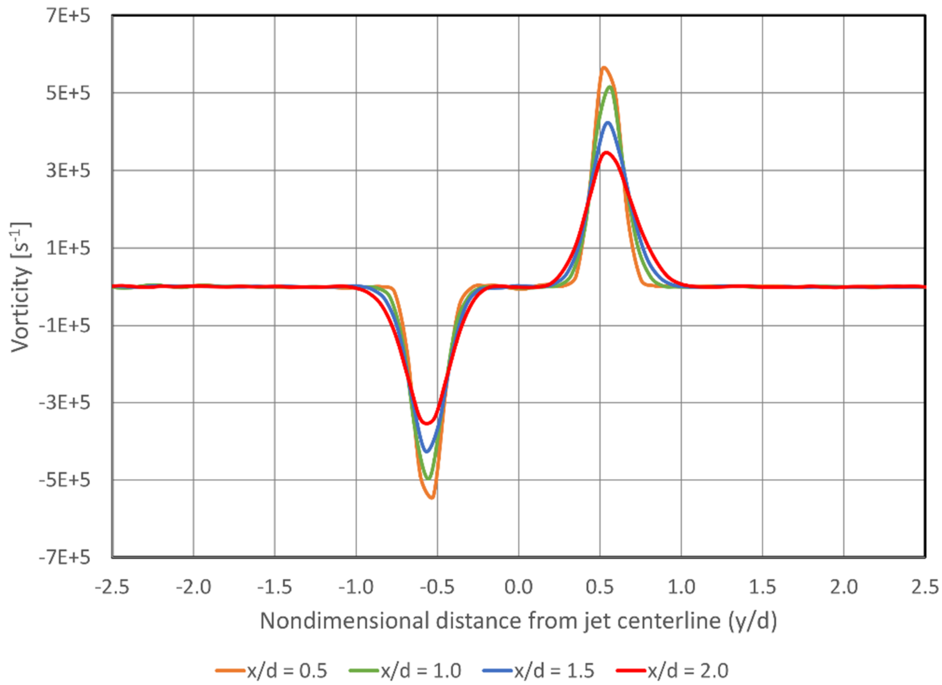

Figure 4.21 Vorticity profiles of the impinging multi-slot jet close to the jet nozzle. V_M = 250 m/s, V_A = 0 m/s, d = 2 mm, h/d = 12.

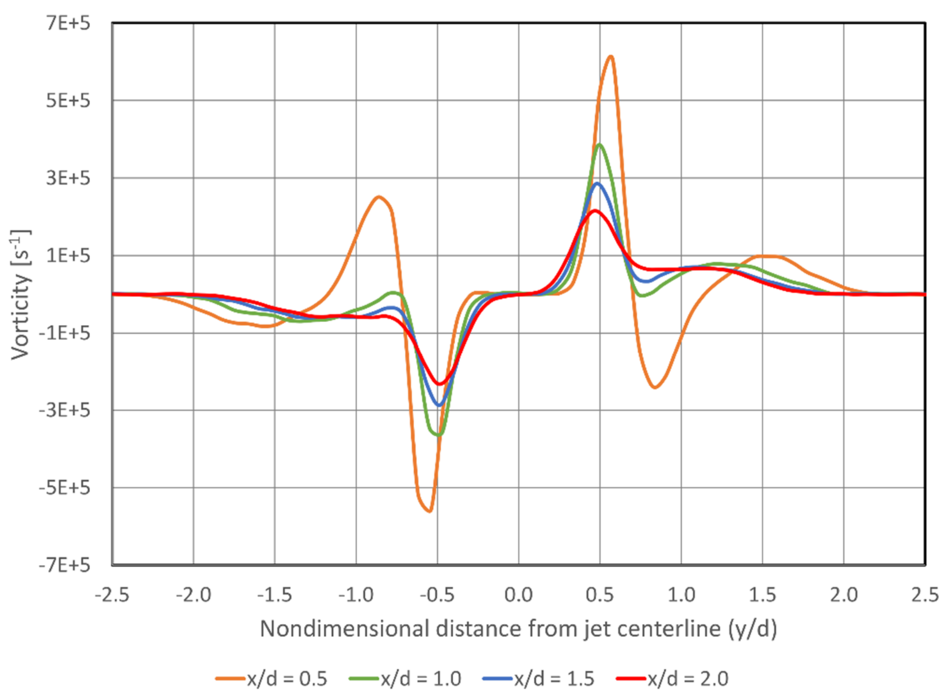

Figure 4.22 Vorticity profiles of the impinging multi-slot jet close to the jet nozzle. V_M = 250 m/s, d = 2 mm, V_A = 100 m/s, a = 1 mm, s = 5 mm, h/d = 12.

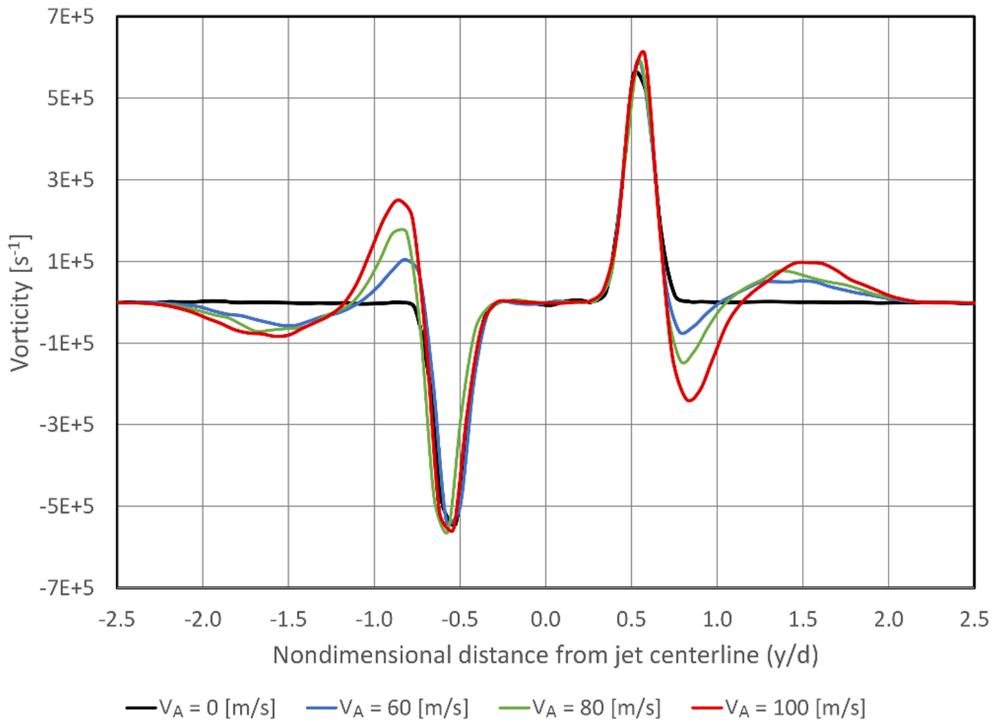

Figure 4.23 Vorticity profiles of the impinging multi-slot jet at x/d = 0.5 for different auxiliary jet velocities. V_M = 250 m/s, d = 2 mm, a = 1 mm, s = 5 mm, h/d = 12.

Similar to the vorticity profiles presented in Figure 4.21, the maximum vorticity of the main jet shear layer in Figure 4.22 decreased as the jet progressed further downstream. This trend in decreasing vorticity magnitude with increasing downstream distance was also true for the inner shear layers of the auxiliary jets. The outer auxiliary jet shear layers did not change significantly in amplitude with downstream distance but changed slightly in shape.

Comparison of the vorticity profiles for different auxiliary jet velocities close to the jet, i.e. at x/d=0.5, are presented in Figure 4.23. As was expected, the magnitude of the inner shear layer for the auxiliary jets was found to be proportional to the velocity of the auxiliary jets.

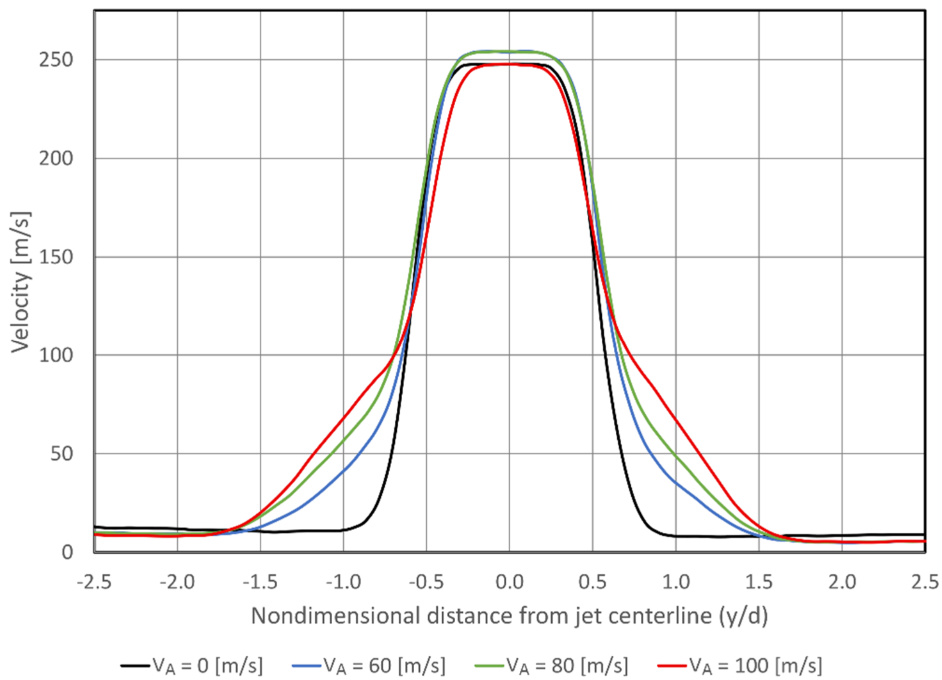

Figure 4.24 Velocity profiles of the impinging multi-slot jet at x/d = 2 for different auxiliary jet velocities. V_M = 250 m/s, d = 2 mm, a = 1 mm, s = 5 mm, h/d = 12.

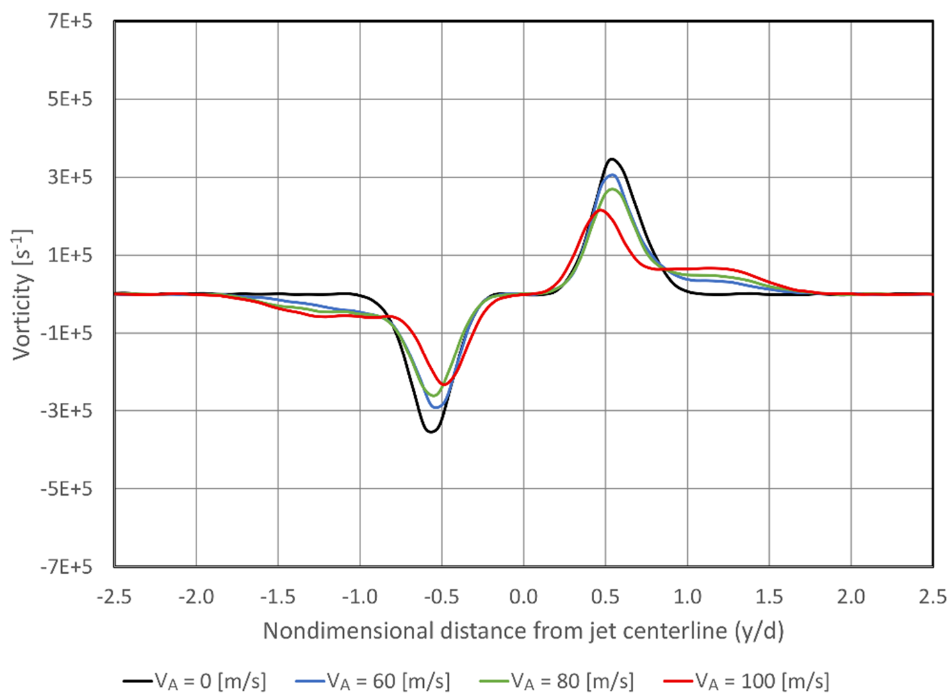

Figure 4.25 Profiles of vorticity of the impinging multi-slot jet at x/d = 2 for different auxiliary jet velocities. V_M = 250 m/s, d = 2 mm, a = 1 mm, s = 5 mm, h/d = 12.

A comparison of the velocity and vorticity profiles of the multi-slot jet for different auxiliary jet velocities after the three jets have merged, two nozzle widths downstream of the nozzle exit (x/d = 2), are presented in Figure 4.24 and Figure 4.25. These profiles show the effect of the merging of the jets on the main jet shear layer for the different auxiliary jet velocities. While the velocity profiles in Figure 4.24 are distorted, it is clear that the auxiliary jets have merged with the main jet at this impingement distance to form a single jet at all tested auxiliary jet velocities.

The vorticity profiles in Figure 4.25 show the vorticity of the shear layers after the jets have completely merged. The shear layers of the merged jets have a magnitude proportional to the combined magnitudes of the shear layers of the main and auxiliary jets prior to their merging. As the vorticity of the auxiliary jet shear layers is proportional to the auxiliary jet velocities, the higher auxiliary jet velocities result in a lower amplitude merged jet shear layer. This is clearly shown by the vorticity profiles in Figure 4.25 where the average maximum merged jet shear layer vorticity were 86%, 76% and 65% of the shear layer of the main jet alone for the auxiliary jet velocities of 60 m/s, 80 m/s and 100 m/s, respectively.

At the halfway point between the jet nozzle and the plate, x/d = 6, the velocity and vorticity profiles for the different auxiliary jet velocities showed very little difference in shape and magnitude. These velocity and vorticity profiles are presented in Figure 4.26 and Figure 4.27. As the flow field of the multi-slot jet with and without auxiliary jets showed no significant differences it indicated that the mechanism responsible for the suppression of the acoustic tone must be in the initial regions of the jet. As the most significant

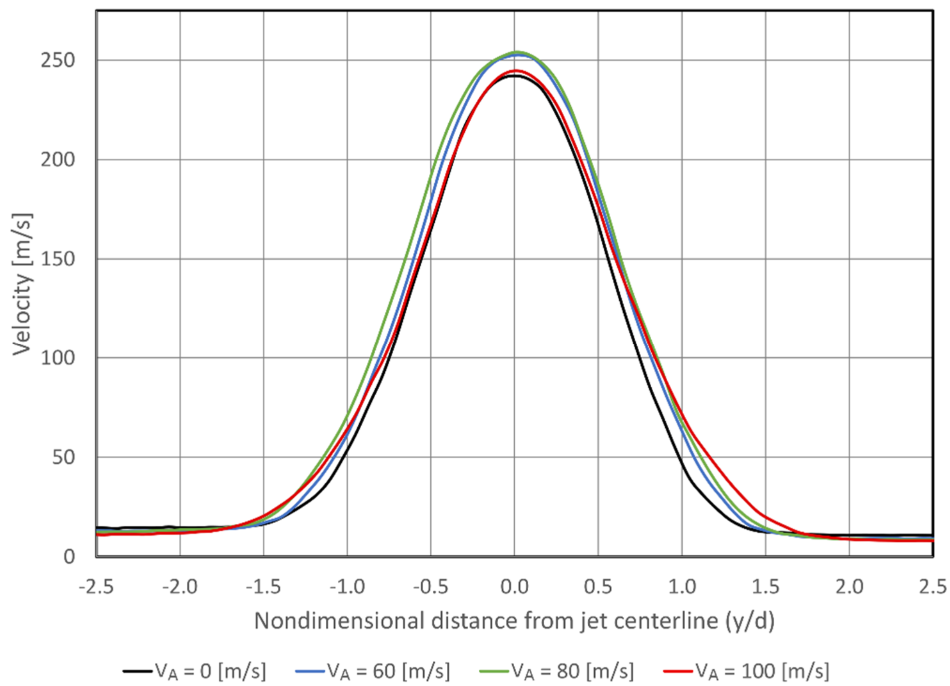

Figure 4.26 Velocity profiles of the impinging multi-slot jet at x/d = 6 for different auxiliary jet velocities. V_M = 250 m/s, d = 2 mm, a = 1 mm, s = 5 mm, h/d = 12.

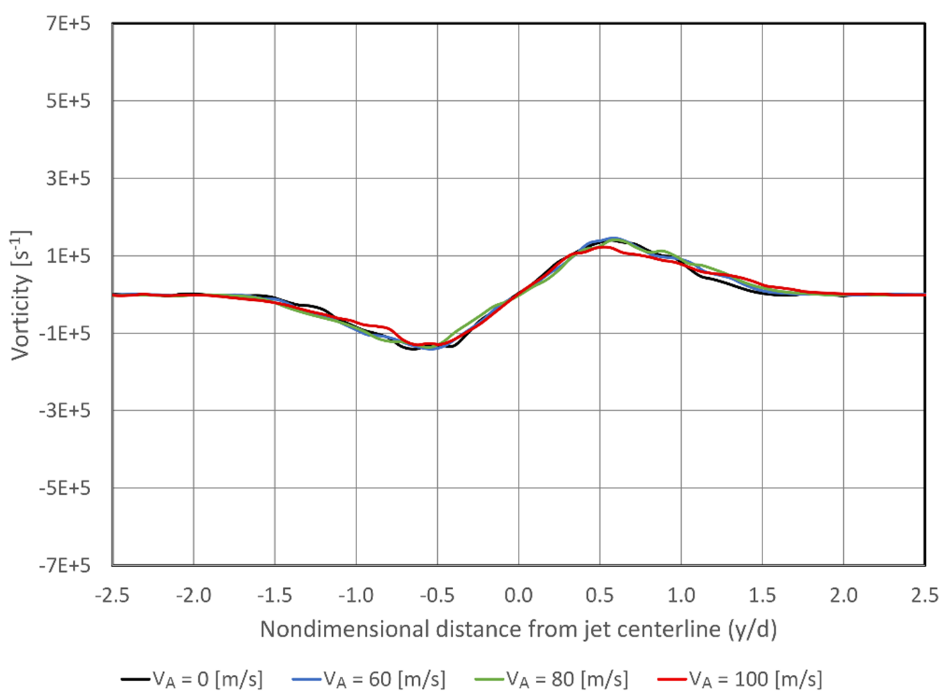

Figure 4.27 Vorticity profiles of the impinging multi-slot jet at x/d = 6 for different auxiliary jet velocities. V_M = 250 m/s, d = 2 mm, a = 1 mm, s = 5 mm, h/d = 12.

difference between the flow field with and without auxiliary jets was the change in the vorticity and velocity gradient it stands to reason that these parameters are responsible for the reduction in the tone amplitude and jet oscillation.

The 6685 Hz 10.8 kPa acoustic tone produced by the impingement of the main jet alone was used as a trigger signal to capture phase-locked PIV images of the flow field of the multi-slot jet when the flow field was generating a large-amplitude acoustic tone. The velocity fields of the jet at the phases of 90°, 180°, 270° and 360° of the acoustic signal are presented in Figure 4.28. The oscillation of the jet can be seen quite clearly in the four panels. Figure 4.28 confirms that the main jet, with no auxiliary jets, was oscillating at the same frequency as the acoustic tone and that the tone was generated through an aeroacoustic feedback mechanism. The corresponding vorticity fields are presented in Figure 4.29.

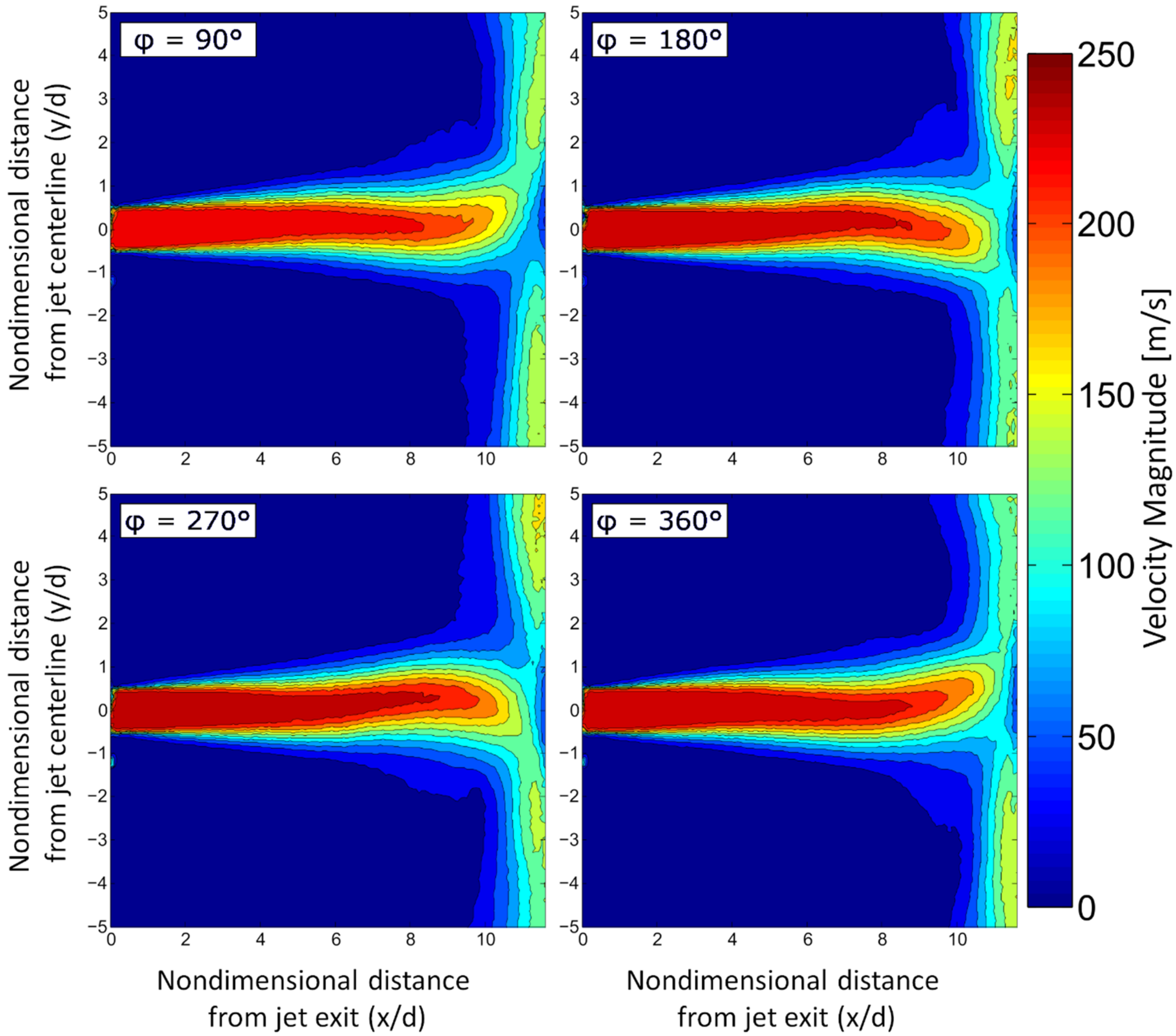

Figure 4.28 Velocity contour plots for the main jet of the multi-slot jet only at four different phases in the oscillation cycle. d = 2 mm, V_M = 250 m/s, a = 1 mm, V_A = 0 m/s, h/d = 12, s = 5 mm.

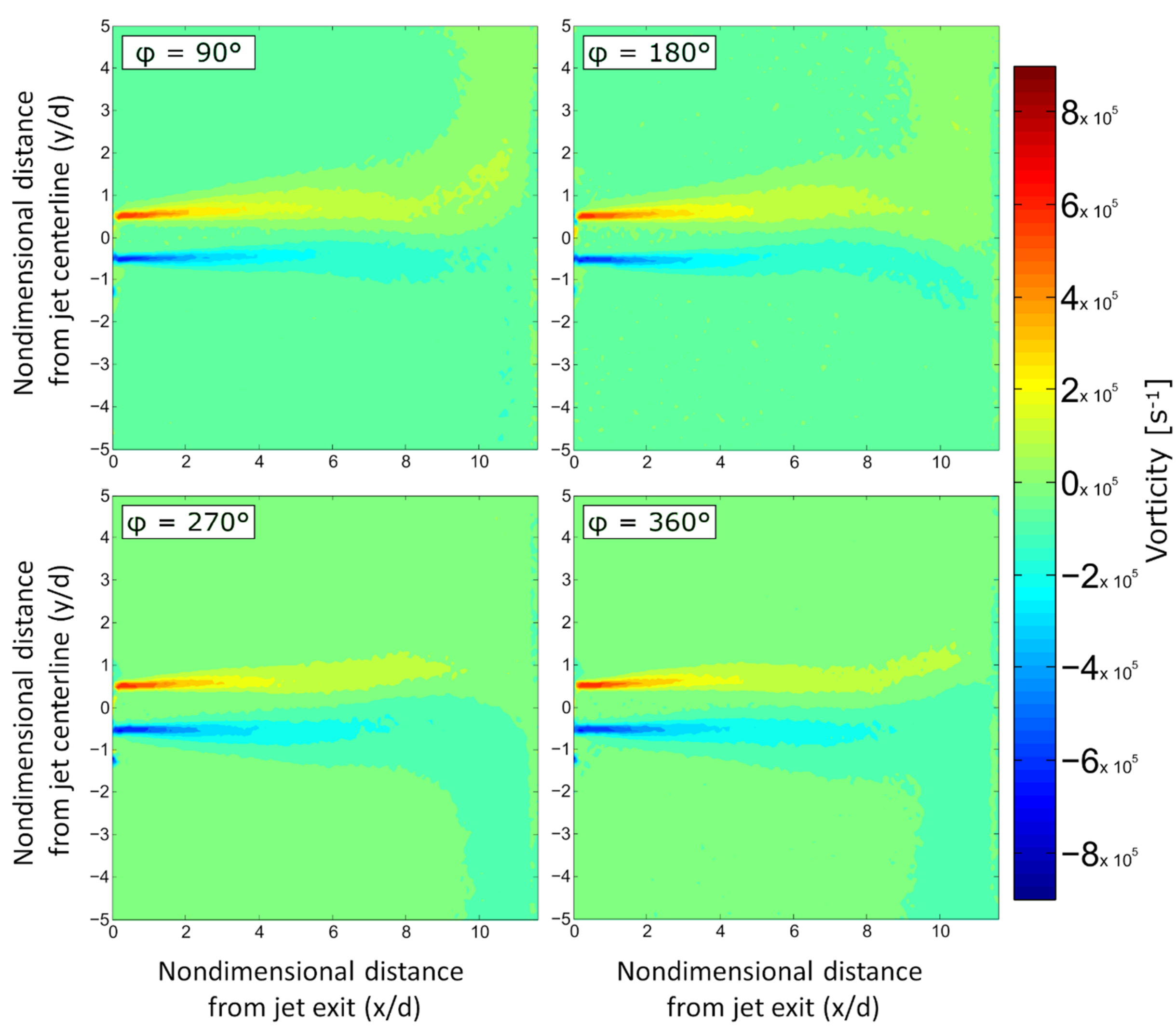

Figure 4.29 Vorticity contour plots for the main jet of the multi-slot jet only at four different phases in the oscillation cycle. d = 2 mm, V_M = 250 m/s, a = 1 mm, V_A = 0 m/s, h/d = 12, s = 5 mm.

4.4 Proper Orthogonal Decomposition

To observe different aspects of the flow field, Proper Orthogonal Decomposition (POD) was performed on snapshots of the flow field acquired using PIV. This analysis allows for the direct measurement of the components of the flow field that caused the jet to oscillate without the need for an acoustic tone to trigger data acquisition. For all the results presented in this sub-section, the jet parameters were the same as those used for Figure 4.7(A),(C),(D) and (E): i.e. a d = 2 mm main jet nozzle at V_M = 250 m/s at an impingement ratio of h/d = 12 from the plate. The auxiliary jets were set back at s = 5 mm from the main jet nozzle exit and the nozzle width set was set at a = 1 mm with auxiliary jet velocities of V_A = 0 m/s, 60 m/s, 80 m/s and 100 m/s.

The POD analysis returned both the eigenfunctions and associated eigenvalues of the supplied velocity fields. The eigenfunctions generated “modes” that are flow fields that combine in a weighted sum to recreate the provided velocity fields. The eigenvalues of those eigenfunctions correspond to the prevalence of the mode in reconstructing the input velocity fields. As such the eigenvalues indicate the kinetic energy associated with each mode.

The eigenvalues returned by the POD analysis are presented in Table 4.2. The sum of all the eigenvalues increased with increasing auxiliary jet velocity, which is to be expected as the kinetic energy of the flow field increased. The 0^{th} mode of the POD analysis corresponds to the mean velocity field and was seen to increase with increasing auxiliary jet velocity. The remaining modes from the analysis account for the motion of the jet column. As the auxiliary jet velocity increased, the sum of the eigenvalues of the

Table 4.2 Eigenvalues from POD analysis of impinging multi-slot jet.

Auxiliary jet velocity	0 m/s	60 m/s	100 m/s
Total sum of eigenvalues	5.85×10^{10}	6.33×10^{10}	6.37×10^{10}
Eigenvalue of 0th mode	5.30×10^{10}	5.91×10^{10}	5.96×10^{10}
(Relative percentage)	90.67%	93.28%	93.59%
Sum of fluctuating modes eigenvalues	5.46×10^{9}	4.26×10^{9}	4.08×10^{9}
(Relative percentage)	9.33%	6.72%	6.41%

fluctuating modes decreased in both magnitude and as a percentage of the total sum. These eigenvalue results corroborate the pressure data at the plate (Figure 4.15). The increase in the kinetic energy of the 0th mode, the mean flow, coincides with the increase in the static pressure at the plate. The decrease in the sum of the eigenvalues of the fluctuating modes coincided with the decrease in the fluctuating pressure at the plate.

Figure 4.30 shows the eigenvalues for the first ten fluctuating modes of the V_A = 0 m/s, 60 m/s and 100 m/s auxiliary jet velocity cases. As expected, given the difference in the sum, the eigenvalues associated with the modes for the V_A = 60 m/s and 100 m/s case were consistently smaller than the V_A = 0 m/s auxiliary jet velocity case. The first two modes of the V_A = 0 m/s case stand out as significantly larger than all the other modes at that velocity, indicating that those modes were significant in shaping the flow field of the jet. The POD analysis returned a time-varying phenomenon that was captured with a fixed spatial frame of reference as two orthogonal sequential modes. This fact and the similarly high amplitude of the eigenvalues of the first two modes of the V_A = 0 m/s auxiliary jet velocity case indicates that they represent a single time-varying phenomenon: the convection of the coherent structures and the oscillation of the jet column corresponding to the acoustic tone and aeroacoustic feedback mechanism.

The “U” and “V” velocity components along with the vorticity for the first two modes of the V_A = 0 m/s and 100 m/s auxiliary jet velocity cases are presented in Figure 4.31. Without the auxiliary jets, the U and V components contain clear and distinct features; i.e. large circles of U component velocity and thick vertical bands of V component velocity. The vorticity field from these combined velocity components results in large vortical structures. These large vortical structures are the POD representation of the coherent structures that are associated with the aeroacoustic feedback mechanism. In comparison,

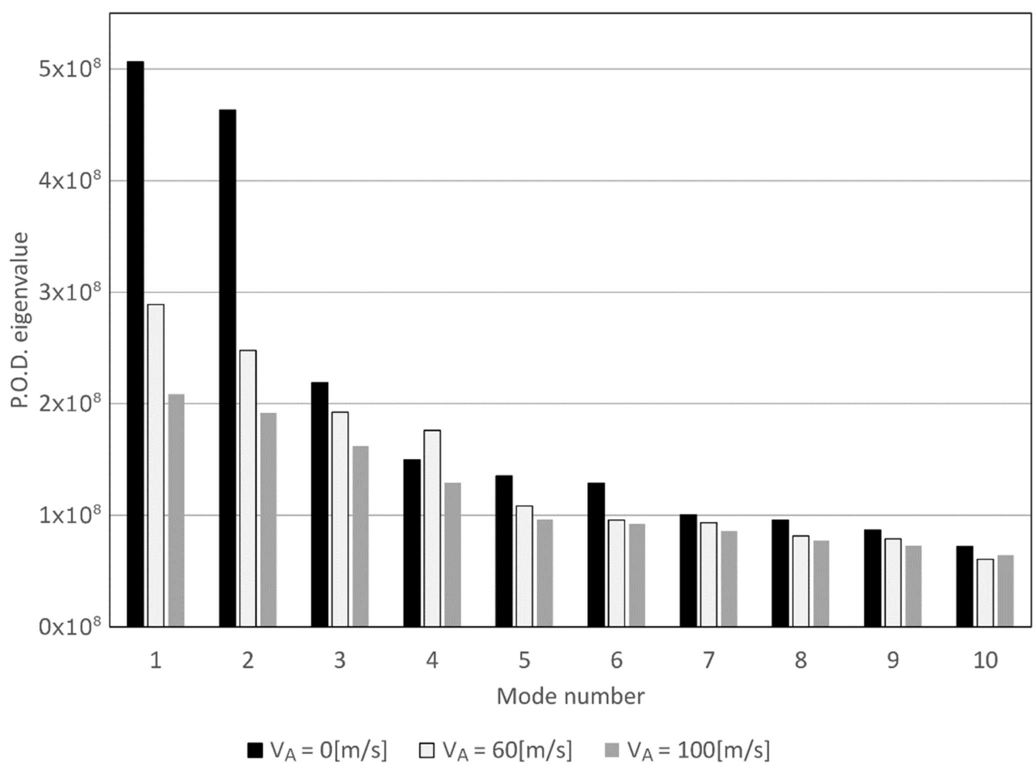

Figure 4.30 Eigenvalues of the first ten POD modes for the impinging multi-slot for different auxiliary jet velocities. V_M = 250 m/s, d = 2 mm, a = 1 mm, s = 5 mm, z/d = 12.

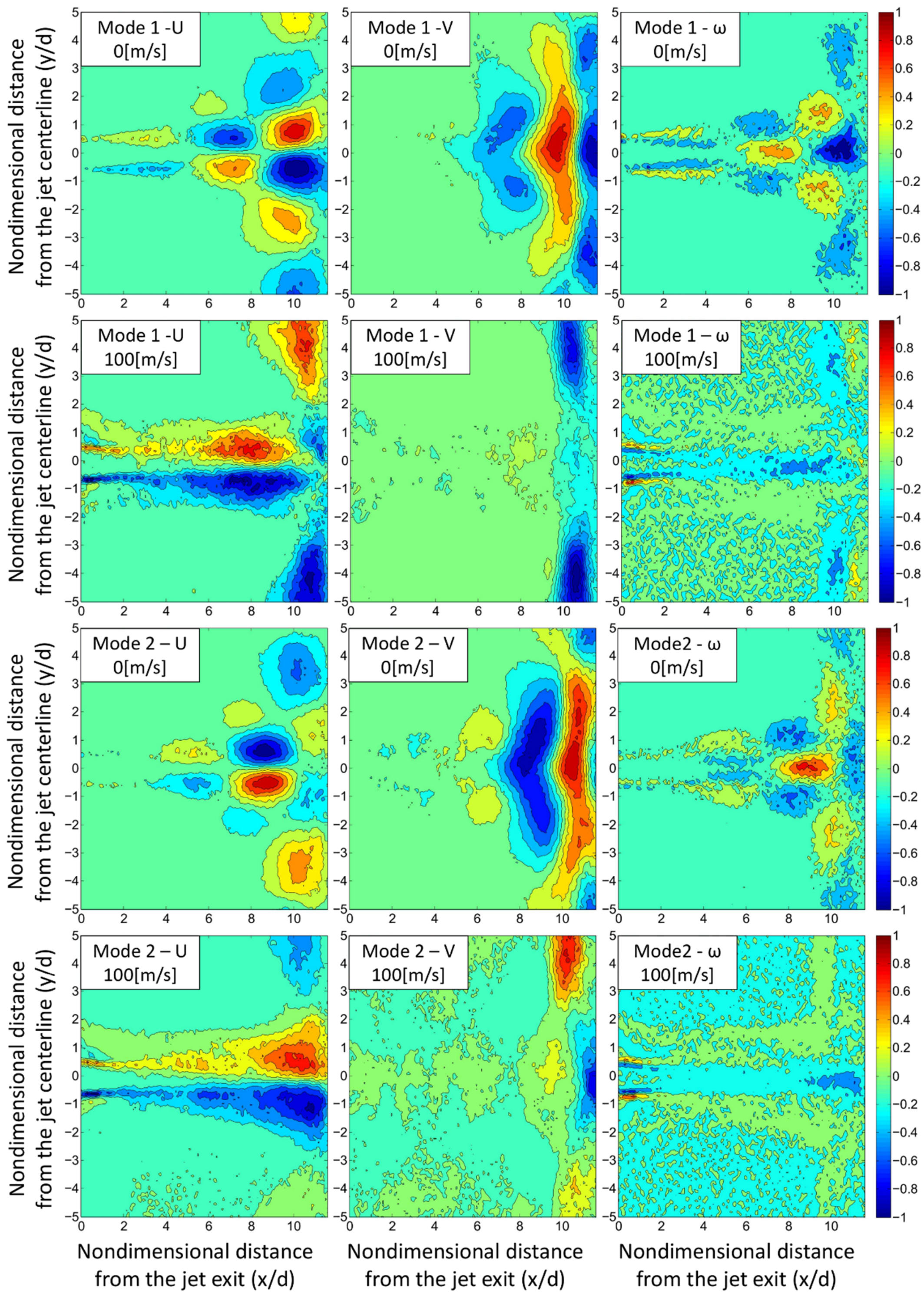

Figure 4.31 Contour plots of the U-component, V-component and vorticity of mode 1 and mode 2 for the impinging multi-slot jet with auxiliary jet velocities of V_A = 0 m/s and 100 m/s. V_M = 250 m/s, d = 2 mm, a = 1 mm, s = 5 mm, h/d = 12.

the U and V components of the modes of the 100 m/s case show very little organisation. The vorticity resulting from these velocity fields shows no coherent structures such as those seen in the V_A = 0 m/s case. The lack of coherent structures confirms what has been observed with the acoustic results and the pressure data at the plate: i.e. the auxiliary jets have arrested the feedback mechanism and the inherent instabilities do not grow into large coherent structures. The U component of both the V_A = 100 m/s modes, while lacking in the features that are associated with the coherent structures, shows two large horizontal bands of opposite magnitude which indicates a “rocking” mode of the jet similar to that found by Arthurs and Ziada [31] in the low-amplitude linear regime of their jet. This “rocking” oscillation will be further explored in the low order reconstructions presented in Figure 4.35.

Figure 4.32 presents the vorticity of the first two modes of the V_A = 0 m/s auxiliary jet case and indicates the approximate centre of the vortical structures. Figure 4.33(A) presents an image from Arthurs and Ziada [32] in which the time-averaged flow field for the impinging planar jet (d = 3 mm, $V_M \approx 310$ m/s, h/d = 10.5) has the mean flow path of the coherent structures superimposed over the image. Figure 4.33(B) presents the time-averaged flow field of the multi-slot jet with no auxiliary jets and the position of the centre of the vortices from the POD analysis superimposed on it. Figure 4.33(B) also includes the mean flow path from Arthurs and Ziada’s coherent structure tracking techniques. Despite the difference in the jet parameters (velocity, nozzle width and impingement ratio) the centres of the vortices from the POD modes roughly follow the path of the coherent structures associated with the aeroacoustic feedback as measured by Arthurs and Ziada [32].

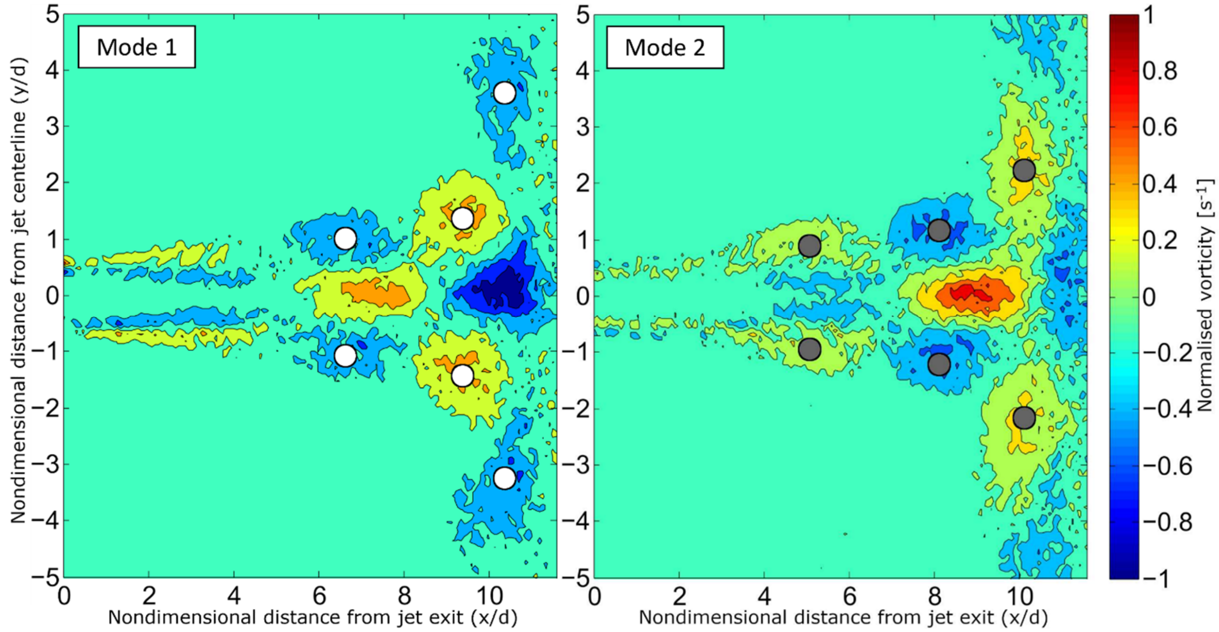

Figure 4.32 Contour plots of the vorticity of modes 1 and 2 of the main of the multi-slot jet alone with approximate centres of the coherent vortices.

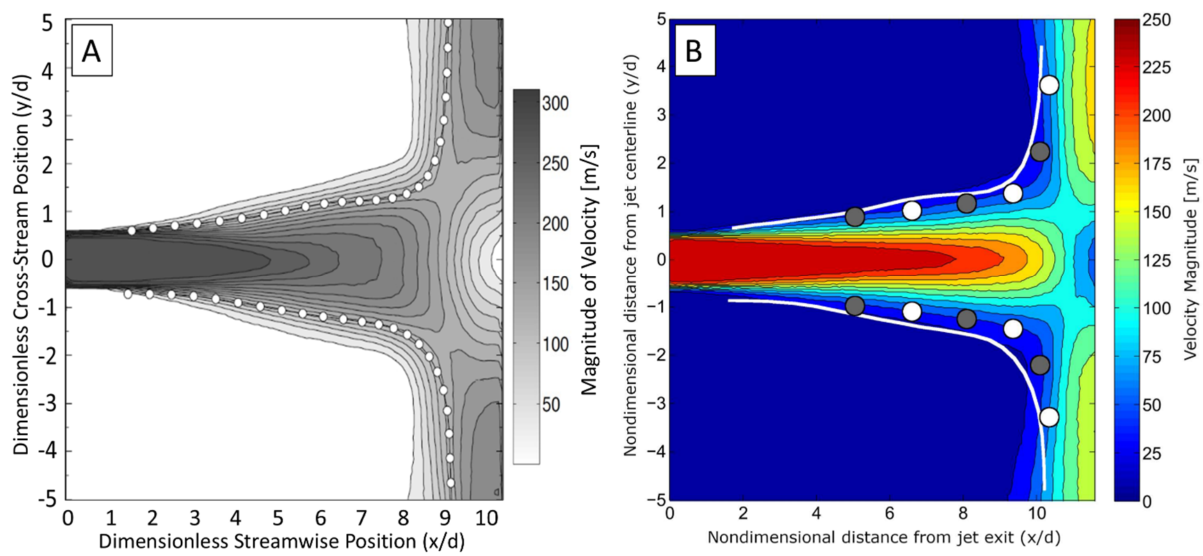

Figure 4.33 Left: Time-averaged flow field for an impinging planar jet with the mean path of coherent flow structures from Arthurs and Ziada [32] (V_M = 310 m/s, d = 3 mm, h/d = 10.5). Right: The time-averaged flow field of the impinging multi-slot jet overlaid with Arthurs and Ziada's mean flow path of coherent structures (white line) and the center of the coherent structures from the vorticity fields of modes 1 & 2, the white and grey circles respectively (V_M = 250 m/s, d = 2 mm, h/d = 12).

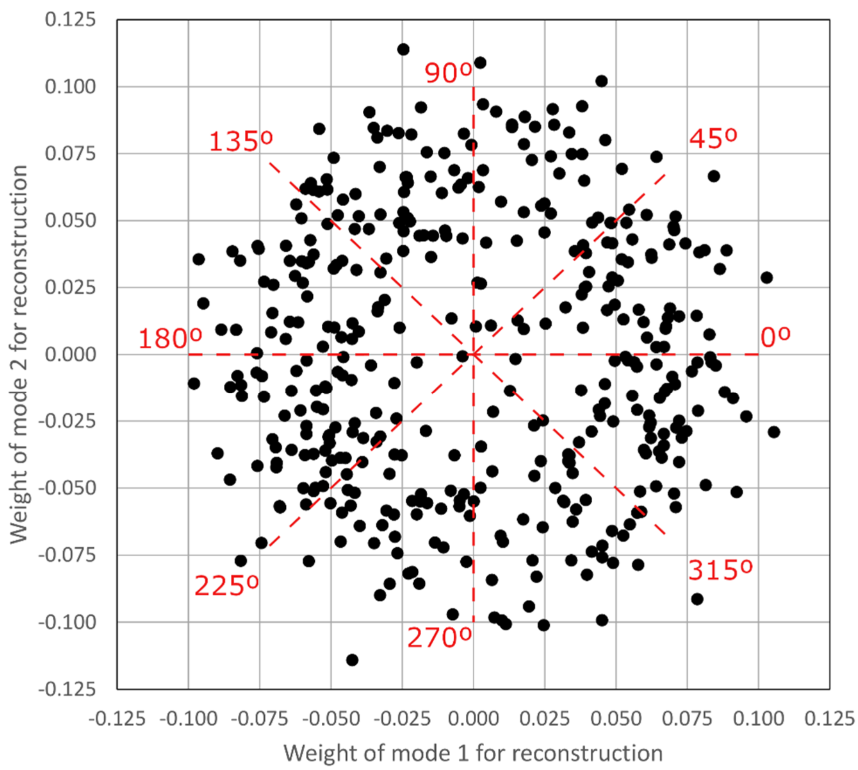

Figure 4.34 The reconstruction weights of Mode 1 plotted against the reconstruction weights of Mode 2 for all the input velocity fields of the 0 m/s auxiliary jet velocity POD analysis.

One of the features of the POD analysis is the ability to reconstruct the input velocity fields from a weighted sum of the modes that the analysis generates. Reconstructing a velocity field with only a few of the more energetic modes is a low-order reconstruction. Such a reconstruction of a velocity field would be akin to the time averaging performed for other averaged velocity fields presented above as it would not include the contribution of the higher modes which are associated with turbulence and fluctuations in the flow field.

As the oscillation of the jet due to the aeroacoustic feedback mechanism is a periodic phenomenon and modes 1 and 2 of POD analysis are orthogonal by definition then the weights associated with those modes can be considered similar to the sine and cosine of

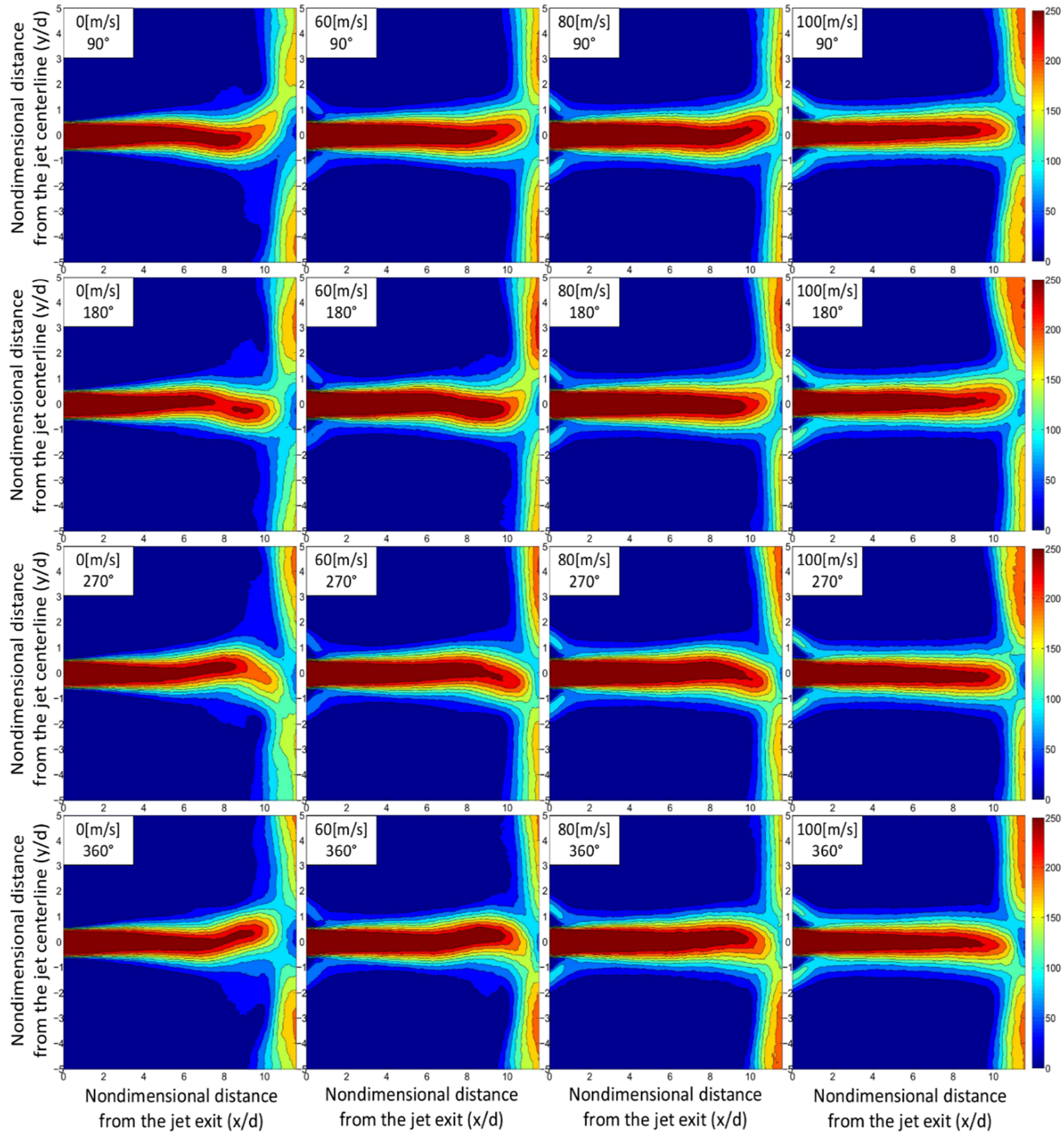

Figure 4.35 Contour plots of the velocity magnitude of the low order reconstructions of select flow fields of the multi-slot jet at specific phases in the jet oscillation for different auxiliary jet velocities.

that periodic phenomenon. The weights for both mode 1 and 2 of every velocity field used in the V_A = 0 m/s auxiliary jet velocity analysis are plotted in Figure 4.34. The plotted weights of the two modes resemble a circle in the same manner as sine and cosine create a unit circle. Just as a combination of sine and cosine represent a specific phase of a wave's oscillation the combination of the weights of modes 1 and 2 represents a specific point in the jet's oscillation. The dotted lines on Figure 4.34 indicate at what phase the oscillation of the jet was when velocity fields on that line were captured.

Figure 4.35 presents low order reconstructions of velocity fields that were found to have weights of modes 1 and 2 that indicated the oscillation of the jet was at 90°, 180°, 270° and 360° in its cycle for different auxiliary jet velocities. Comparing the velocity fields at the same phase for different auxiliary jet velocities, it is clear that the oscillation of the main jet column was significantly reduced with increasing auxiliary jet velocity. For the V_A = 100 m/s auxiliary jet velocity case, while the oscillations of the jet have been reduced significantly, the jet still "rocks" back and forward similar to the first mode of a cantilever beam fixed at the jet exit. This is what was indicated by the thick horizontal bands of U component velocity in the first mode of the POD analysis (Figure 4.31) and what was observed by Arthurs and Ziada [32] in the linear regime of the planar impinging jet.

Input velocity fields of the POD analysis of the multi-slot jet with 0 m/s auxiliary jet velocity are presented in Figure 4.36. These velocity fields were selected based on their weights of mode 1 and 2 to observe the jet at different phases in the oscillation cycle (90°, 180°, 270° and 360°). These velocity fields are overlaid with the velocity half-widths of the POD low-order reconstruction of that velocity field. The velocity half-width is the distance perpendicular from the jet centerline at which the velocity magnitude is half the

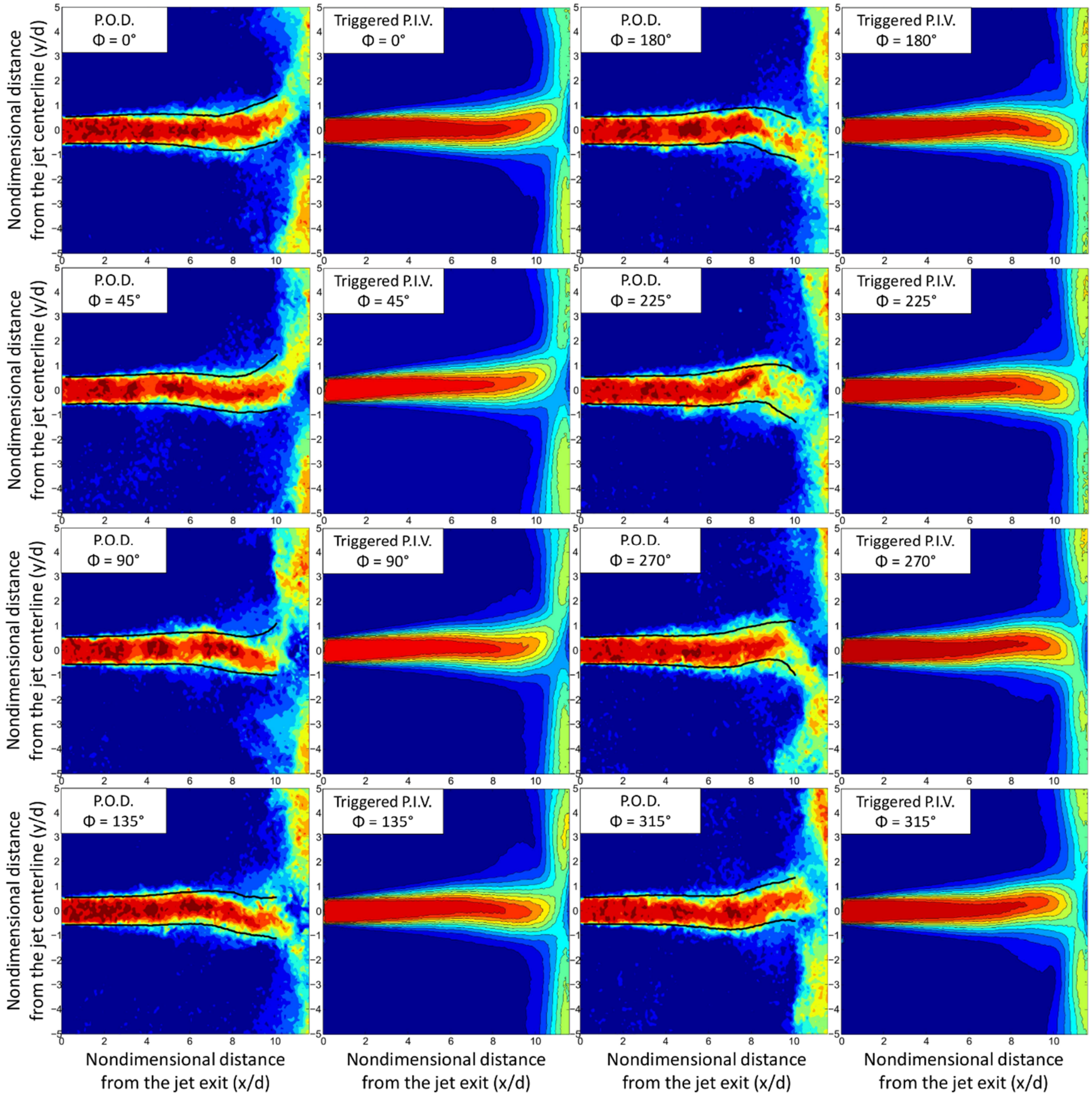

Figure 4.36 Comparison of the jet oscillations captured using phase-locked PIV and POD at different phases in the oscillation cycle. The images labelled "Triggered P.I.V." are the time-averaged images captured using phase-locked PIV. The images labelled "P.O.D." are the raw velocity fields used for the POD analysis with the velocity half-width of the POD reconstruction overlaid as black lines. V_M = 250 m/s, d = 2 mm, V_A = 0 m/s, h/d = 12.

maximum velocity at that axial distance from the jet exit. The overlaid velocity half-widths show the accuracy of the low-order reconstructions in capturing the oscillation of the jet column.

Figure 4.36 also includes the time-averaged velocity fields of the jet at different phases in the oscillation captured with the phase-locked PIV triggered off of the acoustic signal of the tone produced by the aeroacoustic feedback mechanism. A comparison of the shape of the jet columns from both methods, triggered phase-locked PIV and low order reconstructed POD, shows that the selection of velocity fields based on the weights of modes 1 and 2 accurately captures the column of the jet at the intended phase of the oscillation.

4.5 Summary

A fundamental investigation of the multiple slot planar jet oscillator has been presented, which includes three different measurement methods used to ascertain the influence of auxiliary jets on planar jet impingement: acoustic, pressure and optical. The results of each of these separate and independent measurements indicate that the auxiliary jets can significantly reduce the effects of the aeroacoustic feedback mechanism.

The acoustic testing showed the general trend of the reduction of the amplitude of the tones associated with the aeroacoustic feedback mechanism with increasing auxiliary jet nozzle width and velocity. At sufficiently high auxiliary jet velocities the acoustic tones were indistinguishable from the broadband noise of the multi-slot jet. With a wider auxiliary jet nozzle, the tones were found to be suppressed at lower auxiliary jet velocities.

The setback distance was found to have a significant effect on the production of the tones independent of the auxiliary jets with smaller setback distances producing significantly louder tones.

The pressure results at the plate showed an increase in the static pressure at the impingement plate indicating an increase in the steady flow of the jet. The fluctuations of pressure at the plate were seen to reduce in amplitude with increasing auxiliary jet velocity.

The POD results showed an increase in the percentage energy of the flow associated with the mean velocity field of the jet with increasing auxiliary jet velocity. The percentage of the jet energy associated with oscillations of the aeroacoustic feedback mechanism decreased with auxiliary jet velocity. The definition of the velocity patterns and velocity magnitudes of the modes associated with the aeroacoustic feedback mechanism were seen to reduce with increasing auxiliary jet velocity. Reconstruction of select flow fields showed that the oscillation of the jet decreased with increasing auxiliary jet velocity.

The PIV imaging of the time-averaged flow fields of the jet showed that the auxiliary jets resulted in a decrease in the maximum vorticity of the shear layer of the main jet and a reduction in the velocity gradient.

Chapter 5
Discussion

The data presented in the previous chapter show the results of a fundamental investigation into the influence of auxiliary planar jets on the planar impinging jet oscillator. These results show that the auxiliary jets have the ability to influence the aeroacoustic feedback mechanism exhibited by planar jet impingement.

The results of the acoustic testing showed that the auxiliary jets can influence the amplitude of the tones generated by the multi-slot jet. The specific case shown in Figure 4.7 shows that the auxiliary jets have the ability to influence the stage of the jet and

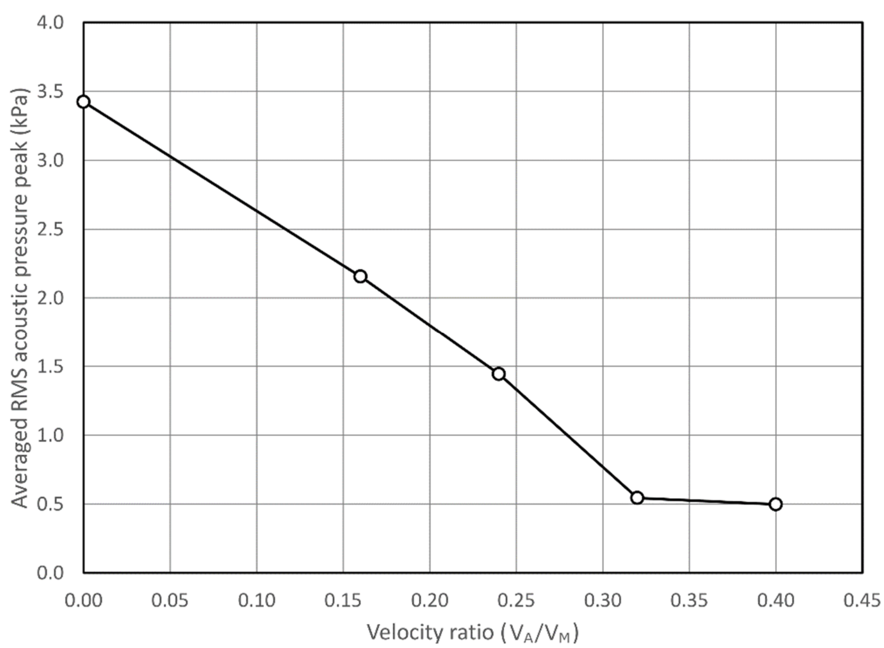

Figure 5.1 Average RMS of the maximum acoustic amplitude of the multi-slot jet for all acoustic tests performed as part of this investigation as a function of auxiliary jet velocity and main jet velocity ratio.

amplitude of the tones produced by the jet as part of the aeroacoustic feedback mechanism.

Figure 5.1 plots the noise produced by the multi-slot jet as a function of the velocity ratio of the auxiliary jets to the main jet. The data points in Figure 5.1 are the average of the RMS acoustic pressure peaks, measured in kPa, for every test performed at that velocity ratio. The decrease in the averaged RMS acoustic pressure peak produced by the multi-slot jet with velocity ratio indicates that the auxiliary jets are diminishing the effect of the aeroacoustic feedback mechanism. The amplitude change between the velocity ratio of 0.32 and 0.4 was insignificant in comparison to the reductions at the lower velocity ratios, indicating a limit on the ability of the auxiliary jets to reduce the noise produced by the multi-slot jet through increasing the velocity ratio.

The data in Figure 5.1 is averaged over every test performed in this investigation and as such it highlights the general trend of the velocity ratio. The averaging suppresses anomalous cases where the jet conditions amplified existing acoustic tones or spontaneously generated acoustic tones where none were found previously (Figure 4.8, 4.9 and 4.10). The data in Figure 5.1 shows that the auxiliary jet flow influences the main jet shear layer as expected, reducing the noise produced by the jet. The instances where the auxiliary jets acted counter to that trend were due to the unstable nature of jet shear layers and the complex flow conditions at the jet exit caused by the multi-slot jet geometry. The amplification of the aeroacoustic tones is caused when the interaction of the auxiliary jet flow, main jet flow, quiescent air and jet geometry result in a more unstable main jet shear layer with a larger growth rate of coherent structures in the jet.

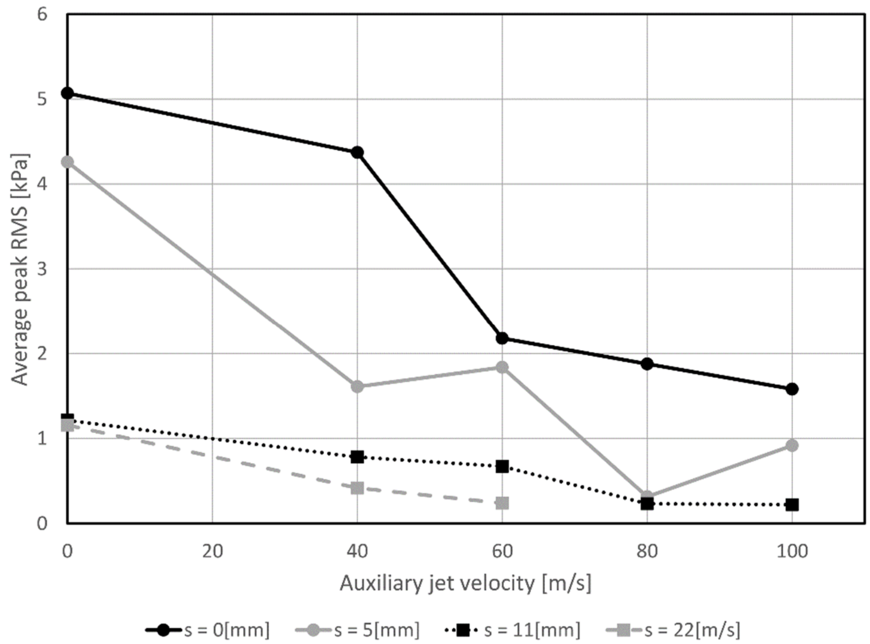

Figure 5.2 Averaged RMS of the maximum acoustic amplitude produced by the multi-slot jet between the impingement ratios of 6 and 16 for different auxiliary jet setback distances and auxiliary jet velocities.V_M = 250 m/s, d = 2 mm, a = 1 mm.

The amplitude of the noise produced by the jet was both a function of the setback distance and the auxiliary jet velocity, as can be seen in Figure 5.2. This Figure shows that the setback distance of the auxiliary jet influenced the tones produced by the impingement of the main jet of the multi-slot jet alone. The main jet produced increasing amounts of tones and stronger tones at smaller setback distances. This indicates that the more relevant effect of the setback distance was not the change in the development length of the auxiliary jets but their influence on the tones produced by the main jet. This change in the main jet tones was due to the position of the auxiliary jet plates determining the flow of quiescent air entrained immediately at the jet exit. The larger setback distances, with the auxiliary jet plates farther away from the impingement plate, could have allowed for more quiescent flow to be picked up by the main jet resulting in a jet velocity profile with “external flow” similar to that seen by Mickalke and Hermann [13]. The position of the auxiliary jet plates could allow for the circulation of fluid immediately at the jet exit influencing the jet velocity profile at the jet exit. These changes to the jet velocity profile at the jet exit resulted in a change in the jet shear layers causing a reduction in the amplitude of the tones produced by the aeroacoustic feedback mechanism. At all the setback distances tested, irrespective to the number of tones produced and the strength of those tones, the average effect of the auxiliary jets was to reduce the amplitude or eliminate the tones with higher velocities, generally resulting in a larger reduction in amplitude.

The effect of the auxiliary jet nozzle width on the noise produced by the multi-slot jet is plotted in Figure 5.3. The graph shows that the wider the auxiliary jet nozzle the more effective the auxiliary jets were at eliminating the tones of the multi-slot jet. While this data indicates that larger auxiliary jet nozzles would result in a more stable air-knife for gas jet wiping the modelling done by Yahyaee et al. [47] indicates that auxiliary jets of larger widths have a lower maximum pressure gradient which indicates that they would adversely affect the minimum coating weight possible for the jet. As their steady-state model did not capture the oscillations of the jet due to the aeroacoustic feedback mechanism, further measurements of the pressure profile at the impingement plate are required to determine the overall effect of the auxiliary jet width.

The reduction in the amplitude of the noise in Figure 5.1, Figure 5.2 and Figure 5.3, along with the more specific examples given in Figure 4.6-4.10, indicate that the auxiliary jets are directly affecting the aeroacoustic feedback mechanism that produces the large

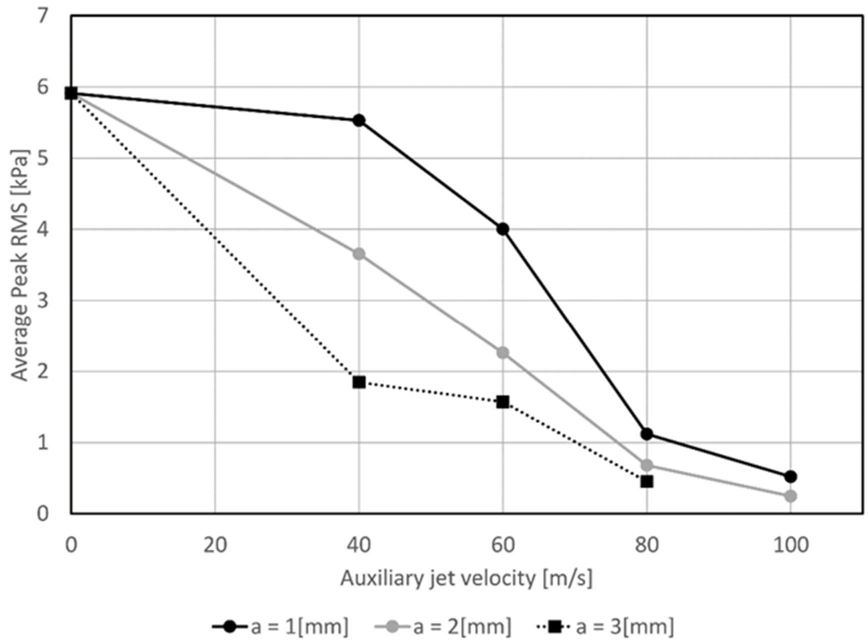

Figure 5.3 Averaged RMS of the maximum acoustic amplitude produced by the multi-slot jet between the impingement ratios of 6 and 16 for different auxiliary jet nozzle widths and auxiliary jet velocities. V_M = 250 m/s, d = 2 mm, s = 5 mm.

amplitude tones. This reduction in the tone amplitude indicates that the jet oscillation, that is also associated with the aeroacoustic feedback mechanism, would also be reduced. This was confirmed by the fluctuating pressure measurements at the impingement plate, Figure 4.15, and the POD analysis, Table 4.2.

The measurements of the static and fluctuating pressures at the plate shows very clear trends with increasing auxiliary jet velocity, as shown in Figure 4.12 and Figure 4.15 respectively, and summarized in Figure 5.4:

1. An increase in the maximum static pressure at the plate.
2. A narrowing of the static pressure profile on the plate.
3. A decrease in the maximum fluctuating pressure at the plate.

The increase in the amplitude of the static pressure at the plate cannot be accounted for by the added momentum of the auxiliary jets. The pressures of the auxiliary jet plenum required to generate the auxiliary jet velocities of 60 m/s and 100 m/s were 5.1% and 14.3% of the pressure in the main jet plenum. The increase of the maximum static pressure at the plate was 20.0% and 30.8% for those auxiliary jet velocities. This increase in the static pressure at the plate, above what can be attributed to the auxiliary jets, indicates that the auxiliary jets were affecting the flow field of the multi-slot jet.

The frequencies of the fluctuating pressures for the 0 m/s, 60 m/s and 100 m/s auxiliary jet velocities presented in Figure 5.4 were the same frequency as the acoustic tones produced by the multi-slot jet. At the auxiliary jet velocity of 100 m/s, the frequency of the fluctuating pressure was 7260 Hz. The jet produced no discernable acoustic tones at this auxiliary jet velocity; however, an effective Strouhal number of those fluctuations is $St_{eff} = 1.25$. As can be seen in Figure 4.11, a Strouhal number of 1.25 is the average value of the second stage of the jet. The Strouhal number of the pressure fluctuations at the auxiliary jet velocity of 100 m/s and the frequency of the noise at the other auxiliary jet velocities indicates that the measured pressure fluctuations of the jet are due to the aeroacoustic feedback mechanism. The amplitude of the fluctuating pressure at the plate decreased with increasing velocity of the auxiliary jets; where the maximum fluctuating pressure decreased by 56% and 76% for the auxiliary jet velocities of 60 m/s and 100 m/s, respectively. This reduction in the magnitude of the fluctuating pressure with increasing auxiliary jet velocity indicates that the auxiliary jets reduced the amplitude of the oscillations associated with the aeroacoustic feedback mechanism.

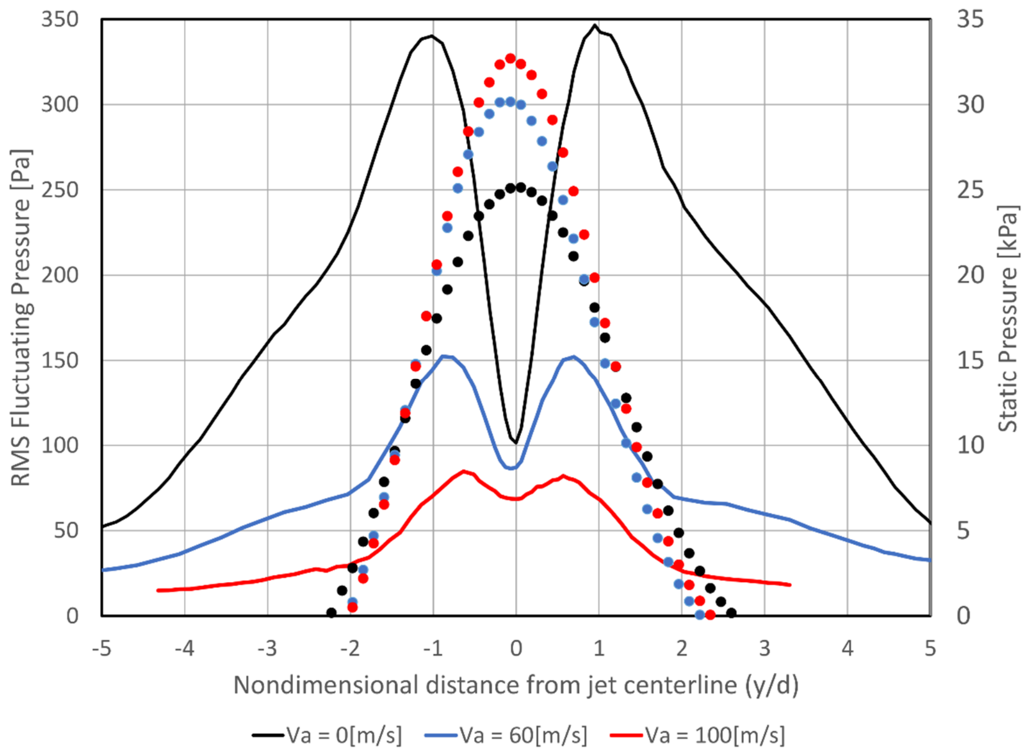

Figure 5.4 The fluctuating and static pressure profiles (solid lines (left) and symbols (right) respectively) at the impingement plate for different auxiliary jet velocities of the multi-slot jet. V_M = 250 m/s, d = 2 mm, a = 1 mm, s = 5 mm, h/d = 12.

The increase in the maximum static pressure, above that added by the momentum of the auxiliary jets, was due to the reduction in the oscillations of the jet indicated by the fluctuating pressures. As the amplitude of the oscillations was reduced, less momentum of the main jet was lost due to the entrainment of quiescent air by the oscillations of the jet column. The reduction of the width of the static pressure profile on the plate was also due to the reduction in the oscillation of the jet column as the momentum of the jet was not spread over a larger area. Both of these changes in the main jet were due to the action of auxiliary jets – i.e. the increased static pressure and decreased width of the static pressure profile combined to result in an increase in the maximum static pressure gradient at the plate, presented in Figure 4.13, which is a major process variable in the wiping ability of an air-knife [3], [45].

The pressure results show that the auxiliary jets decreased the oscillations of the jet, supporting what was inferred from the acoustic results regarding the diminishment of the aeroacoustic feedback mechanism. The pressure results also show that the auxiliary jets could improve the wiping actuator function of an air-knife, increasing the maximum pressure gradient and reducing the oscillations of the jet, while also reducing the workplace hygiene issue of the acoustic tones. This finding supports the work by Yahyaee et al. [47] who found that a multi-slot jet could achieve thinner coatings given some geometry constraints.

The POD analysis of the jet was performed to investigate the shape and energy of the modes of the jet flow associated with the aeroacoustic feedback mechanism. The eigenvalues derived from this analysis are analogous to the kinetic energy as the covariance matrix used in the analysis is a product of the velocity fields [60]. The results from the POD analysis express the oscillations of the jet due to the aeroacoustic feedback mechanism as the 1st and 2nd modes. The 0th mode returned by the analysis is the mean flow of the supplied flow-fields.

The eigenvalues indicate that the kinetic energy of the flow field, Table 4.2, increased with increasing auxiliary jet velocity, which is to be expected. This kinetic energy can be broken down to the energy associated with the mean flow field, the 0th mode, and the deviations or fluctuations from the mean flow, represented by the other modes returned by the analysis. While the total energy of the flow field increased with auxiliary jet velocity, the portion of that energy that was attributed to the oscillations and fluctuations of the jet decreased. This decrease in fluctuating energy corresponds to a decrease in the amplitude of the acoustic tones and fluctuating pressure at the plate due to the aeroacoustic feedback mechanism.

The percentage of the fluctuating energy that is associated with the aeroacoustic feedback mechanism, first and second modes, can be found in Table 5.1. This shows us that, as the auxiliary jet velocity increased, the percentage of fluctuating energy attributed to the oscillations of the jet due to the aeroacoustic feedback mechanism decreased from 17.8% to 9.8% of the fluctuating energy in the flow.

Figure 5.5 shows the velocities and vorticity of modes 1 and 2 from the POD analysis as a function of auxiliary jet velocity. The figure clearly shows that the organisation of the flow decreased with increasing auxiliary jet velocity. The structures found in the flow field retained their same general shape – i.e. circles of U-component velocity and bands of V-

Table 5.1 The eigenvalues of the POD analysis of the multi-slot jet for different auxiliary jet velocities. V_M = 250 m/s, d = 2 mm, a = 1 mm, s = 5 mm, h/d = 12.

Auxiliary jet velocity	Eigenvalues of modes 1 and 2	Eigenvalues of modes 1 and 2 as a percentage of the total fluctuating energy
m/s	[-]	%
0	9.69×10^8	17.77%
60	5.37×10^8	12.61%
80	4.12×10^8	10.19%
100	4.00×10^8	9.80%

component velocity, for all auxiliary jet velocities. The magnitude of these features and the definition of their shape both decrease with increasing auxiliary jet velocity. The vorticity of the two modes show the coherent structures associated with the aeroacoustic feedback mechanism. The definition and magnitude of these structures decreased with increasing auxiliary jet velocity. These vorticity fields show that the coherent structures associated with the aeroacoustic feedback mechanism decrease in "coherence" with auxiliary jet velocity and, at V_A = 100 m/s, the vortical structures are not distinguishable in the jet's flow field. This indicates that the auxiliary jets are interfering with the aeroacoustic feedback mechanism resulting in less developed coherent structures.

The jet centerline of the low-order POD velocity field reconstruction of the multiple-slot jet for different auxiliary jet velocities at the phase angle of 270° are compared in Figure 5.6. The center of the jet columns are defined as the position halfway between the velocity half-widths of the jet. The velocity half-width was defined at each axial distance from the jet exit as the cross-stream position at which the velocity of the jet had reduced to half the maximum at that axial distance. The comparison of the jet centers in Figure 5.6 shows that the oscillation of the jet column was a function of the auxiliary jet velocity and confirms that the jet oscillations due to the aeroacoustic feedback mechanism reduced in amplitude with increasing auxiliary jet velocity, consistent with the results reported for the static and fluctuating pressure profiles (Figure 4.12 and Figure 4.15 respectively).

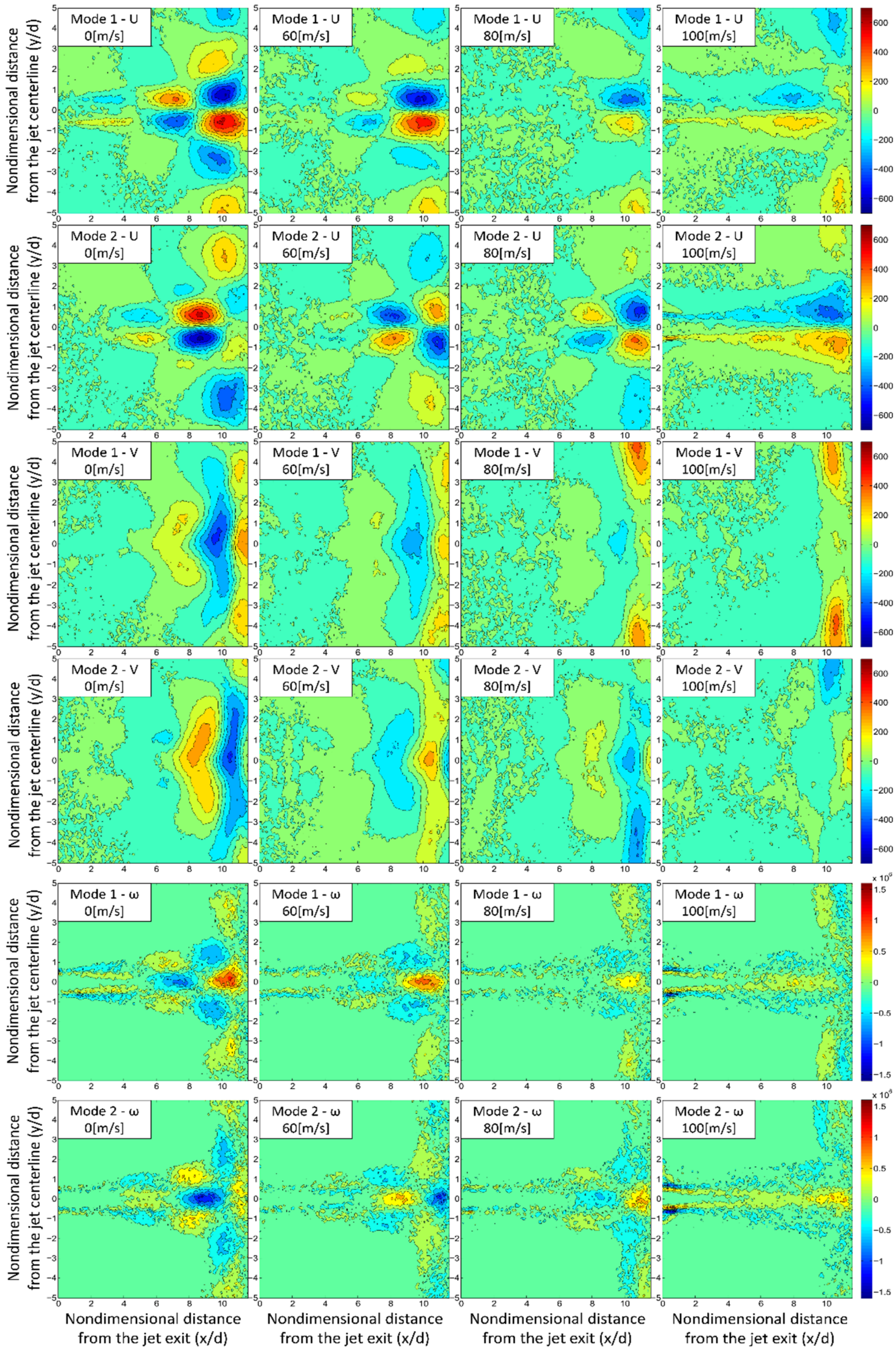

Figure 5.5 The U and V component velocity and vorticity fields of modes 1 and 2 of the multi-slot jet for different auxiliary jet velocities. V_M = 250 m/s, d = 2 mm, a = 1 mm, s = 5 mm, h/d = 12.

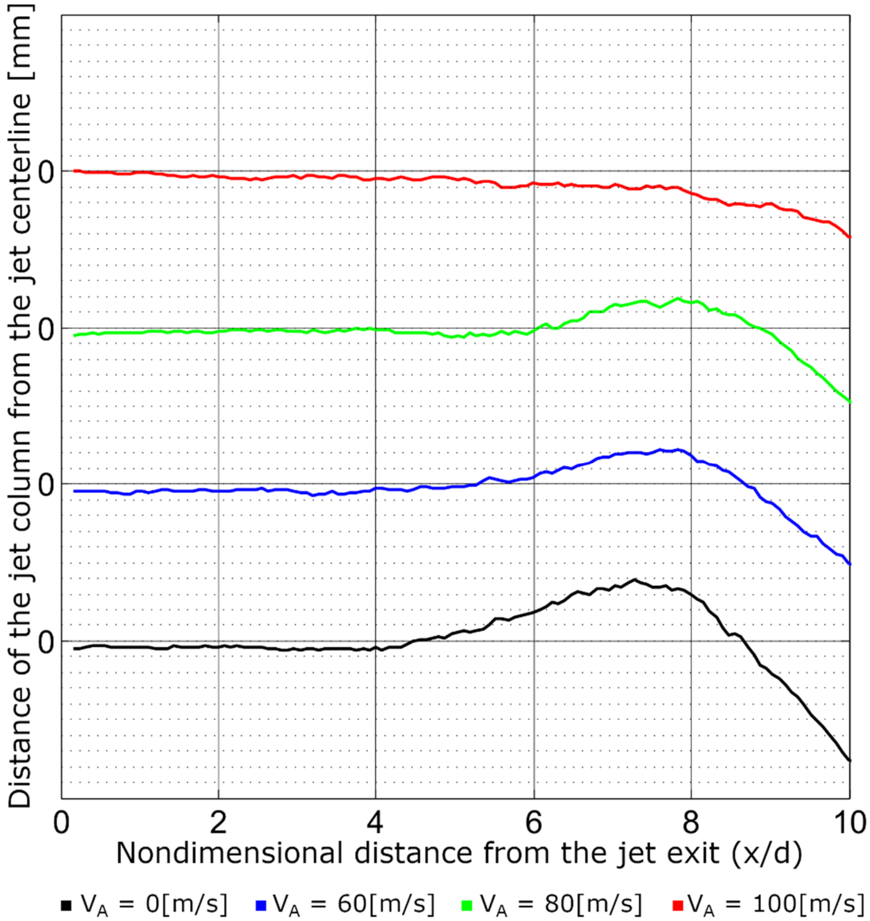

Figure 5.6 Position of the center of the jet column for the multi-slot jet reconstructed from the POD modes at different auxiliary jet velocities. The jet columns were reconstructed at the phase of φ=270° in the oscillation cycle. The center of the jet column was defined as the distance halfway between the jet velocity half-widths of the jet column.

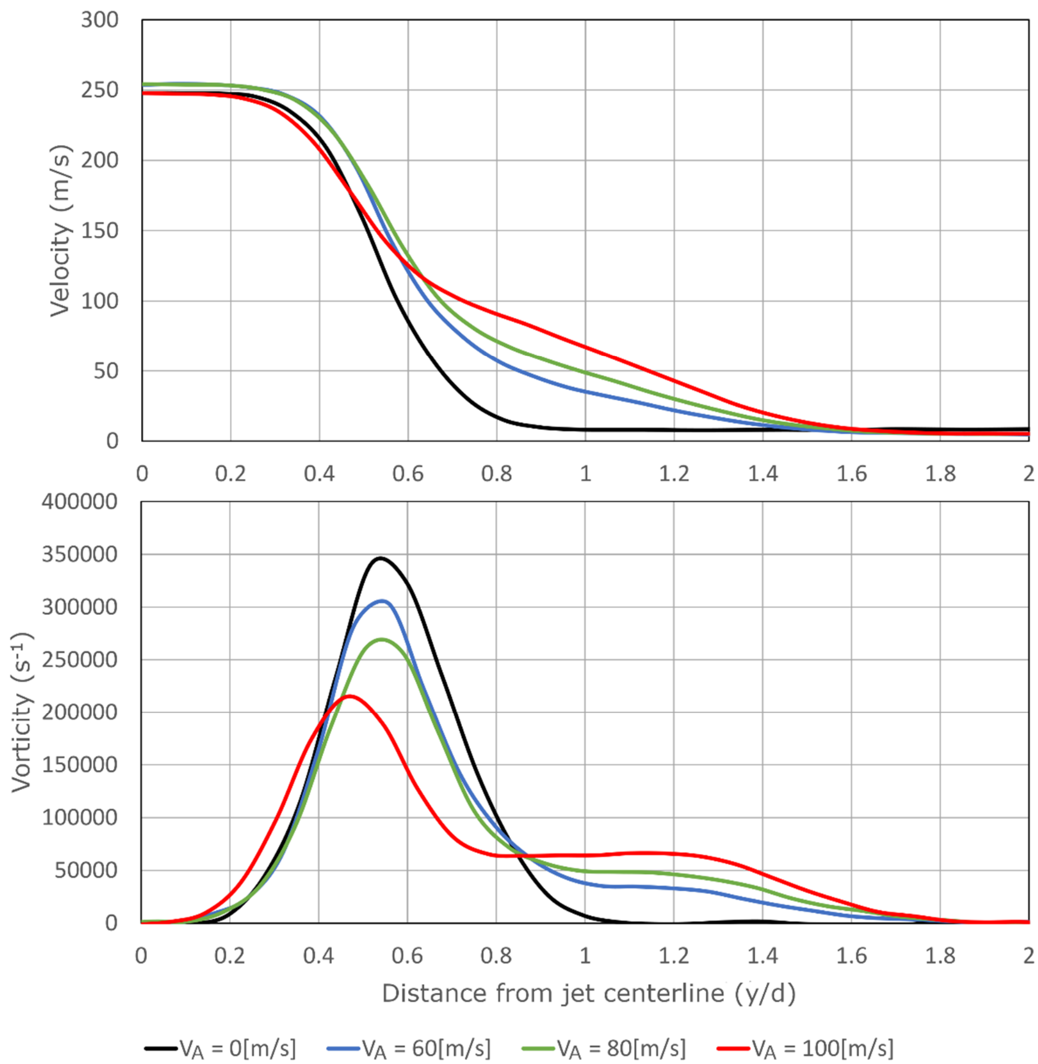

Figure 5.7 Velocity and vorticity profiles for the multi-slot jet for different auxiliary jet velocities at x/d = 2. V_M = 250 m/s, d = 2 mm, a = 1 mm, s = 5 mm, h/d = 12.

The PIV experiments were performed to obtain direct measurements of the velocity and vorticity fields of the multi-slot jet when generating an acoustic tone and when that tone was suppressed using the auxiliary jets. The time-averaged velocity and vorticity profiles, two nozzle widths downstream from the nozzle exit at different auxiliary jet velocities, are presented in Figure 5.7.

The results of Figure 5.1 and Figure 5.3 indicated that the reduction in the tone amplitude was an independent function of both the auxiliary jet velocity and the auxiliary jet nozzle width. The vorticity profiles in Figure 5.7 show a change in the vorticity of the multi-slot jet in two different ways at different auxiliary jet velocities. The peak in vorticity in Figure 5.7 at $y/d \approx 0.5$ is the result of the main jet shear layer and the inner shear layer of the auxiliary jet merging. There is a second area of the vorticity profile that is flat between $y/d \approx 0.8$ and 1.3 that increases in amplitude with increasing auxiliary jet velocity. This area of the vorticity profile is due to the change of the gradient in the velocity profile between those two points which arises from the auxiliary jet merging with the main jet. The width and velocity gradient of this area were determined by the outer shear layer of the auxiliary jet profile.

The amplitudes of these two distinct areas of vorticity can be found in Table 5.2 along with the amplitudes as compared to the maximum single-slot vorticity expressed as a percentage. The tabulated vorticity amplitudes and profile of these regions of vorticity in Figure 5.7 indicate that the shear layer profile of the multi-slot jet is heavily influenced by the auxiliary jets. The reduction in the amplitude of the merged jet shear layer to 65% of the single slot jet with auxiliary jets indicates a reduction in the maximum growth rate of disturbances in the jet shear layer as found by Monkewitz and Heurre [12]. The increase in the magnitude of the “outer shear layer” portion of the merged shear layer could be seen as similar to a thickening of the shear layer that was found to reduce the growth rate of the disturbances of the jet by Michalke and Hermann [13].

Table 5.2 The vorticity amplitude of the merged shear layer and the outer auxiliary jet shear layer of the multi-slot jet at different auxiliary jet velocities. Percentage values are calculated as a percentage of the maximum single slot main jet shear layer vorticity. V_M = 250 m/s, d = 2 mm, a = 1 mm, s = 5 mm, h/d = 12.

V_A	Merged shear layer		Outer auxiliary jet shear layer	
m/s	s^{-1}	%	s^{-1}	%
0	343,612.7	100.0%	-105.9	0.0%
60	295,880.5	86.1%	33,472.0	9.7%
80	260,338.5	75.8%	47,547.1	13.8%
100	223,949.5	65.2%	62,053.1	18.1%

While we do not have velocity profiles for the impinging jet with different auxiliary jet widths the profiles in Figure 5.7 can allow us to speculate as to how the auxiliary jet width influences the amplitude of the aeroacoustic tones. An increase in the auxiliary jet nozzle width would likely decrease the amplitude of both the inner and outer shear layers of the auxiliary jets but would result in a much longer profile for the outer auxiliary jet shear layer. Thus, in terms of Figure 5.7, a wider auxiliary jet nozzle for the same velocity would result in an increase in the amplitude of the merged shear layer and a longer outer shear layer with a lower amplitude. As wider auxiliary jets resulted in further reductions of the tone amplitude for a given auxiliary jet velocity this could indicate that the thickening of the shear layer is more significant in reducing the growth rate of the disturbances associated with the aeroacoustic feedback mechanism in the multi-slot jet.

5.1 Summary

The aeroacoustic feedback mechanism of planar impinging jets is a well-established and robust phenomenon. The mechanism consists of the generation, convection and growth of instabilities into coherent structures in the jet shear layer until they impinge upon a solid surface. This impingement of the coherent structures generates a pressure wave that travels up the jet to trigger another instability. The impingement of the structures and the perturbation of the shear layer by the pressure wave “lock-in”, becoming a periodic phenomenon.

It has been established by the results presented in this work that the auxiliary jets can reduce the amplitude of the acoustic tones and the oscillations of the jet associated with the aeroacoustic feedback mechanism.

The acoustic tones are a result of the periodic nature of the pressure waves generated by the impingement of the coherent structures on a solid surface – i.e. the steel strip in the case of the continuous galvanizing process. The amplitudes of the tones produced by the main jet were proportional to the size and strength of the coherent structures impinging upon the plate. The reduction of the acoustic tones with increasing auxiliary jet velocity indicates that the auxiliary jets reduced the growth rate of the coherent structures by reducing the velocity gradient that drives the growth of those vortices. As the auxiliary jet velocity increased, the larger the reduction in the maximum vorticity and velocity gradient of the shear layer, resulting in a further reduction in the amplitude of the acoustic tones observed.

At sufficiently high auxiliary jet velocities, the size of the coherent structures were reduced such that the pressure waves generated by their impingement were no longer strong enough to generate an acoustic amplitude sufficiently loud to be distinguishable from the broadband noise produced by the jet.

The oscillations of the jet associated with the aeroacoustic feedback mechanism were a result of the large scale structures in the flow as they were convected towards the plate. The magnitude of those oscillations was determined by the size and strength of the coherent structures. As the coherent structures reduced in size and magnitude their effect on the jet column also reduced. As was seen in the velocity components of Figure 5.5, the nature of the oscillations changed between the auxiliary jet velocities of 0 m/s and 100 m/s but they were still governed by the aeroacoustic feedback mechanism, as indicated by the frequency of the pressure fluctuations.

The driving force for the growth of the instabilities is the shear layer of the jet. In the initial region of the jet, the collective interaction, as described by Nosseir and Ho [25], [26], causes the rapid growth of the vortices. Figure 5.7 shows that the auxiliary jets changed the shear layer of the main jet in two separate ways that resulted in a reduction in the maximum vorticity and the velocity gradient between the main jet and the quiescent air. The reduction of the intensity and increase in the thickness of the shear layer reduced the growth rate of the coherent structures, which led to the reduction in the amplitude of the acoustic tones and oscillations.

Chapter 6
Conclusions and Future Work

This thesis summarises an in-depth investigation into the behaviour and interactions of the planar jet plate oscillator with auxiliary planar jets in a novel multi-slot jet air-knife prototype. The purpose of this study was to quantify the influence of auxiliary jets on the self-excited oscillations of the impinging planar jet for their use in industrial applications. The aeroacoustic feedback mechanism of the impinging planar jet leads to large amplitude acoustic tones, which present a workplace hygiene issue, and significant oscillations of the jet column which leads to inconsistent final coating weights in the continuous hot-dip galvanising process

This investigation experimentally quantifies the effect of auxiliary planar jets on the aeroacoustic feedback mechanism and the flow field of an impinging planar jet. The fundamental physics and fluid mechanics of the self-excited planar jet-plate oscillator are observed under the influence of the auxiliary planar jets to quantify and isolate the mechanisms by which the interaction of the multiple jets results in a change in the aeroacoustic feedback mechanism.

The results of different auxiliary jet operating parameters investigated in this work are briefly summarised in §6.1. Novel conclusions that can be drawn from these results are outlined in §6.2. §6.3 includes an in-depth discussion of future work based on conclusions hinted at in the results but not definitively proven by the data collected.

6.1 Summary of results

The testing performed on the multi-slot planar jet showed that the large amplitude tones of the main jet alone were, in general, reduced in amplitude with increasing auxiliary jet velocity. Static and fluctuating pressure measurements performed at the impingement plate showed that the decrease in acoustic tones was accompanied by increased static pressure and a reduction in the magnitude of pressure fluctuations. Phase-locked PIV of the main jet alone confirmed that the large amplitude tones were accompanied by significant oscillations of the jet, as in previous studies Arthurs and Ziada [30]. To investigate the flow field of the multi-slot jet, a POD analysis was performed on PIV vector fields of the jet at different auxiliary jet velocities where acoustic tones were produced and suppressed. The POD analysis showed that, while the kinetic energy of the jet increased with increased auxiliary jet velocity, the proportion of kinetic energy in the fluctuating components decreased with increasing auxiliary jet velocity. The POD analysis also showed that, for the main jet alone, the first two modes had significantly more kinetic energy than any other mode and contained large vortical structures that are known to be associated with the aeroacoustic feedback mechanism. The amplitude of those large vortical structures was found to reduce with increasing auxiliary jet velocity. Low-order reconstructions of selected flow fields allowed for the comparison of the oscillation of the multi-slot jet at different auxiliary jet velocities. The comparison of these select flow fields showed that at increased auxiliary jet velocities, the magnitude of the jet oscillation was reduced. Time-averaged PIV was used to observe the interaction of the main and auxiliary jet's velocity and vorticity for different auxiliary jet velocities. The PIV profiles show that the auxiliary jets reduce the maximum vorticity of the shear layer and result in a wider shear layer of the multi-slot jet both of which are known to reduce the maximum growth rate of disturbances in the shear layer.

6.2 Conclusions and Contributions

The initial hypothesis of this work was that the auxiliary jets could eliminate or suppress the aeroacoustic feedback mechanism of the impinging planar jet. This hypothesis has been borne out by the experimental results from which the following contributions have been made:

- The observed aeroacoustic feedback mechanism in the self-excited planar jet-plate oscillator can be diminished through the use of auxiliary planar jets to stabilise the jet shear layer.

  The essential component of the aeroacoustic feedback mechanism is the inherent instability of the intense shear layer at the nozzle exit of the jet [25], [27]. The velocity gradient of the shear layer is directly linked to the growth rate of instabilities as they propagate down the shear layer [12]. The reduction in the velocity gradient, as seen in the time-averaged PIV velocity fields, shows that the auxiliary jets were responsible for the reduction in the large-scale coherent structures seen in the POD analysis. As these coherent structures were responsible for the oscillation of the jet column and the acoustic tones produced, the reduction in the velocity gradient due to the auxiliary jets caused the reduction in the amplitude of both.

- The influence of auxiliary jets on the self-excited planar jet-plate oscillator is a function of the velocity ratio between the main and auxiliary jets.

  All the data presented in this thesis shows a general trend of a reduction in the amplitude of the acoustic tones and the jet column oscillations with increasing auxiliary jet velocity. The auxiliary jets significantly change the vorticity of the shear layer of the multi-slot jet resulting in lower maximum vorticity and thicker shear layers. These changes in the vorticity profile increase with increasing auxiliary jet velocity. These changes in the vorticity profile of the jet corresponding with reductions in the oscillations of the jet and amplitudes of the tones show that these phenomena are controllable through the use of the velocity of the auxiliary jets.

- The average tonal amplitude data showed a critical velocity ratio between the main and auxiliary jets.

  The average tonal amplitude data showed that above the velocity ratio between the main and auxiliary jets, V_A/V_M, of 0.4 the auxiliary jets had no further effect on the aeroacoustic feedback mechanism. The modes generated by the POD analysis agreed with this limit to a velocity ratio as the mode shapes had drastically changed in shape at that velocity ratio. This velocity ratio was similar to the velocity ratio of Sheplak and Spina [35–37] at which the acoustic tones of the jet were found to be reduced to the minimum value in their study: $V_A/V_M = 0.5$.

6.3 Future work

Several operating parameters of the multi-slot jet showed promise in their ability to affect the aeroacoustic feedback mechanism produced by the impinging planar jet. These operating parameters require further investigation to confirm the extent of their influence on the self-excited impinging planar jet.

- The setback distance, “s”

  The design of the multi-slot jet did not allow for the decoupling of the effect the two changes made to the jet-plate apparatus caused by changing the setback distance. Without any influence of the auxiliary jets, i.e. at V_A = 0 m/s, the tones produced by the multi-slot jet were found to be proportional to the setback distances; smaller setback distances producing more and larger amplitude tones. The acoustic results indicated that larger setback distances, which increased the development length of the auxiliary jet, resulted in larger reductions in the amplitude of the tones produced at the same auxiliary jet velocity. However, as the two effects of the setback distance cannot be separated, the influence of the setback distances on the reduction of acoustic tone amplitude due to the auxiliary jet velocity cannot be conclusively defined. As the data alludes to the auxiliary jets suppressing tones at lower auxiliary jet velocities for larger setback distances this avenue should be investigated further for practical applications.

- The auxiliary jet thickness, “a”

  Auxiliary jets with wider openings were found to suppress the aeroacoustic feedback mechanism more than smaller jet nozzle widths at the same auxiliary jet velocities. While it is almost certain that this is due to the larger auxiliary jet nozzles resulting in a further reduction in the velocity gradient of the shear layer, no PIV images were taken at larger auxiliary jet thicknesses to confirm this.

An interesting avenue of investigation that was not possible to be investigated as part of this thesis, due to the limitations of the multi-slot jet, is the relative angle between the main and auxiliary jets. This angle would have major influences on how the shear layers of the jets interact and could be exploited to result in the suppression of the aeroacoustic feedback mechanism at lower auxiliary jet velocities. The angle would also change the distance from the jet nozzle exit at which the jets merge which would allow for a more fundamental understanding of the mechanism involved in suppressing the aeroacoustic feedback mechanism.

REFERENCES

[1] S. M. A. Shibli, B. N. Meena, and R. Remya, “A review on recent approaches in the field of hot dip zinc galvanizing process,” *Surf. Coatings Technol.*, vol. 262, pp. 210–215, 2015.

[2] A. R. Marder, “The metallurgy of zinc-coated steel,” *Prog. Mater. Sci.*, vol. 45, no. 3, pp. 191–271, Jun. 2000.

[3] C. H. Ellen and C. V. Tu, “An analysis of jet stripping of liquid coatings,” *J. Fluids Eng.*, vol. 106, no. 4, p. 399, 1984.

[4] Canada Labour Code Part II (R.S.C. 1985 c. L-2), *Canada Occupational Safety and Health Regulations, (SOR/86-304)*. p. Section 7.4(b).

[5] C. Pfeiler, W. Eßl, G. Reiss, C. K. Riener, G. Angeli, and A. Kharicha, “Investigation of the gas-jet wiping process − Two-phase large eddy simulations elucidate impingement dynamics and wave formation on zinc coatings,” *Steel Res. Int.*, vol. 88, no. 9, pp. 1–10, 2017.

[6] A. D. Johnstone, B. Kosasih, L. Q. Phan, A. Dixon, and W. Renshaw, “Coating film profiles generated by fluctuating location of the wiping pressure and shear stress,” *ISIJ Int.*, vol. 59, no. 2, pp. 319–325, 2019.

[7] G.-Y. Kim, H.-D. Park, D.-E. Lee, and W.-C. Chung, “Gas wiping apparatus having multiple nozzles,” WO 2008/069362 A1, 2008.

[8] K. Myrillas, A. Gosset, P. Rambaud, M. Anderhuber, J. M. Mataigne, and J. M.

Buchlin, “Technique for delaying splashing in jet wiping process,” *Chem. Eng. Process. Process Intensif.*, vol. 50, no. 5–6, pp. 466–470, 2011.

[9] H. G. Yoon, G. J. Ahn, S. J. Kim, and M. K. Chung, “Aerodynamic investigation about the cause of check-mark stain of the galvanized steel surface,” *ISIJ Int.*, vol. 49, no. 11, pp. 1755–1761, 2009.

[10] P. Tamadonfar, J. R. McDermid, A. N. Hrymak, and F. E. Goodwin, “Numerical investigation of air knives with multiple-impinging slot jets in continuous hot-dip galvanizing,” *AISTech - Iron Steel Technol. Conf. Proc.*, no. June 2016, 2010.

[11] J. R. McDermid, S. Alibeigi, S. Ziada, and F. E. Goodwin, “Modelling and Measurement of Novel Air-Knife Designs,” in *106th Galvanizers Association Meeting*, 2014, pp. 1–11.

[12] P. A. Monkewitz and P. Huerre, “Influence of the velocity ratio on the spatial instability of mixing layers,” *Phys. Fluids*, vol. 25, no. 7, pp. 1137–1143, 1982.

[13] A. Michalke and G. Hermann, “On the inviscid instability of a circular jet with external flow,” *J. Fluid Mech.*, vol. 114, p. 343, Jan. 1982.

[14] L. Rayleigh, “On the stability, or instability, of certain fluid motions,” *Proc. London Math. Soc.*, vol. x, no. 4, pp. 57–72, 1879.

[15] A. Michalke, “On spatially growing disturbances in an inviscid shear layer,” *J. Fluid Mech.*, vol. 23, no. 3, pp. 521–544, 1965.

[16] P. Freymuth, “On transition in a separated laminar boundary layer,” *J. Fluid*

Mech., vol. 25, no. 04, pp. 683–704, Mar. 1965.

[17] R. W. Miksad, “Experiments on the nonlinear stages of free-shear-layer transition,” *J. Fluid Mech.*, vol. 56, no. 4, pp. 695–719, Mar. 1972.

[18] R. W. Miksad, “Experiments on nonlinear interactions in the transition of a free shear layer,” *J. Fluid Mech.*, vol. 59, no. 1, pp. 1–21, Mar. 1973.

[19] C.-M. Ho and L.-S. Huang, “Subharmonics and vortex merging in mixing layers,” *J. Fluid Mech.*, vol. 119, pp. 443–473, Jun. 1982.

[20] A. K. M. F. Hussain, “Coherent strucutres and turbulence,” *J. Fluid Mech.*, 1986.

[21] F. Hsiao and J. Huang, “On the evolution of instabilities in the near field of a plane jet,” *Phys. Fluids A Fluid Dyn.*, vol. 2, no. 3, pp. 400–412, Mar. 1990.

[22] D. Rockwell and E. Naudascher, “Self-sustained oscillations of impinging free shear layers,” *Annu. Rev. Fluid Mech.*, vol. 11, no. 1, pp. 67–94, Jan. 1979.

[23] A. H. Marsh, “Noise measurements around a subsonic air jet impinging on a plane, rigid surface,” *J. Acoust. Soc. Am.*, vol. 33, no. 8, pp. 1065–1066, Aug. 1961.

[24] F. R. Wagner, “The sound and flow field of an axially symmetric free jet upon impact on a wall,” 1971.

[25] C. Ho and N. Nosseir, “Dynamics of an impinging jet. Part 1. The feedback phenomenon,” *J. Fluid Mech.*, vol. 105, pp. 119–142, 1981.

[26] N. S. Nosseir and C.-M. Ho, “Dynamics of an impinging jet. Part 2. The noise

generation," *J. Fluid Mech.*, vol. 116, pp. 379–391, Apr. 1982.

[27] C. K. W. Tam and K. K. Ahuja, "Theoretical model of discrete tone generation by impinging jets," *J. Fluid Mech.*, vol. 214, pp. 67–87, 1990.

[28] P. Panickar and G. Raman, "Criteria for the existence of helical instabilities in subsonic impinging jets," *Phys. Fluids*, vol. 19, no. 10, p. 106103, 2007.

[29] P. Panickar and G. Raman, "Using linear stability analysis as a tool to evaluate jet and cavity flow control situations," *Int. J. Flow Control*, vol. 1, no. 1, pp. 43–72, Mar. 2009.

[30] D. Arthurs and S. Ziada, "The planar jet-plate oscillator," *J. Fluids Struct.*, vol. 27, no. 1, pp. 105–120, 2011.

[31] D. Arthurs and S. Ziada, "Self-excited oscillations of a high-speed impinging planar jet," *J. Fluids Struct.*, vol. 34, pp. 236–258, Oct. 2012.

[32] D. Arthurs and S. Ziada, "Development of a feedback model for the high-speed impinging planar jet," *Exp. Fluids*, vol. 55, no. 5, 2014.

[33] J. E. Rossiter, "Wind-tunnel experiments on the flow over rectangular cavities at subsonic and transonic speeds," 1964.

[34] W. Eßl, C. Pfeiler, G. Reiss, W. Ecker, C. K. Riener, and G. Angeli, "LES-VOF simulation and POD analysis of the gas-jet wiping process in continuous galvanizing lines," *Steel Res. Int.*, vol. 89, no. 2, pp. 3–10, 2018.

[35] M. Sheplak, "Passive control of impinging jet resonance," Syracuse University,

1992.

[36] M. Sheplak and E. Spina, “Elimination of impinging-jet resonance,” in *31st Aerospace Sciences Meeting*, 1993.

[37] M. Sheplak and E. F. Spina, “Control of high-speed impinging-jet resonance,” *AIAA J.*, vol. 32, no. 8, pp. 1583–1588, Aug. 1994.

[38] K. Ahuja and D. Dosanjh, “Heated fluid shroud as an acoustic shield for noise reduction - An experimental study,” in *4th Aeroacoustics Conference*, 1977, pp. 1–11.

[39] F. S. Alvi, R. Elavarasan, C. Shih, G. Garg, and A. Krothapalli, “Active control of supersonic impinging jets using microjets,” *AIAA J.*, pp. 1–13, 2000.

[40] H. Lou, F. S. Alvi, C. Shih, J. Choi, and A. Annaswamy, “Active control of supersonic impinging jets: Flowfield properties and closed-loop strategies,” *AIAA J.*, 2002.

[41] H. Lou, F. S. Alvi, and C. Shih, “Active and adaptive control of supersonic impinging jets,” *AIAA J.*, vol. 44, no. 1, pp. 58–66, Jan. 2006.

[42] F. S. Alvi, H. Lou, C. Shih, and R. Kumar, “Experimental study of physical mechanisms in the control of supersonic impinging jets using microjets,” *J. Fluid Mech.*, vol. 613, pp. 55–83, 2008.

[43] R. Kumar, A. Wiley, L. Venkatakrishnan, and F. Alvi, “Role of coherent structures in supersonic impinging jets,” *Phys. Fluids*, vol. 25, no. 7, 2013.

[44] H. G. Yoon and M. K. Chung, “Development of novel air-knife system to prevent check-mark stain on galvanized strip surface,” *ISIJ Int.*, vol. 50, no. 5, pp. 752–759, 2010.

[45] E. A. Elsaadawy, G. S. Hanumanth, A. K. S. Balthazaar, J. R. McDermid, A. N. Hrymak, and J. F. Forbes, “Coating weight model for the continuous hot-dip galvanizing process,” *Metall. Mater. Trans. B*, vol. 38, no. 3, pp. 413–424, 2007.

[46] G. Takeda, H. Takahashi, and K. Kabeya, “Jet flow characteristics of 3-slot nozzle at gas wiping process in continuous galvanizing line,” *Tak. Gentaro Tak. Hideyuki Kabeya, Kazuhisa*, vol. 57, no. 6, pp. 1087–1093, 2017.

[47] A. Yahyaee Soufiani, J. R. McDermid, A. N. Hrymak, and F. E. Goodwin, “Numerical investigation of multiple-slot jets in air-knife wiping,” *J. Coatings Technol. Res.*, vol. 14, no. 5, pp. 1015–1028, 2017.

[48] J. L. Lumley, “The structure of inhomogeneous turbulence,” in *Atmospheric Turbulence and Radio Wave Propagation, edited by A. M. Yaglom and V. I. Tatarski (Nauka, Moscow)*, 1967, pp. 166–178.

[49] H. P. Bakewell and J. L. Lumley, “Viscous sublayer and adjacent wall region in turbulent pipe flow,” *Phys. Fluids*, vol. 10, no. 9, pp. 1880–1889, 1967.

[50] D. Rempfer, “On the structure of dynamical systems describing the evolution of coherent structures in a convective boundary layer,” *Phys. Fluids*, vol. 6, no. 3, pp. 1402–1404, 1994.

[51] R. E. A. Arndt, D. F. Long, and M. N. Glauser, "The proper orthogonal decomposition of pressure fluctuations surrounding a turbulent jet," *J. Fluid Mech.*, vol. 340, pp. 1–33, Jun. 1997.

[52] J. Delville, L. Ukeiley, L. Cordier, J. P. Bonnet, and M. Glauser, "Examination of large-scale structures in a turbulent plane mixing layer. Part 1. Proper orthogonal decomposition," *J. Fluid Mech.*, vol. 391, pp. 91–122, 1999.

[53] J. H. Citriniti and W. K. George, "Reconstruction of the global velocity field in the axisymmetric mixing layer utilizing the proper orthogonal decomposition," *J. Fluid Mech.*, vol. 418, pp. 137–166, 2000.

[54] K. J. Hammad and I. M. Milanovic, "A POD study of an impinging jet flowfield," in *Volume 1: Symposia, Parts A, B and C*, 2009, pp. 1477–1485.

[55] S. Gadiraju *et al.*, "Application of proper orthogonal decomposition to high speed imaging for the study of combustion oscillations," in *Volume 4B: Combustion, Fuels and Emissions*, 2017, vol. 45, no. 2, p. V04BT04A031.

[56] S. Alibeigi, J. R. McDermid, S. Ziada, and F. E. Goodwin, "Effect of Air Knife Geometry on Coating Weight Control in the Continuous Galvanizing Line," *Galvatech 2013 9th Int. Conf. Zinc Zinc Alloy Coat. Steel Sheet 2nd Asia-Pacific Galvaniz. Conf.*, pp. 437–440, 2013.

[57] R. D. Mehta and P. Bradshaw, "Design rules for small low speed wind tunnels," *Aeronaut. J.*, vol. 83, no. 827, pp. 443–453, 1979.

[58] S. Alibeigi, "Experimental Investigation of Air-Knife Geometry in Continuous Hot-Dip Galvanizing," McMaster University, 2013.

[59] A. Melling, "Tracer particles and seeding for particle image velocimetry," *Meas. Sci. Technol.*, vol. 8, no. 12, pp. 1406–1416, 1997.

[60] K. Fukunaga, *Introduction to Statistical Pattern Stastical Pattern Recognition*. 1990.

[61] F. Chen, H. Liu, Z. Yang, and H. Hu, "Tracking characteristics of tracer particles for PIV measurements in supersonic flows," *Chinese J. Aeronaut.*, vol. 30, no. 2, pp. 577–585, 2017.

[62] S. K. Mylona, M. J. Assael, K. D. Antoniadis, S. K. Polymatidou, and L. Karagiannidis, "Measurements of the viscosity of Bis(2-ethylhexyl) sebacate, squalane, and bis(2-ethylhexyl) phthalate between (283 and 363) K at 0.1 MPa," *J. Chem. Eng. Data*, vol. 58, no. 10, pp. 2805–2808, 2013.

Appendix A
Uncertainty Analysis

A.1 Pressure

Two kinds of pressure measurements were reported in this thesis: static pressure and fluctuating pressure. The static pressure was measured in the jet's plenums to calculate the velocity of the jet, on the impingement plate to ascertain the pressure profile created by the jet and using the simple Pitot tube to measure the velocity of the jet directly. Fluctuating pressure was measured on the impingement plate to measure the fluctuations of the pressure due to the jet oscillation.

The static pressure measurements were made with a Validyne DP 15 pressure transducer coupled with a Validyne CD23 carrier demodulator. The DP15 pressure transducer has a stated accuracy of 0.5% over the full scale output and the CD23 carrier demodulator has a frequency response stability of 0.1% over the full scale output. The standard deviation of the pressure was measured to be ±0.33 kPa over all experimental jet velocities. The pressure transducers measured the pressure relative to the atmospheric pressure in the room, which was monitored using a standing digital barometer and the maximum fluctuations were found to be ±0.25 kPa. These sources of error compound to result in an average error of 0.0082 kPa/kPa for a pressure measurement in the plenum of a 250 m/s jet.

The fluctuating pressure measurements were captured with a PCB model 112A21 ICP pressure sensor coupled with a Kistler 4 Channel Piezoelectric Sensor Power Supply and Signal Conditioner. The sensor resolution was 14 Pa with a sensitivity 7.25 mV/kPa which was further improved with an in-built low-noise amplifier to a resolution of 7 Pa. This resolution resulted in an error of 0.145%, 0.700% and 1.650% for the peak value of the fluctuating pressure profiles of the 0 m/s, 60 m/s and 100 m/s auxiliary jet velocity cases.

A.2 Velocity

The velocity of the jets in this investigation were calculated from pressure measurements in the plenum chambers for each jet. The calculation of the velocity was made using equation A.1 derived for compressible flow through an isentropic nozzle [A.1].

$$U = c \cdot \eta \cdot \sqrt{\frac{2}{\gamma - 1}\left[\left(\frac{P_S + P_\infty}{P_\infty}\right)^{\left(\gamma-1/\gamma\right)} - 1\right]} \qquad \text{(A.2)}$$

In the above equation "U" is the velocity of the jet, "c" is the speed of sound, "η" is the isentropic efficiency of the jet, "γ" is the ratio of specific heats of air and "P_S" and "P_∞" are the plenum and ambient pressures, respectively.

The isentropic efficiency of the nozzles of the multi-slot jet were measured by comparing the pressure measured inside the plenum to the pressure in the jet column measured using a simple pitot tube. The main jet nozzle efficiency was found to be η = 0.989 and the auxiliary jet nozzles were found to be of a slightly lower efficiency at η = 0.963. The air used in the experiment was assumed to behave as an ideal gas with a constant ratio of specific heats of γ = 1.4.

The uncertainty of the calculated jet velocity was determined using the Kline and McClintock method [A.2] where the uncertainty of the dependent variable is equal to the sum of the square of the uncertainties associated with each independent variable, as outlined in equation A.2:

$$\delta Y = \sqrt{\sum_{i=1}^{n}\left(\frac{\partial Y}{\partial X_i}\delta X_i\right)^2} \tag{A.2}$$

Applying this method for calculating the uncertainty, the contribution of the uncertainty of the measured pressures to the uncertainty of the jet velocity measurement was calculated with formulas A.3 and A.4 and found to be, on average, 0.382% of the measured velocity.

$$\delta U = \sqrt{\left(\frac{\partial U}{\partial P_S}\delta P_S\right)^2 + \left(\frac{\partial U}{\partial P_\infty}\delta P_\infty\right)^2} \tag{A.3}$$

$$\partial U = \sqrt{\frac{c^2(\gamma-1)\left(\frac{P_S+P_\infty}{P_\infty}\right)^{\frac{-2}{\gamma}}}{2\gamma^2 {P_\infty}^2\left[\left(\frac{P_S+P_\infty}{P_\infty}\right)^{\frac{\gamma-1}{\gamma}}-1\right]}\left[\frac{{\delta P_S}^2{P_\infty}^2+{\delta P_\infty}^2{P_S}^2}{{P_\infty}^2}\right]} \tag{A.4}$$

Formula A.4 predicts an error of 1.12 m/s in calculating the velocity of a 250 m/s jet from the main jet plenum pressure resulting in a relative error of 0.45%.

A.3 Acoustics

Acoustics measurements were made with a GRAS 40BP condenser microphone coupled with a GRAS 26AB pre-amplifier and GRAS 12AA power supply. The microphone has a stated flat frequency response from 10 Hz-25 kHz of ±1 db. The microphones were calibrated using a GRAS 42AB pistonphone. The data acquisition of the acoustic signals was performed using a National Instruments PCI 4452 card with a maximum sample rate of 204.8 kS/s. The microphone and transducers communicated to the data acquisition card via a NI BNC 2140 signal conditioner.

The acoustic data for this investigation was acquired as a pressure-time signal of 50 continuous acquisitions of 204,800 samples with no overlap. The amplitude spectra of RMS acoustic pressure for each of the 50 sections were calculated individually. The 50 spectra were averaged to produce an average acoustic spectrum for each data point reported in this thesis.

The combined uncertainties of the measurement equipment correspond to an uncertainty of the RMS pressure amplitudes of 3%. As a result of Fast-Fourier Transforms being applied to 1 second samples of the microphone signal, the resolution of the frequency content is within ±0.5 Hz.

A.4 PIV Error

The contour plots of velocity and the extracted cross-sections are averages of 400 PIV images. The camera CCD chip has 2048×2048 pixel sensors which result in a resolution of 75 px/mm for the PIV images. The time delay between the two laser pulses was controlled using a TSI LaserPulse 610035 synchroniser and, for the PIV images, was 2×10^{-7} seconds.

Two types of errors are associated with the displacement of the fluid captured by the PIV: the error due to the signal to noise ratio of the cross-correlation functions used to calculate the displacement of the fluid and the error associated with the ability of the spatial resolution of the image to capture the displacement and gradient of the fluid.

Charonko and Vlachos [A.3] performed work on synthetic and experimental flows to ascertain a correlation between the cross-correlation peak ratio and the standard deviation of displacement error in PIV imaging. The cross-correlation peak ratio of the PIV analysis (CPR) is a measure of the ratio of the height of the largest correlation peak to the second highest, and can be considered a measure of the signal to noise ratio of the correlation function used to calculate the displacement of the fluid. Equation A.5 is their correlation between the CPR and the uncertainty of the displacement magnitude. The CPR value used in the calculation was an average of CPR values extracted at random from 50 PIV images. The displacement error used in the calculation is the error reduced to the averaging of the 400 images.

$$\widehat{\varepsilon_U}^2 = \left(13.1 \times e^{-\frac{1}{2}\left(\frac{CPR-1}{0.317}\right)^2}\right)^2 + (0.226 \times CPR^{-1})^2 + (0.08)^2 \tag{A.5}$$

The displacement error due to the velocity gradient and the spatial resolution of the image was based on the work by Scarano and Riethmuller [A.4]. The displacement error was calculated using their data based on the maximum pixel displacement gradient of the flow in the time-averaged PIV images. The velocity gradient error was calculated using equation A.6 where the factor of 0.7 is used to account for the uncertainty of the central differencing scheme used to calculate the velocity gradient per Raffel et. al [A.5].

$$\varepsilon_{\left(\frac{\delta U}{\delta Y}\right)} = \frac{0.7 \times \varepsilon_U}{\Delta Y} \tag{A.6}$$

Figure A.1 is a contour plot of the time-averaged velocity magnitude of the 0 m/s auxiliary jet velocity case. The plots of the velocity magnitude have been extracted from the image at the indicated dashed white lines and inset alongside the contour plot. The maximum gradient of those

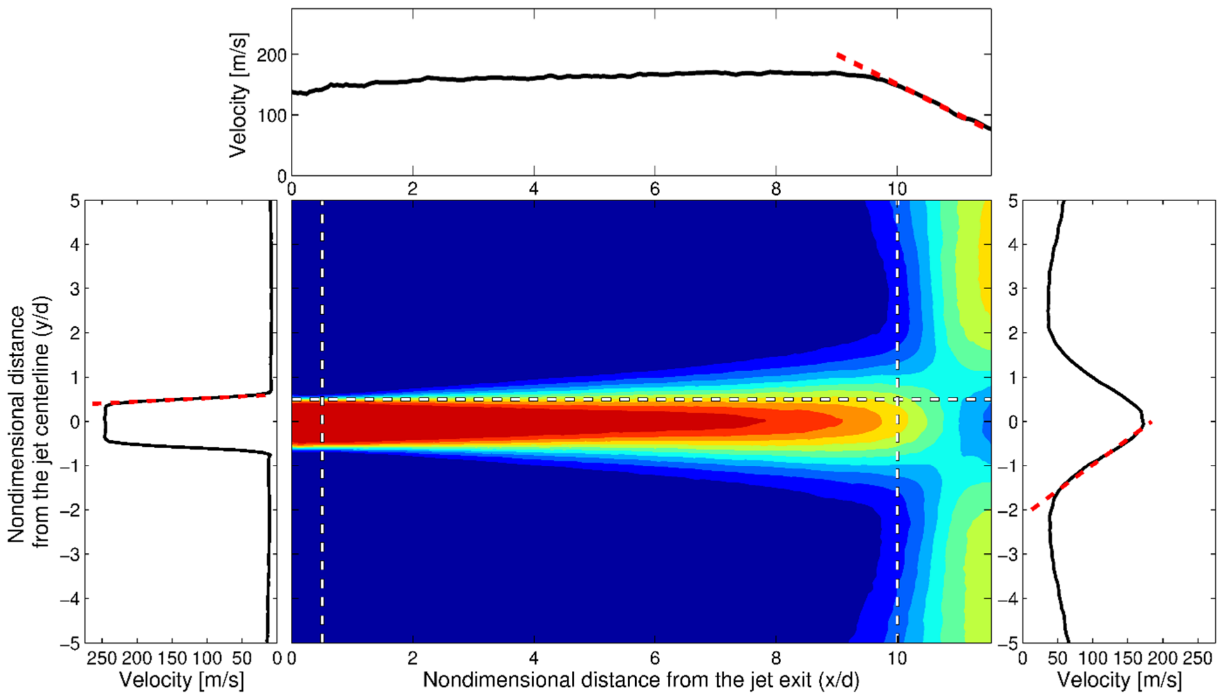

Figure A.1 Contour plot of the time-averaged velocity magnitude of the impinging planar jet. V_M = 250 m/s, d = 2 mm, V_A = 0 m/s, s = 5 mm, h/d = 12. The surrounding plots are the velocity magnitude corresponding to the white dashed lines overlaid on the contour plot. The maximum velocity gradients of those plots are indicated with dashed red lines.

plots are indicated as the dashed red lines. The error of the velocity and velocity gradient reported at these locations of maximum gradient were calculated and tabulated in Table A.. Table A. contains the same calculations of velocity and velocity gradient error made for the 100 m/s auxiliary jet velocity case at the maximum gradient of the same profile locations x/d = 0.5, 10 and y/x = 0.5.

The profiles of velocity and velocity gradient for the 0 m/s auxiliary jet velocity case are also plotted in Figure A.2. The error bar for each measured data point is plotted on the velocity and velocity gradient profiles. It can be seen in Figure A.2 that the velocity error and the velocity gradient error are so small as to be hidden by the profile line for the velocity for most data points.

Table A.1 PIV error calculations for the maximum gradients at the indicated locations for the 0 m/s and 100 m/s auxiliary jet velocity case.

		V_A = 0 m/s			V_A = 100 m/s		
		x/d = 0.5	x/d = 10	y/d = 0.5	x/d = 0.5	x/d = 10	y/d = 0.5
Displacement Gradient	px/px	0.1071	0.0119	0.00102	0.1133	0.015	0.002
Displacement Error (Spatial Resolution)	px/px	0.0058	0.00106	0.00043	0.00608	0.00122	0.00037
Average Cross-correlation Peak Ratio		5.3056	5.3056	5.3056	5.3625	5.3625	5.3625
Displacement Error (CPR)	px/px	0.0906	0.0906	0.0906	0.0904	0.0904	0.0904
Averaged Displacement Error (CPR)	px/px	0.0045	0.0045	0.0045	0.0045	0.0045	0.0045
Combined Displacement Error	px/px	0.0074	0.0047	0.0046	0.0076	0.0047	0.0045
Relative Velocity Error		0.30%	0.34%	3.36%	0.32%	0.20%	5.07%
Velocity	m/s	161.77	92.16	9.04	157.67	154.75	5.96
Velocity Error	m/s	0.4907	0.3103	0.3035	0.5051	0.3122	0.3024
Absolute Velocity Gradient Error	px/px	0.215 $\times10^{-3}$	0.136 $\times10^{-3}$	0.133 $\times10^{-3}$	0.222 $\times10^{-3}$	0.137 $\times10^{-3}$	0.133 $\times10^{-3}$
Relative Velocity Gradient Error		0.20%	1.14%	13.05%	0.20%	0.91%	6.63%
Velocity Gradient	(m/s)/m	535.7k	59.6k	5.1k	566.3k	75.2k	10.0k
Velocity Gradient Error	(m/s)/m	1076.4	681.6	665.5	1107.3	686.4	663.2

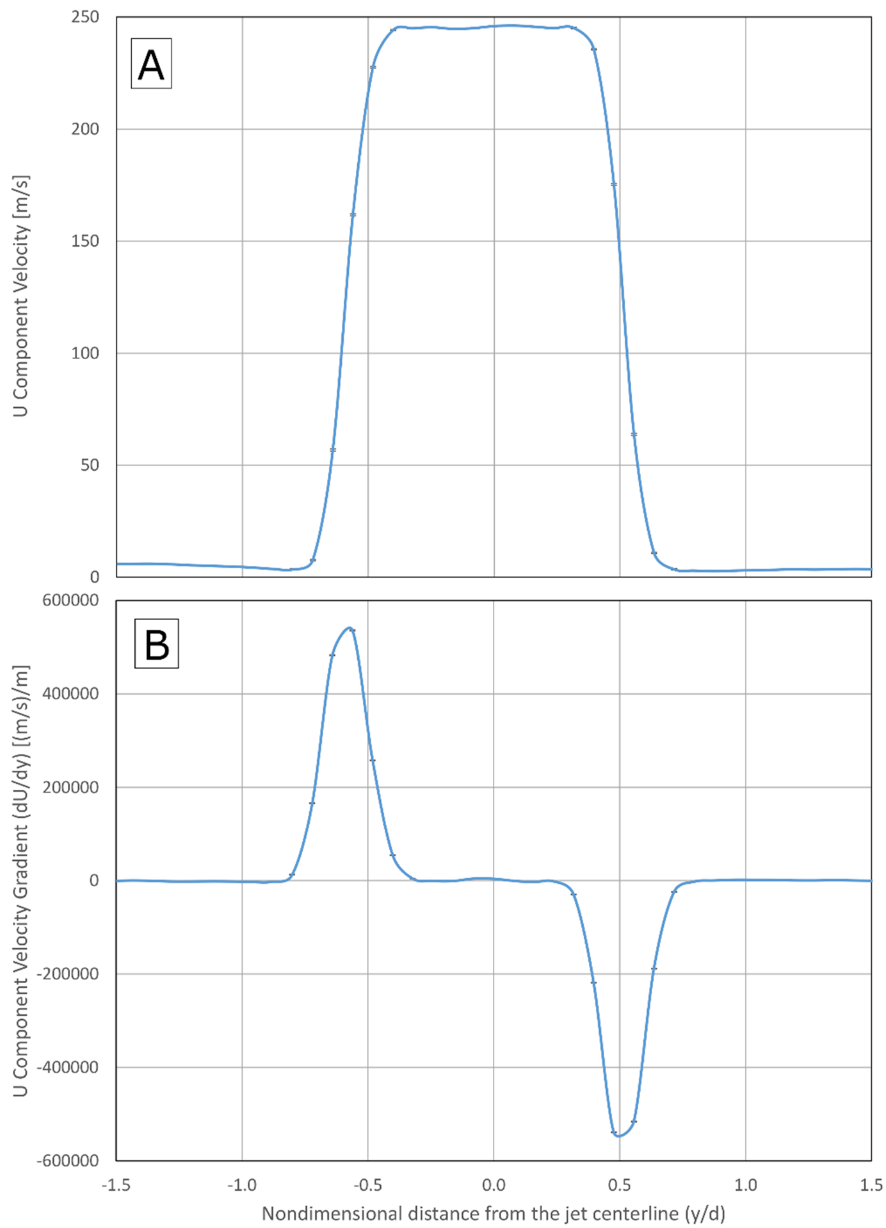

Figure A.2 Profiles of the U-component velocity (A) and U-component velocity gradient (B) of the 0 m/s auxiliary jet velocity case at x/d = 0.5. Error bars are indicate the velocity and velocity gradient error in the profiles.

Appendix B
Particle Image Velocimetry Calibration

During the course of this work it was determined that the particle induced velocimetry (PIV) technique did not accurately report high velocity flows. Velocity fields of the multiple-slot jet for high main jet speeds (e.g. 250 m/s) and lower auxiliary jet velocities (e.g. 60 m/s) accurately reported the auxiliary jet velocity but the main jet velocities were consistently lower than those determined using direct measurements – e.g. simple Pitot tubes. The pressure measurements using the Pitot tube were made using the DP15 Validyne pressure transducer and CD23 carrier demodulator and were further confirmed by direct pressure measurements using both an Omega PCL240 and Crystal IS33 pressure calibrator.

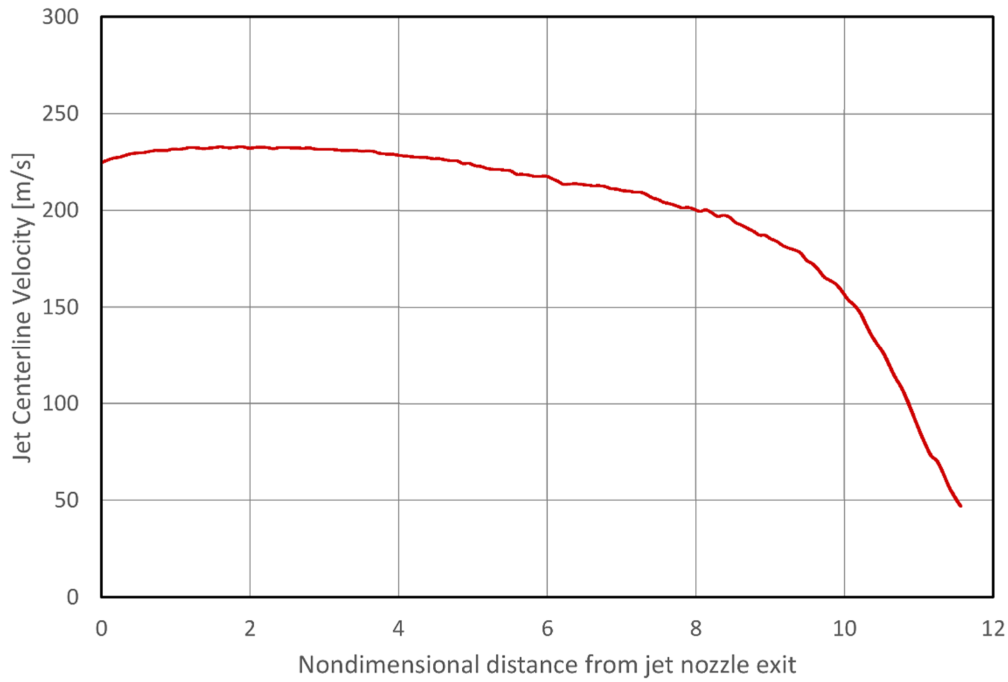

Figure B.3 Jet centerline velocity of the main jet alone of the multi-slot jet measured by the P.I.V.. V_M = 250 m/s, d = 2 mm, V_A = 0 m/s, s = 5 mm, h/d = 12.

The jet centerline velocity of the jet column for a main jet velocity of 250 m/s of the multi-slot jet is plotted in Figure B.1, showing that the velocity reported by the PIV was consistently lower than the jet velocity measured using the plenum pressure.

Figure B.2 shows the velocity of the jet potential core as measured by the PIV plotted against the velocity as measured by the Pitot tube for different main jet velocities. The solid line in the figure indicates where the data points should lie if both measurement methods resulted in the same velocities. The contour plot insert in Figure B.2 has a black box indicating the area over which the vectors were averaged to measure the potential core velocity. The velocity vectors in this area were essentially uniform velocity and unidirectional. For each PIV velocity data point in Figure B.2 the potential core velocity of 100 images were averaged.

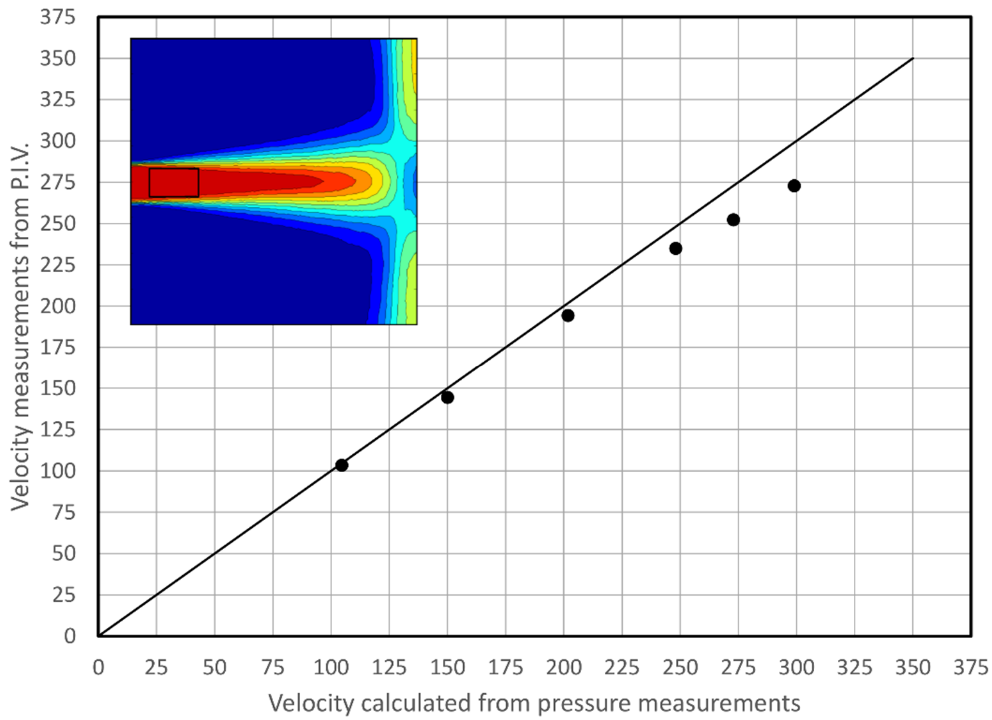

Figure B.2 Jet velocity measured with PIV vs Pitot tube (solid circles). The solid line indicates where data points would be if measurements agreed. Inset is a contour plot of velocity with a square indicating area over which PIV velocities are averaged.

As the Insight 4G software did not flag these incorrect velocity vectors generated as “bad vectors”, it indicates that they were not a result of insufficient illumination of the field by the laser sheet or improper seeding of the flow. If the flow was not two-dimensional, particles from above or below the laser sheet could enter the illuminated field and affect the cross-correlation method used to calculate the movement of particles. However, the introduction of new particles would result in a degree of randomness of the direction and magnitude of the vectors as the cross-correlation technique interprets their appearance. The incorrect vectors were consistent in both direction and magnitude indicating that this error was not due to out of plane motion of the flow.

The lower velocity measured by the PIV could be due to the seeding particles not accurately following the flow due to particle slip or lag [59], [61]. Particle slip and lag are due to the mass of the particle causing the seeding to not react in real time with the flow. Particle lag is most commonly a concern where the fluid experiences an acceleration or a change of direction. As the lower velocity vectors were found in the potential core of the jet, particle lag would not normally be a concern as it is an area of near constant velocity.

Particle velocity calculations for a particle in a flow were performed using equation B.1 for the relaxation time of the particle in the flow and equation B.2 for the particle velocity based on the relaxation time.

$$\tau = \frac{d^2\rho}{18\mu} \tag{B.1}$$

$$U_{Particle} = U_{Flow}\left(1 - e^{-t/\tau}\right) \tag{B.2}$$

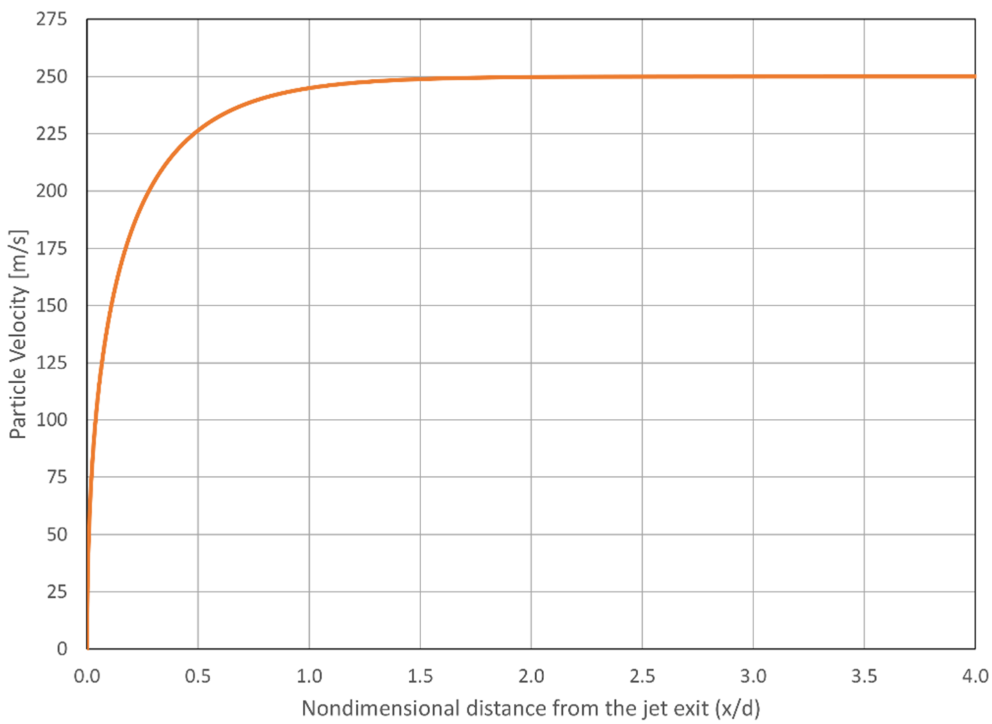

Figure B.3 Velocity of a 1μm particle of bis(2-ethylhexyl) sebacate in a constant 250 m/s velocity air flow.

In equations B.1 the diameter, “d”, and density, “ρ”, are the properties of the particle while the viscosity is the fluid viscosity; these quantities were assigned values of 1μm, 910 kg/m and 1.85x10^{-5} Pa.s [62], respectively. Figure B.3 shows the velocity of a seeding particle calculated using equations B.1 and B.2. For the purposes of the velocity calculations the seeding particle was initially assumed to be 0 m/s immediately at the jet exit. This is not physical as the flow of the jet accelerates through the nozzle and exits at the velocity of the potential core, but this assumption provides a conservative estimate as to the reaction of the particle. As shown in Figure B.3, a seeding particle in a constant 250 m/s velocity flow reaches the velocity of the flow within 2 nozzle widths, i.e. 4 mm, from the jet exit. This indicates that the erroneous vectors were not due to particle lag as they persisted over the full length of the potential core of the jet which can be seen in Figure B.1 to least 4-6 nozzle widths.

As the source of the error of the velocity measurement was not identifiable, the PIV data was calibrated using a simple pitot tube: the data presented in Figure B.2.. A second order polynomial was fit to the data with an R-squared value of 0.9994 and is presented as equation B.3. This equation converts the magnitude of the vector from the lower value reported by the PIV to the value measured by the simple Pitot tube.

$$Vel_{Calib} = 9.36 \times 10^{-4} \times {Vel_{PIV}}^{2} + 9.70 \times 10^{-1} \times Vel_{PIV} + 2.47 \tag{B.3}$$

The vector fields returned from the Insight 4G program are returned as two separate fields of both “U” and “V” velocity components. The calibration equation was applied to all the individual vectors of both component velocity fields that were greater than 100 m/s. These corrected velocity fields were then used for the data presented in this thesis. The results of the corrected velocity vectors are presented in Figure B.4 as the jet centerline velocity of a 250 m/s jet alongside the original jet centerline velocity. The figure shows that the calibration method can correctly scale the velocity to the expected value, as measured using the pressure using the Pitot tube.

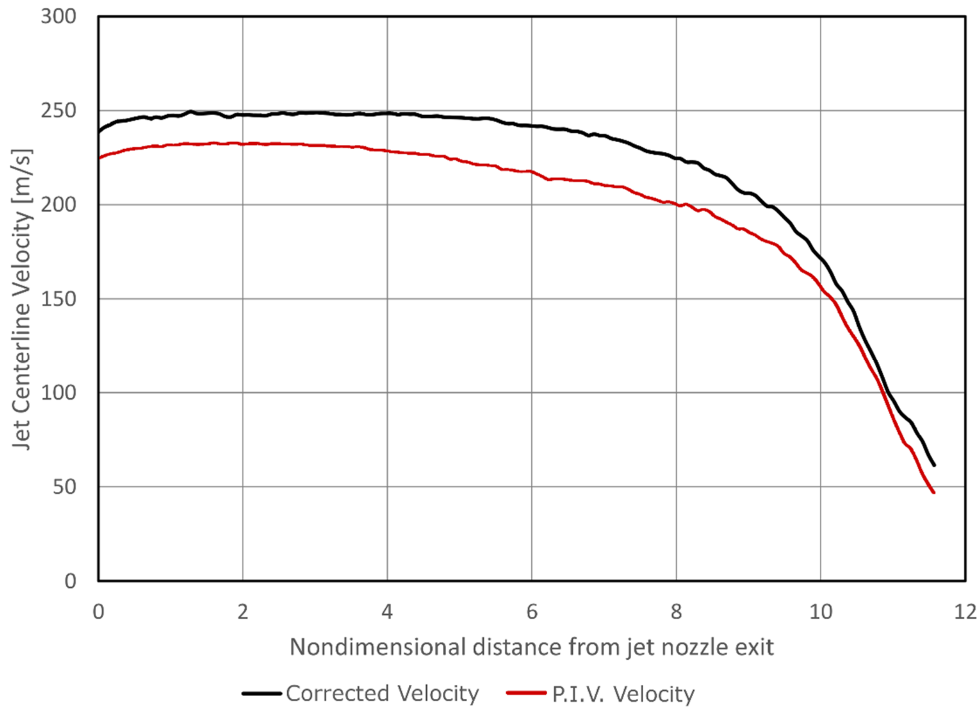

Figure B.4 Jet centerline velocity of the main jet alone of the multi-slot jet measured by the PIV plotted against the velocity of the PIV corrected using equation B.3. VM = 250 m/s, d = 2 mm, VA = 0 m/s, s = 5 mm, h/d = 12.

Appendix C

P.O.D. Analysis

A proper orthogonal decomposition for each individual auxiliary jet velocity case was performed with 400 PIV velocity vector fields taken at random. These PIV snapshots are taken in the center of the span of the planar jet with the experimental apparatus in Chapter 3. The conditioning of the PIV vector fields was performed as laid out in Chapter 3.

C.1 POD Code

```
%The number of snapshots you want to use
num_images = 400;

% Create matrix with all U and V velocity components for
% each snapshot in a column
% This assumes the U and V components are already in a 2D matrix
for k = 1:num_images
    Uf(:,k) = [reshape(U(:,:,k),[],1);reshape(V(:,:,k),[],1)];
end

% Not removing the mean velocity (this returns the mean velocity as the
1st
% mode)
Uall = Uf;

% % Removing the mean velocity to converts this matrix into the velocity
% % fluctuations of the snapshots (this analysis will not return a mean
% % velocity)
% Uall = bsxfun(@minus,Uf,mean(Uf,2));

% Create the Autocovariance matrix
R=Uall'*Uall;
% produces a diagonal matrix D of eigenvalues and a full matrix eV whose
% columns are the corresponding eigenvectors so that R*eV = eV*D.
[eV,D]=eig(R);
% sort eigenvalues in order of ascending magnitude
[L,M]=sort(diag(D));
% sort eigenvectors in the same order as eigenvalues
for i=1:length(D)
    eValue(length(D)+1-i)=L(i); % Store sorted eigenvalues in a new
matrix
```

```
    eVec(:,length(D)+1-i)=eV(:,M(i)); % Sort eigenvectors in a new
matrix
end;
% calculate the relative energy associated with each mode
menergy=eValue/sum(eValue);

% calculate the modes, "phi", from the eigenvectors and Autocovariance
matrix
for i=1:num_images
    phi(:,i)=Uall*eVec(:,i);
end;

% create low order reconstructions of the supplied snapshots of the
system
Nrec = 3; %number of modes with which to generate the reconstruction
% creating an empty array
phiRec = zeros(size(phi));
% filling that array with only the modes to use for the reconstruction
phiRec(:,1:Nrec) = phi(:,1:Nrec);
% creating the low order reconstructions of the supplied snapshots
for i = 1:1:num_images
    Urec(:,i) = phiRec*eVec(i,:)';
end
```

Appendix D

Acoustic Waterfall Plots

The following section contains the waterfall plots for the acoustic data presented in this thesis. The first section contains enlarged waterfall plots from Figures 4.6 and 4.7. The next three sections contain waterfall plots of the data used in Figures 4.8, 4.9 and 4.10.

<u>Data of thesis base case:</u>

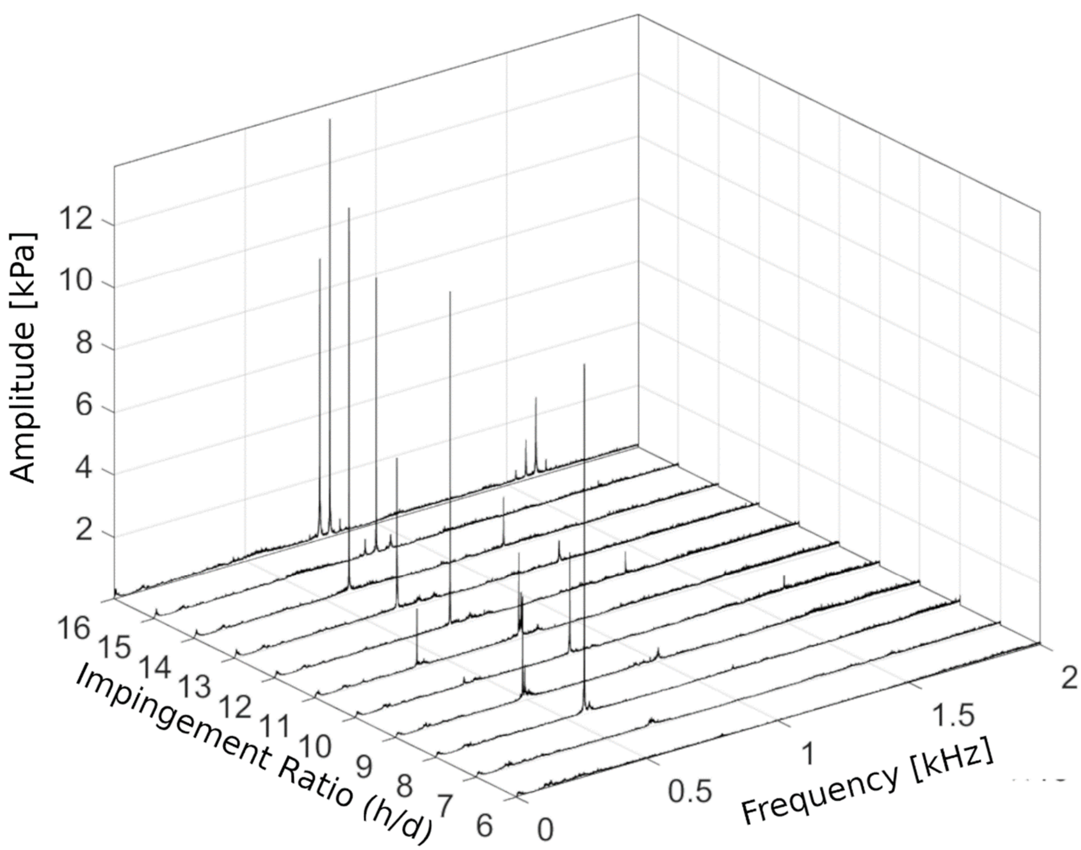

Figure D.1 Waterfall plot of sound produced by multi-slot jet main jet impinging on a flat plate. V_M = 250 m/s, d = 2 mm, V_A = 0 m/s, a = 1 mm, s = 5 mm.

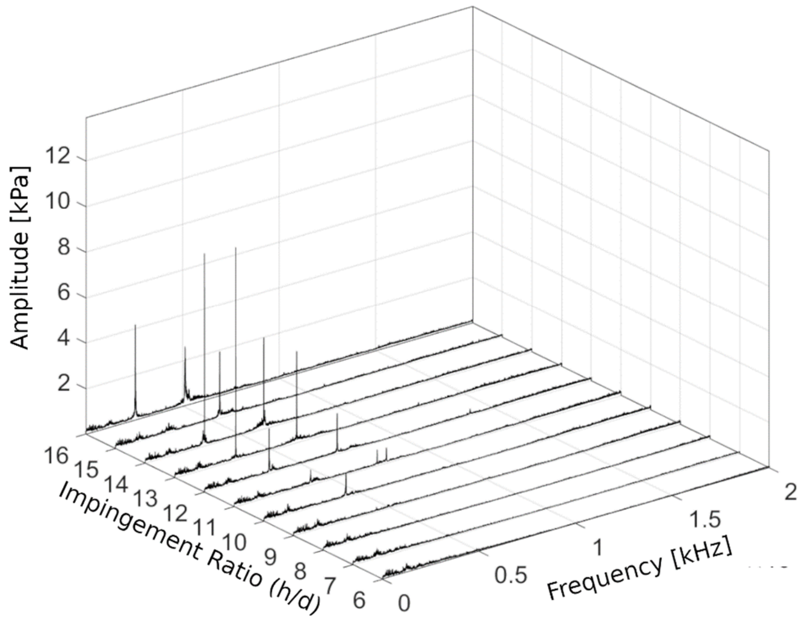

Figure D.2 Waterfall plot of sound produced by multi-slot jet main jet impinging on a flat plate. V_M = 250 m/s, d = 2 mm, V_A = 40 m/s, a = 1 mm, s = 5 mm.

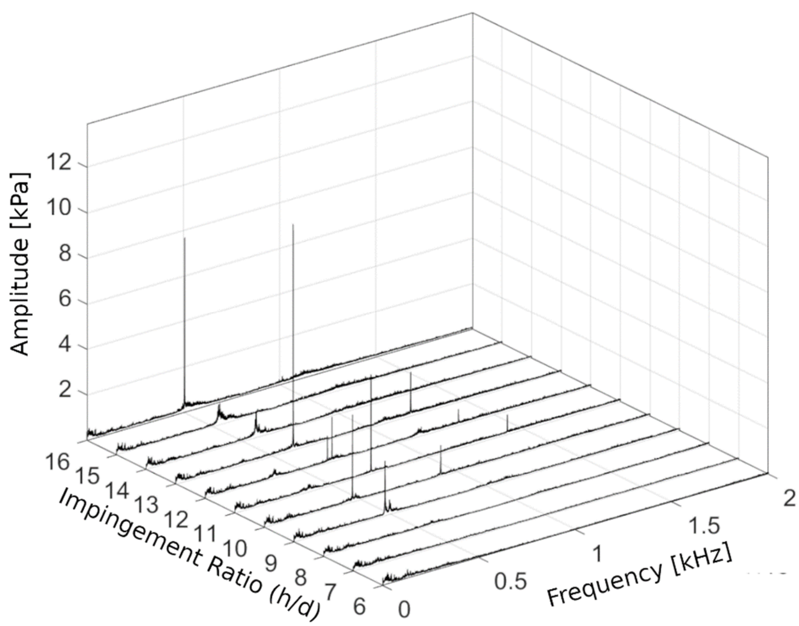

Figure D.3 Waterfall plot of sound produced by multi-slot jet main jet impinging on a flat plate. V_M = 250 m/s, d = 2 mm, V_A = 60 m/s, a = 1 mm, s = 5 mm.

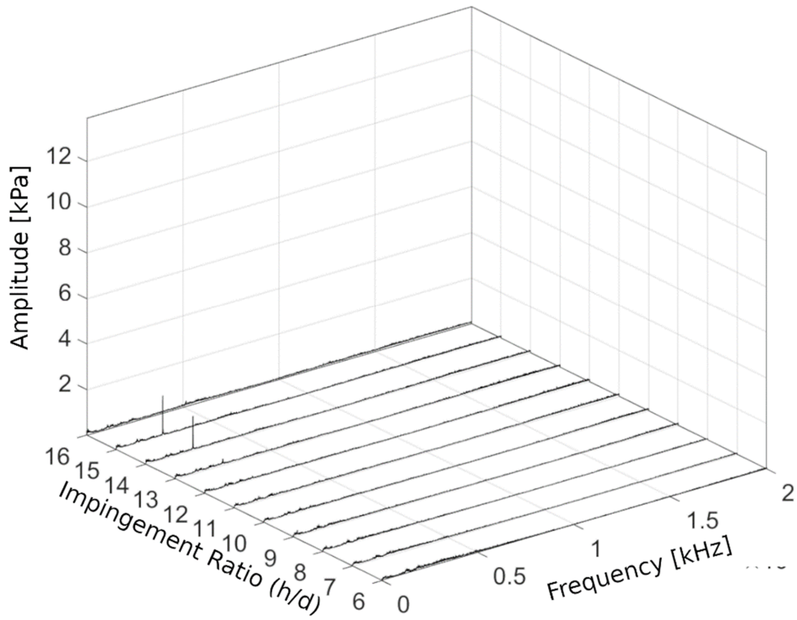

Figure D.4 Waterfall plot of sound produced by multi-slot jet main jet impinging on a flat plate. V_M = 250 m/s, d = 2 mm, V_A = 80 m/s, a = 1 mm, s = 5 mm.

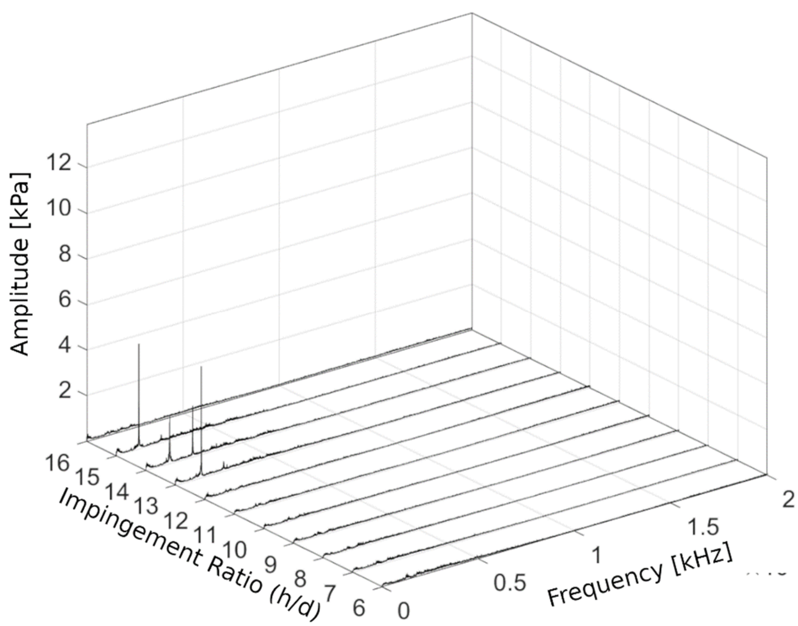

Figure D.5 Waterfall plot of sound produced by multi-slot jet main jet impinging on a flat plate. V_M = 250 m/s, d = 2 mm, V_A = 100 m/s, a = 1 mm, s = 5 mm.

Data from Figure 4.8 showing the effect of V_M:

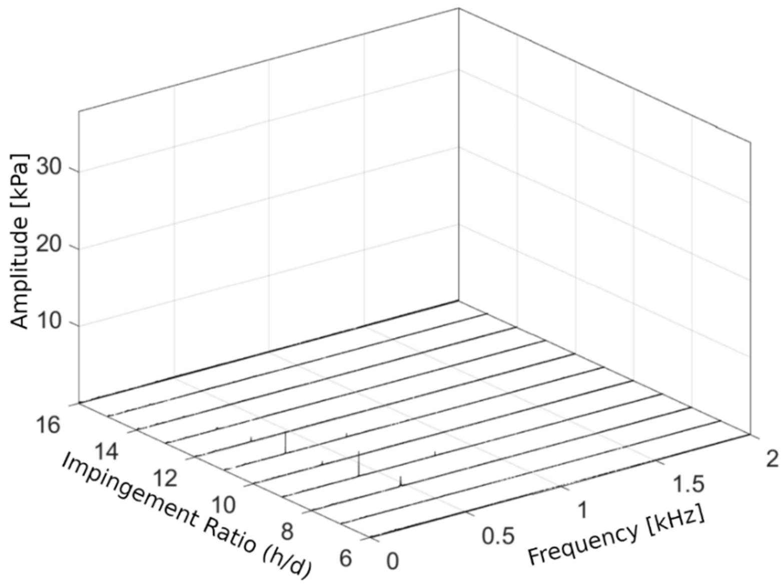

Figure D.6 Waterfall plot of sound produced by multi-slot jet main jet impinging on a flat plate. V_M = 200 m/s, d = 2 mm, V_A = 0 m/s, a = 1 mm, s = 5 mm.

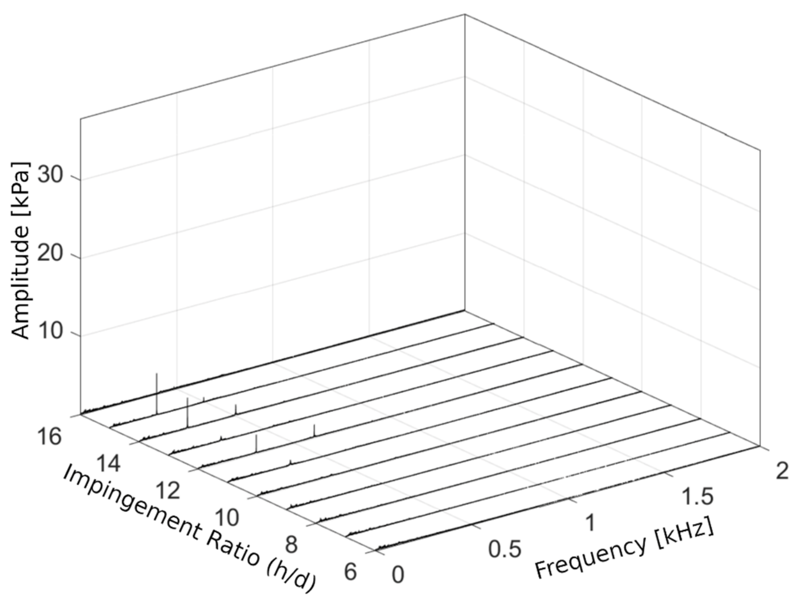

Figure D.7 Waterfall plot of sound produced by multi-slot jet main jet impinging on a flat plate. V_M = 200 m/s, d = 2 mm, V_A = 30 m/s, a = 1 mm, s = 5 mm.

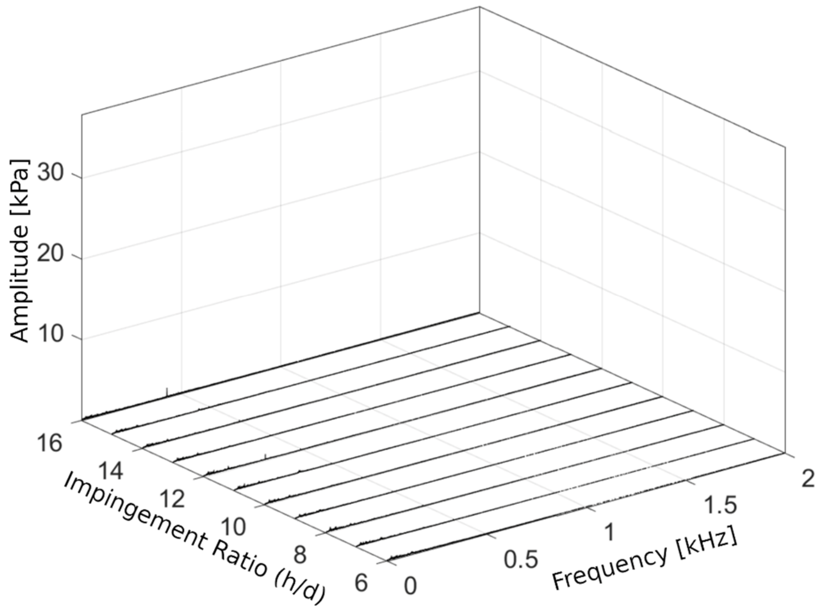

Figure D.8 Waterfall plot of sound produced by multi-slot jet main jet impinging on a flat plate. V_M = 200 m/s, d = 2 mm, V_A = 50 m/s, a = 1 mm, s = 5 mm.

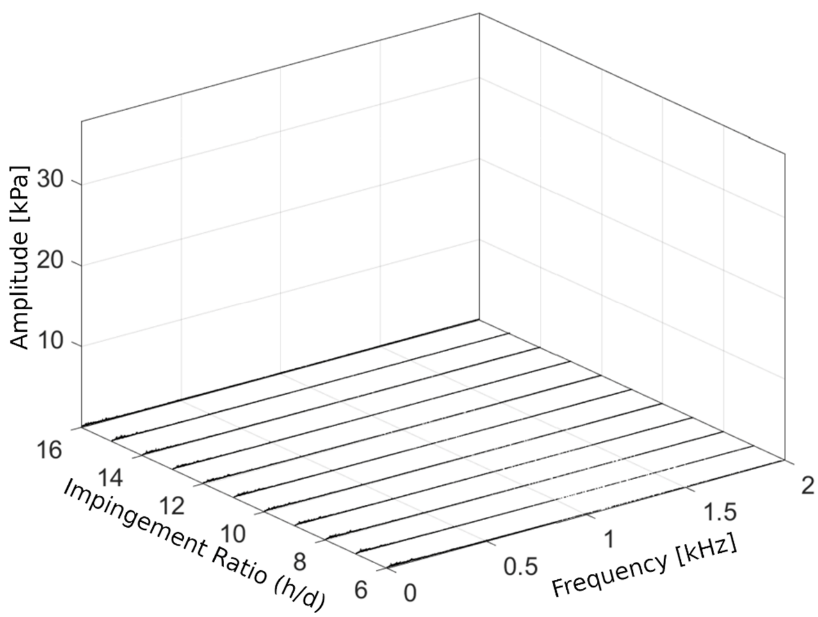

Figure D.9 Waterfall plot of sound produced by multi-slot jet main jet impinging on a flat plate. V_M = 200 m/s, d = 2 mm, V_A = 65 m/s, a = 1 mm, s = 5 mm.

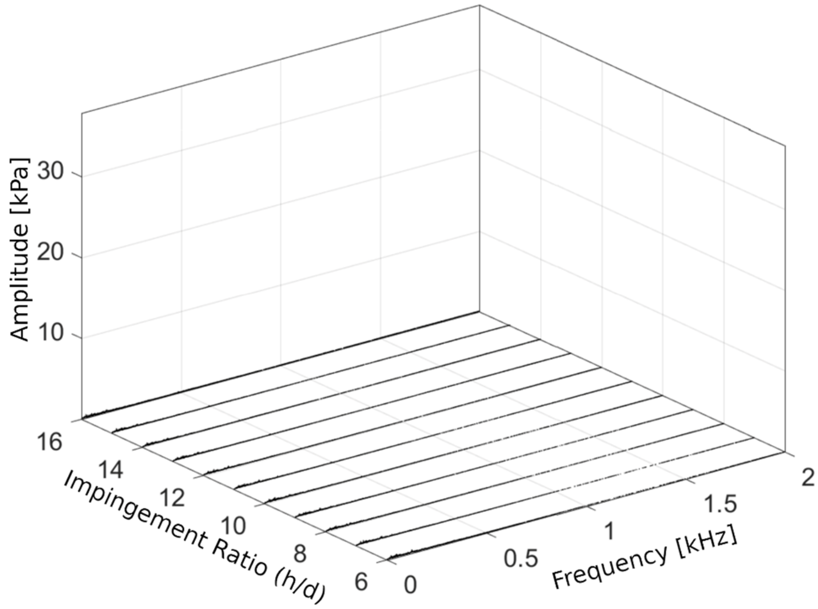

Figure D.10 Waterfall plot of sound produced by multi-slot jet main jet impinging on a flat plate. V_M = 200 m/s, d = 2 mm, V_A = 80 m/s, a = 1 mm, s = 5 mm.

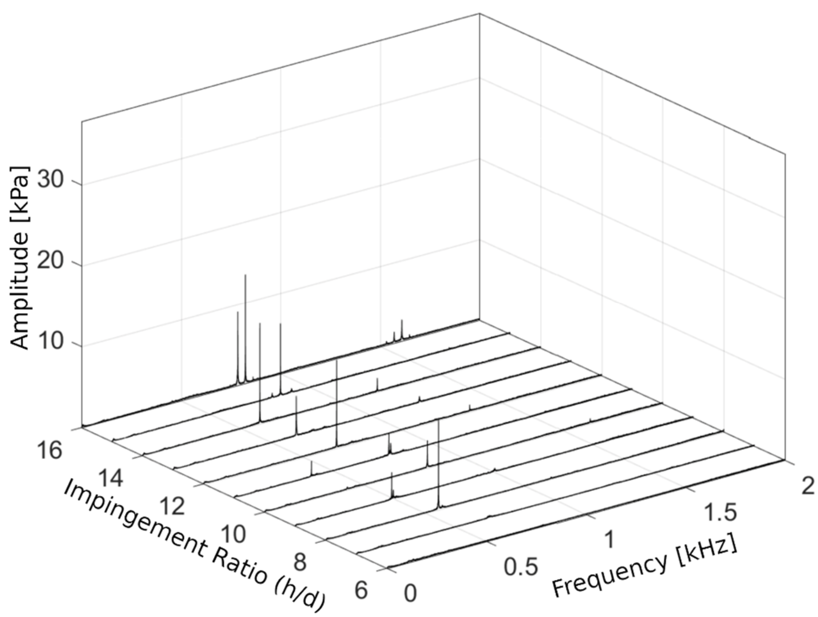

Figure D.11 Waterfall plot of sound produced by multi-slot jet main jet impinging on a flat plate. V_M = 250 m/s, d = 2 mm, V_A = 0 m/s, a = 1 mm, s = 5 mm.

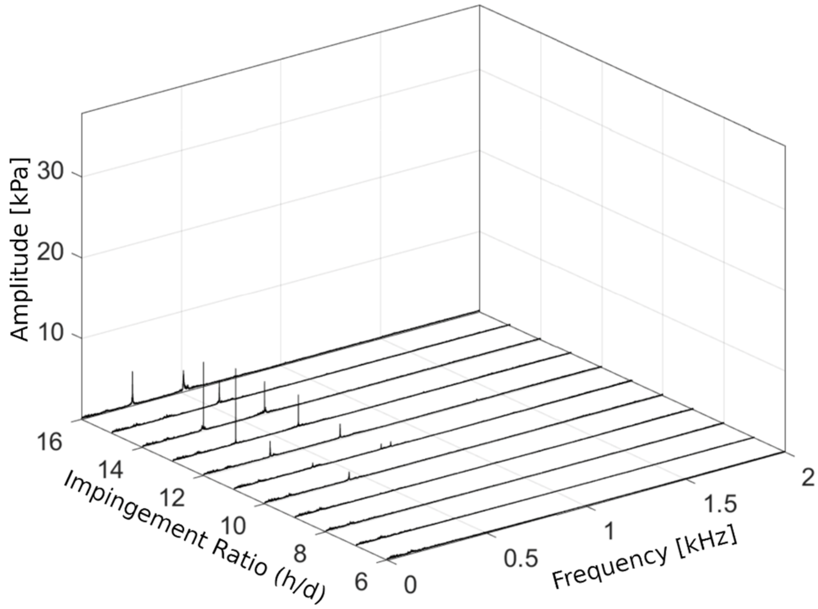

Figure D.12 Waterfall plot of sound produced by multi-slot jet main jet impinging on a flat plate. V_M = 250 m/s, d = 2 mm, V_A = 40 m/s, a = 1 mm, s = 5 mm.

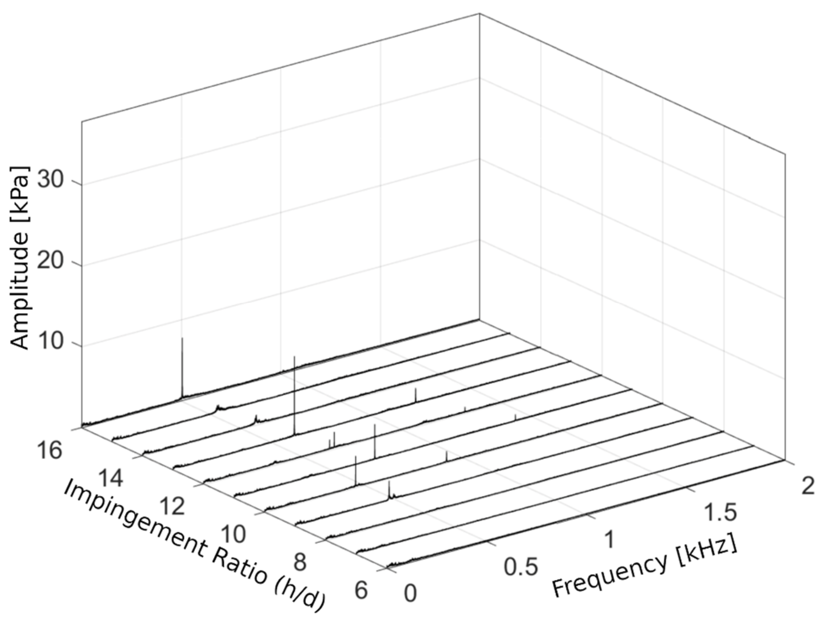

Figure D.13 Waterfall plot of sound produced by multi-slot jet main jet impinging on a flat plate. V_M = 250 m/s, d = 2 mm, V_A = 60 m/s, a = 1 mm, s = 5 mm.

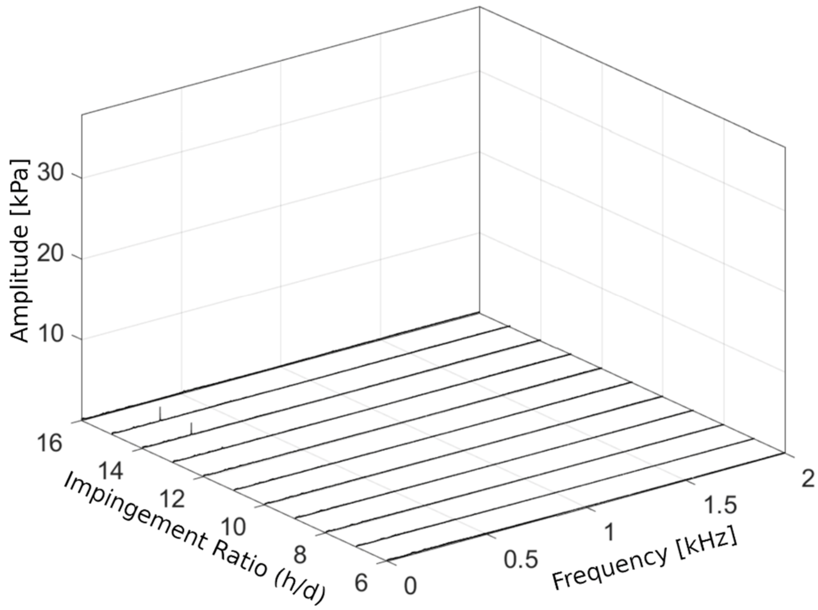

Figure D.14 Waterfall plot of sound produced by multi-slot jet main jet impinging on a flat plate. V_M = 250 m/s, d = 2 mm, V_A = 80 m/s, a = 1 mm, s = 5 mm.

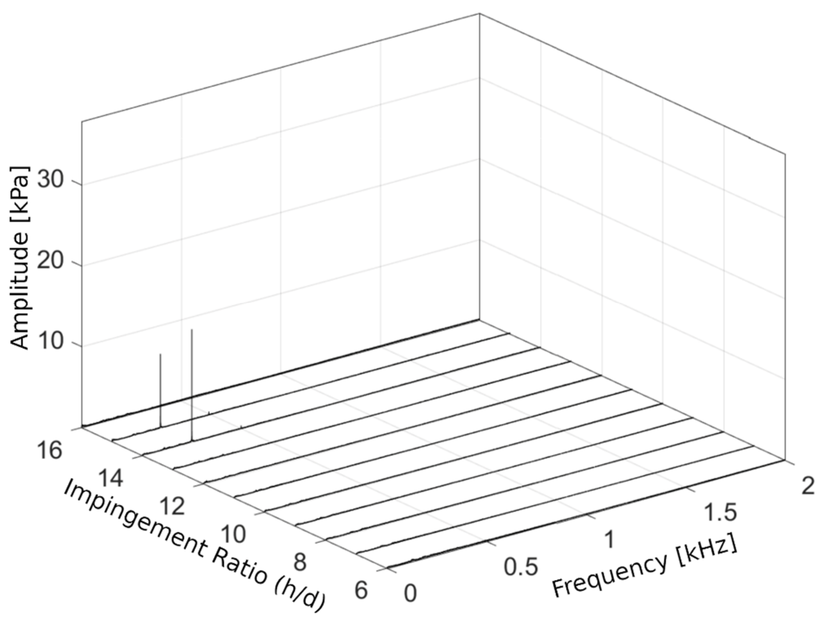

Figure D.15 Waterfall plot of sound produced by multi-slot jet main jet impinging on a flat plate. V_M = 250 m/s, d = 2 mm, V_A = 100 m/s, a = 1 mm, s = 5 mm.

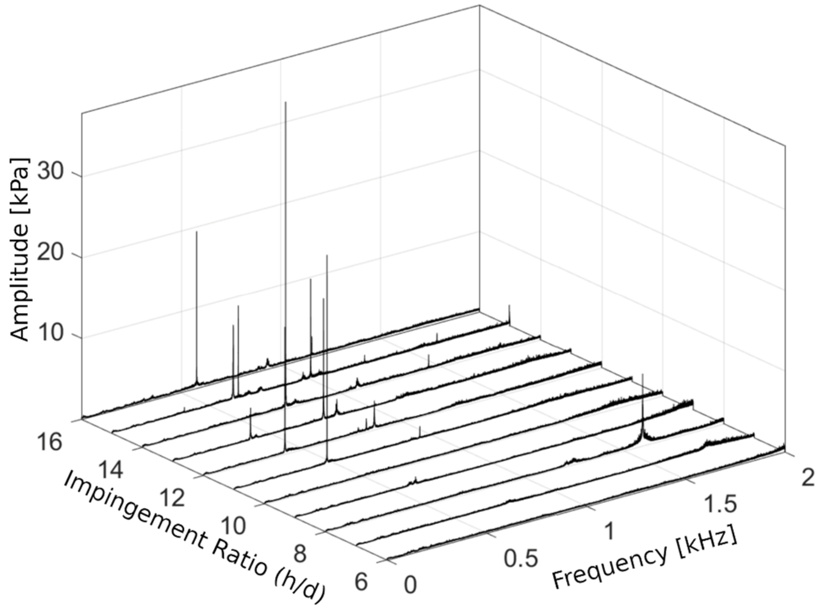

Figure D.16 Waterfall plot of sound produced by multi-slot jet main jet impinging on a flat plate. V_M = 300 m/s, d = 2 mm, V_A = 0 m/s, a = 1 mm, s = 5 mm.

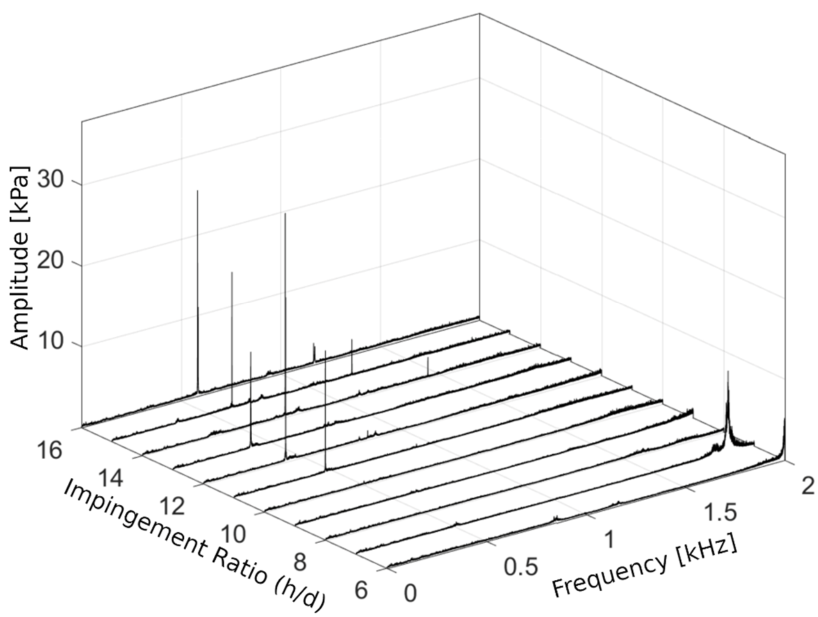

Figure D.17 Waterfall plot of sound produced by multi-slot jet main jet impinging on a flat plate. V_M = 300 m/s, d = 2 mm, V_A = 50 m/s, a = 1 mm, s = 5 mm.

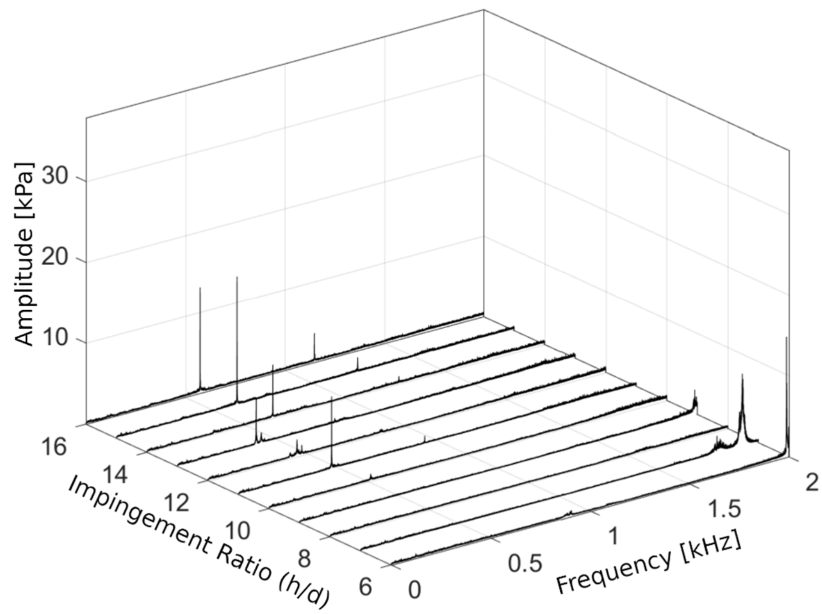

Figure D.18 Waterfall plot of sound produced by multi-slot jet main jet impinging on a flat plate. V_M = 300 m/s, d = 2 mm, V_A = 70 m/s, a = 1 mm, s = 5 mm.

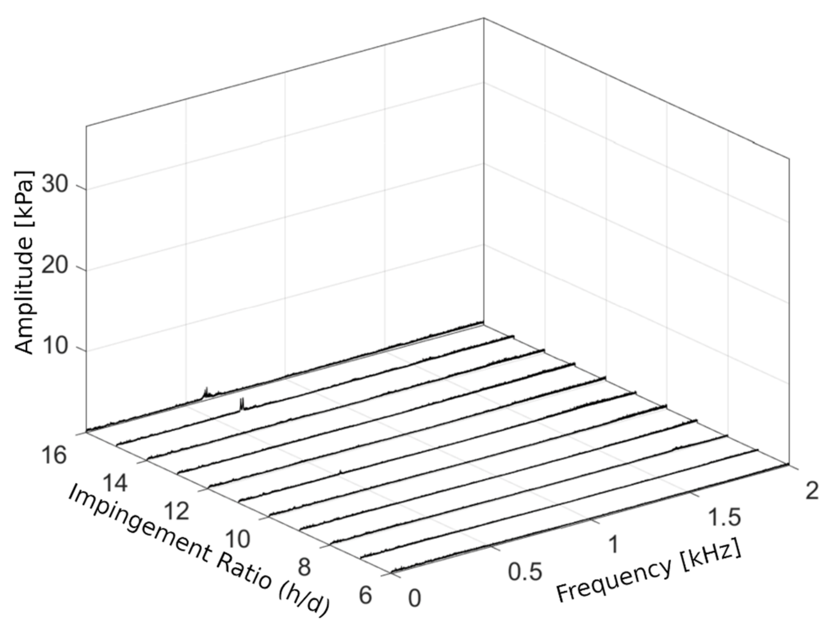

Figure D.19 Waterfall plot of sound produced by multi-slot jet main jet impinging on a flat plate. V_M = 300 m/s, d = 2 mm, V_A = 95 m/s, a = 1 mm, s = 5 mm.

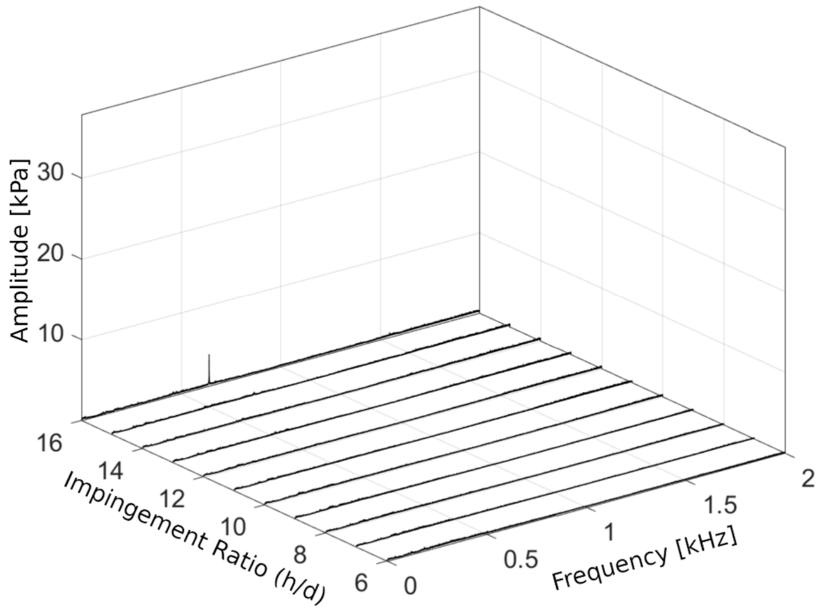

Figure D.20 Waterfall plot of sound produced by multi-slot jet main jet impinging on a flat plate. V_M = 300 m/s, d = 2 mm, V_A = 120 m/s, a = 1 mm, s = 5 mm.

<u>Data from Figure 4.9 showing the effect of "s":</u>

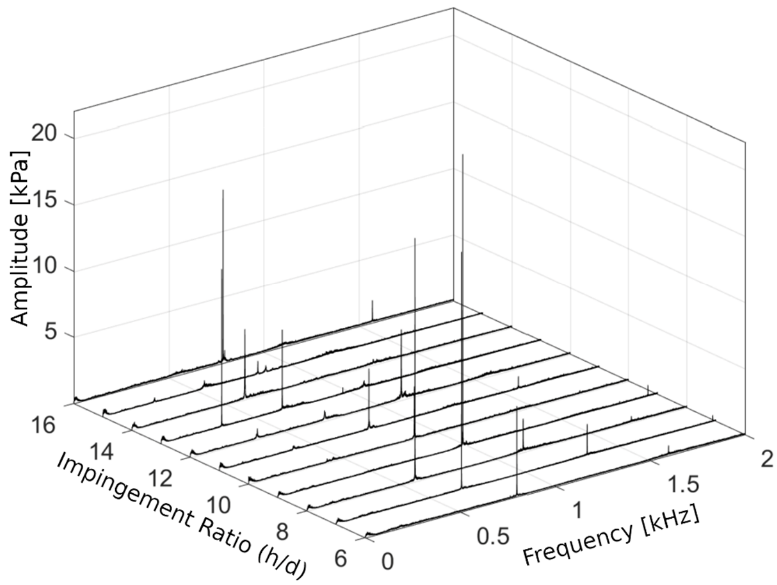

Figure D.21 Waterfall plot of sound produced by multi-slot jet main jet impinging on a flat plate. V_M = 250 m/s, d = 2 mm, V_A = 0 m/s, a = 1 mm, s = 0 mm.

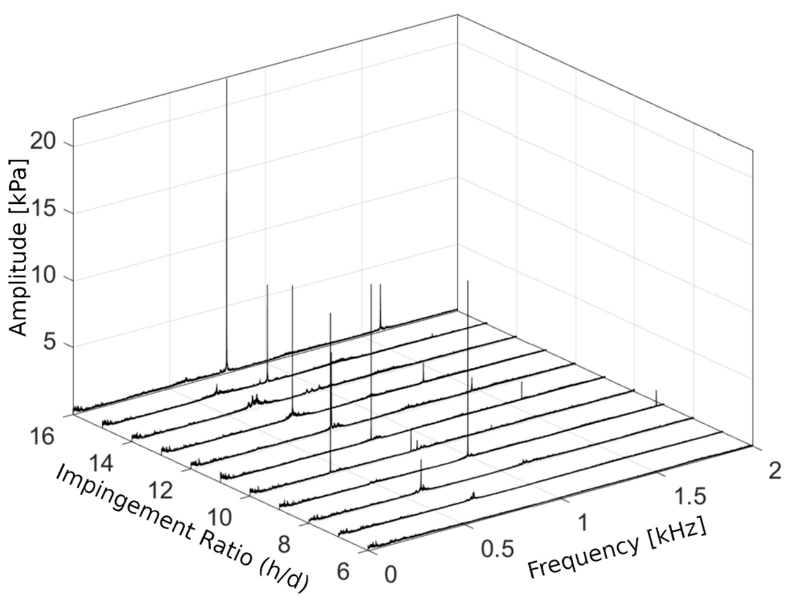

Figure D.22 Waterfall plot of sound produced by multi-slot jet main jet impinging on a flat plate. V_M = 250 m/s, d = 2 mm, V_A = 40 m/s, a = 1 mm, s = 0 mm.

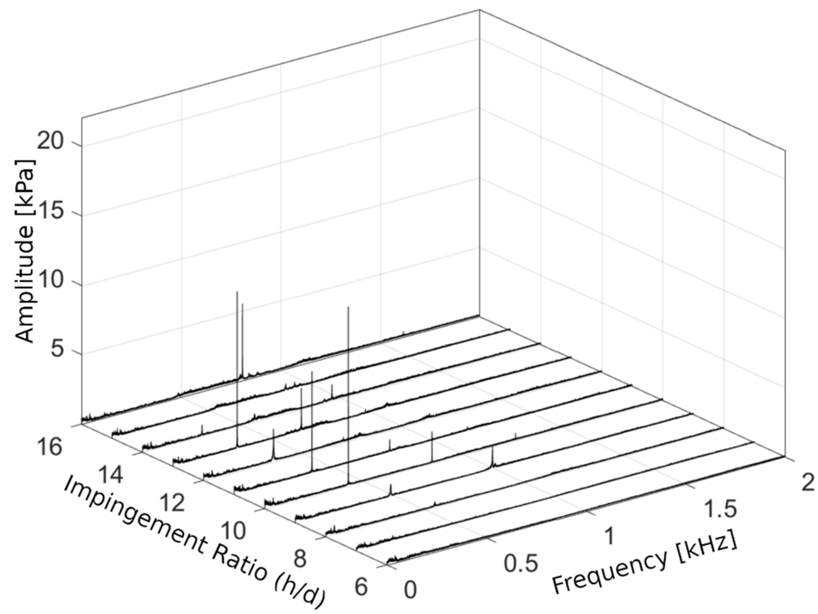

Figure D.23 Waterfall plot of sound produced by multi-slot jet main jet impinging on a flat plate. V_M = 250 m/s, d = 2 mm, V_A = 60 m/s, a = 1 mm, s = 0 mm.

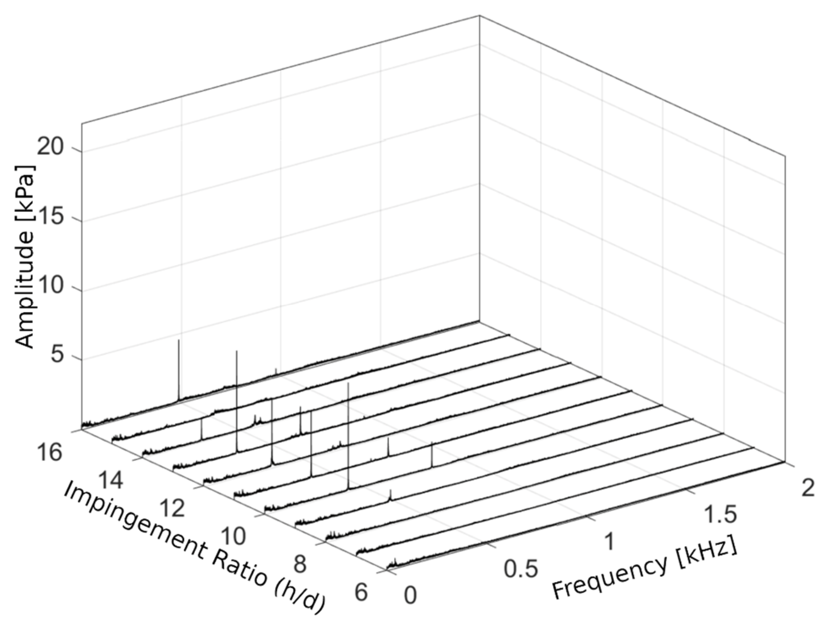

Figure D.24 Waterfall plot of sound produced by multi-slot jet main jet impinging on a flat plate. V_M = 250 m/s, d = 2 mm, V_A = 80 m/s, a = 1 mm, s = 0 mm.

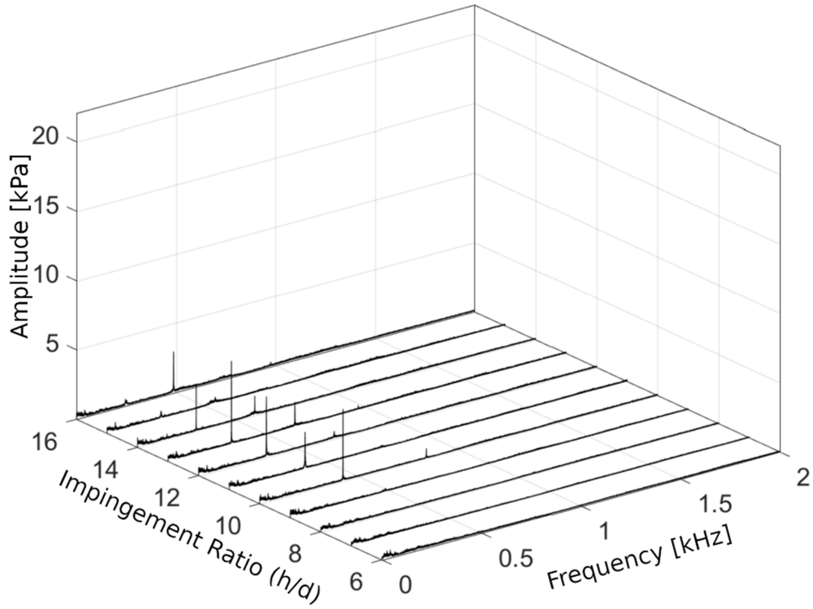

Figure D.25 Waterfall plot of sound produced by multi-slot jet main jet impinging on a flat plate. V_M = 250 m/s, d = 2 mm, V_A = 100 m/s, a = 1 mm, s = 0 mm.

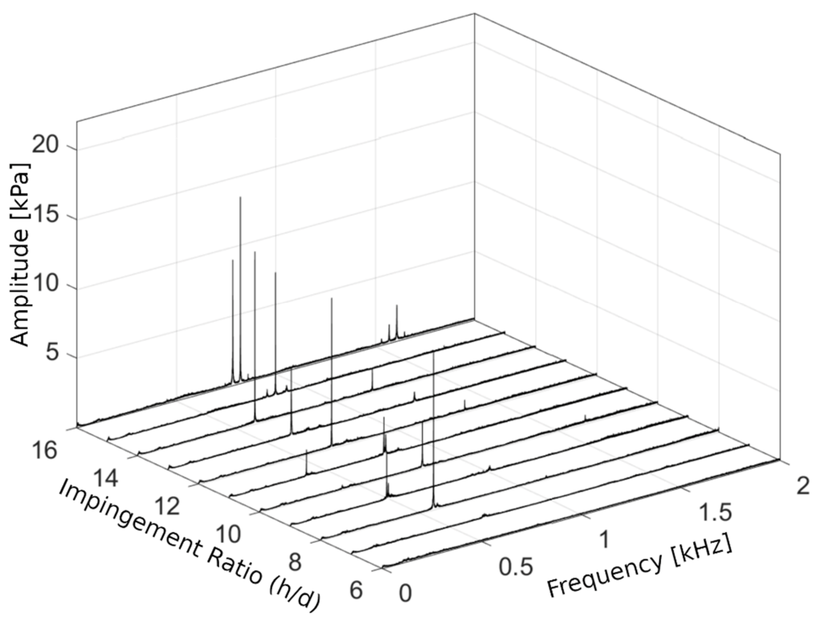

Figure D.26 Waterfall plot of sound produced by multi-slot jet main jet impinging on a flat plate. V_M = 250 m/s, d = 2 mm, V_A = 0 m/s, a = 1 mm, s = 5 mm.

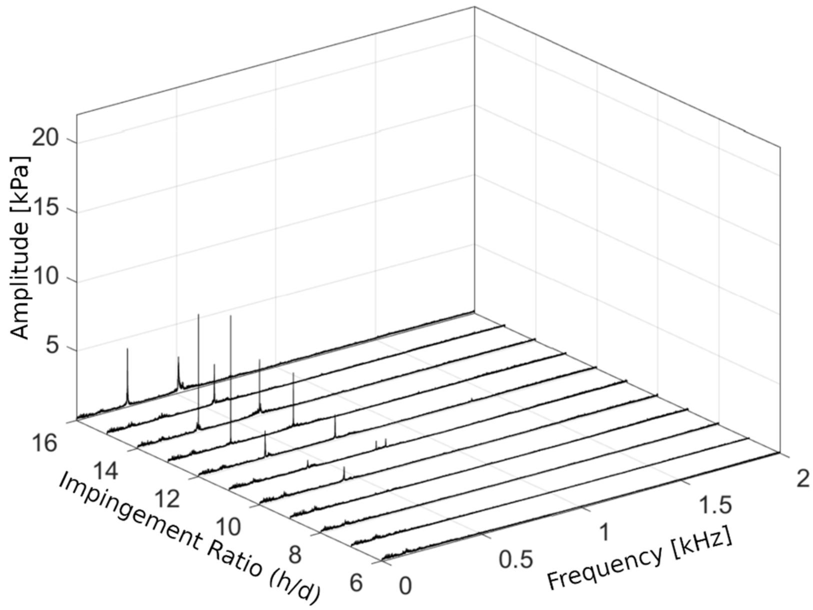

Figure D.27 Waterfall plot of sound produced by multi-slot jet main jet impinging on a flat plate. V_M = 250 m/s, d = 2 mm, V_A = 40 m/s, a = 1 mm, s = 5 mm.

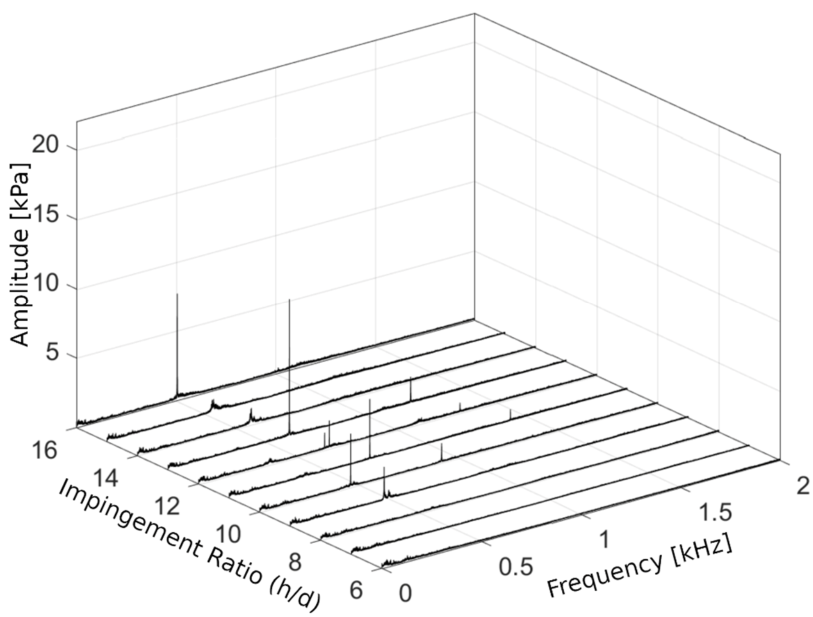

Figure D.28 Waterfall plot of sound produced by multi-slot jet main jet impinging on a flat plate. V_M = 250 m/s, d = 2 mm, V_A = 60 m/s, a = 1 mm, s = 5 mm.

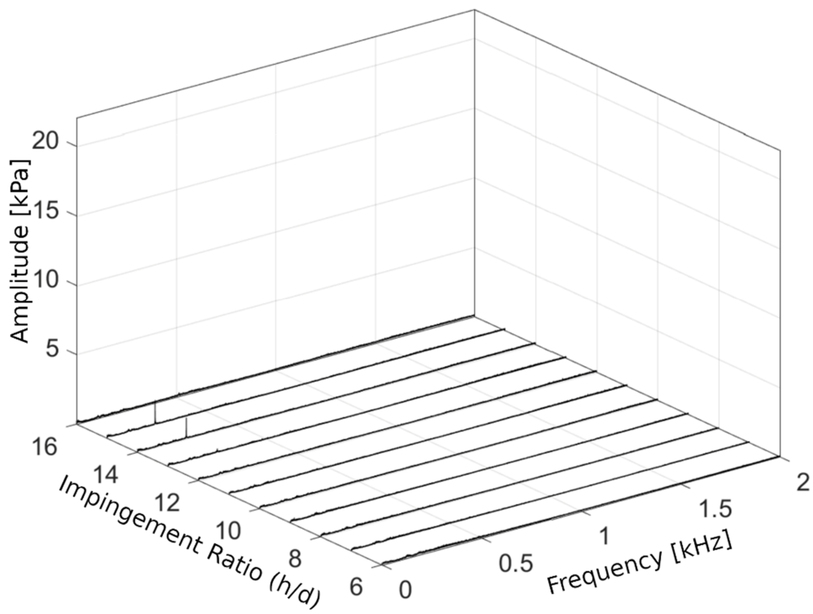

Figure D.29 Waterfall plot of sound produced by multi-slot jet main jet impinging on a flat plate. V_M = 250 m/s, d = 2 mm, V_A = 80 m/s, a = 1 mm, s = 5 mm.

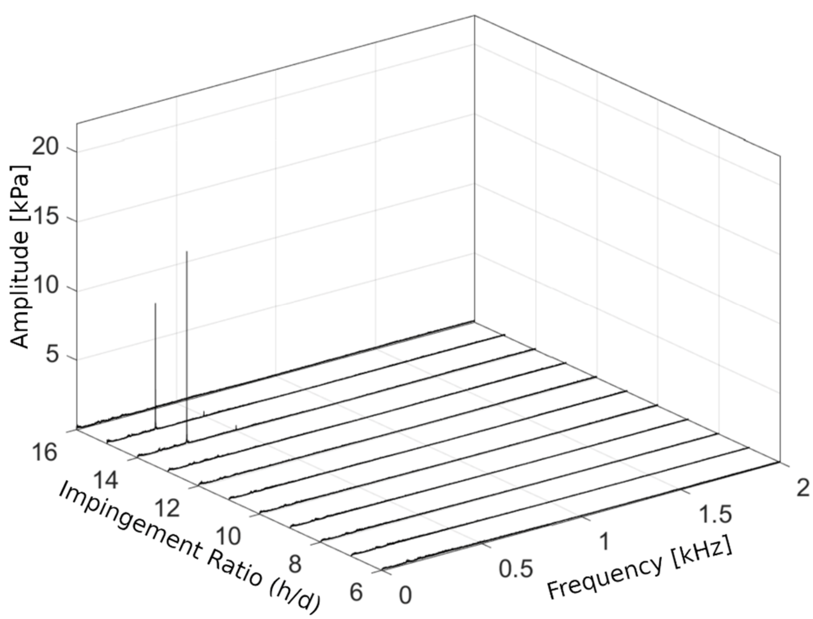

Figure D.30 Waterfall plot of sound produced by multi-slot jet main jet impinging on a flat plate. V_M = 250 m/s, d = 2 mm, V_A = 100 m/s, a = 1 mm, s = 5 mm.

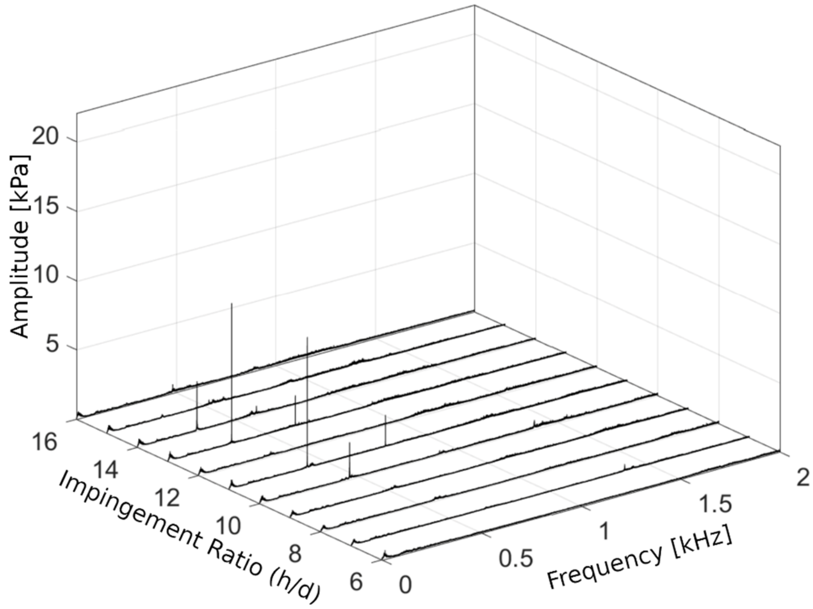

Figure D.31 Waterfall plot of sound produced by multi-slot jet main jet impinging on a flat plate. V_M = 250 m/s, d = 2 mm, V_A = 0 m/s, a = 1 mm, s = 11 mm.

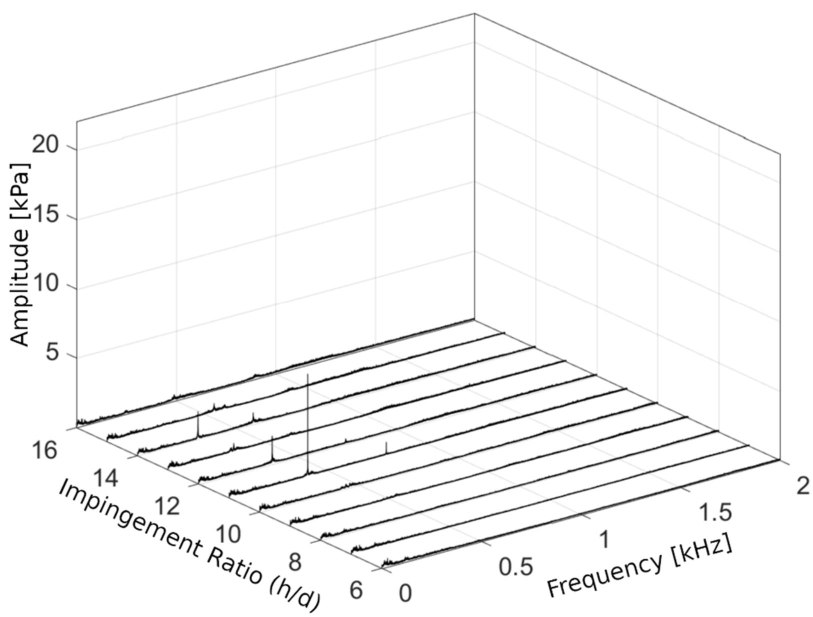

Figure D.32 Waterfall plot of sound produced by multi-slot jet main jet impinging on a flat plate. V_M = 250 m/s, d = 2 mm, V_A = 40 m/s, a = 1 mm, s = 11 mm.

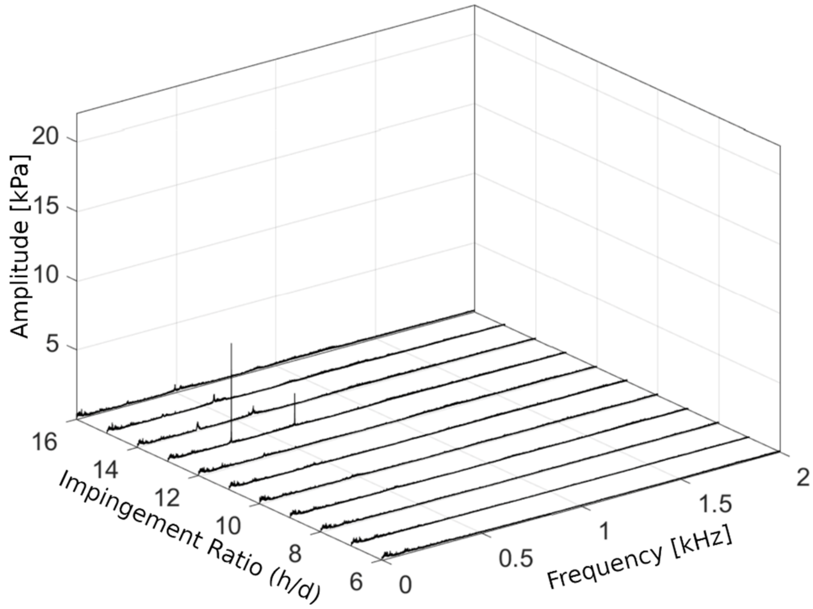

Figure D.33 Waterfall plot of sound produced by multi-slot jet main jet impinging on a flat plate. V_M = 250 m/s, d = 2 mm, V_A = 60 m/s, a = 1 mm, s = 11 mm.

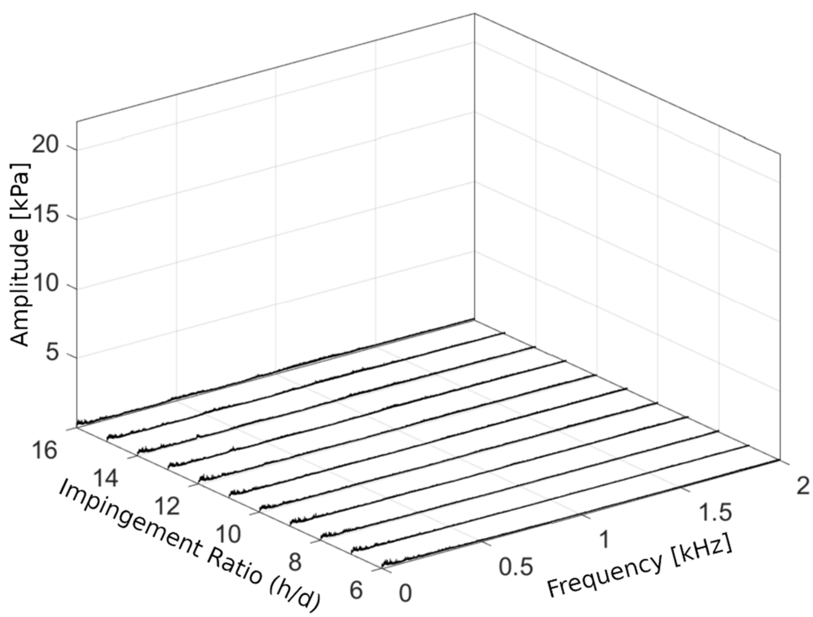

Figure D.34 Waterfall plot of sound produced by multi-slot jet main jet impinging on a flat plate. V_M = 250 m/s, d = 2 mm, V_A = 80 m/s, a = 1 mm, s = 11 mm.

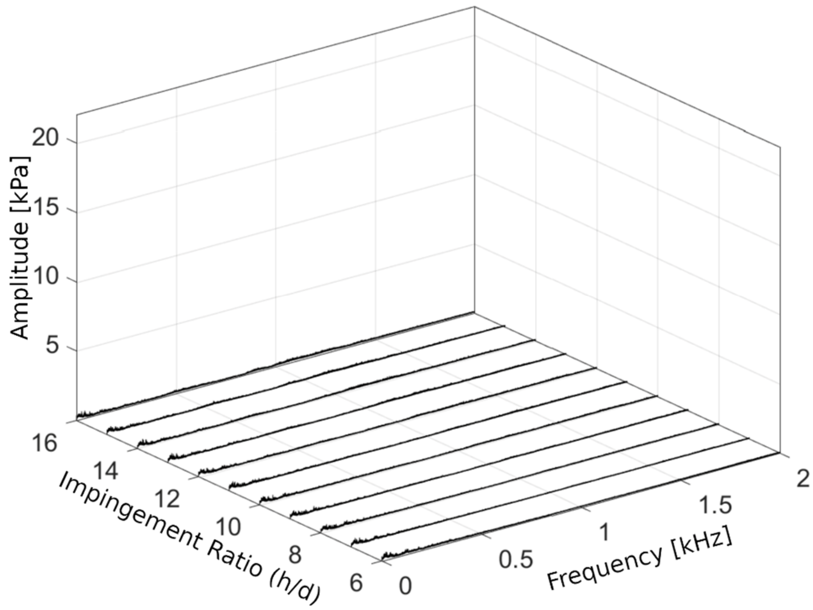

Figure D.35 Waterfall plot of sound produced by multi-slot jet main jet impinging on a flat plate. V_M = 250 m/s, d = 2 mm, V_A = 100 m/s, a = 1 mm, s = 11 mm.

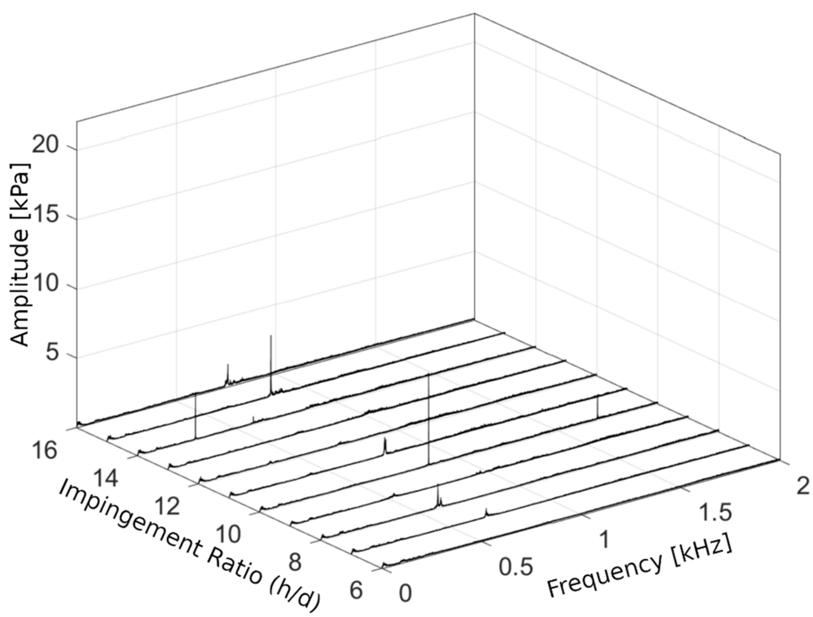

Figure D.36 Waterfall plot of sound produced by multi-slot jet main jet impinging on a flat plate. V_M = 250 m/s, d = 2 mm, V_A = 0 m/s, a = 1 mm, s = 22 mm.

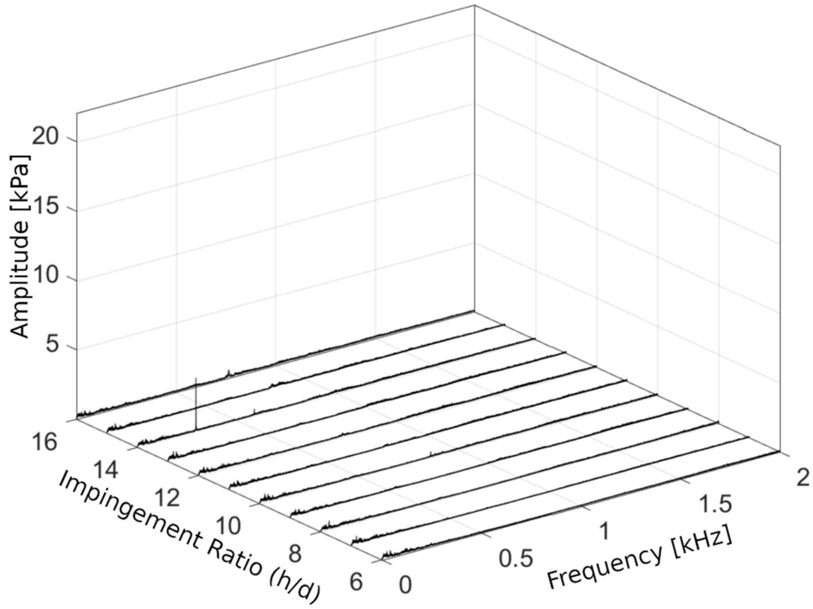

Figure D.37 Waterfall plot of sound produced by multi-slot jet main jet impinging on a flat plate. V_M = 250 m/s, d = 2 mm, V_A = 40 m/s, a = 1 mm, s = 22 mm.

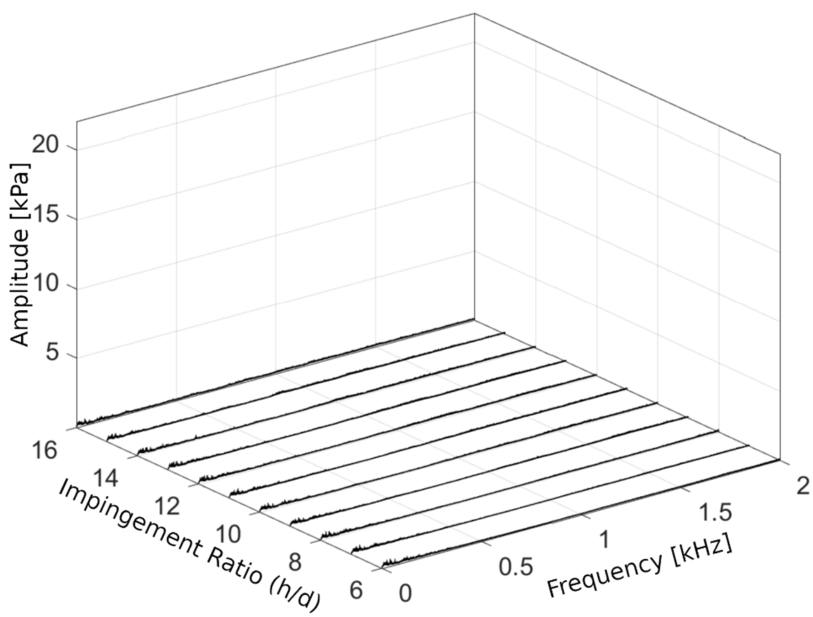

Figure D.38 Waterfall plot of sound produced by multi-slot jet main jet impinging on a flat plate. V_M = 250 m/s, d = 2 mm, V_A = 60 m/s, a = 1 mm, s = 22 mm.

Data from Figure 4.10 showing the effect of “a”:

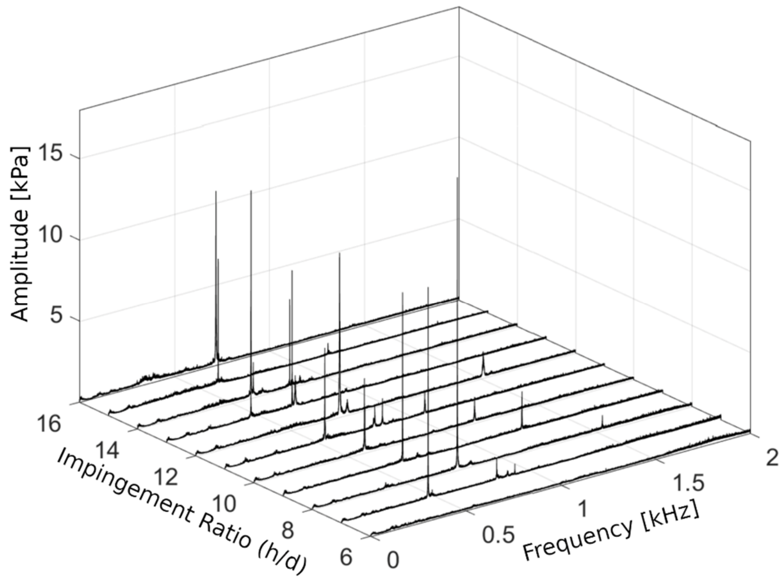

Figure D.39 Waterfall plot of sound produced by multi-slot jet main jet impinging on a flat plate. V_M = 250 m/s, d = 3 mm, V_A = 0 m/s, a = 1 mm, s = 5 mm.

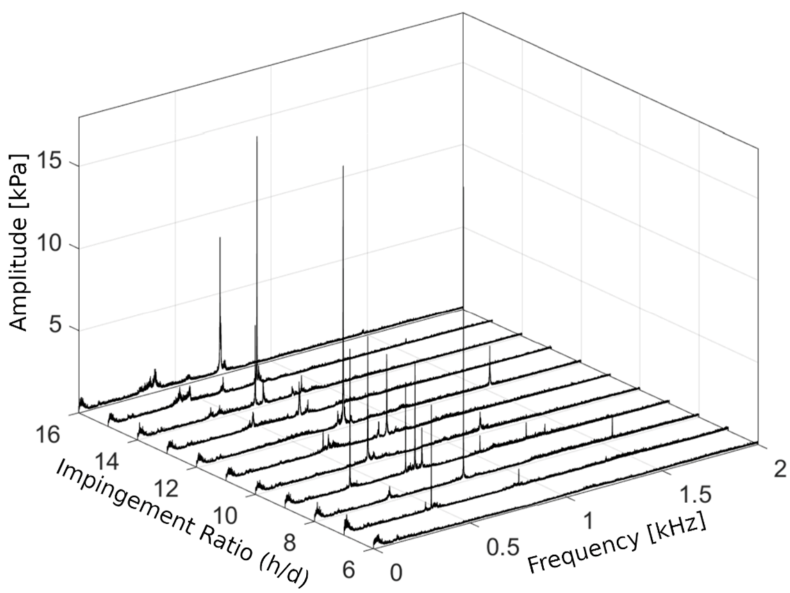

Figure D.40 Waterfall plot of sound produced by multi-slot jet main jet impinging on a flat plate. V_M = 250 m/s, d = 3 mm, V_A = 40 m/s, a = 1 mm, s = 5 mm.

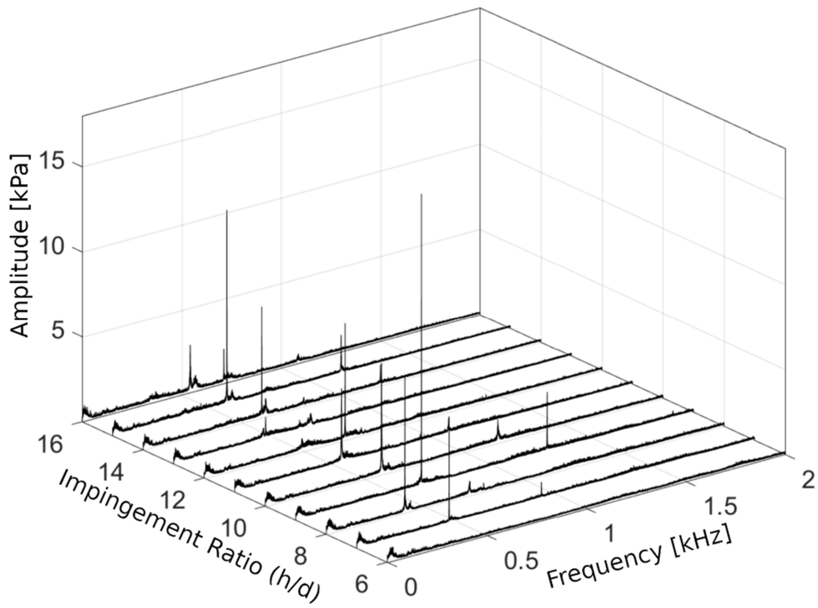

Figure D.41 Waterfall plot of sound produced by multi-slot jet main jet impinging on a flat plate. V_M = 250 m/s, d = 3 mm, V_A = 60 m/s, a = 1 mm, s = 5 mm.

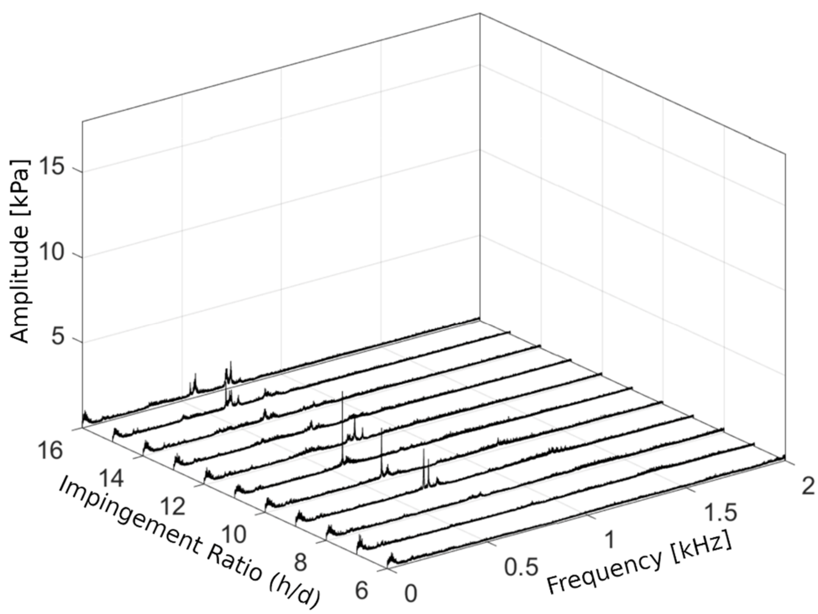

Figure D.42 Waterfall plot of sound produced by multi-slot jet main jet impinging on a flat plate. V_M = 250 m/s, d = 3 mm, V_A = 80 m/s, a = 1 mm, s = 5 mm.

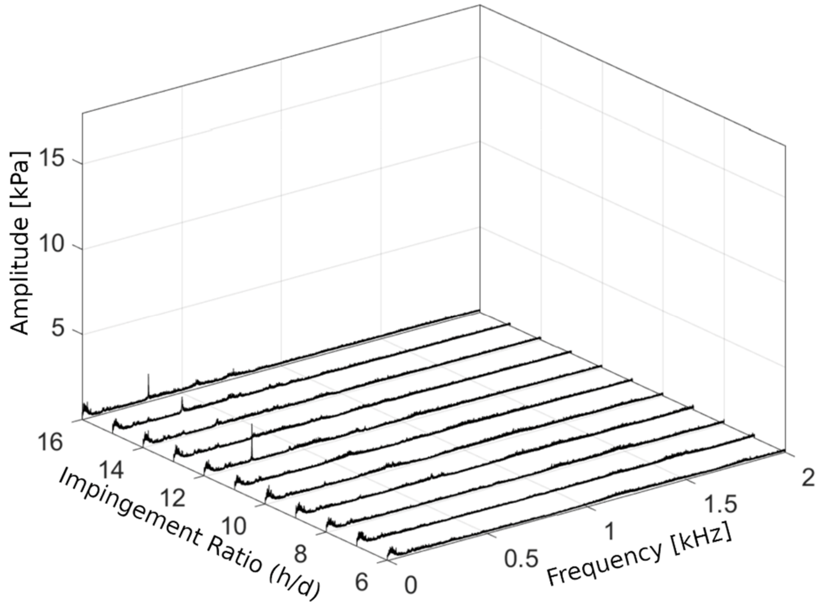

Figure D.43 Waterfall plot of sound produced by multi-slot jet main jet impinging on a flat plate. V_M = 250 m/s, d = 3 mm, V_A = 100 m/s, a = 1 mm, s = 5 mm.

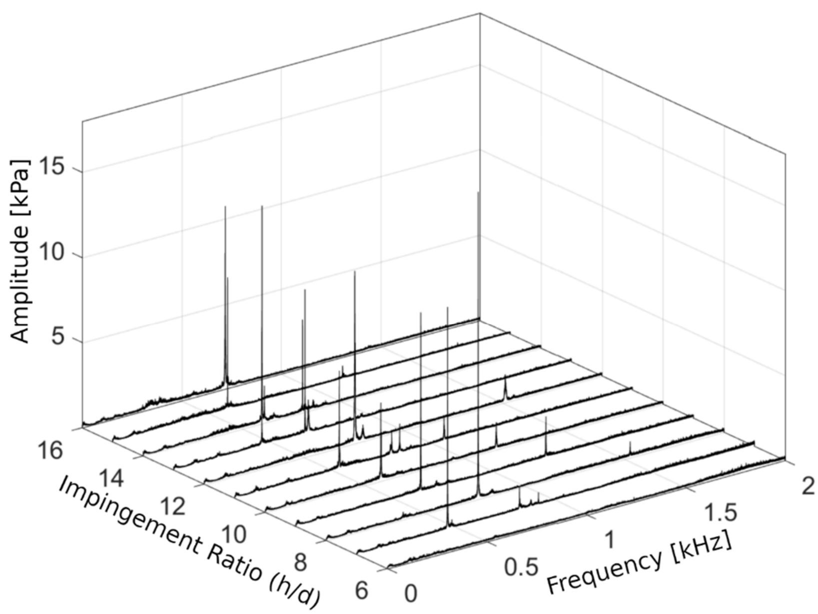

Figure D.44 Waterfall plot of sound produced by multi-slot jet main jet impinging on a flat plate. V_M = 250 m/s, d = 3 mm, V_A = 0 m/s, a = 1.5 mm, s = 5 mm.

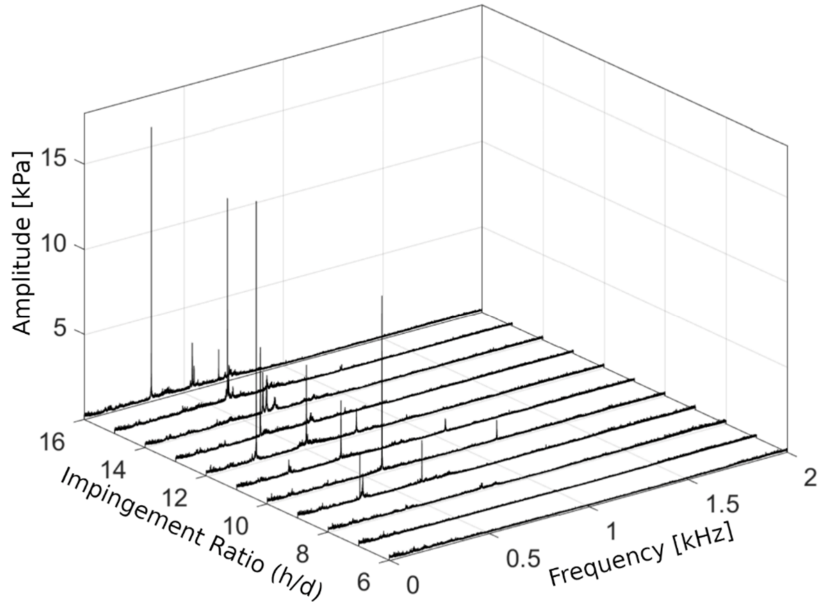

Figure D.45 Waterfall plot of sound produced by multi-slot jet main jet impinging on a flat plate. V_M = 250 m/s, d = 3 mm, V_A = 40 m/s, a = 1.5 mm, s = 5 mm.

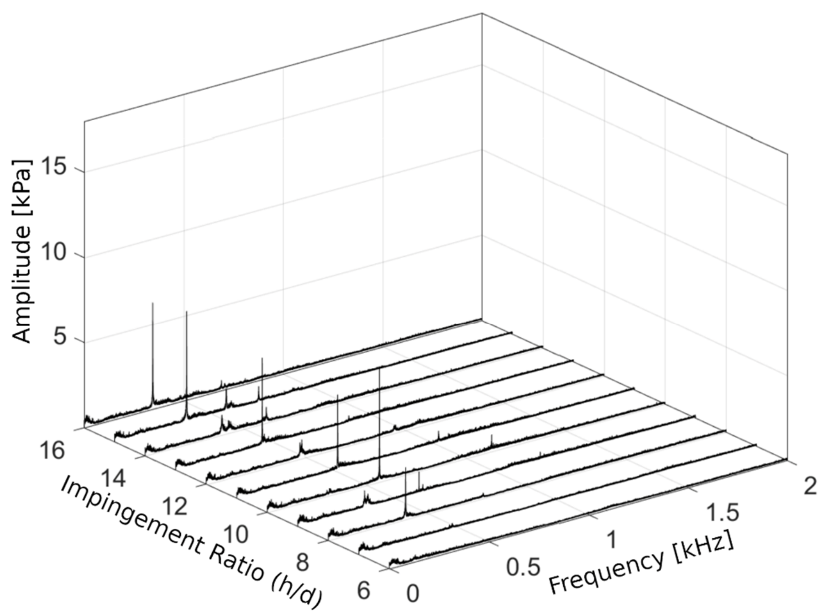

Figure D.46 Waterfall plot of sound produced by multi-slot jet main jet impinging on a flat plate. V_M = 250 m/s, d = 3 mm, V_A = 60 m/s, a = 1.5 mm, s = 5 mm.

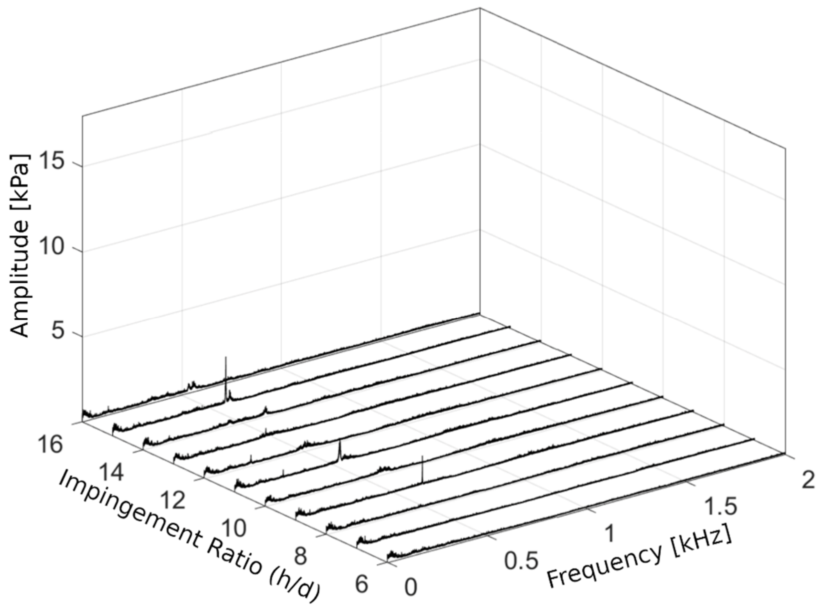

Figure D.47 Waterfall plot of sound produced by multi-slot jet main jet impinging on a flat plate. V_M = 250 m/s, d = 3 mm, V_A = 80 m/s, a = 1.5 mm, s = 5 mm.

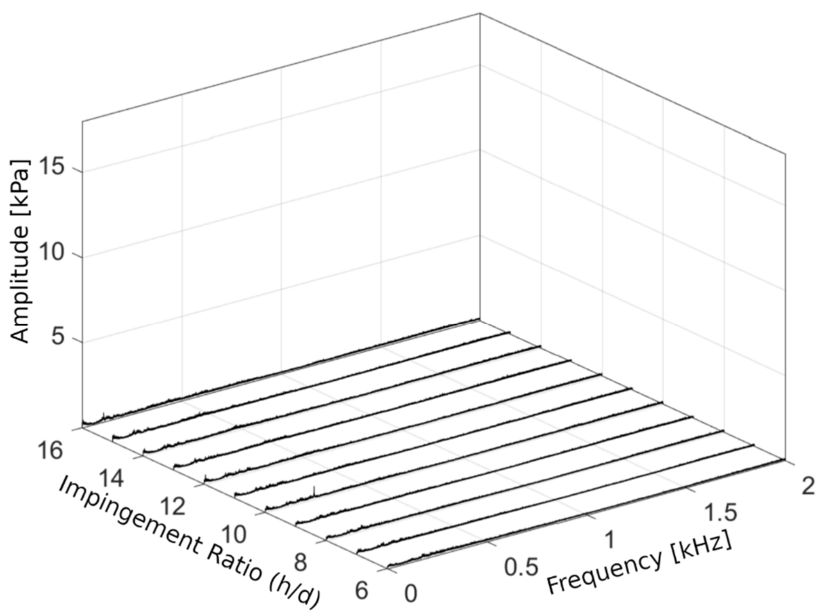

Figure D.48 Waterfall plot of sound produced by multi-slot jet main jet impinging on a flat plate. V_M = 250 m/s, d = 3 mm, V_A = 100 m/s, a = 1.5 mm, s = 5 mm.

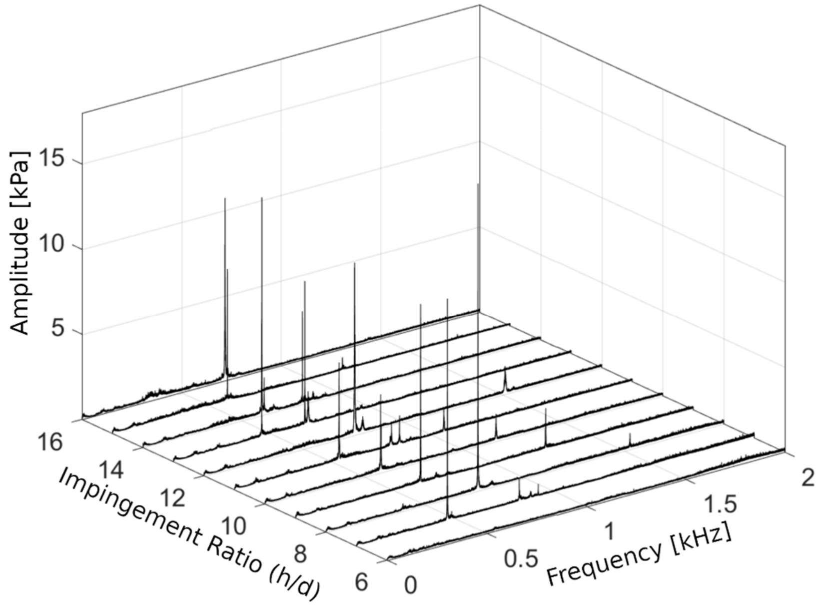

Figure D.49 Waterfall plot of sound produced by multi-slot jet main jet impinging on a flat plate. V_M = 250 m/s, d = 3 mm, V_A = 0 m/s, a = 3 mm, s = 5 mm.

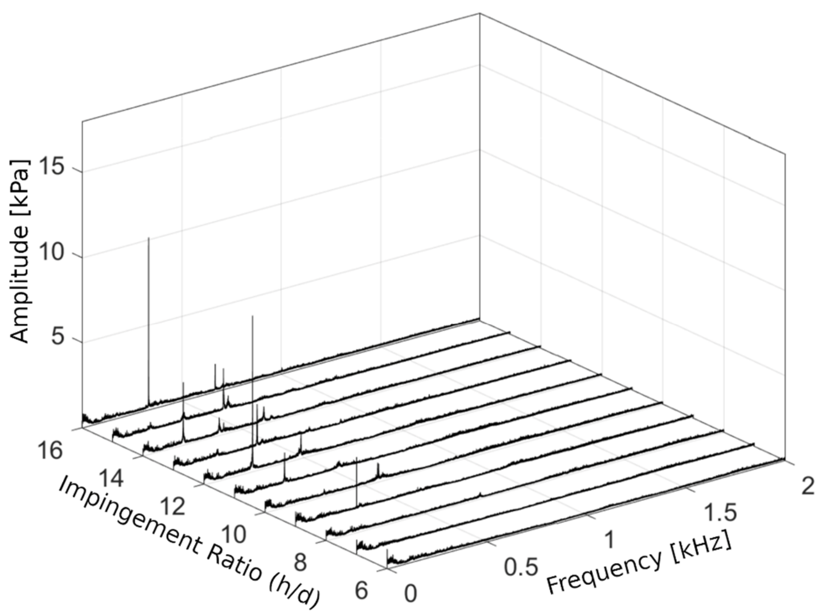

Figure D.50 Waterfall plot of sound produced by multi-slot jet main jet impinging on a flat plate. V_M = 250 m/s, d = 3 mm, V_A = 40 m/s, a = 3 mm, s = 5 mm.

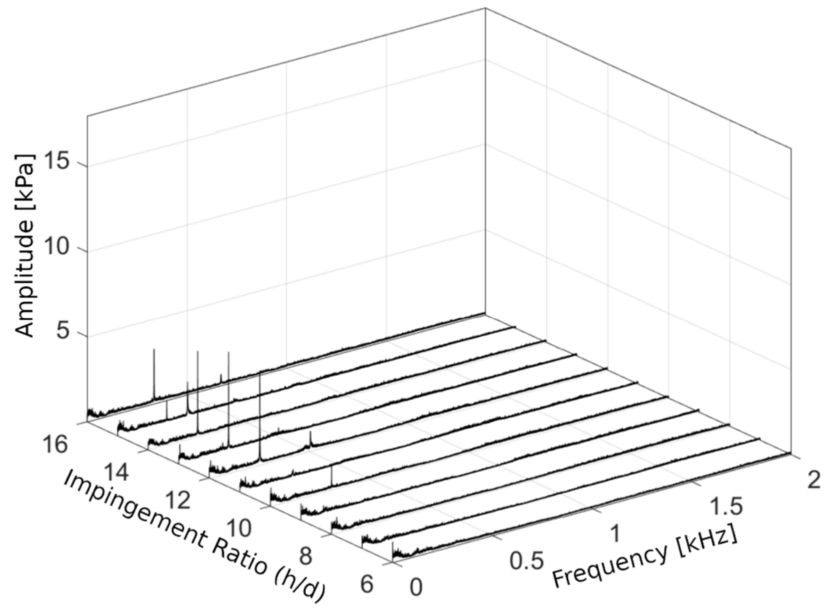

Figure D.51 Waterfall plot of sound produced by multi-slot jet main jet impinging on a flat plate. V_M = 250 m/s, d = 3 mm, V_A = 60 m/s, a = 3 mm, s = 5 mm.

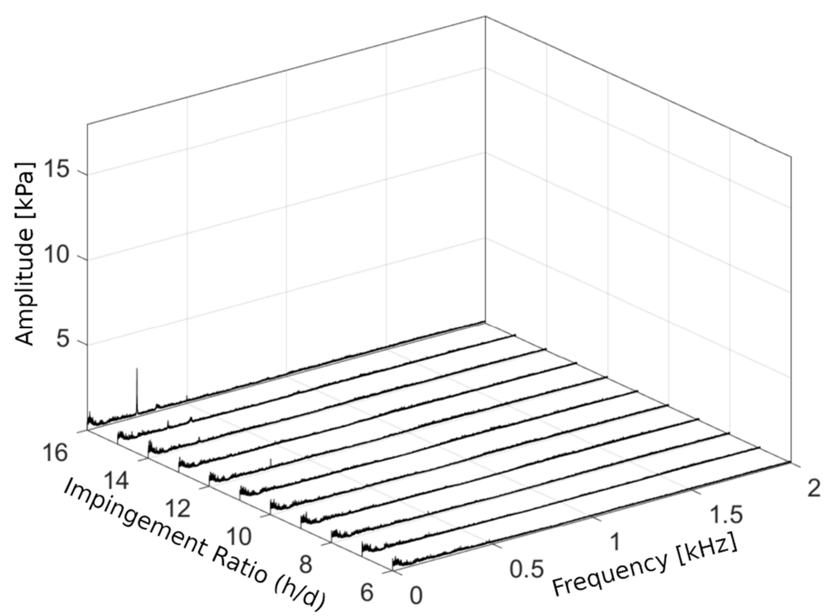

Figure D.52 Waterfall plot of sound produced by multi-slot jet main jet impinging on a flat plate. V_M = 250 m/s, d = 3 mm, V_A = 80 m/s, a = 3 mm, s = 5 mm.